Opto-electrical surface engineering of wafer based c-Si solar cells

Ingenito, Andrea

DOI
10.4233/uuid:1cc31eff-4871-4d6f-8f32-8669257dc1ab

Publication date
2016

Document Version
Final published version

Citation (APA)
Ingenito, A. (2016). *Opto-electrical surface engineering of wafer based c-Si solar cells*. [Dissertation (TU Delft), Delft University of Technology]. https://doi.org/10.4233/uuid:1cc31eff-4871-4d6f-8f32-8669257dc1ab

Opto-electrical surface engineering of wafer based c-Si solar cells

Andrea Ingenito

Opto-electrical surface engineering of wafer based c-Si solar cells

Proefschrift

ter verkrijging van de graad van doctor
aan de Technische Universiteit Delft,
op gezag van de Rector Magnificus prof. ir. K.C.A.M Luyben,
voorzitter van het College voor Promoties,
in het openbaar te verdedigen op 18 April 2016 om 10:00 uur

door

Andrea Ingenito

Master of Science, University of Naples Federico II
geboren te Salerno, Italy

This dissertation has been approved by the promotor:
prof. dr. M. Zeman

and

copromotor:
dr. O. Isabella

Composition of the doctoral committee:

Rector Magnificus,	chairperson
prof. dr. M. Zeman,	Technische Universiteit Delft, promotor
dr. O. Isabella,	Technische Universiteit Delft, copromotor

Independent members:

prof. dr. A. Weeber	Technische Universiteit Delft and ECN
dr. P. P. Altermatt	Trina solar l.t.d.
prof. dr. J. Poortmans	imec
dr. A. Poruba	Institute of Physics, Academy of Sciences of the Czech republic, v.v.i. and Fill Factory s.r.o.
prof. dr. S. W. Glunz	Fraunhofer-Institut für Solare Energiesysteme ISE

This thesis project was carried with a subsidy from the Dutch Ministry of Economic Affairs under the EOS-LT program (Project No. EOSLT10037).

Front and back cover is from a picture taken by Chantal Jimenez and designed by Andrea Ingenito
Thesis printed by: CPI-Koninklijke Wöhrmann – Zutphen

ISBN: 978-94-6328-033-4

A digital copy of this thesis is available at: http://repository.tudelft.nl

Per Ilaria, Chantal e

i miei genitori.

Contents

1

Introduction

1.1 The promise of Photovoltaics

Average human power consumption in 2015 has been of ~17 TW [1] and according to recent prediction provided by the International Energy Agency (IEA), such number is expected to double by 2050 [2]. To meet the continuous increase of mankind's energy demand, renewable energy sources alternative to commonly used fossil fuels are necessary. In fact, fossil fuels not only constitute a limited energy source but are also the culprits of increased air pollution and global warming [3]. Climate changes due to increase of CO_2 emission are becoming a serious issue for this planet. The so called *climate crises* has been the main topic of the last United Nations Climate Change Conference, COP 21 or CMP 11 which was held in Paris, France, from 30 November to 12 December 2015. As result of the conference a global agreement between 196 countries representing more than 55% of the greenhouse emission has been reached [4]. The agreement calls for zero greenhouse emission for the first half of the 21th century [4]. Direct conversion of sunlight into electricity is one of the most promising technologies for achieving the COP21 agreement. At 2015 G-20 Summit, the Indian Prime Minister Narendra Modi along with French President François Hollande, proposed to create an alliance of solar-rich countries similar to the Organization of the Petroleum Exporting Countries (OPEC) [5]. At COP 21 Summit, the two leaders sent written invitations to over 100 countries to join the coalition proposed to be called the International Agency for Solar Policy and Application (InSPA) [6]. This clearly indicates that the attention of world leaders towards solar energy is finally stronger. Solar energy is the most abundant renewable energy source on Earth. In particular, the amount of energy that the sun strikes every year on emerged continents is more than 30 times larger than the total reserve of coal and 1500 times larger than the current human energy consumption [3]. To be used by our society, solar energy must be converted in other energy forms adopted by humans such as electricity or cell-fuels. The physical effect for which solar energy is converted into electricity by a semiconductor material is known as photovoltaic (PV) effect. The semiconductor employed in most of today's solar cells is crystalline silicon (c-Si). Silicon is in fact an abundant element in Earth's crust and is non-toxic. In addition, c-Si solar modules have demonstrated high durability and long term stability making this technology to be a PV market leader with a share higher than 90% [7]-[10].

Global cumulative installed PV capacity in 2014 is estimated to be around 170 GW_p [11] and additional 50 GW_p are expected to be installed in 2015 [12]. Although this seems still a small number, it should be seen in the contest of the exponential growth over the last 10 years of the cumulative PV installed capacity (see Figure 1.1). In addition, despite the ongoing economic crisis and political uncertainties, the number and volume of the PV market is still increasing, mainly driven by the fast growing Asian PV market [11] (especially in China and Japan).

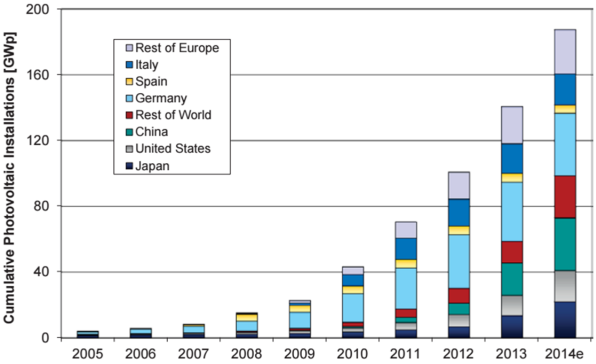

Figure 1.1. Annual PV installations from 2005 to 2014 per different counties and geographic area, taken from [11].

One of the reasons for the exponential increase of the cumulative installed PV capacity is related to the constant price reduction of the PV modules which within the last 30 years has followed a learning curve with a learning factor of 20% [13] which has been driven by continuous technology development. The PV price reduction has been even stronger (~80 %) between 2008 and 2012 due to the entry of the Chinese PV market and economic crises. This has brought the price of PV modules, commonly expressed in euro per watt peak (€/W_p), below 0.6 €/W_p (in Germany) [14]. To evaluate how cost-effective is the energy generated by a certain technology the so-called Levelized Cost of Electricity (LCoE) has been introduced [15]. The LCoE is defined as the total cost of installing and operating a project expressed in dollars or euros per kilowatt-hour (kWh) of electricity generated by the system over its life [15]. Therefore, it includes: the initial investment, cost of capital, maintenance, installations and cost of fuel. For instance, the LCoE in Germany has reached values between 0.078 and 0.124 € / kWh in 2013, leading to a cost of a solar power plant between 1000 and 1800 € / kW_p [16]. The average end-costumer electricity price from conventional power generation technologies in Germany in 2013 was of 0.289 Euro/kWh. These data indicate that the LCoE of PV plants has reached the grid parity with other power generating technologies [16]. Even more impressive results have been obtained in India where electricity produced by large PV plant has reached the value of 0.05 cents/kWh. Despite that, pressure on manufacturing companies for price reduction will substantially remain also in 2015 since the anticipated PV production will be > 60 GW_p while the demand is expected to be around 50 GW_p [7] [12] [17]. Therefore, there will be an overcapacity of PV production also in 2015 that leads to a gap between the demand and the offer. Notice that, this gap is constantly decreasing thanks to the reduction of PV module cost. Therefore, PV module price is one of the key for boosting solar energy installation and utilization. The International Roadmap for Photovoltaics (ITRPV) foresees three strategies [7] to make PV more cost-effective:

i. Continue the cost reduction per piece along the entire value chain by optimizing the utilization of the installed production capacity and by using Si and non-Si materials more efficiently.
ii. Introduce specialized module products for different market applications (i.e. trade-off between cost-optimized, highest volume products and fully customized niche products).
iii. Improve module power/cell efficiency without significantly increasing processing costs.

To meet the goal of strategy (i) raw material costs need to be reduced. In fact, as shown in [8], the cost of a PV module is mainly determined by the silicon wafer, the metallization and the module. Therefore, a possible solution to reduce solar cell price would require the usage of thinner wafers or cheaper substrates. When focusing on the first solution, ITRPV predictions indicate that the minimum as cut wafer thickness is expected to decrease from the current 180 μm to 100 μm in 2025 [8]. However, wafer thickness reduction needs to be accompanied by innovative cutting and handling methods, high efficiency cell concepts and new interconnection and module encapsulation methods capable to minimize breakage. In addition, metallization paste/inks containing Ag or Al constitute the most expensive (10-20% of the cell costs) non-silicon material forming a c-Si solar cell [7]. In fact, current Ag consumption for a 156 x 156 mm^2 wafer is of 100 mg and is expected to decrease to 40 mg in 2025 [7]. Despite its lower consumption Ag price is expected to remain constant in the coming years. Copper has been proposed as a valid candidate for replacing Ag metallization, however, its introduction in mass production is not expected to happen before 2018 [7]. Building integrated photovoltaic (BIPV) is an emerging field in PV industry [39]. In the framework of strategy (ii), BIPV can be seen as a strong candidate to decrease the LCOE of PV modules by integrating the PV functionality to the building elements. Aside improving material utilization, cell / module efficiency should also be increased (see strategy (iii)). Focusing on cell efficiency, recombination in the bulk, front and rear side needs to be minimized. The reduction of each recombination component at industrial level should be achieved by using lean processes requiring minimum investments in new tools.

1.2 Light management in c-Si solar cells

As stated in Section 1.1, for continuing large-scale implementation of c-Si solar cells, their cost must be further lowered by optimizing manufacturing processes, offering customized products and using fewer materials without sacrificing the efficiency [19]-[21]. Focussing on the last strategy, the Si wafer contributes to more than 50% of the total cell cost, therefore a possible solution to decrease material costs would require the usage of thinner wafer. Thinner wafers are not only cheaper but also lighter and more flexible [22], exhibit a lower bulk recombination and [6] and in case of Czochralski wafers also a lower light-induced degradation [23][24]. However, as c-Si is an indirect band-gap semiconductor, the absorption in the infrared region (IR) of the solar spectrum is significantly reduced when the wafer thickness is reduced. Therefore, advanced light trapping schemes are essential to enhance light absorption in thin c-Si solar cells [25]. The main aspects of light management in (thin) c-Si solar cells are:

1. Light in-coupling;
2. Light scattering;
3. Internal reflectance;

These three techniques have to be optimal and concurrently active in order to achieve broad band light absorption enhancement. In addition, when pushing them to their ideal limits of: (i) perfect broad-band light-in coupling (reflectance $R = 0 \ \forall \ \lambda$), (ii) totally randomized and ideally diffused light inside the slab (the so-called Lambertian scattering), and (iii) ideal internal reflectance ($R_b = 1 \ \forall \ \lambda$), they fulfil the ideal assumptions of the so-called $4n^2$ classical absorption limit in a dielectric slab [26], where n is the real part of its complex refractive index. In such case, in the wavelength region of weak absorption such light trapping scheme theoretically results in an absorption enhancement factor of 50 ($4n^2$) [26]. In other words this means that by employing such advanced light management techniques the optical thickness of the absorber becomes 50 times larger than its geometrical one. In Table 1.1 state-of-the-art and advanced light management techniques are summarized.

	Light-in coupling	Light scattering	Back reflector
State-of-the-art	Random pyramids + ARC	Random pyramids, iso-textures	Metals, Metal/dielectric
Advanced	Nano-texturing, Mie coating, NWs	NWs, MST, gratings, plasmonic, honey comb	Dielectric, plasmonic

Table 1.1. State-of-the-art and advanced light management techniques. The abbreviation NWs stays for nano-wires while MST for modulated surface textures.

1.2.1 Light in-coupling

Light in-coupling is a light management technique aiming to minimize the front reflectance losses. In Figure 1.2 (d), (e), (f) is reported the so-called first reflectance (R_f), obtained from linear extrapolation at long wavelengths of the measured R for four different optical systems. As Figure 1.2 (d) clearly shows, for polished Si in air (see sketch in Figure 1.2 (a)) more than 30% of the incoming light is lost in reflection. Such R losses are not tolerable to reach high absorption and therefore high conversion efficiency. A well-established technique to reduce R_f, consists in texturing of the front surface. Random pyramidal texturing (see in Figure 1.2 (b)) is typically employed in state-of-the-art c-Si solar cells and leads to Rf around 10% (see red curve in Figure 1.2 (e)). Such surface texturing is fabricated by using alkaline etching of a <100> Si wafers leading to random pyramids with <111> surface orientation. To further, reduce R_f, random textured surfaces are usually coated with an ARC of a thickness (d_{ARC}) designed to minimize R around the wavelength of design (λ_{ARC}) according to the following equation:

$$d_{ARC} = \frac{\lambda_{ARC}}{4 \cdot n_{ARC}} \quad 1.1$$

where, n_{ARC} is the real part of complex refractive index of the ARC. An example is presented in Figure 1.2 (e), where a SiN_x with real part of the complex refractive index (n_{ARC} = 2.03 at λ = 600 nm)[1] is used. However, as Figure 1.2 (e) indicates, the antireflective effect of the ARC leads to R_f values below 5% only within a certain wavelength range [450-850] nm.

Advanced light in-coupling such as surface nano-texturing can feature a strong and broad-band anti-reflective effect (see Table 1.1). As shown in Figure 1.2 (f) measured R_f below 1% can be achieved by nano-textured surfaces even without additional ARC. Such anti-reflection properties are achieved due to a gradual refractive index matching between the incident medium (air) and Si nano-cones which minimize the intensity of

---

[1] Such value constitutes the optimal value between parasitic absorption at short wavelengths and refractive index matching after cell encapsulation.

the reflected wave-vector (k). The nano-texturing, studied in this work, was fabricated by using a mask-less process implemented in commercially available reactive ion etcher (RIE) tool. Other advanced light-in coupling techniques such as Mie coating are also capable to deliver low R_f (<2%) on broad wavelength range even without ARC [27]. However, Mie coatings are usually fabricated by using advanced lithographic techniques (such as ion beam or nano-imprinting) which at the moment are less suitable for large scale application.

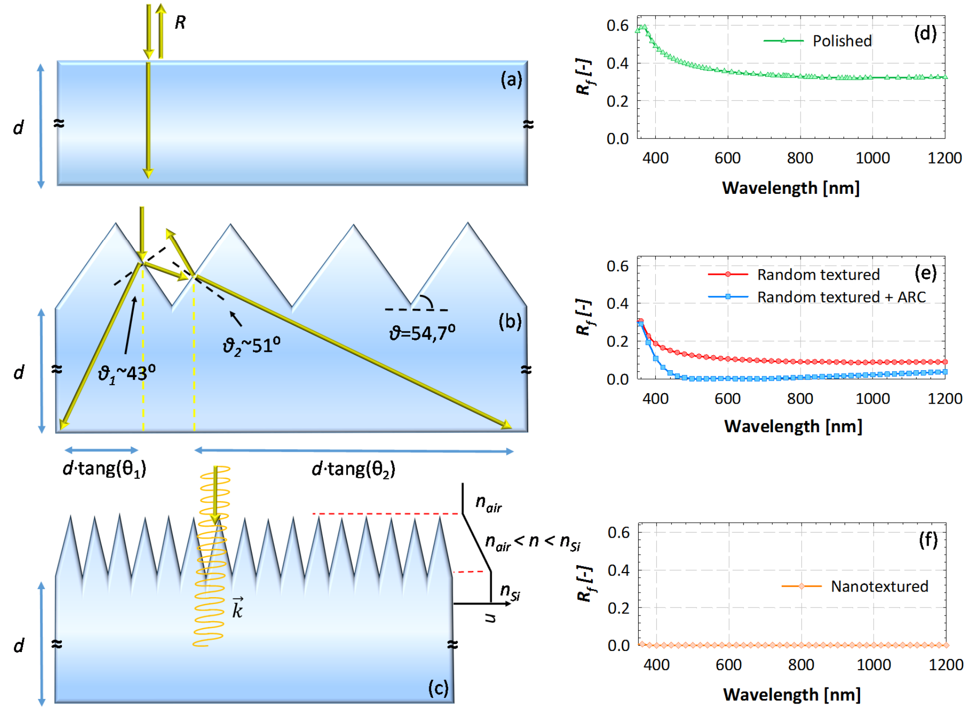

Figure 1.2. Ray diagram of normally incident light on (a) polished, (b) random pyramids texturing and (c) nano-textured Si. R_f calculated by linear extrapolation at long wavelengths of measured R in case of (d) polished surface, (e) random pyramids with and without ARC, (f) nano-texturing without ARC.

1.2.2 Light scattering

Light scattering is a light management technique devoted to increase the optical light path length in the absorber layer. In fact, when the product $\alpha \cdot d$ (where α and d, are the Si absorption coefficient and Si thickness, respectively) becomes lower than 1, Si starts to be a weak absorber[2]. In addition, when decreasing d the wavelength region of weak

---

[2] $\alpha d < 1$, where α and d are respectively, the Si absorption coefficient and thickness, for d = 180 μm the weak absorption region is defined by $\lambda \geq 1020$ nm.

abortion becomes larger. Therefore, increasing the optical path length inside the absorber layer becomes essential to enhance optical absorption at long wavelengths.

In case of Si with polished surface, a ray of light impinging with normal incidence will just propagates straight through the absorber leading to an optical light path equal to geometrical thickness of the absorber. State-of-the-art light scattering in c-Si solar cells is achieved by using random pyramids. This type of texturing exhibits features size in the micro-meter scale allowing the usage geometrical optics to describe the propagation of the light in the absorber layer. As sketched in Figure 1.2 (b), the optical path length of the first and second transmitted rays through a random pyramidal textured surface are increased of a factor of 1.36 and 1.7 (1/cos(θ_1=43°) and 1/cos(θ_2=51°)), respectively, with respect to the normal direction (λ=700 nm). In addition, as shown in [28] at long wavelengths random pyramids exhibit a nearly ideal light scattering (i.e. Lambertian) and therefore a fully randomization of the light in the absorber.

Optical light path enhancement delivered by advanced texturing in the subwavelength range is not yet well understood. As presented in Chapters 4 and 6 of this thesis, light scattering properties of the nano-textured surfaces (fabricated in this work) are found to be inferior to the ones delivered by standard random pyramids. Therefore, to enhance light scattering at long wavelengths, advanced surface texturing approaches combining nano- and micro- texturing scale (in a decoupled front and rear texturing or modulated surface texturing (MST)) are required. Other advanced light scattering techniques such as nano-wires (NWs) [29][30], nanodomes [31], periodic grating [32][33] and plasmonic nano-particles [34][35] (see Table 1.1) have also been extensively studied for enhancing light scattering in thin film Si solar cells. However, their application in real devices has so far demonstrated much lower performance with respect to the theory, mainly due to significant increase of the parasitic absorption in the solar cell supporting layers.

1.2.3 Internal rear reflectance

Back reflectors are essential to avoid transmittance losses through the absorber layer in the weak absorption region and at least double (in case of specular BRs) the optical light path. Metals are the most well-known and used BRs for c-Si solar cells since they can play the double role of rear electrode and BR. Ideally the most performant metallic BR would be made of Ag. However, this metal is expensive and in reality exhibits parasitic plasmonic losses [36]. In commercial c-Si solar cells (see section 2.5.2.1), BRs are made of Al (typically screen printed) which is more cost effective than Ag but exhibits poor internal rear reflectance (R_b), usually between 60 and 70% [37] [38]. To reduce metal parasitic absorption and enhance R_b, a non-absorbing dielectric locally opened in correspondence of the contacts is usually placed in between the Si and the metal [36]. The dielectric plays the roles of: (i) increasing the refractive index mismatch between Si and the BR; (ii) shift the metal surface plasmon at short wavelengths where light is totally absorbed in the Si [36]; (iii) reduce recombination rate at rear contact. In this thesis metal-free back reflectors are studied (notice that a certain amount of metal is still required for collecting the carriers) as alternative to metal back reflectors. In particular, dielectric BRs based on distributed Bragg reflectors (DBR), TiO_2 diluted in water in the role of white paint are proposed.

1.3 Aim of the thesis

The aim of this thesis is to provide valid solutions for strategies (i) and (ii) proposed by the ITRPV (see Section 1.1). According to strategy (i), a possible solution to reduce the cell price is to use thinner wafers. As discussed in the previous sections, advanced light management techniques, represent a key aspect to enhance light absorption and maintain high efficiency in thin c-Si solar cells. In Chapter 4, the design and fabrication of an advanced light trapping scheme capable to deliver optical absorption comparable to the upper $4n^2$ limit is shown. In particular, the proposed light trapping scheme combines nano-texturing at front side, micro-texturing at back side and advanced back reflectors, in order to deliver nearly ideal light in coupling, light scattering and internal rear reflection, respectively. However, such optical absorption enhancement can be translated in an increase of the final conversion efficiency if, and only if, a proper passivation of the surface textures is employed.

Combining the advanced light trapping and passivation schemes, nano-textured IBC c-Si solar cell with conversion efficiency of 19.8% is presented in Chapter 6. This device shows perfect light-in coupling and same spectral response around the wavelength corresponding to the band-gap of Si of solar cells endowed with the micro-textured surfaces and constitutes the technological platform for fabricating highly efficient ultra-thin ($<50\mu m$) c-Si solar cells. As for strategy (ii), manipulating light interaction at front and/or rear side of a solar cell is not only instrumental to enhance its optical absorption but also enables the fabrication of customized PV products. Building integrated photovoltaic (BIPV) is an emerging field in PV industry [39] and constitutes a concrete possibility to decrease the LCOE by integrating the PV functionalities to building elements. Black modules are one of the most requested PV products for residential application [40]. PV modules based on IBC solar cell technology exhibit a pretty dark colour appearance. However, colour perception of IBC fabricated with state-of-the-art random pyramids coated with ARC, depends by the angle of incidence. High efficiency nano-textured, aesthetically black, IBC devices are demonstrated in see Chapter 6 of this thesis, and can be seen in the BIPV framework where black modules with colour resilience also for large angles of incidence are requested.

For BIPV application where the PV module is used as façade a glass/glass module configuration is often employed. In such case the rear side of the cell presents is either coated with Al-paste (exhibiting a grey colour) or in case of bi-facial cells with rear passivation layer (usually exhibiting a blue colour). In addition, for bi-facial cells such layer is transparent to the light (leading to *T* losses) and might be in low albedo light conditions. Therefore, to offer a larger variety of rear colours and increase internal rear reflectance dielectric back reflectors with tuneable colour perceptions are demonstrated in Chapter 7.

1.4 Outline of the thesis

Aside this Chapter, where introduction and motivation of this thesis are given and light management techniques are introduced, this thesis contains other seven Chapters.

In Chapter 2, general working principle and recombination mechanisms in wafer based c-Si solar cells are described. State-of-the-art at both (laboratory and industrial scale) of fabricated wafer based (n-type and p-type) c-Si solar cells with different architectures is also presented.

In Chapter 3, an accurate analysis of the main opto-electrical losses for a fabricated mc-Si solar cell is performed by using Advanced Semiconductor Analysis simulation (ASA) tool. The analysis showed that the main optical losses for a mc-Si solar cell are due to high *R*, incomplete absorption at long wavelength and poor internal rear reflectance of the Al-BSF.

In Chapter 4 an advanced light trapping scheme aiming to minimize optical losses in thin Si absorbers is presented. For such light trapping scheme a combination of surface textures with different geometrical dimension was applied in order to trigger different optical effects and therefore enhance Si absorption on a broad wavelength range. In particular, nano-texturing fabricated via reactive ion etching (RIE) on the front side and micro-texturing based on alkaline etching on the rear side were used. Nearly ideal back reflectors such as Ag or Distributed Bragg reflectors (DBR) are applied on the rear side. Interdigitated back contacted (IBC) solar cell was indicated as the most promising architecture for demonstrating the capability of such light trapping scheme.

In Chapter 5, a simplified process for fabrication high efficiency IBC c-Si solar cells is demonstrated. The process was designed in order to be self-aligned and involved the combination of phosphorus ion implantation and is situ boron doped epitaxial growth of Si. The usage of these doping techniques enables high flexibility, and quality of the doped layers together with process simplifications.

In Chapter 6, the application in IBC device of the advanced light management technique as proposed in Chapter 4 is demonstrated. A novel and cost effective process to remove surface defects induced by the nano-texturing process is proposed. The application of such etching to the nano-textured samples resulted in a decrease of the surface recombination while still maintaining its light in-coupling properties. The implementation of the light trapping scheme (see Chapter 4) to the developed IBC (see Chapter 5) was not straightforward. In fact, the IBC process developed in this thesis requires a polished rear side. Therefore, the decoupled front and rear side light trapping scheme of Chapter 4 was modified in order to be applied in the IBC device. In particular, the two textures were superposed on the front side leading to the so called modulated surface texture (MST) demonstrating comparable absorption enhancement with respect to the decoupled approach. The combination of the advanced light trapping and passivation schemes were employed in IBC c-Si solar cells.

Chapter 7 focuses on the application of advanced back reflectors for bifacial c-Si solar cells. The advanced BRs here used pursue the roles of: (i) enhancing cell efficiency by increasing its internal rear reflectance (ii) providing novel solutions BIPV applications. In particular, DBR and TiO_2 diluted in H_2O in the role of white paint (WP) are used as back reflectors of bifacial c-Si solar cells. The WP BR showed higher solar cells performance enhancement compared with DBR. However, the colour tuning possibilities of the DBR enables to fabricate rear side coloured bifacial modules which can be used for BIPV applications.

In Chapter 8, conclusions of this thesis are reported. In addition, an outlook is given on a roadmap to follow in order to realize record ultra-thin c-Si solar cells.

1.5 Main contributions to the field

In this section the main contribution to the PV field from this thesis contribution are presented.

- Classical $4n^2$ absorption enhancement limit was experimentally demonstrated;
- An analytical model to calculate the light absorption in Si (from the measured total absorption) for an optical system formed by Si / BR was proposed;
- High efficiency IBC c-Si solar cells based on self-aligned process were designed and fabricated;
- Defect removal etching (DRE) was demonstrated as a possible solution to eliminate surface defects induced by RIE process;
- Application of the advanced light management technique and surface passivation in IBC c-Si solar cells was reported with top efficiency of 19.8%;

- Dielectric BRs for bi-facial c-Si solar cells were designed and fabricated. Bi-facial c-Si solar cells coated on the rear side with dielectric BRs with conversion efficiency comparable to Ag BRs, were demonstrated.

1.6 References

[1] Available on line on: http://www.bp.com/content/dam/bp/pdf/energy-economics/statistical-review-2015/bp-statistical-review-of-world-energy-2015-full-report.pdf, pp. 40.

[2] Available on line on: http://www.iea.org/etp/etp2015/.

[3] R. Perez, M. Perez, A fundamental look at energy reserves for the planet, IEA SHC Solar Update (2009).

[4] Adoption of the Paris agreement—Proposal by the President—Draft decision -/CP.21 (PDF). UNFCCC. 2015-12-12.

[5] G20 summit: Modi pushes for $100 bn finances to pursue clean energy, proposes grand global solar alliance. Firstpost. 15 November 2015. Retrieved 30 November 2015.

[6] Narendra Modi, Francois Hollande invite over 100 countries for solar alliance. Economictimes.indiatimes.com. 25 November 2015.

[7] Available online on: http://www.itrpv.net/Reports/Downloads/2014.

[8] Available on line on: http://www.itrpv.net/Reports/Downloads/2015.

[9] Available on : https://www.ise.fraunhofer.de/de/downloads/pdf-files/aktuelles/photovoltaics-report-in-englischer-sprache.pdf

[10] Opportunities in the Solar Market for Crystalline and Thin Film Solar Cells, ID: 2693699, (2015).

[11] Available on line on: http://iet.jrc.ec.europa.eu/remea/sites/remea/files/pv_status_report_2014_online.pdf.

[12] http://www.pv-magazine.com/news/details/beitrag/the-big-55-gw--solar-to-run-hot-this-year--says-gtm-research_100019860/#axzz41fjnKytx

[13] F. Kersten, R. Doll, A. Kux, D. M. Huljic, M. A. Görig, C. Berger, J. W. Müller. P. Wawer, PV learning curves: Past and future drivers of cost reduction, Proceedings of the 26th European Photovoltaic Solar Energy Conference, 4697-4702, (2011).

[14] http://pvxchange.com/priceindex/Default.aspx?template_id=1&langTag=en-GB.

[15] LCOE defined by the National Renewable Energy Laboratory (NREL): http://www.nrel.gov/analysis/tech_lcoe_documentation.html

[16] Available on: http://www.ise.fraunhofer.de/en/publications/veroeffentlichungen-pdf-dateien-en/studien-und-konzeptpapiere/study-levelized-cost-of-electricity-renewable-energies.pdf

[17] S. de Hann, in IHS iSuppli Whitepaper, Predictions for the Solar Industry in 2014 – Top 10 Trends for the Year Ahead, IHS iSuppli, www.isupplis.com/Photovoltaics/News, (2013).

[18] J. Zhao, A. Wang, P. P. Altermatt, M. A. Green, 24% efficient silicon solar cells with double layer antireflection coatings and reduced resistance loss. Appl. Phys. Lett., 66 (26), 3636-3638, (1995).

[19] A. Jäger-Waldau, PV Status Report 2012. Joint Research Centre, Institute for Energy and Transport, (2012).

[20] C. del Cañizo, G. del Coso, W. C. Sinke, Crystalline silicon solar module technology: Towards the 1 € per watt-peak goal. Prog. Photovolt Res. Appl. 17, 199-209, (2008).

[21] A. Goodrich, P. Hacke, Q. Wang, B Sopori, R. Margolis, T. L. James, M. A. Woodhouse, Wafer-based monocrystalline silicon photovoltaics road map: Utilizing known technology improvement opportunities for further reductions in manufacturing costs. Sol. Energ. Mat. Sol., 114, 110-135 (2013).

[22] B. Micciche, B. Dingle, Understanding the causes for cell breakage during the cell interconnecting process – part I. Proceedings of the 21st European Photovoltaic Solar Energy Conference (2006).

[23] K. A. Munzer, K. T. Holdermann, R. E. Schlosser, S. Sterk, Thin monocrystalline silicon solar cells. Electron Devices, IEEE Transactions on. , 46 (10), 2055-2061 (1999).

[24] S. W. Glunz, S. Rein, W. Warta, J. Knobloch, W. Wettling, On the degradation of Cz-silicon solar cells. Proceedings of the 2nd World Conference on Photovoltaic Energy Conversion, 1343-1346 (1998).

[25] D. Kray, H. Kampwerth, E. Schneiderlochner, Comprehensive experimental study on the performance of very thin laser-fired high-efficiency solar cells. Proceedings of the 19th European Photovoltaic Solar Energy Conference, 608-611 (2004).

[26] T. Tiedje, E. Yablonovitch, G. D. Cody, B. G. Brooks, Limiting efficiency of silicon solar cells. Electron Devices, IEEE Transactions on., 31 (5), 711-716, (1984).

[27] P. Spinelli, Broadband omnidirectional antireflection coating based on subwavelength surface Mie resonators. Nat. Commun. (3) 692 doi: 10.1038/ncomms1691 (2012).

[28] P. Campbell, M. A. Green, Light trapping properties of pyramidally textured surfaces. J. Appl. Phys. 1987, 62, 243.

[29] E. C. Garnett, M. L. Brongersma, Y. Cui, M.D. McGehee, Nanowires solar cell, Ann. Rev. Mat. Lett. 1616-1619 (2012).

[30] E.C. Garnett, P. Yang, Light trapping in silicon nanowire solar cells, Nano. Lett. 10 1057-1060 (2010).

[31] J. Zhu, C.-M. Hsu, Z. Yu, S. Fan, Y. Cui, Nanodome Solar Cells with Efficient Light Management and Self-Cleaning Nano Letters 10 (6), 1979-1984 DOI: 10.1021/nl9034237 (2010).

[32] K. R. Catchpole, S. Mokkapati, F. Beck, E.-C. Wang, A. McKinley, A. Basch, J. Lee, Plasmonics and nanophotonics for photovoltaics, MRS Bulletin, 36,461-467, , doi:10.1557/mrs.2011.132, (2011).

[33] C. Haase, H. Stiebig, Optical properties of thin-film silicon solar cells with grating couplers, Prog. Photovoltaics Res. App. 14, 629-641, (2006).

[34] J. N. Munday, H. A. Atwater, Large Integrated Absorption Enhancement in Plasmonic Solar Cells by Combining Metallic Gratings and Antireflection Coatings, Nano Letters, 11 (6), 2195-2201, DOI: 10.1021/nl101875t, (2011).

[35] H. Atwater, A. Polman, Plasmonics for improved photovoltaic devices, Nat. Mat2r. 9 205-2013, (2010).

[36] Z. C. Holman, M. Filipič, B. Lipovšek, S. De Wolf, F. Smole, M. Topič, C. Ballif, Parasitic absorption in the rear reflector of a silicon solar cell: Simulation and measurement of the sub-bandgap reflectance for common dielectric/metal reflectors, Sol. Energ. Mat. Sol., 120, 426-430, (2014).

[37] F. Huster, Investigation of the alloy process of screen printed aluminium pastes for the BSF formation of silicon solar cells, , Proceedings of the 20th European Photovoltaic Solar Energy Conference and Exhibition (2005), 2DV2.49.

[38] T. Dullweber, S. Gatz, H. Hannebauer, T. Falcon, R. Hesse, J. Schmidt, R. Brendel, 19.4% -Efficient Large Area Rear-Passivated Screen-Printed Silicon Solar Cells, 26th European Photovoltaic Solar Energy Conference and Exhibition, 811-816, (2011), DOI: 10.4229/26thEUPVSEC2011-2BP.1.4

[39] Available on: http://www.seac.cc/fileadmin/seac/user/doc/SEAC_Meerjarenprogramma_2012-2016_update_2014.pdf.

[40] P. de Jong, The development of back-contact glass-glass modules, 7th workshop on Back contact solar cells and module technology, Freiburg, (2015).

2

Wafer-based c-Si solar cells

2.1 Working principles of c-Si solar cells

For a working solar cell at least three elements are required:

1. An absorber layer which absorbs the incoming photons and convert them into electrons-holes (*e-h*) pairs;
2. A membrane which allows to selectively collecting one type of photo-generated charge carrier. Typically a *pn* junction formed of adjacent p-doped and n-doped semiconductors is used;
3. Contacts which allow carriers transfer to an external load;

In the language of semiconductor physics, the first process is known as generation. In case of Si, after photon excitation an *e* is created in the conduction band (E_c) leaving an *h* in the valence band (E_v). As consequence of this process *e-h* pairs are formed. After generation *e* and *h* can randomly diffuse in the semiconductor lattice resulting in a zero photo-generated current flow. In order to create a net current flow after light excitation *e* and *h* need to be collected at two different terminals. This is usually obtained by forming selective contacts which can collect only type of charge carrier. In c-Si solar cells this is achieved by forming a *pn* junction and a *high-low* junction also known as emitter and surface field, respectively. For instance, in a p-type substrate, the emitter is a n-type doped region usually located at front side, while the back surface filed (BSF) is a p-type doped region located at rear side. Therefore, for this solar cell architecture, photo-generated electrons would be collected at emitter while holes at BSF. Such flow of carriers is called photo-generated current (I_L) and under the assumptions of infinite thickness of the *pn* doped regions and uniform generation (*G*), can be written as:

$$I_L = qAG(L_e + w + L_h) \tag{2.1}$$

where, q is the elementary charge, A is the cross-sectional area of the *pn* diode, w is the width of the depletion region and L_e (L_h) is the diffusion length for the electrons (holes). Therefore, Equation 2.1 indicates that only carriers generated within the depletion region and in the region up to the minority-carrier-diffusion length from the depletion region contribute to the photo-generated current. In a solar cell, on the opposite direction to the drift current of the photo-generated carriers, a diffusion current composed of e from the electron-rich n+ emitter diffusing to the electron-poor p-type base is also flowing. Such current flow can be simply expressed as the *I-V* relationship of a forward-biased diode and is usually called dark current (I_{Dark}). Mathematically, the current voltage (*I-V*) output of a c-Si solar cell under illumination, under the assumptions of the superposition principle, can be written as:

$$I(V) = I_{Dark} - I_L = I_0\left(e^{\frac{qV}{nkT}} - 1\right) - I_L \qquad 2.2$$

where, q is the elementary charge, k the Boltzmann constant, T the temperature, I_0 the saturation current and n the ideality factor. Usually Equation 2.2 is formulated in terms of positive current density (J) as:

$$J(V) = J_L - J_{Dark} = J_L - J_0\left(e^{\frac{qV}{nkT}} - 1\right) \qquad 2.3$$

Important operational modes of a solar cell are short circuit (SC) and open circuit (OC). At short circuit conditions V=0 and Equation 2.3 leads to $J(V=0) = J_{SC} \approx J_L$, where J_{SC} is called short circuit current density and is the maximum current density deliverable by the device. At open circuit conditions ($J=0$) and Equation 2.3 becomes:

$$V_{OC} = \frac{nkT}{q} ln\left(\frac{J_{SC}}{J_0} + 1\right) \qquad 2.4$$

Where, V_{OC} is defined as open circuit voltage. Notice that an increase of J_0 leads to a decrease of both J_{SC} and V_{OC}. For an ideal *pn* junction n=1, however, in real devices such quantity can be larger than 1. To describe mathematically ideal and non-ideal behaviours of a real solar cell a double diode model is often used:

$$J(V) = J_{SC} - J_{01}\left(e^{\frac{qV}{n_1kT}} - 1\right) - J_{02}\left(e^{\frac{qV}{n_2kT}} - 1\right) \qquad 2.5$$

where, n_1= 1 and J_{01} are the ideality factor and saturation current density of an ideal diode, respectively, and J_{02} and n_2 represent the same components of a non-ideal diode. The second diode is traditionally linked to recombination in the depletion regions where $n_2 \leq 2$. However, in real devices, n_2 is often even larger than 2 due to various recombination phenomena [1]. When describing the *J-V* behaviour of a real solar cell, Equations 2.4 and 2.5, are yet not sufficient because they only account for recombination losses. For a more accurate description of the *J-V* behaviour of real solar cells resistive losses need to be considered. This leads to a more general version of Equation 2.5 which becomes:

$$J(V) = J_{SC} - J_{01}\left(e^{\frac{qV - J(V)R_S}{n_1 kT}} - 1\right) - J_{02}\left(e^{\frac{qV - J(V)R_S}{n_2 kT}} - 1\right) - \frac{V - J(V)R_S}{R_{sh}} \qquad 2.6$$

where R_s and R_{sh} are the series and shunt resistance, respectively. The R_s contains the contributions of the grid lines, contact resistances, lateral current flow in the doped layers, and current flow in the base. Possible current leakage across the *pn* junction is taken into account by the ohmic parallel resistance R_{sh}. Both resistive losses lead to power losses in the solar cell which are described by the fill factor (*FF*). The efficiency (η) of a c-Si solar cell is defined as the ratio between the maximal deliverable power and the incident power (P_{in}):

$$\eta = \frac{V_{MPP} \cdot I_{MPP}}{P_{in}} = \frac{V_{OC} \cdot I_{SC} \cdot FF}{P_{in}} \qquad 2.7$$

where, V_{MPP} and I_{MPP} are the voltage and current at maximum power point (MPP),

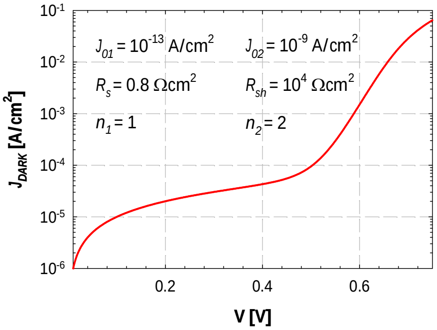

Figure 2.1. J_{Dark}-*V* characteristic of the c-Si solar cell calculated by using Equation 2.6 with parameters listed in the figure and $J_{ph}=0$.

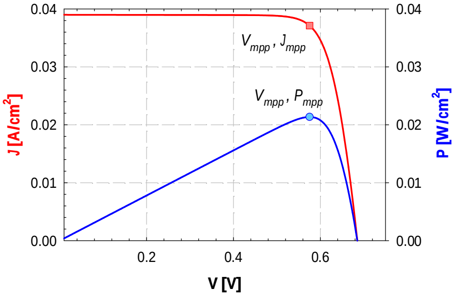

Figure 2.2. *J-V* and *P-V* characteristics of c-Si solar cells under illumination calculated by using Equation 2.6. Maximum power point is also reported.

respectively. The MPP defines the operational point of a solar cell. The J_{Dark}-V and illuminated J-V characteristics of a c-Si solar cell (calculated with equation 2.6 and the parameters (R_s, R_{sh}, J_{01}, J_{02}, n_1 and n_2) reported in Figure 2.1) are depicted in Figure 2.1 and Figure 2.2, respectively.

2.2 Spectral response and quantum efficiency of c-Si solar cell

Spectral response (*SR*) of a c-Si solar cell is measured in order to evaluate the response of the device for different wavelengths of the incident light. In particular, the spectral response is calculated as the ratio between the current generated by the solar cell over the incident power. Such quantity is very important because allows to calculate the so-called external quantum efficiency (*EQE*). The *EQE* of a solar cell indicates the fraction of photons incident on the solar cell that creates *e-h* pairs which are also successfully collected at the solar cell terminal. This quantity is generally wavelength (λ) and bias light and voltage dependent. Usually *EQE* is measured at short circuit condition (V=0 V) and is expressed as:

$$EQE(\lambda) = \frac{I(\lambda)}{q\Phi_{in}(\lambda)} \qquad 2.8$$

where, Φ_{in} is the spectral photon flux incident on the solar cell. The *EQE* spectra are usually measured by means of a *spectral response* setup. As Equation 2.8 indicates, to measure the *EQE* (at V=0 V), solar cell current and incident photon flux at each λ are required. The first can be easily measured with an Ampere-meter while the second is indirectly evaluated by performing a measurement with a calibrated photodetector whose *EQE* is known. Therefore, the *EQE* is mathematically expressed as:

$$EQE(\lambda) = EQE(\lambda)_{ref}\,\frac{I(\lambda)}{I_{ref}(\lambda)} \qquad 2.9$$

For an accurate evaluation of the *EQE* it is extremely important that light source is sufficiently stable during the whole measurements. In fact, Equation 2.8 assumes that Φ_{in} is the same for both calibration and actual measurement. Finally the short circuit current density (J_{SC}) can be calculated by convoluting the *EQE* with the photon flux across the relevant wavelength of interest.

$$J_{SC} = \int_{\lambda_2}^{\lambda_1} EQE(\lambda)\cdot\Phi_{in}(\lambda)d\lambda \qquad 2.10$$

Typical wavelength range [λ_1, λ_2] for terrestrial c-Si solar cells is between 300 and 1200 nm and Φ_{in} fixed by the AM 1.5 standard. In this thesis the measured *EQE* are reported with respect to a photodiode calibrated at Fraunhofer ISE CalLab. The *EQE* includes all optical losses of a solar cell such as reflectance (*R*) and or transmittance (*T*). However, it is often useful to look at quantum efficiency of a solar cell after correcting for its *R* ant *T* losses. Such quantity is called internal quantum efficiency (*IQE*) and refers to the photons that are not reflected or transmitted out of the cell and which generated carriers that are collected at solar cell terminals. Mathematically the *IQE* is expressed as:

$$IQE(\lambda) = \frac{EQE(\lambda)}{1 - R(\lambda) - T(\lambda)} \qquad 2.11$$

To accurately evaluate carrier collection efficiency, Equation 2.11 should further include additional optical losses of the solar cell such as parasitic absorption in the ARC and free carrier absorption in the doped regions.

2.3 Efficiency limit for single junction c-Si solar cells

For a c-Si absorber layer with band gap around 1.1 eV, Shockley and Queisser (S-Q) in the '60s [2] calculated a maximal conversion efficiency of 33% under AM 1.5 illumination and no concentration [3]. Such calculations were based on the ideal case in which the only mechanism of recombination occurring was the radiative one. In this case the efficiency limitations were set by thermalization losses of photons with energy higher than band-gap and non-absorption of photons with energy lower than the band-gap (see Figure 2.3). However, in a real c-Si solar cell the radiative recombination does not play the major role as in the calculations of S-Q due to the indirect band structure of Si.

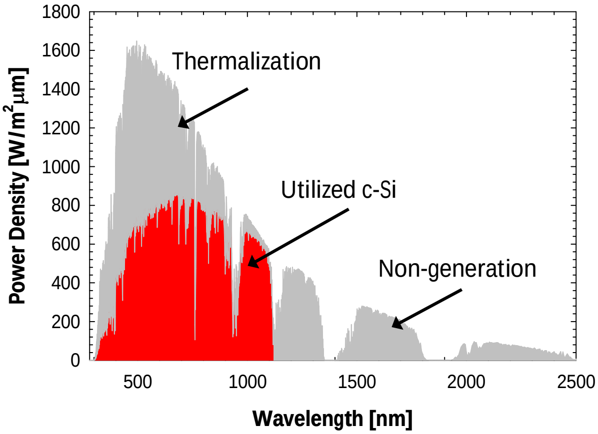

Figure 2.3. Photon losses due to thermalization and non-generation for c-Si semiconductor as absorber material.

W_{opt} [μm]	J_{SC} [mA/cm^2]	V_{OC} [mV]	*FF* [%]	η [%]
110	43.3	761.3	89.26	29.43

Table 2.1. Optimal wafer thickness and limiting efficiency calculations proposed by Richter [5].

The main intrinsic recombination mechanism in Si is instead Auger recombination. Recently, combining accurate models of intrinsic recombination losses in c-Si [4], Richter *et al.* [5] assessed the efficiency limit for a single junction c-Si solar cell at 29.4%. The calculated external parameters of the optimal silicon solar cell under 1 sun illumination [5] are reported in Table 2.1. This is yet an ideal calculation which only serves to understand what is the maximal theoretical efficiency achievable and cannot be realized in practice. For devices actually manufactured, additional mechanisms of recombination occur, setting the maximal conversion efficiency to 26% as calculated by Swanson [6].

2.4 Mechanisms of recombination

The main mechanisms of recombination in a semiconductor are:

a. Radiative recombination
b. Auger recombination
c. Recombination via defect states in the semiconductor band-gap (also called Shockley-Read-Hall or SRH recombination).
d. Surface recombination (treated as a special case of bulk SRH recombination applied to a two-dimensional surface).

Typically, injection level dependent minority carrier lifetime ($\tau(\Delta n)$), is used to quantify recombination losses in a solar cell. Such quantity represents the amount of time that a photo-generated carrier *survives* before recombining and it is expressed in terms of ratio between a volumetric recombination rate (*U*) and the excess carrier concentration (Δn) as:

$$\tau = \frac{\Delta n}{U} \tag{2.12}$$

This quantity is also the sum of the invers of the lifetimes associated to each recombination mechanism:

$$\frac{1}{\tau} = \frac{1}{\tau_{Rad}} + \frac{1}{\tau_{SRH}} + \frac{1}{\tau_{Auger}} + \frac{1}{\tau_{s}} = \sum_i \frac{U_i}{\Delta n} \tag{2.13}$$

where τ_{Rad}, τ_{SRH}, τ_{Auger}, τ_s indicate the minority carrier lifetime associated to radiative, Shockley-Read-Hall, Auger, and surface recombination mechanisms, respectively.

2.4.1 Radiative recombination

Radiative recombination (U_{Rad}) refers to a direct recombination process between *e* and *h* and is the opposite of the generation process. The energy released during such process results in photon emission. The U_{Rad} rate is mathematically expressed as:

$$U_{Rad} = Bnp = B(n_0 + \Delta n)(p_0 + \Delta p) \tag{2.14}$$

where B is the radiative recombination coefficient, n and p are the electron and hole volumetric concentrations, n_0 and p_0 are the equilibrium doping concentrations and Δn and Δp are the excess concentrations (generated by light in the case of a solar cell). In silicon solar cells direct recombination is usually negligible. In fact, silicon is a semiconductor with indirect band gap, which means that the bottom of the conduction and valance bands do not line up in k-space (momentum). As recombination requires that both energy and momentum are conserved, radiative recombination in Si requires the participation of a phonon of the right momentum. This extra requirement reduces the probability of radiative recombination and is reflected in the low value of B around $4.73 \cdot 10^{-15} cm^{-3} s^{-1}$ at 300 K [8].

2.4.2 Auger recombination

Auger recombination is a process whereas the energy released by an electron-hole recombination is transferred to a second electron instead of being emitted as heat or photons. If such energy is high enough, it can allow the electron (hole) to jump to the higher (lower) level of conduction (valence) band. Such *e* (*h*) thermalizes back down to the conduction (valence) band edge. According to the advanced parametrization presented by Richter et al. [5], the Auger recombination rate (U_{Auger}) can be written as:

$$U_{Auger} = (np - n_{ieff}^2)(C_n n_0 + C_p p_0 + C_a \Delta n^{0.92}) \tag{2.15}$$

where, n_{ieff} is the Si effective intrinsic carrier concentration and:

$$C_n = 2.5 \cdot 10^{-31} g_{eeh}(n_0) \tag{2.16}$$

$$C_p = 8.5 \cdot 10^{-32} g_{hhe}(p_0) \tag{2.17}$$

$$C_a = 3 \cdot 10^{-29} \tag{2.18}$$

where, C_n and C_p are the Auger coefficients for *h* and *e*, respectively, while g_{eeh} and g_{hhe} the enhancement factors describing the Coulomb-enhanced Auger recombination introduced by Altermatt [10], [11]. From Equation 2.15 it appears clear that Auger recombination increases with square of the doping concentration and therefore is one of the dominant recombination mechanisms for heavily doped semiconductors.

2.4.3 Shockley-Read-Hall (SRH) recombination

The presence of defects within the semiconductor bandgap can significantly contribute to decrease the energy of a photo-generated carrier. Such defect states might be due to impurities and/or crystal defects in the semiconductor lattice. Under 1-Sun illumination, SRH recombination is the dominant mechanism in the base (also known as bulk region) of solar cells fabricated on defective (such as multi-crystalline silicon) or impurities-contaminated materials. The recombination rate due to defect levels in the bandgap was first analysed by Shockley, Read and Hall for a single defect level:

$$U_{SRH} = \frac{np - n_i^2}{\tau_{p0}(n + n_1) + \tau_{n0}(p + p_1)} \tag{2.19}$$

where n_i is the intrinsic carrier concentration, τ_{p0} and τ_{n0} are the volumetric electrons and holes lifetime, which are related to the thermal velocity (v_{th}), the volumetric trap density (N_T), and the capture cross-section for electrons (σ_n) and holes (σ_p), respectively, as:

$$\tau_{n0} = \frac{1}{\sigma_n v_{th} N_T} \tag{2.20}$$

$$\tau_{p0} = \frac{1}{\sigma_p v_{th} N_T} \tag{2.21}$$

The capture cross-sections (σ_p and σ_n) define the probability of a defect state to capture an electron or a hole, respectively. Finally, n_1 and p_1 are volumetric concentration related to the filling of the trap level with carriers, and are given by:

$$n_1 = n_i e^{\left(\frac{E_T - E_i}{kT}\right)} \tag{2.22}$$

$$p_1 = n_i e^{\left(\frac{E_i - E_T}{kT}\right)} \tag{2.23}$$

where, E_i is the intrinsic energy level respectively, T is the temperature and k is the Boltzmann constant. It can be seen from Equation 2.19 that the SRH recombination depends on the dopant levels, injection level and defect-specific properties, like the capture cross-section and the defect energy level.

2.4.4 Surface recombination

Surface recombination can be treated as a special case of SRH recombination. Assuming single defect level at mid-gap of the semiconductor, the surface recombination rate (U_S) can be written as [12][13]:

$$U_s = \frac{n_s p_s - n_i^2}{\frac{n_s + n_1}{S_p} + \frac{p_s + p_1}{S_n}} \tag{2.24}$$

where, n_s (p_s) is the surface concentration of the e (h), n_1, p_1 are statistical parameters, $S_n = \sigma_n v_{th} N_{it}$ ($S_p = \sigma_p v_{th} N_{it}$) is the surface recombination velocity of the electrons (holes) with σ_n (σ_p) capture cross section of electrons (holes), surface defect density (N_{it}). In reality, the wafer surface has a large number of surface states at various energy levels $D_{it}(E)$, therefore, U_S is calculated by replacing S_n and S_p in Equation 2.24 with $N_{it} = \int_{E_V}^{E_C} D_{it}(E)dE$ and integrating over the entire bandgap as:

$$U_s = \int_{E_V}^{E_C} \frac{n_s p_s - n_i^2}{\frac{n_s + n_1(E)}{\sigma_p(E)} + \frac{p_s + p_1(E)}{\sigma_n(E)}} v_{th} D_{it}(E) dE \tag{2.25}$$

Finally the effective surface recombination velocity (S_{eff}) is defined as:

$$S_{eff} \cong \frac{U_s}{\Delta n(z = d)} \tag{2.26}$$

where Δn is the injection density and d is the edge of the c-Si surface space charge region. Surface recombination rate is one of the most important source of recombination in c-Si solar cells. Therefore, it is extremely important to minimize its contribution. According to Equations 2.25 and 2.26 to S_{eff} can be decreased by:

1) Reducing the interface density of state D_{it} (this mechanism is known as chemical passivation).
2) Reducing the surface concentration of one of the two carriers (also known as field effect)

Chemical passivation is the driving mechanisms of passivation for a-Si:H or thermally grown SiO_2. Passivation of SiO_2 is further enhanced by using annealing in H_2 mixture or other H treatment in order to decrease the D_{it} [14].

On the other hand, since recombination to occur it requires the presence of both carriers type, field effect can be employed to alter surface concentration of one carrier type.

Possible ways to obtain such effect are via doping or application of highly charged dielectric.

For instance, field effect passivation of the rear side of a p-type c-Si solar cell is typically achieved by employing p^+-doped (high-low junction) region known as BSF. Dielectrics with high density of fixed charges can induce, (depending on doping type and surface concentration), accumulation, depletion or strong inversion of the surface doping concentration. For example, a dielectric with high density of positive fixed charges ($+Q_f$) as SiN_x, is typically used to further decrease minority carrier concentration of a P-doped region. However, a positive Q_f can also be used to achieve an efficient field effect passivation of a p-type doped Si if strong inversion conditions at surface are reached. In fact, according to Equation 2.25 in case of strong inversion $U_s \propto \sigma_p$ with $\sigma_p \ll \sigma_n$.

2.5 History of c-Si solar cells

2.5.1 History repeats itself: continuous swinging between n- and p-type wafer based c-Si solar cells

The historical efficiency trend of c-Si solar cells is reported in Figure 2.4. The first c-Si solar cell ever reported in literature was fabricated in the 1941 and delivered efficiency below 1% [15]. Almost fifteen years later, at Bell laboratory, Pearson, Fuller and Chapin fabricated the first p-type diffused *pn* junction solar cell with efficiency around 4.5% [16]. Later they switched to n-type Si arsenic doped wafers achieving almost 6% efficiency [17]. Such device was presented as candidate in a contest for power suppliers in space application. Its success at that competition drastically increased the attention towards PV modules, which are nowadays still the dominant energy source for space applications. The continuous development of n-type devices led to conversion efficiency around 15% in the 1950. In the same period it was found that the space radiation hardness was less detrimental for p-type rather than n-type wafers [18]. Due to this effect, a new switch from n-type to p-type wafer based c-Si solar cells started. The efficiency of such devices was lower than the n-type and took more than 10 years to develop p-type wafer based c-Si solar cells with same conversion efficiency of n-type (15%) [19]. After this initial phase p-type wafer based c-Si solar cells have dominated the PV scenario for more than 30 years, as Figure 2.4 shows. In particular, in the 80ties strong effort was put in the development of p-type c-Si solar cells which led to excellent results[3]. All began with the introduction of the so-called passivated emitter solar cell (PESC) architecture which showed an important breakthrough reaching 20% conversion efficiency [20]. This technology was the first ancestor of the well-known passivated emitter rear locally

---

[3] This was related to the simple fabrication process of p-type solar cells based on low temperature P-diffusion (~850 °C) passivated with SiN_x on the front side and Al-BSF on the rear side.

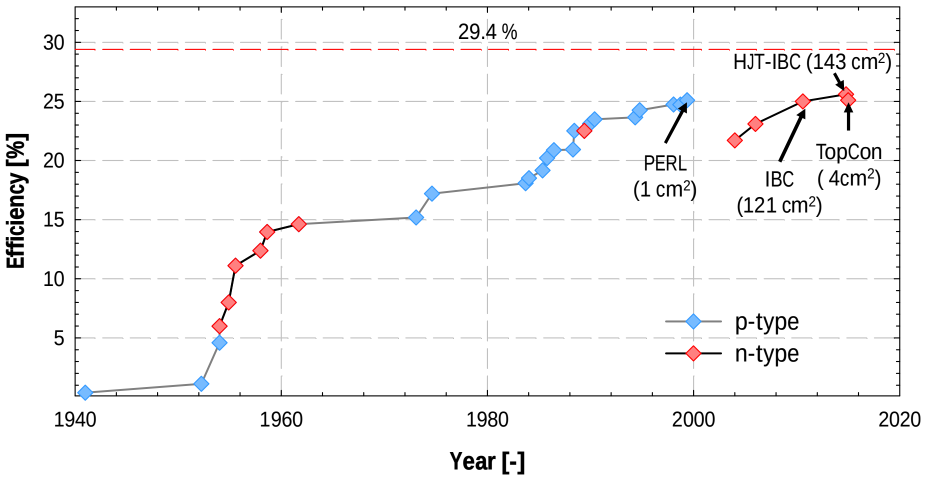

Figure 2.4. History of c-Si solar cell efficiency on p- (blue symbols) and n- (red symbols) type wafer based devices. The plot is reproduced from [23] and [26].

diffused (PERL) solar cells. In the 1996, a PERL solar cell with efficiency around 24% was fabricated at UNSW [21]. Its further optimization led to solar cells with conversion efficiency of 24.7% in the 1999 [22]. Such device was later re-measured using the current standard showing conversion efficiency of 25.0% [23]. The important feature introduced by the p-type PERL architecture was the high passivation quality of the front and back surfaces which minimizes the minority carrier recombination.

Over the last ten years history is repeating itself again with a new attention towards n-type wafer based c-Si solar cells. A strong contribution for reaching high efficiency has been given by the introduction of n-type interdigitated back contacted (IBC) solar cell architecture. In particular, n-type IBC c-Si solar cells are taking the lead in this special efficiency race thanks to two major contributors: Sunpower Corporation [24] and Panasonic [25]. Sunpower is a company leader in producing IBC with the highest efficiency at cell (24%) and module level (21%) commercially available [27], [28]. Panasonic has demonstrated world record efficiency IBC of 25.6% at R&D level on large area [29]. A more detailed analysis of the solar cell structure is presented in Section 2.6.4.

2.5.2 Mass production and laboratory scale p-type c-Si solar cells

2.5.2.1 Mass production p-type Al-BSF c-Si solar cells

The current PV market is dominated by p-type multi c-Si (mc-Si) solar cells based on a front diffused emitter and screen printed aluminium back surface field (Al-BSF) [30] (see sketch in Figure 2.5). The success of this technology is attributed to the low cost and high throughput nature of the fabrication process. However, the high scalability of the process is paid in terms of limited conversion efficiency.

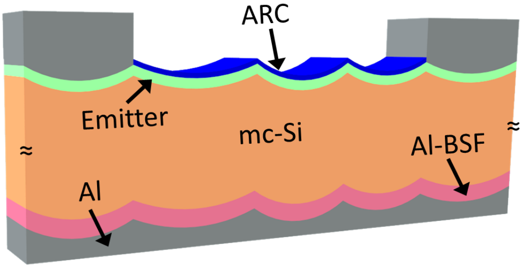

Figure 2.5. Typical p-type mc-Si solar cell with P-doped emitter and Al-BSF.

In general, conversion efficiency of Al-BSF solar cells has a plateau around 18-19% for mono-Si and 17-18% for multi c-Si (mc-Si) solar cells [31]. In fact, the Al-BSF results in fairly high rear recombination losses and has a high degree of parasitic light absorption. An extensive modelling of such device together with its loss analysis cells is presented in [31], [32] and in Chapter 3 of this thesis. Another limitation of such technology is related to the thermal coefficient mismatch between the Al and Si which often results in warping of wafers after the firing of Al necessary for the formation of the Al-BSF. The warping worsens as the wafer thickness drops. Thinning wafers down to ≤ 150 μm is an important commercial goal for decreasing PV costs, as discussed in section 1.1. However, warping of thin wafers can lead to wafer breakage/cracking thereby reducing yields to unacceptably low levels. Therefore, to avoid wrapping caused by Al-BSF firing standard doping techniques as diffusion, ion implantation, laser doping [33] or past adjustment can be implemented.

2.5.3 Laboratory scale p-type wafer based c-Si solar cells

2.5.3.1 High efficiency p-type passivated emitter and rear solar cells

High efficiency solar cells have been achieved at laboratory scale in many research centres and R&D. Usually, high efficiency devices are processed in very clean environment with complicated process steps and high quality materials which makes them not directly transferable to the PV industry. For instance, passivated emitter and rear cell (PERC), and passivated emitter rear locally diffused (PERL), sketched in Figure 2.6 (a) and (b) respectively, have demonstrated the capability to reach high efficiency already 15 years ago (23% PERC in the 1989 [34] and 25% PERL in the 1999 [22]).

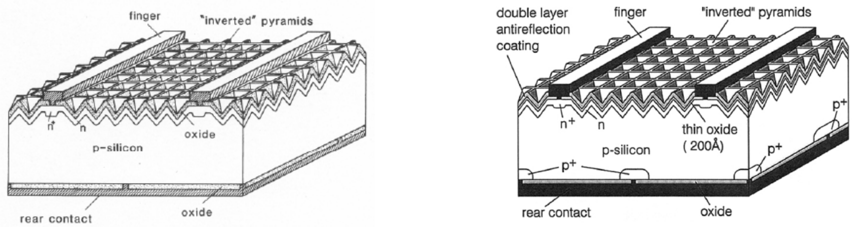

Figure 2.6 (a). Passivated emitter and rear cell (PERC), (b) passivated emitter rear locally diffused (PERL) c-Si solar cells architectures. PERC and PERL figures are taken form [34] and [22], respectively.

However, their process simplification for industrial application is still under development. The fabrication complexity of the PERL cells has been drastically reduced within the years. Inverted pyramids have been replaced by random pyramids saving 4 lithographic steps and still leading to efficiency higher than 21% [35]. More recently laser fired contact (LFC) has brought a significant contribution in reducing the fabrication steps for the formation of the locally-passivated back side [36]. In fact, point contacts can be created by locally firing the metal at the back side through the dielectric layer. The usage of more industrially compatible processes has brought to the so called industrial-PERC (i-PERC) technology which has been recently introduced in mass production [37]. Excellent results of 22.13% efficiency with i-PERC on large area (156 x 156 mm) mc-Si wafers have been shown by Trina solar.

2.5.3.2 Metal wrap through (MWT) p-type c-Si solar cells

In conventional industrial c-Si solar cells with front and rear contacts, front metal bus-bars cover the 3-4% of the front surface area. To avoid the optical shading losses of the bus-bars, Kerschaver *et al.*, introduced the metal wrap through concept [38]. In this architecture only the bus-bars are moved at back side of the wafers and are connected to the front metal grid via holes drilled through the wafer fabricated by using laser etching. At ECN the concept was optimized by employing fewer holes and customized by using natural pattern shapes. Having both bus-bars at the back side allows also the usage of new module concepts in which series interconnection between cells is managed by using conductive substrates. As estimated by Solland the application of such technology leads to efficiency gain of 3% at cell level, 3% on module level and additional 3% thanks to a higher packing density [39]. Based on ECN technology, Canadian Solar manufactures EWT modules with cell efficiency of 21.2% [40]. To further enhance their conversion efficiency MWT cells have also been combined with PERC in MWT-PERC device. In this case the bus-bar is placed at the back side on top of the passivation layer reducing not only optical shading losses but also recombination. MWT-PERC on large area float zone substrate with efficiency of 20.2% has been demonstrated [41].

2.5.3.3 Emitter wrap through (EWT) p-type c –Si solar cells

In EWT solar cells the collecting emitter stays at the front side and is contacted through highly density holes doped via diffusion with metallic fingers and bus-bars which are located at the rear side (see Figure 2.7). The presence of the diffused region at front and back side of the wafer makes this technology suitable for substrates with low bulk lifetime. Kray *et al.* have demonstrated EWT with efficiency of 22 % [42].

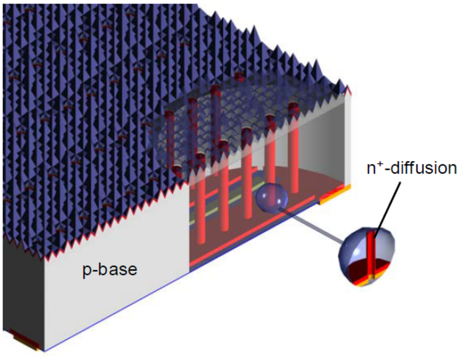

Figure 2.7. Structure of EWT c-Si solar cells, taken form [42].

2.6 Mass production and laboratory scale high efficiency n-type c-Si solar cells

2.6.1 Why n-type wafers?

As discussed in the previous sections high quality surface passivation at passivated and contacted regions are instrumental to reach high efficiency solar cells. However, once that surface recombination is minimized, solar cell efficiency might become bulk lifetime limited. Most of the cell manufactures uses either mc-Si or mono- Czochralski-grown (Cz) p-type wafers. The electrical properties of the first are limited by high metallic impurities and crystal defects. While B doped Si Czochralski-grown (Cz) wafers suffer from the so called light induced degradation (LID) effect [43]. In fact, metastable defects related to boron oxygen complex are activated after light illumination or carrier injection. This leads to a decrease of the bulk lifetime and therefore solar cell performance. There are several methodologies to reduce the LID effect such as: the usage of thinner wafer, decrease of boron and/or oxygen [44] concentration and regeneration processes [45]. LID can also be reduced by using different growth method than Cz. For instance p-type FZ wafers show better stability against LID but are not industrially feasible. Other possibilities are based on cast Si, for which quasi-mono crystalline materials can be obtained. The crystallization process is based on a standard directional solidification starting from a mono-Si seed layer [46], [47]. For such material very low oxygen concentration can be achieved. The final possibility to avoid LID is to switch to n-type doping. In addition, P-doped wafers are less sensible to the most common metallic impurities [48] than B-doped making them more suitable for reaching high efficiency [49].

2.6.2 Rear junction n-type solar cells

In principle, the easiest way to switch from p-type to n-type solar cell would consist in using the same process sequence already well-known for fabricating a p-type solar cell. For instance, the standard Al-BSF process developed for p-type solar cells could be straightforward applied to fabricate the rear emitter of an n-type solar cell. On the same way the front side P-doped diffusion would create the so called front surface field (FSF). If in terms of processing sequence the two devices are equivalent but they present strong differences in their working principle. In fact for the n-type device the *pn* junction collecting minority is located at rear side while most of the photo-generation (~2/3) occurs at front side (FS). In this case, to achieve efficient carrier collection, high FS passivation and minority bulk lifetime are required. Rear junction n-type solar cells with efficiency of 19.8% (without selective FSF) have been demonstrated at laboratory scale [50]. At industrial level remarkable results of 20.8% have been achieved by Trina solar [51]. At imec n-type rear emitter based on passivated emitter rear totally diffused (PERT) on large area (152 x 152 mm) with conversion efficiency of 22.5% have been reported [52]. For devices light induced plating of Cu was used to create the front side metal H pattern. By using such technique very fine and thick metal fingers can be achieved in order to reduce optical shading losses without increasing series resistance losses of the metal grid. The FSF design is strongly affected by the trade-off between low doping concentration necessary to minimize recombination and high doping concentration necessary to minimize R_S. Such trade-off can be partially solved by using a selective FSF with high doping concentration underneath the metal contacts and low doping concentration underneath the passivation layer.

2.6.3 Front junction n-type solar cells

To benefit from the high quality properties of the n-type bulk material front and rear side diffusions well passivated and locally opened in correspondence of the contacts are usually employed. In this case boron diffusion is used to create the front side emitter while phosphorous diffusion for the BSF. If the P-diffused BSF can be well contacted and passivated by using the well-established know-how of P emitter in p-type devices, the passivation of the B-emitter requires special attention. Standard SiN_x is not ideal to passivate B doped layers due to non-optimal field effect. Usually a stack formed by SiO_2 (chemically or thermally grown) or Al_2O_3 coated with SiN_x is used. Combining locally diffused P-doped BSF passivated with thermal SiO_2 and boron-diffused emitter passivated with Al_2O_3 / SiN stack, (see Figure 2.8) efficiency of 23.9% have been demonstrated [53]. Another n-type solar cell architecture which employs front and rear diffusion is the so called bifacial or open rear as depicted in Figure 2.9. For such solar cell architecture screen printing of Ag is performed to fabricate the H grid pattern on both front and rear sides. This allows to reduce the rear contacted area and its metal recombination with respect to the standard fully metallized device. However, this type of device exhibits high transmittance losses at long wavelengths. To overcome such limitation bifacial cells are encapsulated, either with a white foil placed on the rear side or in a glass/glass configuration. In the latter case light can enter from both sides of the cell and depending on the albedo light and the bifaciality factor of the cell a certain increase of output module power is achieved. Currently, bifacial devices are available on the market. Yingli Solar [54][55][56] and Megacell [57] have demonstrated efficiency around 20% in pilot line, based on the process developed at ECN and ISC Constance, respectively.

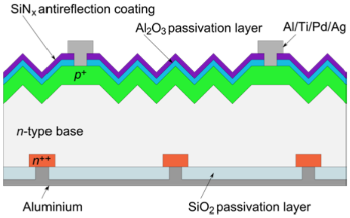

Figure 2.8. Structure of n-type c-Si solar cell with front side B-doped, image taken from [53].

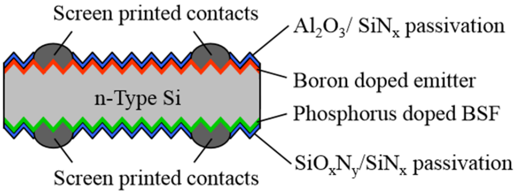

Figure 2.9. Structure of n-type bifacial c-Si solar cells fabricated via P and B diffusion, taken from [56].

2.6.4 Back contacted back junction c-Si solar cells

Interdigitated back contacted back junction (IBC) c-Si solar cells were developed at Stanford University in 1986 for concentrator applications. In IBC c-Si solar cell architecture contacts are placed at the back side in interdigitated fashion which alternates both polarities (see Figure 2.10). The IBC architecture is a very elegant solution to avoid optical shading losses at front side of the cell. In addition, it introduces several electrical advantages as described more accurately in Chapter 5. This technology was adopted by Sunpower Corporation which has simplified the fabrication steps and brought it to mass production in 2007 with conversion efficiency of 22% [58]. The company has recently demonstrated 25% conversion efficiency on 121 cm^2 area at R&D level [28] which is very close to the 26% efficiency limit calculated for a potentially manufactured single junction c-Si solar cell proposed by Swanson [6]. Sunpower produces solar cell and modules with the highest conversion efficiency commercially available [27]. The design and fabrication of such solar cell architecture will be extensively presented in Chapter 5.

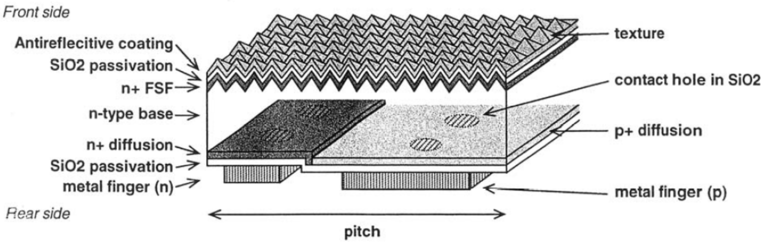

Figure 2.10. IBC c-Si solar cells fabricated by Sunpower, figure taken from [58].

2.6.5 Passivating contacts for high efficiency c-Si solar cells

In high efficiency c-Si solar cells recombination at metal contacts plays the major role. This is also the case of PERL or IBC devices where only point contacts are implemented. A possible solution to further reduce the surface recombination at metal contact requires its passivation. The most well-known passivating contacts technology is based on placing a layer with wider bandgap than Si, usually hydrogenated amorphous silicon (a-Si:H), in between the interface Si / metal. Such solar cell architecture is called hetero-junction (HJT). Its main drawback is related to the high parasitic absorption in the a-Si and transparent conductive oxide used at front side which typically leads to a poor cell response in the blue part of the spectra. Accurate optimization of HIT cells has been reported by Panasonic demonstrating efficiency of 24.7% on large area 102 cm^2 [59]. In order to reduce the parasitic absorption at front side HJT and IBC have been combined by Panasonic in so-called HJT-IBC device demonstrating a new world record efficiency of 25.6% on large area substrates (143.7 cm^2) [29]. From such results, it appears clear that the reduction of the contact recombination is instrumental to approach and maybe overcome the 26% efficiency limit for a fabricated c-Si solar cell as calculated by Swanson. Notice that at time of his calculations, passivated contacts were not available yet. Passivating contacts as alternative to a-Si:H, have been recently introduced by several groups. Doped polysilicon in combination with a thin (< 1.5 nm) tunnelling SiO_2 chemically grown has demonstrated excellent passivation quality and electrical transport [62]. Using such approach fully-rear metallized c-Si solar cells with world record conversion efficiency of 25.1% have been reported by Fraunhofer ISE [63].

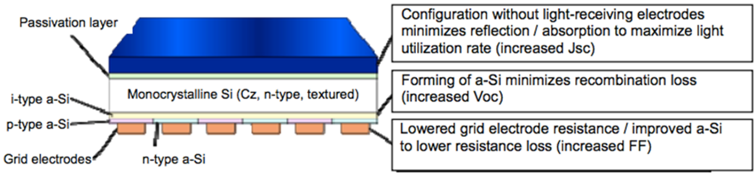

Figure 2.11. HIT-IBC world record c-Si solar cell structure fabricated by Panasonic, taken form [60] and [39].

2.7 References

[1] K. McIntosh, Lumps, Humps and Bumps: Three Detrimential Effects in the Current-Voltage Curve of Silicon Solar Cells. PhD Thesis, UNSW, (2011).

[2] W. Shockley, H. J. Queisser, Detailed Balance Limit of Efficiency of p-n Junction Solar Cells, J. Appl. Phys., 32, 510, (1961).

[3] P. Wurfel, Physics of Solar Cells – From Principles to New Concepts, Wiley - Vch Verlag GmbH & Co KgaA, Weinheim, (2005).

[4] A. Richter, S. W. Glunz, F. Werner, J. Schmidt, A. Cuevas, Improved quantitative description of Auger recombination in crystalline silicon, Physical review B 86, 165202, DOI: 10.1103/PhysRevB.86.165202, (2012).

[5] A. Richter, M. Hermle, S.W. Glunz, Improved quantitative description of Auger recombination in crystalline silicon IEEE J. Photovoltaics, 3, 1184, (2013).

[6] R. M. Swanson, Approaching the 29% limit efficiency of silicon solar cell Proceedings of the 31st IEEE Photovoltaic Specialists Conference, Orlando, USA, 889, (2205).

[7] M. J. Kerr and A. Cuevas, M. J. Kerr and A. Cuevas, J. Appl. Phys., 2002, 91, 2473. J. Appl. Phys., 91, 2473, (2002).

[8] T. Trupke, M. A. Green, P. Würfel, P. P. Altermatt, A. Wang, J. Zhao, R. Corkish, Temperature dependence of the radiative recombination coefficient of intrinsic crystalline silicon, Journal of Applied Physics 94, 4930 – 4937, DOI: 10.1063/1.1610231, (2003).

[9] Altermatt PP, Geelhaar F, Trupke T, Dai X, Neisser A, and Daub E. Injection dependence of spontaneous radiative recombination in c-Si: experiment, theoretical analysis, and simulation. Proceedings of the 5th International Conference on Numerical Simulation of Optoelectronic Devices, Berlin, Germany, 2005.

[10] P. P. Altermatt, S. Ronald, A. G. Heiser, Improvements in numerical modelling of highly injected crystalline silicon solar cells, Solar Energy Materials and Solar Cells 65, 149 - 255, DOI: 10.1016/S0927-0248(00)00089-1, (2001).

[11] P. P Altermatt, J. Schmidt, G. Heiser, A. G. Aberle, Assessment and parameterization of Coulomb-enhanced Auger recombination coefficients in lowly injected crystalline silicon, Journal of Applied Physics 82 4938, DOI: 10.1063/1.366360, (1997).

[12] W. Shockley, W. T. Read, Statistics of the recombination of holes and electrons, Physical Review 87, 835-842, (1952).

[13] R. N. Hall, Electron-hole recombination in germanium, Physical Review 87, 387-387, (1952).

[14] O. Schultz, A. Mette, M. Hermle, S.W. Glunz, Thermal oxidation for crystalline silicon solar cells exceeding 19% efficiency applying industrially feasible process technology. Prog. Photovolt: Res. Appl., 16, 317–324. doi:10.1002/pip.814, (2008).

[15] R.S. Ohl, Light sensitive electric device, US patent 240252, (1941).

[16] D. M. Chapin, C. S. Fuller, G. L. Pearson , A New Silicon p-n Junction Photocell for Converting Solar Radiation into Electrical Power, Journal of Applied Physics, 25, 5, 676-677, (1954).

[17] P. Perlin, From space to earth, aatec publications, Ann Arbor, Michigan, (1999).

[18] M. Wolf, The effect of drif filed on solar cells, Proceeding of the 3th IEEE Photovoltaic Specialists Conference, B12, Washington, (1963).

[19] J. Mandelkorn, C. McAfee, J. Kesperis, L. Schwart, W. Pharo. Fabrication and characterization of Phosphorous-diffused silicon solar cells, Journal of Electrochemical society, 109 (4), 313-318, (1962).

[20] A. W. Blanker, M. A. Green, 20% efficiency silicon solar cells, Applied Physic letter, 48 (3), 215-217, (1986).

[21] J. Zhao, A. Wang, P. Altermatt, M. A. Green, 24% efficient silicon solar cells with double layer antireflection coatings and reduced resistance loss, Applied Physics Letters 66 26, 3636 - 3638, DOI: 10.1063/1.103610, (1995).

[22] J. Zhao, A. Wang, M.A. Green, 24.5 % efficiency PERT cells on MCZ substrates and 24.7 % efficiency PERL cells on FZ substrates, Progress in Photovoltaics Research and Applications, 7 (6), 471-474, (1999).

[23] M. A. Green, The path to 25% silicon solar cell efficiency: History of silicon cell evolution, Prog. Photovolt: Res. Appl. 17 (3), 183-189, DOI: 10.1002/pip.892, (2009).

[24] Sunpower: http://us.sunpowercorp.com/

[25] Panasonic: http://panasonic.net/energy/solar/

[26] S. W. Glunz, available on: https://workspace.imperial.ac.uk/climatechange/Public/pdfs/presentations/solar%202050/Glunz_ImperialCollege_2014_v4_pdf.pdf

[27] P.J. Cousins, D.D. Smith, H.C. Luan, J. Manning, T.D. Dennis, A. Waldhauer, K.E. Wilson, G. Harley, W.P. MulliganGeneration 3: improved performance at lower

cost, in Proceedings of the 35th IEEE Photovoltaic Specialists Conference (PVSC '10), 275–278, (2010).

[28] D. Smith, P. Cousins, S. Westerberg, R. Jesus-Tabajonda , G. Aniero, Y. Shen. Towards the Practical Limits of Silicon Solar Cells, Photovoltaics, IEEE Journal of, 4, 6, 1465- 1469, (2014).

[29] K. Masuko, M. Shigematsu, T. Hashiguchi, D. Fujishima, M. Kai, N. Yoshimura, T. Yamaguchi, Y. Ichihashi, T. Mishima, N. Matsubara, T. Yamanishi, T. Takahama, M. Taguchi, E. Maruyama, S. Okamoto. Achievement of more than 25% conversion efficiency with crystalline silicon heterojunction solar cell, IEEE Journal of Photovoltaics, Denver, (2014).

[30] Available online on: http://www.itrpv.net/Reports/Downloads/2014.

[31] S. W. Glunz, Crystalline Silicon Solar Cells with High Efficiency in Advanced concepts in photovoltaics, The Royal Society of Chemistry, 1-29, DOI: 10.1039/9781849739955-00001, (2014).

[32] A. Ingenito, O. Isabella, M. Zeman, Accurate opto-electrical modeling of multi-crystalline silicon wafer-based solar cells, Sol. Energ. Mat. Sol., 123, 17-29, http://dx.doi.org/10.1016/j.solmat.2013.12.019, (2014).

[33] S. Wenham, M. A. Green. Self-aligning method for forming a selective emitter and metallization in a solar cell. Patent US 6429037 B1, (2002).

[34] A. W. Blakers, A. Wang, A. M. Milne, J. Zhao, M. A. Green, 22.8% efficient solar cells, Applied Phisics Letters 55 (13), 1363- 1365, (1989).

[35] S.W. Glunz, R. Preu, S. Schaefer, E. Schneiderlochner, W. Pfleging, R. Ludemann, G. Willeke, New simplified methods for patterning the rear contact of RP-PERC high-efficiency solar cells, Photovoltaic Specialists Conference, Conference Record of the Twenty-Eighth IEEE, 168, 171, doi: 10.1109/PVSC.2000.915780, (2000).

[36] E. Preu, E. Schneiderlochner, A. Grohe, S. W. Glunz, G. Willeke, Laser-fired contacts - transfer of a simple high efficiency process scheme to industrial production, Photovoltaic Specialists Conference, Conference Record of the Twenty-Ninth IEEE , 130,133, (2002).

[37] G. Agostinelli, P. Choulat, H. F. W. Dekkers, S. De Wolf, G. Beaucarne, Advanced dry processes for crystalline silicon solar cells, Photovoltaic Specialists Conference, Conference Record of the Thirty-first IEEE,1149,1152, doi: 10.1109/PVSC.2005.1488341, (2005).

[38] E. Van Kerschaver, R. Einhaus, J. Szlufcik, J. Nijs, R. Mertens, A novel silicon solar cell structure with both external polarity contacts on the back surface, 2nd World Conference and Exhibition on Photovoltaic Solar Energy Conversion, 1479–1482, (1998).

[39] N. Guillevin, B. Heurtault, L.J. Geerligs, B.B. Van Aken, I.J. Bennett, M.J. Jansen, A.W. Weeber, J. Bultman, J. Wang, Z. Wang, J. Zhai, Z. Wan, S. Tian, W. Zhao, Z. Hu, G. Li, B. Yu, J. Xiong, High Power n-Type Metal-Wrap-through Cells and Modules Using Industrial Processes, 28th European Photovoltaic Solar Energy Conference and Exhibition, (2013).

[40] http://www.aksent-pro.nl/Upload/Downloads/elps-module.pdf

[41] D. Biro, B. Thaidigsmann, F. Clement, A. Wolf, E. Lohmuller, S. Mack, T. Fellmeth, A. Drews, A. Spribille, E. A. Wotke, F. Lottspeich, M. Hofmann, U. Jager, R. Preu, MWT meets PERC: Towards 20% efficient industrial silicon solar cells, Photovoltaic Specialists Conference (PVSC), 37th IEEE , 1395, 1399, doi: 10.1109/PVSC.2011.6186217, (2011).

[42] D. Kray, J. Dicker, D. Osswald, A. Leimenstoll, S. W. Glunz, W. Zimmermann, K. H. Tentscher, G. Strobl, Progress in high-efficiency emitter-wrap-through cells on medium quality substrates, in: Proceedings of the Third World Conference on Photovoltaic Energy Conversion, 1340–1343, Osaka, Japan, (203).

[43] S. W. Glunz, S. Rein, J. Y. Lee, W. Warta, Minority carrier lifetime degradation in boron-doped Czochralski silicon, Journal of Applied Physics, 90, 5, 2397–2404, (2001).

[44] A. Munzer, K. T. Holdermann, R. E. Schlosser, S. Sterk, Improvements and benefits of thin crystalline silicon solar cells. Proceedings of the 2nd World Conference on Photovoltaic Energy Conversion, Vienna, 1214, 1998.

[45] B. Lim, V.V. Voronkov, R. Falster, K. Bothe, J. Schmidt, Lifetime recovery in p-type Czochralski silicon due to the reconfiguration of boron-oxygen complexes via a hole-emitting process Applied Physics Letters, AIP, 98, 162104/1-3, DOI: 10.1063/1.3581215, (2011).

[46] N. Stoddard, B. Wu, I. Witting , M. Wagener, Y. Park, G. Rozgonyi , R. Clark, Casting single crystal silicon: novel defect profiles from BP solar's mono 2™ wafers. Diffusion and Defect Data Pt.B: Solid State Phenomena 1 (8), 131-133, (2008).

[47] K. Fujiwara, W. Pan, N. Usami, K. Sawada, M. Tokairin, Y. Nose, A. Nomura, T. Shishido, K. Nakajima, Growth of structure-controlled polycrystalline silicon ingots for solar cells by casting Acta Material, 54, 3191–3197, (2006).

[48] S.A. McHugo, H. Hieslmair, E.R. Weber, Gettering of metallic impurities in photovoltaic silicon Appl. Phys. A Mater. Sci., 64, 127–137, (1997).

[49] K. R. McIntosh, M. J. Cudzinovic, D. D. Smith, W. P. Mulligan, and R. M. Swanson, The choice of silicon wafer for the production of low-cost rear-contact solar cells, in Proc. 3rd World Conf. Photovoltaic Energy Convers. Conf., Osaka, 971–974, (2003).

[50] C. Schmiga, M. Hörteis, M. Rauer, K. Meyer, J. Lossen, H.-J. Krokoszinski, M. Hermle, S.W. Glunz, Large-Area n-Type Silicon Solar Cells with Printed Contacts and Aluminium-Alloyed Rear Emitter, 24th European Photovoltaic Solar Energy Conference, 21-25, Hamburg, Germany, DOI: 10.4229/24thEUPVSEC2009-2DO.3.3, (2009).

[51] W. Wei, S. Jian, Y. Shengzhao, S. Yun, C. Wenhao, C. Yifeng, Z. Chun, F. Zhiqiang, P.J. Verlinden, Industrial Screen-Printed n-Type Rear-Junction Solar Cells With 20.6% Efficiency, in Photovoltaics, IEEE Journal of,5, 4, 1245-1249, ,DOI: 10.1109/JPHOTOV.2015.2416919, (2015).

[52] A. Uruena, M. Aleman, E. Cornagliotti, A. Sharma, J. Deckers, M. Haslinger, L. Tous, R. Russel, J. Jhon, Y. Yao, F. Duerinckx, J. Szlufcik, Beyond 22% large area n-type silicon solar cells with front laser doping and rear emitter, in Proceedings of the 31th EU-PVSEC, 410-413, (2015).

[53] B. Hoex, J. Schmidt, R. Bock, P. P. Altermatt, M. C. M. van de Sanden, W. M. M. Kessels, Excellent passivation of highly doped p-type Si surfaces by the negative-charge-dielectric Al_2O_3 Applied Physics Letters, 91, 112107, DOI: 10.1063/1.2784168, (2007).

[54] I. G. Romijn, A. Gutjahr, D. Saynova, J. Anker, E.J Kossen, K. Tool. Cost effective n-Pasha solar cells with efficiency above 20%, Photovoltaics International, 20, 33-40, (2013).

[55] I. G. Romijn, G. Janssen, M. Koppes, J. Liu, Y. Komatsu, J. Anker, A. Gutjahr, E. Kossen, A. Mewe, K.. Tool, O. Siarheyeva, M. Ernst, Towards 21%: front side improvements for n-Pasha solar cells, Proceedings of SNEC 8th International Photovoltaic Power Generation Conference & Exhibition, Shanghai, China, (2014).

[56] T. S. Boscke, D. Kania, A. Helbig, C. Schollhorn, M. Dupke, P. Sadler, M. Braun, T. Roth, D. Stichtenoth, T. Wutherich, R. Jesswein, D. Fiedler, R. Carl, J. Lossen, A. Grohe, H.-J. Krokoszinski, Bifacial n-Type Cells With >20% Front-Side Efficiency for Industrial Production, Photovoltaics, IEEE Journal of, 3, 2, 674-677, DOI: 10.1109/JPHOTOV.2012.2236145, (2013).

[57] P. Rothhard, S. Meier, K. Jiang , A. Wolf, D. Biro, 19.9% efficienct bifacial n-type solar cells produced by co-diffusion-cobin, in Proceedings of the 29th European Photovoltaic Solar Energy Conference, Amsterdam, (2014).

[58] W. P. Mulligan, D. H. Rose, M. J. Cudzinovic, D. M. De Ceuster, K. R. McIntosh, D. D., Smith, R. M. Swanson, Manufacture of solar cells with 21% efficiency, in Proceedings of the 19Th European Photovoltaic Solar Energy Conference, 387-390, Paris, (2004).

[59] M. Taguchi, A. Yano, S. Tohoda, K. Matsuyama, Y. Nakamura, T. Nishiwaki, K. Fujita, E. Maruyama, 24.7% Record Efficiency HIT Solar Cell on Thin Silicon

Wafer, Photovoltaics, IEEE Journal of, 4, 1, 96-99, DOI: 10.1109/JPHOTOV.2013.2282737, (2014).

[60] Available on: http://news.panasonic.com/press/news/official.data/data.dir/2014/04/en140410-4/en140410-4.html

[61] Available on: http://www.seac.cc/fileadmin/seac/user/doc/SEAC_Meerjarenprogramma_2012-2016_update_2014.pdf.

[62] F. Feldmann, M. Simon, M. Bivour, C. Reichel, M. Hermle, S.W. Glunz, Efficient carrier-selective p- and n-contacts for Si solar cells, Sol. Energy Mater. Sol. Cells, 131, 100–104, (2014).

[63] S. W. Glunz, F. Feldmann, A. Richter, M. Bivour, C. Reichel, J. Benick, M. Hermle, The Irresistible Charm of a Simple Current Flow Pattern – Approaching 25% with a Solar Cell Featuring a Full-Area Back Contact, 31st European Photovoltaic Solar Energy Conference and exhibition, Hamburg, Germany, (2015).

3

Accurate opto-electrical modelling of multi-crystalline silicon wafer-based solar cells

3.1 Abstract

Modelling of multi-crystalline silicon solar cells has been recently widely used to identify in a fast and cost-effective way performance improvements. The optimization of device performance requires deep understanding of the opto-electrical losses of a reference (fabricated) solar cell. To carry out trustworthy analysis and optimization, the simulation program has to be calibrated to the performance of the fabricated device. In this chapter an accurate opto-electrical modelling of multi-crystalline silicon solar cells is presented. Specific issues arose during the calibration process were addressed, such as the optical model describing light scattering due to wafer texturing, the electrical modelling of heavily doped emitter and the opto-electrical modelling of the back surface field. Model parameters, obtained from theory or measurements, led to an excellent simultaneous matching of simulated and measured reflectance spectrum, internal and external quantum efficiencies and dark and illuminated current-voltage characteristics of the multi-crystalline silicon solar cells. In addition, opto-electrical losses in the investigated solar cells were determined and quantified. Based on such results the design of an optimized device is proposed.

This Chapter is based on the following publication: A. Ingenito, O. Isabella, S. Solntsev, M. Zeman - Solar Energy Materials and Solar Cells, 123, 17-19, 2014, DOI:10.1016/j.solmat.2013.12.019

3.2 Introduction

The structure of wafer based crystalline silicon (c-Si) solar cells is a complex opto-electrical system. In particular, to enhance the absorption in the Si absorber layer several light management techniques are employed at the same time. Anti-reflective coating(s), surface textures for decreasing front reflectance and enhancing light scattering and efficient back reflectors can be typically found in nowadays' solar cells. In addition, to create a net photo-generated current, carriers need to be selectively collected. For this reason the bulk region is sandwiched between an electron collector (also known as emitter) at the front side and a hole collector (also known as back surface field (BSF)) at the rear side. To reduce carrier recombination front and back passivation layers are employed [1]. Hence, for integrated analysis and optimization of the opto-electrical performance of this complex device, computer modelling has become an extremely important tool [2]. In addition, the computer model should use Fermi-Dirac statistics to properly describe the behaviour of the heavily doped regions [3]. In this chapter is presented: (i) a detailed opto-electrical model based on the Advanced Semiconductor Analysis (ASA) program [4] of an industrial multi-crystalline silicon (mc-Si) solar cell that was used as a reference (ii) the analysis of opto-electrical losses of these devices and (iii) based on such analysis, an optimized device where opto-electrical losses are reduced. Special care was devoted to the assignment of proper values to the input parameters of the numerical model. This step is known as *calibration* of model parameters [5]-[6]-[7].

Generally a calibration process consists of tuning a number of input parameters until a good matching between measured and simulated characteristics of the reference solar cell is achieved. Despite the simplicity of this approach, it must be noted that the

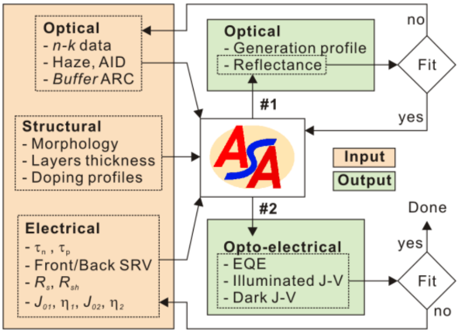

Figure 3.1. Flow-chart for obtaining calibrated input parameters fitting measured R, EQE and *J*–*V* characteristics of the calibrated mc-Si solar cells. The chart starts at step #1 using optical and structural input data. Upon fitting the measured reflectance, step #2 is triggered with the usage of electrical input data. Finally, *EQE* and dark and illuminated *J*–*V* characteristics are carried out and simultaneously fit with measured curves.

extracted values of the input parameters might not be unique or represent realistic values. To avoid this situation, values predicted by theory or experimentally determined can be used as a starting point. A schematic flow-chart of the calibration process followed in this chapter is depicted in Figure 3.1. In particular, for proper modelling of anti-reflective effect and light trapping in mc-Si solar cells, the morphological analysis together with the measurements of the optical properties of the device were carried out (step #1 in Figure 3.1). In order to realistically represent the front emitter, the mechanisms of electrical recombination were investigated and the values of fitting parameters such as surface recombination velocity (SRV) and minority carrier lifetime were compared with those predicted by the theory (step #2 in Figure 3.1). The electrical recombination in the bulk was modelled by using the effective minority carrier diffusion length of the wafer. The rear reflectance was described with optical properties of Si-Al alloy. Recombination losses for the rear side were also modelled in terms of the effective minority carrier diffusion length. Using the parameters of our calibrated opto-electrical model, the simulated reflectance spectrum (*R*), the internal and external quantum efficiencies (*QE*) and (iii) the dark and illuminated current-voltage characteristics (*J-V*) were simultaneously matched very well the measured curves of a commercial reference mc-Si solar cell. Furthermore, the opto-electrical losses in all supporting layers of the reference solar cell were determined and quantified.

3.3 Overview of opto-electrical device simulators for c-Si solar cells

Numerical modelling has been widely applied to c-Si solar cells both by academic institutions and industries. Commercially available software programs like ATLAS [8], SENTAURUS [9][10], and MICROTECH [11] are the most common software programs used by the photovoltaic (PV) industry. However, specific physical models may be absent in these commercial software programs or have to be adapted. For these reasons, many research groups have developed their own advanced physical models describing processes in solar cells that are not implemented yet in commercial computer programs. For simulating the electrical operation of c-Si wafer-based solar cells, it is sufficient to solve the two-carrier time-dependent semiconductor transport equations in one dimension. In 1960s, Gummel from Bell Laboratories introduced an iterative method to solve this set of equations in steady state condition [12]. Since then, several models based on his numerical approach were developed and applied to Si wafer-based solar cells. Around ten years later, a numerical code was written and used at Bell Laboratories to investigate and design solar cells with conversion efficiency higher than 20% [13][14]. In 1980s, the SCAP1D software was developed at Purdue University. This software program was later extended into two dimensions and enabled to simulate a broad variety of solar cell structures such as interdigitated back contact solar cells [15][16]. In mid-1980s, a one-dimensional (1-D) semiconductor simulator called PC-1D [17] was developed as free-available software. In contrast with most of the device simulators at the time, it solved the equations not using the finite difference method but the finite element method. This software, broadly used by the PV community, has strongly contributed to the progress in design of highly efficient c-Si solar cells [18][19]. Recently, the PC-1D software has been used together with the optical modelling of the so-called isotexture [20] to simulate the opto-electrical behaviour of mc-Si solar cells [21]. The AFORSHET software, developed at Helmholtz Centre in Berlin, has been mainly used for simulating hetero-junction silicon-based solar cells [22]. The DESSIS software was used at University of New South Wales in Sydney to analyse c-Si solar cells. Simulation results were employed to realize a solar cell with a record efficiency of 24.7% in 1994 [23][24][25] and to optimize the design of a solar cell on a 47 µm thick float-zone c-Si wafer with record efficiency of 21.5% [26]. In 2011 the PV Lighthouse website was launched. The web site offers online free calculators that simulate various aspects of solar cell operation [27]. Recently on the website a very versatile simulation tool called QUOKKA has been introduced. The program can simulate front and rear or all rear contacted c-Si solar cells in 2D or 3D. The abovementioned software programs are mainly suited for analysis and optimization of the electrical performance of solar cells. The trend in PV industry towards the use of fewer raw materials demands the development and application of advanced light management techniques in order to maximize light absorption in thinner c-Si wafers. This trend also requires that modelling can correctly handle optical processes such as scattering, diffraction and plasmonic absorption using textured surfaces in c-Si solar cells. Since typical c-Si solar cells accommodate textures whose features are much larger than the incident wavelengths, ray tracing approach is widely employed to calculate the optical properties of c-Si solar cells. The most frequent models RAYN [28], TEXTURE [29], SUNRAYS [30], RAYSIM [31], SONNE [32] and recently introduced DAIDALOS [33] or CROWM [34] are three dimensional (3-D). To incorporate optical results of 3-D models into a 1-D device simulator, the 3-D generation profile $G(x,y,z)$ is usually averaged in a 1-D generation profile $G(z)$ which describes the optical situation inside the device along its depth [7]. Recently, better light in-coupling and light scattering triggered by textures with smaller-than-wavelength features are being implemented also in c-Si wafer solar cells [35]. In this case, both coherent non-scattered (i.e. specular) and incoherent scattered (i.e. diffused) light inside the device must be considered [36]. Examples of optical simulators that take into account both specular and scattered light propagation are optical models from École Polytechnique Palaiseau [37], SUNSHINE program from Ljubljana University [38], GENPRO3 optical module implemented in the ASA program of Delft University of Technology [39][40] and the Prague optical model [41]. The ASA program was developed and used at Delft University of Technology to simulate thin-film amorphous Si solar cells. For this purpose advanced models for describing the properties of the amorphous silicon were implemented in this program. Later the ASA program was extended with the models that enabled the program to simulate c-Si solar cells. In this chapter we demonstrate that the optical and electronic models that are implemented in the ASA program can be used for simulating state-of-the-art mc-Si solar cells fabricated with industrial-scale processes.

3.3.1 The ASA device simulator

The ASA program is a 1-D device simulator that integrates both optical and electrical simulations for the complete modelling of solar cell operation. From optical point of view, solar cells are multi-layered optical systems with flat and/or textured interfaces. Since all practical c-Si solar cells use textured surfaces, modelling must take into account refraction and scattering at these surfaces in order to calculate the absorption profile accurately. In case of scattering, an optical model has to take into account both coherent and incoherent light propagation throughout the simulated device [38]. The optical model GENPRO3 implemented in the ASA program fulfils this requirement and, in addition to wavelength-dependent complex refractive indices of individual layers, uses as input descriptive scattering parameters of a rough interface, like haze and angular intensity distribution (*AID*) [42]. Simulating a solar cell with the ASA program, optical outputs are *R* and *T* spectra, the absorptance spectrum (*A*) in each layer of the multi-layered structure and the generation rate related to the optical absorption profile. Once the generation rate is determined, it is used as an input for the electrical simulations. The electrical part of the ASA device simulator is based on semiconductor equations and includes, among other models, Shockley-Read-Hall (SRH) and Auger recombination-generation rates as well as Fermi-Dirac statistics. Particularly, the dependence of carrier mobility (Klaassen's model [43] [44]), diffusion lengths, band-gap narrowing (Shank's model [45]) and minority-carrier lifetime on the doping densities of donors (N_D) and acceptors (N_A) is included. The steady state operation of homo-junction semiconductor device is described by a set of coupled differential equations which, in general, cannot be solved analytically. In the ASA program, this set of equations it is solved by means of numerical methods. The free electron concentration, n, the hole concentration, p, and the electrostatic potential, ψ, are used as variables. After reading structure-statements from an input file, the ASA engine (i) generates via finite element method a grid along the depth of the device (set by the user), (ii) carries out the spectral absorption rate and the reflectance / transmittance spectra, (iii) solves the Poisson equation at thermal equilibrium and finally (iv) computes the current density-voltage characteristic with Newton-Raphson [46] and/or Gummel [12] methods. Once the set of equations has been solved, quantities such as energy band diagram, electron-hole concentration and electric field profile can be also carried out. Finally, external parameters of the device performance such as spectral response, dark and illuminated current-voltage characteristics are calculated. Lumped elements such as series (R_S), and parallel (R_{sh}) resistance and parallel diode [47] can be included in the equivalent circuit to model the final *J-V* characteristics.

3.4 Structure and characterization of the reference mc-Si solar cell

Calibration of the ASA model parameters was carried out with respect to a typical p-type mc-Si solar cell fabricated at Solland Company. The mc-Si wafer-based solar cell had a laterally homogeneous emitter and a full-area aluminium back surface field. The structure of such reference solar cell is schematically shown in Figure 3.2(a). Wafer's thickness was initially around 200 µm with uniform boron doping concentration (N_A) of 10^{16} cm^{-3}. Wafer was textured by using a mixture of HF and HNO_3, which removed about 10 µm of the bulk. The emitter of the cell, located at the front side, was fabricated by using in-diffusion of phosphorus from spray-on source. During this process, phosphoric acid is employed as P-doping source, which diffuses into the silicon by subsequent heating (typically employed at 850 °C).

A SIMS profile of the donor concentration (N_D) in the emitter fabricated at Solland showed a Gaussian-like profile of phosphorous distribution with a peak in the doping concentration $N_{D\text{-}max}$ = $5.2 \cdot 10^{20}$ cm^{-3} and a thickness of approximately 320 nm. Figure 3.3(a) shows the SIMS profile of the P-emitter provided by Solland and one simulated in ASA program consisting of sixteen layers. The vertical dashed lines define the heavily

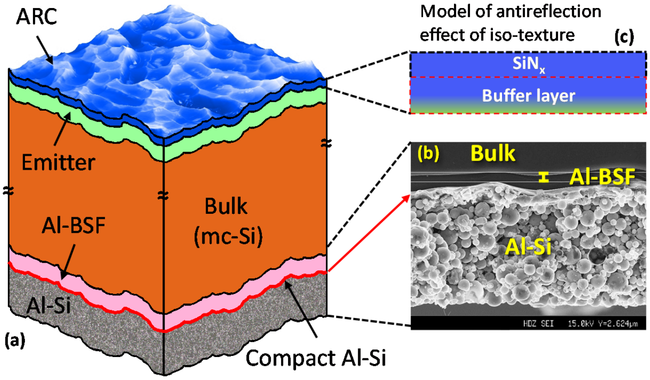

Figure 3.2. (a) Schematic sketch of a typical mc-Si solar cell fabricated by Solland (thicknesses are not in scale); (b) cross-sectional SEM image of the fabricated rear back reflector. The firing process led to the formation of the Al-Si and Al-BSF; (c) model the antireflective effect of the iso-textures coated with SiN_x was modelled with SiN_x / synthetic buffer layer (dashed boxes indicate textured interfaces, see Section 4.1).

doped (A), moderately doped (B) and lightly doped (C-D) regions, respectively. Table 3.1 summarizes the number of layers and grid points for each region of the simulated emitter. After this process, an appropriate wet etching based on HF was used to remove the residual of phosphosilicate glass (PSG). A SiN_x layer was deposited by PECVD on top of the emitter. It served as emitter front side passivation as well as anti-reflective coating (ARC) of solar cell. Its thickness of 75 nm is designed for minimizing reflectance losses at wavelengths around 650 nm. This thickness was optimized for surface passivation purposes rather than maximizing current output. For the formation of front and back contacts, a typical industrial process involving screen-printing and co-firing was used.

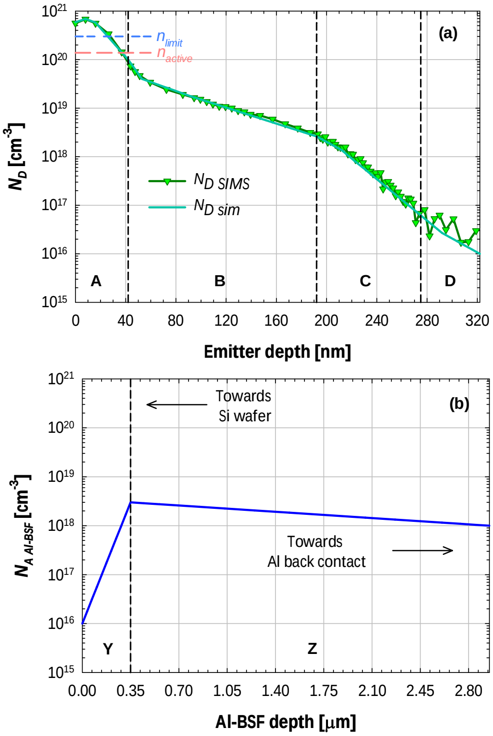

Figure 3.3. (a) SIMS profile of the doped diffused emitter provided by Solland compared with the one simulated in the ASA program composed by sixteen regions (see Table 3.1); the vertical dashed lines define the heavily doped (A), moderately doped (B) and lowly doped (C-D) regions, respectively. The averaged relative deviation between the doping profile measured and simulated $|1-N_{Dsim}/N_{DSims}|$ is less than 7% in the regions A-C. Such quantity rises for region D because of noise in the SIMS measurements. The limit of the solid solubility of P in Si is $n_{limit} = 2.9\ 10^{20}\ cm^{-3}$ at 850 °C [56] and the active doping concentration as found in Section 3.5.2.1, are also reported. (b) Al-BSF doping profile simulated with the ASA program divided in seven layers (see Table 3.2). Zero depth indicates the position of the p/p+ interface.

During the co-firing, the frit contained into the silver paste printed on the front surface penetrates through the ARC allowing the of the Ag contact with underlying silicon, while full-area Al-BSF forms at the rear side. In particular, by alloying o the Al paste screen printed at the back side an aluminium-doped p+ region is formed. This process has been widely studied in literature [49]-[53] and consists of the following phases: at melting temperature, Al liquidizes within the stable paste and Si dissolves from the surface into the Al melt according to the phase binary diagram. As consequence, Al diffuses to the Si surface forming an Al-Si alloy. At peak temperature (typically between 850 and 950 °C), the Si reaches the maximum concentration within the melt. When the cooling starts, the Si is rejected from the melt and recrystallize epitaxially at Si surface with Al incorporated into the Si lattice. This leads to the formation of the Al-doped p+ region. When the temperature reaches the 570 °C (i.e. eutectic temperature), the remaining melt solidifies forming the Al-Si eutectic (i.e. 12.6 w.t.% in Si). In addition, to the Al-Si eutectic layer within the particles composing the paste a compact eutectic layer with a lamellar structure is also formed at interface between the Si and the Al-doped region [54]. This layer sets the internal real reflectance of the cell [54]. The p+-type Si layer forming BSF and had a doping concentration between 10^{18} to $3{\cdot}10^{18}$ cm^{-3} within a thickness of around 3 µm. The agglomerated Al-Si layer was around 30 µm thick. The real Al-BSF doping profile of the reference cell couldn't be provided by the company for confidential reasons. Therefore, we used a typical doping profile measured for standard Al-BSF reported in [50] and [55] (see Figure 3.3(b)). As the Al solubility decreases with decreasing the temperature the doping profile shows the typical decrease of Al concentration when going from the bulk/Al-BSF towards the Al-BSF surface [50] [51]. The vertical dashed lines in Figure 3.3(b) define the moderately doped (Z) and lightly doped (Y) regions respectively. The latter region was included in order to include process in-homogeneities [50]. Table 3.2 summarizes the number of layers and grid points used for each region of the simulated Al-BSF. A cross-sectional scanning electron microscopy (SEM) image of the back contact in the fabricated reference cell is reported in Figure 3.2(b).

Region	**# Layers**	**# Grid points**
A	3	60
B	4	60
C	8	150
D	1	50

Table 3.1. Number of layers and grid points for each region of the simulated emitter (1 nm / point).

Region	**# Layers**	**# Grid points**
Y	5	150
Z	2	80

Table 3.2. Number of layers and grid points for each region of the simulated Al-BSF (13 nm / point).

Layer	**Thickness**
SiN_x	80 nm
Emitter (see Figure 3.3 (a))	322 nm
Bulk mc-Si layer ($N_A \approx 10^{16}$cm^{-3})	190 µm
Al-BSF (Figure 3.3 (b))	2.95 µm
Si-Al	~ 1 µm
Al	30 µm

Table 3.3. Layer thickness of the reference mc-Si solar cell

An overview of layers thickness related to the reference solar cell is presented in Table 3.3 The characterization of such reference mc-Si solar cell was carried out at Solland, where dark and illuminated J-V characteristics, series and shunt resistance, EQE and total reflectance R were measured. The latter two quantities were measured between two metal fingers in order to avoid optical shading losses from the front metal grid which covered 6.5% of the total area. Further morphological and optical characterizations were carried out at Delft University of Technology. Atomic force microscopy (AFM) image of wafer's textured surface is presented in Figure 3.4, where large random features with peak-to-peak height larger than 4 µm are recognizable. The scattering parameters of the cell were characterized with an Automated Reflectance / Transmittance Analyser (ARTA) and Integrating Sphere (IS), accessories of a Perkin Elmer Lambda 950 spectrophotometer [57]. Diffused and total components of reflected and transmitted light where measured and their ratios (haze parameters H) were calculated as follows:

$$H_T = \frac{T_D}{T_T}; H_R = \frac{R_D}{R_T} \qquad 3.1$$

Noteworthy, both H_R and H_T were almost equal to one in the whole wavelength range of interest. This means that light in both reflectance and transmittance is fully diffused by wafer's surface. Figure 3.5 demonstrates that there is almost no dominant specular component or wavelength dependence in the measured AID at air/Si interface (AID_R). This quantity is defined as:

$$AID_R = 10^{-I(\lambda,\vartheta,\varphi)} \qquad 3.2$$

where I the measured intensity as function of the wavelength scattering angle (θ) and azimuth angle φ.

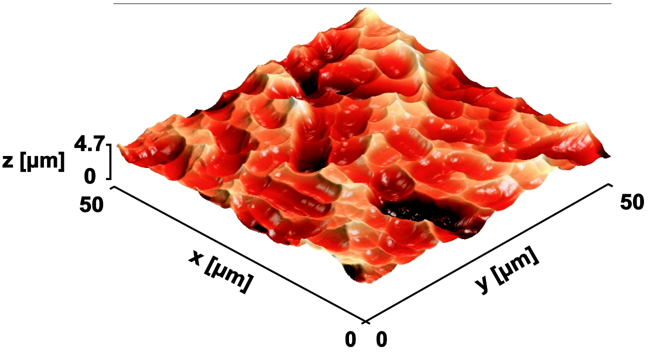

Figure 3.4. AFM scan of mc-Si wafer textured surface.

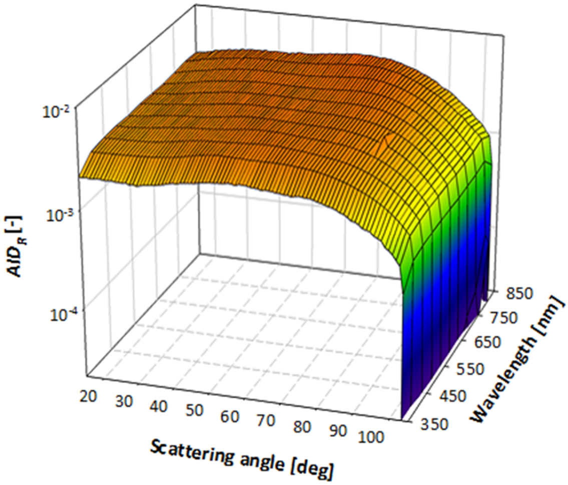

Figure 3.5. *AID* in reflectance (*AID*$_R$) of the mc-Si etched surface measured with the ARTA accessory. The measured sample was covered with 100 nm of Ag to avoid Si absorption.

3.5 Calibration procedure

3.5.1 Optical modelling of front texture and anti-reflective coating

The surface texture of the wafer serves to scatter light into the solar cell but also to introduce an anti-reflective effect. Such combined effects can be simulated either by ray-tracing or by decoupling the anti-reflection from the scattering effect with appropriate optical models. The second approach was chosen as compatible with the optical capabilities of the ASA program. The optical model called GENPRO3 implemented in ASA was used to simulate the light scattering. This model required as input parameter the measured Haze (*H*) and *AID* reflected and transmitted at each interface as function of the wavelength and scattering angle. Unfortunately, the measured AID_R, presented in Figure 3.5, only contains information regarding light scattering in reflectance at air / Si interface. As presented in [20], the optical model of the AID in transmittance (AID_T) of isotextured surface by means of ray-tracing follows a cos(3/2·θ) distribution rather than an ideal Lambertian distribution (i.e. cos(θ)). Here θ is the angle at which a ray traverses the substrate with respect to the surface normal (scattering angle). In the ASA program the measured AID_R distribution to describe the scattering at front texturing in reflectance (see Figure 3.5) and a cos(3/2·θ) to describe the scattering in transmittance through the front surface (see Figure 3.7) were finally used. The anti-reflective effect, due to random features of the surface texture and enhanced by the presence of SiN_x in the role of ARC, was simulated by adding an additional buffer layer on the top of the SiN_x layer, whose purpose was to decrease the total reflectance by improving the light in-coupling at the front interface. As sketched in Figure 3.2(c), such buffer layer was modelled by using a synthetic non-absorbing layer with a refractive index averaged between those of air and SiN_x (at 600nm).

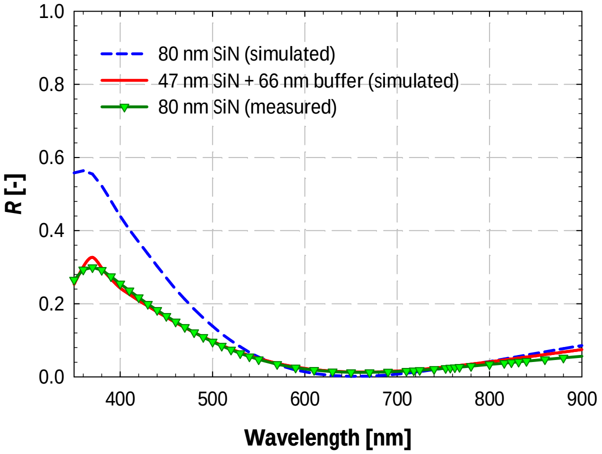

Figure 3.6. Measured total reflectance of mc-Si reference solar cell. The antireflective effect was simulated by combining SiN_x layer with an additional non-absorptive buffer layer.

Varying the thickness of both buffer and SiN_x layers, a good matching between the measured and simulated total reflectance was achieved until around 900 nm (d_{SiN} = 47 nm and d_{buffer} = 63 nm, see Figure 3.6). This approach is only suited in case of non-absorbing SiN_x ARC otherwise it leads to an underestimation of the parasitic absorption into the SiN layer. The complex refractive index provided by Solland showed an imaginary part equal to zero in the wavelength range of interest.

At longer wavelengths Si becomes weak absorber and the total reflectance measured at front side is also depending by the rear internal reflectance. In Section 3.5.4, where the rear side of the device will be opto- electrically modelled, the modelling of total reflectance will be properly extended.

3.5.2 Opto-electrical modelling of the emitter

As depicted in Figure 3.2(b), the emitter doping concentration varies over many orders of magnitude in a narrow region of few hundreds nanometres. Such doping profile causes variation in its optical properties and recombination mechanisms. The recombination in standard industrial emitters is often affected by the formation of inactive phosphorous precipitates. As the SIMS in Figure 3.3 (a) shows, the first 20 nm of the fabricated emitter present a doping concentration higher than the P solid solubility in Si at 850° C ($n_{limit} = 2.9{\cdot}10^{20}$ cm^{-3} [56]), meaning that for $N_D > n_{limit}$, P is electrically inactive. Such region is called *P-supersaturated* [62]. Based on experimental data, researchers have demonstrated that to model the recombination losses in highly P-doped industrial emitters two approaches can be followed [62]:

i. Assume that the Auger recombination in the supersaturated emitter region is determined by the electrically active doping concentration and the surface recombination velocity at emitter surface (S_{p0}) depends on the chemical doping concentration at surface (x=0);
ii. Assume that the recombination rate in the emitter is function of the undissolved P-doping concentration (measured by SIMS) and S_{p0} is set by the electrically active P concentration at emitter surface;

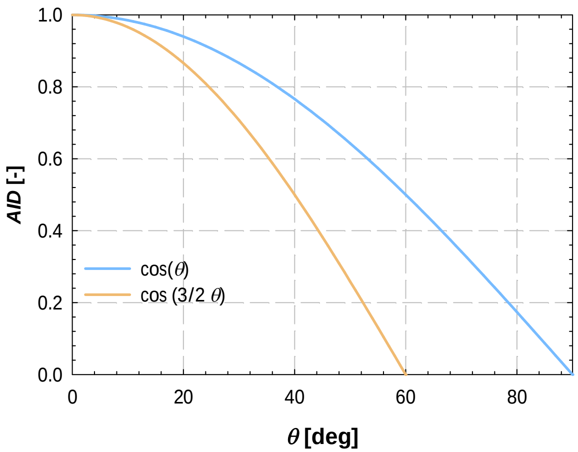

Figure 3.7. Comparison between normalized cos(θ) (i.e. Lambertian) and cos(3/2·θ) angular intensity distributions.

3.5.2.1 Modelling of SRH emitter recombination rate

Quantify S_{p0} is rather challenging because it depends on many parameters as surface doping concentration and properties of the passivation layer [59]. The total electrical losses of a passivated emitter are usually quantified by measuring its emitter saturation current density (J_{0e}). Various models have been proposed to extract S_{p0} from J_{0e}. A well-established model for P-doped silicon emitters based on Fermi-Dirac statistics has been proposed by Altermatt *et al*. [60]. According to such model, S_{p0} can be expressed as function of the surface doping concentration $N_D(0)$ as follows [60]:

$$S_{p0} = S_{p1}\left(\frac{N_D(0)}{N_{p1}}\right)^{\gamma_{p1}} + S_{p2}\left(\frac{N_D(0)}{N_{p2}}\right)^{\gamma_{p2}} \tag{3.3}$$

where $N_{p1} = N_{p2} = 10^{19}$ cm^{-3}, S_{p1} = 500 cm/s, S_{p2} = 60 cm/s, γ_{p1} = 0.4 and γ_{p2} = 3 are numerically derived in [60]. In this case, the recombination rate in the emitter is modelled following the second approach (ii). To strictly follow this approach both SIMS and Electrochemical capacitance voltage (ECV) doping profiles would be required. Since only SIMS measurements were performed, in this work the value of S_{p0}, and thus $N_D(0)$, was extracted via matching of measured and simulated characteristics. In particular, by using equation 3.3 and $N_D(0) = 5.2{\cdot}10^{20}$ cm^{-3} a $S_{p0} = 8.44{\cdot}10^{6}$ cm/s would be expected. However, when referring to the results of our calibration (see Section 3.6.1), a good agreement between measured and simulated solar cell external parameters was found for a $S_{p0} = 1.3{\cdot}10^{5}$ cm/s. To achieve such value of S_{p0}, a $N_D(0) = 1.3{\cdot}10^{20}$ cm^{-3} has to be used in Equation 3.3. This indicates that the electrically activated doping concentration (n_{active}) at emitter surface might be lower than the one measured via SIMS. ECV not performed in this work is required to confirm such assumption. Finally, the extracted S_{p0} includes all front side recombination including these happening at emitter \ metal interface (S_{met}). However, in case of homogeneous emitter with low R_{SH} and low metal surface coverage, as in this case, the S_{met} contribution on S_{p0} becomes negligible [63]. The SRH recombination in the emitter was modelled by using the model proposed by Min *et al.* [64]. This model showed that the recombination losses in most of industrial emitters are limited by SRH rather than Auger mechanisms. In particular, the SRH was modelled by using an effective capture-cross section, $\sigma_p = 7.5{\cdot}10^{-18}$ cm^2, and an effective defect of density (N_T) given by the difference between total (SIMS) and active (ECV) P-doping concertation. Therefore, we calculated the minority carrier lifetime in the emitter for SRH recombination ($\tau_{p0\ SRH}$) in ASA by using equation 2.21. In this work N_T was only estimated for the first 40 nm of the emitter as the difference between n_{active} (constant with emitter depth) and $N_D(x)_{SIMS}$ with $0 < x < 40$ nm of the emitter.

3.5.2.2 Modelling of Auger emitter recombination rate

Auger recombination also constitutes an important recombination mechanism in heavily doped emitter. In standard illumination conditions and for heavily doped emitter, the excess of carrier concentration is smaller than the concentration of donors (N_D), which means that the emitter generally operates at low injection conditions. The ASA software calculates the Auger recombination rate as follows [65]:

$$U_{Auger} = C_{neff}\, n^2 p + C_{peff}\, p^2 n \tag{3.4}$$

with:

$$C_{neff} = C_n \left(\frac{N_D}{N_D + p} \right) + \frac{C_a}{2} \left(\frac{p}{N_D + p} \right) \tag{3.5}$$

$$C_{peff} = C_p \left(\frac{N_A}{N_A + n} \right) + \frac{C_a}{2} \left(\frac{n}{N_A + n} \right) \tag{3.6}$$

where $C_{n(p)}$ is the Auger coefficient for electrons (holes) at low injection levels, C_a is the ambipolar Auger coefficient at high injection levels, n(p) is the thickness dependent concentration of majority (minority) carriers in the emitter (see Figure 3.3(a)) and N_A is the acceptors concentration. In Equations 3.5 and 3.6, the thickness dependency is not explicitly stated but contained in the doping concentrations. Inputs were the so-called effective Auger coefficients C_{neff} and C_{peff} indicated in Equations 3.5 and 3.6. One of the first parametrization of the Auger coefficients was proposed by Dziewior and Schmid, for which $C_n = 2.8 \cdot 10^{-31}$ cm^6/s and $C_p = 0.99 \cdot 10^{-31}$ cm^6/s, while the implied ambipolar Auger coefficient is expressed as the sum of C_n and C_p ($C_a = 3.79 \cdot 10^{-31}$ cm^6/s) [66]. The thickness-dependent carrier lifetime in Auger-dominated emitter is automatically calculated in ASA as follows [65]:

$$\tau_{Auger\_emitter} = \frac{\Delta n}{U_{Auger}} \tag{3.7}$$

In case of high doping concentration and low injection condition of the emitter, the second factor on the right side of Equation 3.4 becomes negligible. Despite Equation 3.4 physically describes the Auger recombination, Equations 3.5 and 3.6, that model the effective Auger coefficients tend to underestimate the Auger recombination rate as they do not include the Coulomb enhancement effects at high and low injection levels [67]. The most comprehensive determination of Auger coefficients for low injection levels and low doping concentration was proposed by Altermatt *et al.* [68]. They performed an empirical parameterization of Auger coefficients by multiplying the Dziewior and Schmid Auger coefficients with the enhancement factors (g_{eeh}, g_{ehh}) [67][68]. According to this modified model, the Auger recombination rate is calculated by replacing C_{neff} and C_{peff} in Equation 3.4 with $g_{eeh}C_n$ and $g_{ehh}C_p$, respectively. However, at intermediate doping concentration ($1{\cdot}10^{17}$ cm^{-3} < N_{dop} < $5{\cdot}10^{18}$ cm^{-3}), also this modified model is not accurate. A more general parameterization of Auger recombination rate for a wide range of dopant concentration and injection levels was proposed by Kerr & Cuevas [65]. However, this model does not include Coulomb enhancement effects. Finally, the model proposed by Richter *et al.* [69] adds to the model of Kerr & Cuevas [65] the enhancement factors (g_{eeh}, g_{ehh}) as introduced by Altermatt. According to Richter model, the Auger recombination rate can be written as:

$$U_{Auger} = (np - n_{ieff}^2)(C_n n_0 + C_p p_0 + C_a \Delta n^{0.92}) \quad 3.8$$

with:

$$C_n(n_0) = 2.5 \times 10^{-31} \cdot g_{eeh}(n_0) \quad 3.9$$

$$C_p(p_0) = 8.5 \times 10^{-32} \cdot g_{hhe}(p_0) \quad 3.10$$

$$C_a(n_0) = 3 \times 10^{-29} \quad 3.11$$

Where, n is equal to n_0 in condition of low injection ($\Delta n \ll n_0$), $p_0 = n_i^2 / n_0$, n_i is the intrinsic carrier concentration in silicon and g_{eeh} and g_{ehh} are those defined in the Altermatt model [67][68]. To strictly implement Richter model in computer software, one should describe the emitter with *many* layers, each characterized by (i) thickness equal to the measurement step in the SIMS profile and (ii) doping concentration at that specific depth. Using certain C_n and C_p in the approach implemented in ASA, one can eventually calculate accurate R_{Auger} for different doping levels at low injection levels. To this aim, the emitter was divided in sixteen regions in order to ensure a physically trustworthy modelling of this layer. These sixteen layers in the ASA program had different optical properties, doping concentrations and thicknesses. Simulated doping concentration in each layer was linearly approximated to the SIMS profile as shown in Figure 3.3(a). The set of C_n used in this work is illustrated in Figure 3.8 together with C_n predicted by the Richter and Altermatt models calculated for the simulated doping profile. The C_n extracted with ASA followed the trend predicted by the Richter model, showing the capabilities of our computer model in handling both dopant density and injection levels. In addition, in Figure 3.9, the Auger recombination rate calculated with the Richter and Altermatt models were compared to the one simulated by the ASA software. By using the Equations 3.4-3.6 with Auger coefficients expressed by Equations 3.9-3.11 the Auger recombination rate calculated in ASA matched to the one predicted by the Richter model.

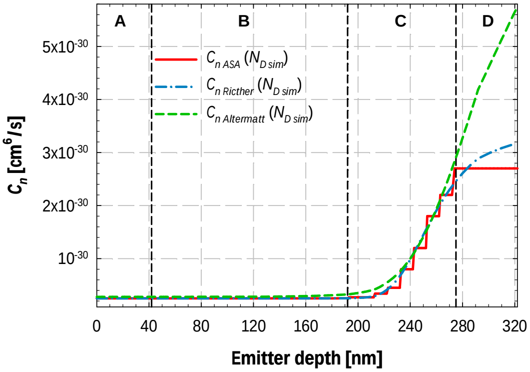

Figure 3.8. C_n Auger coefficient for the simulated doping profile predicted by the Richter model (blue dash-dotted line), the Altermatt model (green dashed line) and the one extracted with ASA (red solid line). The averaged relative deviation (in the regions A-C) between the C_n extracted with ASA and the C_n calculated with Richter model for the simulated doping profile was found to be $|1-(C_{n\ ASA}/C_{n\ Richter(sim)})|<7\%$.

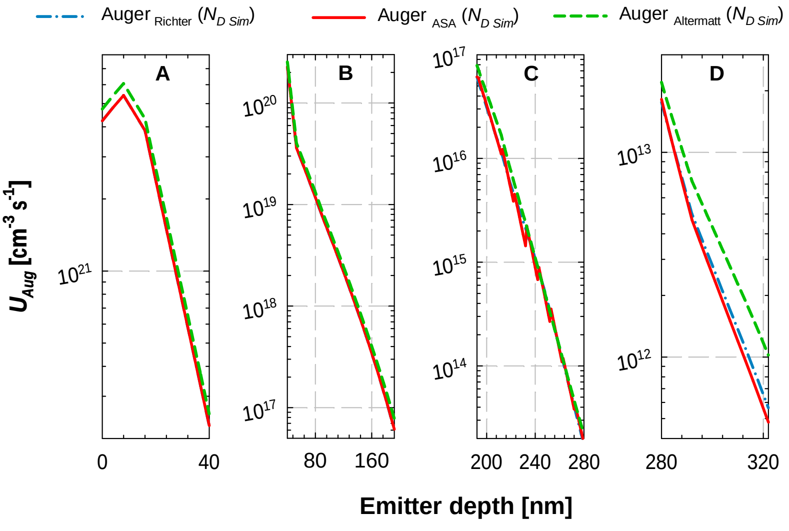

Figure 3.9. Auger recombination rate predicted by the Altermatt (green dashed line) and the Richter (blue dash-dotted line) models compared to the Auger recombination rate extracted from ASA simulations (red solid line). Auger recombination calculated with the Altermatt model showed slightly larger deviation from Richter and ASA models in regions A and D.

3.5.2.3 Modelling of Radiative emitter recombination rate

Aside Auger recombination mechanism, also radiative recombination was taken into account. It is calculated in ASA as:

$$R_{radiative} = B(np - n_i^2) \qquad 3.12$$

where B is a constant equal to $4.7 \cdot 10^{-15} cm^{-3} s^{-1}$ [71]. This recombination mechanism was set for all electrical active layers of the simulated device (emitter, bulk and BSF).

3.5.2.4 Optical modelling of the emitter

The optical properties of the emitter were modelled by using the complex refractive index of Si as reported in [73]. However, due to heavy doping of this layer parasitic losses due to free carrier absorption occur. To include such losses Rudiger et. model presented in [70] was used. For the regions A, B, C in Figure 3.3(a) the extinction coefficient (*k*) calculated at doping concentrations of $1 \cdot 10^{20}$, 10^{19}, and 10^{18} cm^{-3}, respectively, for region D, the *k* of *undoped* Si was used (see Figure 3.10).

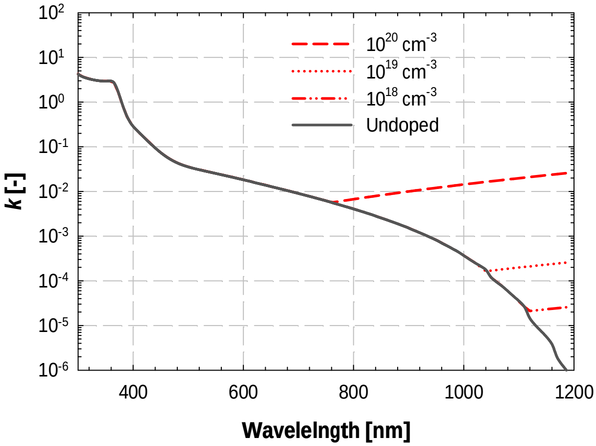

Figure 3.10. Imaginary part of the complex refractive index for un-doped, P and B doped Si calculated according to [70]. For the regions A, B, C in Figure 3.3 (a) the calculated k values for doping concentrations of $1 \cdot 10^{20}$, 10^{19}, and 10^{18} cm^{-3}, respectively, were used. For region D, *k* for *undoped* Si was used.

3.5.3 Opto-electrical modelling of the bulk mc-Si

Passing to the bulk region, which is p-type mc-Si doped (10^{16} cm^{-3}), the modelling parameter describing the SRH bulk recombination is the minority carrier lifetime (τ_{n_bulk}). In case of high quality mono c-Si material such quantity is spatially constant over the bulk. However, in mc-Si materials, recombination also occurs at the boundaries between crystalline grains [72]. Usually such grains have different shapes, sizes, dislocations and recombination mechanisms. This leads to a distribution of the value of $\tau_{n\ bulk}$ which is difficult to determine. In the proposed model it was assumed that the mc-Si bulk is composed of equal grains with identical electronic properties leading to a unique value of τ_{n_bulk}. The SRH τ_{n0_bulk} was set as free-parameter in the simulations and the extracted was 70 µs, corresponding to minority carrier diffusion length of 450 µm. This value was in agreement with Solland expectations. The optical modelling of the bulk was performed by using the surface morphology as discussed in Section 3.5.1 and the Si complex refractive index as reported in [73].

3.5.4 Opto-electrical modelling of Al-BSF

A typical industrial process for Al-BSF formation involves screen printing of Al paste followed by a firing step. As result an Al-p+ doped region is formed together with a Si-Al eutectic layer. In this section, the optical model of the rear reflectance set by Si-Al eutectic and the electrical model of the Al-BSF are presented. The optical characterization of Si-Al eutectic layer is not a trivial task because of its location at the rear side of the solar cell and its formation on a textured morphology. To model the back reflectance in absence of optical properties of Si-Al eutectic layer, a common way is to assign a constant value of rear internal reflectance together with Brendel's approach [75] or Phong factor [76] to describe the light scattering. In this work, simulated and measured total reflectance of our reference cell were matched at wavelengths longer than 900 nm by using constant values for the real part (n) and the imaginary part (k) of the complex refractive index and previously mentioned scattering properties of the isotextured surface (see Section 3.5.1). More details about the optical properties of the Al-Si are shown in the Appendix 3.9.1. Four back reflectors applied to the same solar cell structure were simulated: two modelling the reference cell (Si-Al / Al) with flat interfaces and rough interfaces, respectively, and two (Si / Al) with textured and flat interfaces for reference purposes. For the two textured cases, scattering properties at front and back sides were taken into account. In Figure 3.11, the solution Si-Al/Al textured resulted in lowered escaped reflectance at long wavelength (compared with flat case) which fairly enough matched the measured reflectance of the reference cell. As reported in Section 3.6.2, at long wavelengths the Si-Al alloy exhibits considerable absorptance, and therefore lower reflectance with respect to Al. This result also points out that the reflectivity of the back contact has to be strongly improved in order to increase the absorption of light in the absorber layer of the reference solar cell. The purpose of a BSF is also to *electrically reflect* the minority carriers back in the bulk and to decrease the back surface recombination velocity (BSRV) at the rear contact. In other words, the BSF essentially decreases the high BSRV at Si / Al interface (typically, $S_{Al} = 10^7$ cm/s) in a lower BSRV at the interface bulk / p+ [78] ($S_{p/p+} < 1000$ cm/s, depending by the quality of the Al paste and sintering process). When modelling the Al-doped Si, together with SRH and Auger recombination mechanisms, also lateral doping in-homogeneities and effect of incomplete ionization need to be taken into account [79]. Following a similar approach to that described in Section 4.3 for modelling the emitter, the Al-BSF was divided in two regions (Y-Z, see Figure 3.3(b)) including a total of 7 layers (see Table 3.2).

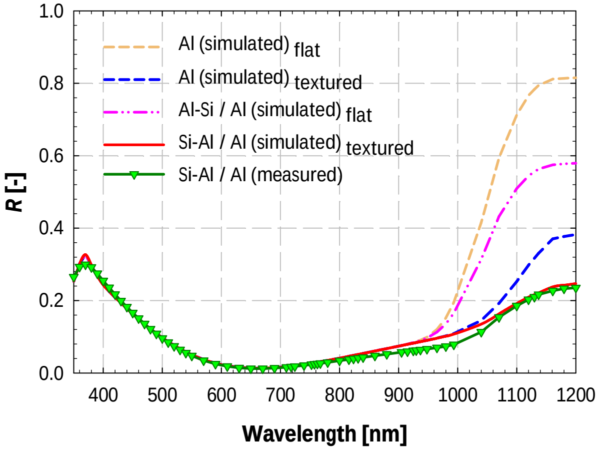

Figure 3.11. Measured and simulated total reflectance of the reference mc-Si solar cell. Flat (textured) in the legend indicates that front and back side are assumed to be flat (textured). Free carrier absorption (FCA) in both emitter and BSF is included.

In Figure 3.12(a) the C_p Auger coefficient calculated according to the Richter model and the one used in ASA are reported. The averaged relative deviation (in the regions Y-Z) between the C_p extracted with ASA and that calculated with the Richter's model for the simulated Al-BSF doping profile was found to be less than 6%. The SRH recombination model, associated to the Si-Al doped region used in this work is based on the incomplete ionization model for Al doped silicon [79]. According to such model, the knowledge of the absolute defect concentration and capture cross section would be required. Due to restriction of the simulation tool, the parameterization of the SHR minority carrier lifetime due to incomplete ionization as proposed by Altermatt was used [80][81]. Such analytical model calculates the SRH recombination ($\tau_{SRH\ Altermatt}$) due to incomplete ionization by only using the Al doping profile ($N_{Al\text{-}BSF}$):

$$\tau_{SRH\ Altermatt}\,(\mu s) = \frac{1}{\left(\dfrac{N_{Al\text{-}BSF}\,(cm^{-3})}{1\,cm^{-3}}\right) + 2.8339\times 10^{-24}\cdot f} \qquad 3.13$$

where f is a dimensionless scaling factor given in literature [82]. In ASA is possible to model doping dependent minority carrier lifetime for used for calculating the SRH ($\tau_{SRH\ ASA}$) as:

$$\tau_{SRHASA} = \tau_0\left(\frac{N_A}{N_{onset}}\right)^{\beta} \qquad 3.14$$

where, N_A is the acceptor concentration (as reported in Figure 3.3 (b)) and τ_0, β and N_{onset} are constants. The $\tau_{SRH\ Altermatt}$ was matched with $\tau_{SRH\ ASA}$ as function of the doping profile by using the set of values: $\tau_0 = 1.18 \cdot 10^{-6}$ s, $\beta = -1.5$, $N_{onset} = 2.3 \cdot 10^{17}$ cm^{-3} and $N_A = N_{Al\text{-}BSF}$. The relative deviation between these two lifetime values calculated as $|1-\tau_{SRH\ ASA} / \tau_{SRH\ Altermatt}|$ was found to be less than 4%. The effective carrier lifetime in Al-BSF ($\tau_{Al\text{-}BSF}$) can be expressed as:

$$\frac{1}{\tau_{Al-BSF}} = \frac{1}{\tau_{SRH}} + \frac{1}{\tau_{Auger}} \qquad 3.15$$

Where, both τ_{SRH} and τ_{Auger} are automatically calculated in the ASA program from the related recombination mechanism. As Figure 3.12 (b) depicts, as expected, the dominant mechanism of recombination in the Al-BSF region is SRH rather than Auger recombination. The spatially average effective lifetime calculated with Equation 3.15 for the intermediate doped region was 370 ns, which is in good agreement with the value found in literature [79].

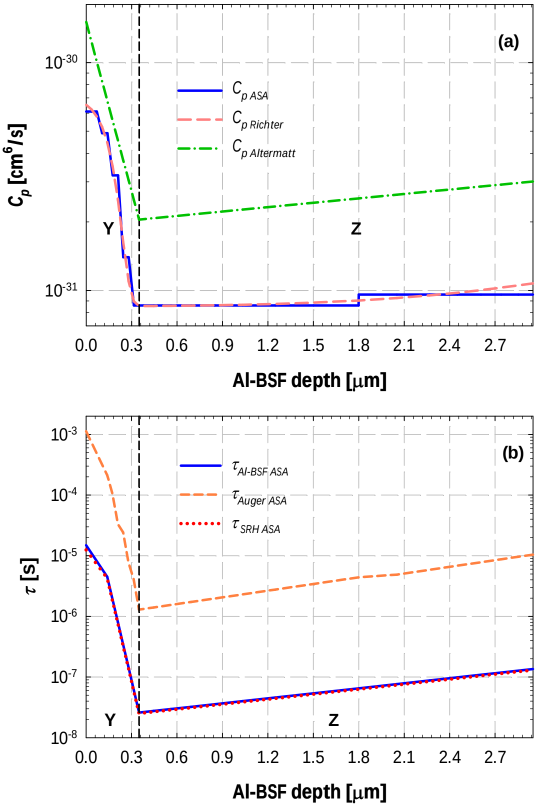

Figure 3.12. (a) C_p Auger coefficient predicted by the Altermatt (green line with dots) and the Richter models (red dashed line). Auger coefficient extracted from ASA simulations in both Y and Z regions is in good agreement with the Richter model (blue line). The relative deviation $|1\text{-}C_{p\ ASA}/C_{p\ Richter}|$ was found to be less than 6%. (b) Effective lifetime from Equation 3.15 (blue line) and its Auger ($\tau_{Auger\ ASA}$) and SRH ($\tau_{SRH\ ASA}$) components (orange and red lines, respectively) simulated with ASA program.

3.6 Results

3.6.1 Calibration results

By using previously calculated or measured input values, in this section, the results of the calibrated model are reported. Measured and simulated *IQE*, *R* and illuminated *J*-*V* characteristics of reference mc-Si solar cell are presented in Figure 3.13 (a) and (b). In Table 3.4, measured and simulated external parameters of the reference device are summarized, showing an excellent matching. The J_{SC} here compared does not include the optical shading losses of the front grid covering the front surface. The J_{SC} of illuminated *J*-*V* characteristic was corrected for the optical shading losses which are estimated to be around 6.5%. In addition, the dark *J*-*V* characteristic of our reference cell was also modelled. In Figure 3.14 (a), measured and simulated dark current densities as function of the voltage are illustrated. Series (R_s) and shunt resistance (R_{sh}), and diode were added as lumped elements in the solar cell equivalent circuit. The measured and simulated dark *J*-*V* characteristics were found to deviate in the voltage range between 0.3 and 0.5 V. In particular, the measured dark *J* curve is higher than the simulated one between the voltage range of 0.3 and 0.5 V. A better matching between simulated and measured *J*-*V* on the full voltage range was achieved by adding a lumped parallel diode [47] to the equivalent circuit with the J_{02} and ideality factor (η_2) reported in Table 3.5. Such diode is added to describe the in-homogeneities of the mc-Si material. In particular, between 0.3 and 0.5 volt, R_{sh} and recombination losses in the space charge region (SCR) of the *pn* junction become dominant. Higher recombination losses in the SCR could originate from recombination at grain boundaries, as well as a possible in-diffusion of Ag acting as recombination centres in the SCR [48].

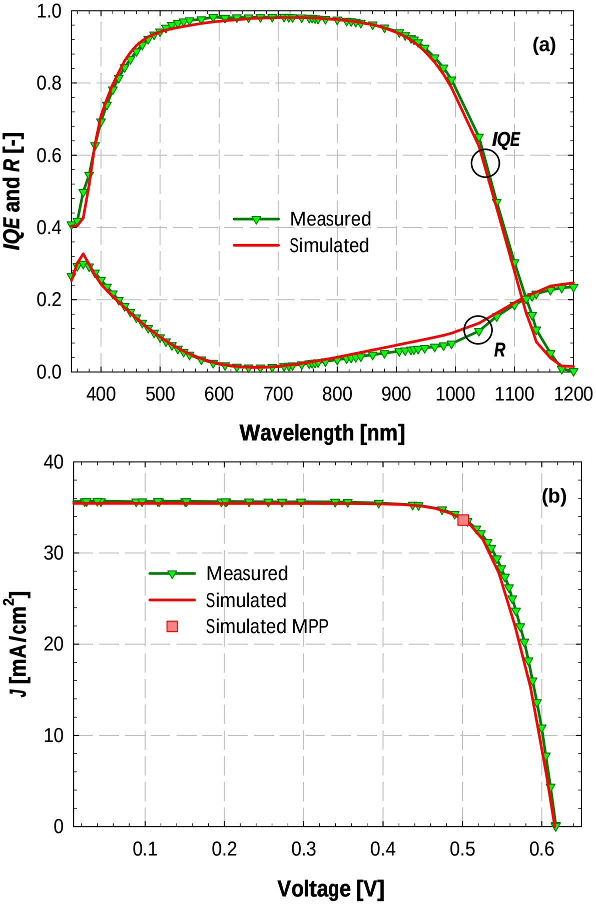

Figure 3.13. Measured and simulated (a) *IQE* and total reflectance (*R*) and (b) illuminated *J*-*V* characteristic of the mc-Si reference solar cell. The square indicates the maximum power point (*MPP*).

	Measured	**Simulated**
V_{OC} [V]	0.617	0.613
J_{SC} [mA/cm^2]	35.71	35.65
FF [-]	0.773	0.775
η [%]	17.03	16.93

Table 3.4. Measured and simulated external parameters of the calibrated mc-Si solar cell.

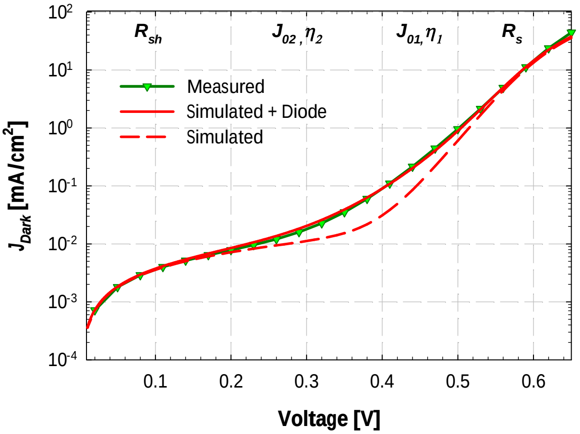

Figure 3.14. Measured and simulated dark *J-V* characteristic of the mc-Si reference solar cell. A better fitting between measured and simulated characteristic was achieved by adding a lumped parallel diode. The voltage regions where R_s and R_{sh}, n_1, J_{01}, n_2 and J_{02} are dominant are indicated. The values of such parameters are summarized in Table 3.5.

	R_s [Ωcm^2]	**R_{sh}** [kΩcm^2]	**J_{01}** [mA/cm^2]	**J_{02}** [mA/cm^2]	**η_1** [-]	**η_2** [-]
Measured	0.93	25	$1.10 \cdot 10^{-9}$	$6.4 \cdot 10^{-6}$	-	-
ASA	1.1	28	$1.5 \cdot 10^{-9}$	-	1.0	
ASA + diode	1.1	28	$1.5 \cdot 10^{-9}$	$5.8 \cdot 10^{-5}$	1.0	2.1

Table 3.5. Measured and simulated external parameters of the calibrated mc-Si solar cell and extracted values from the equivalent circuit.

3.6.2 Analysis of the optical and electrical losses of the calibrated mc-Si solar cell

Understanding and quantifying the electrical and optical losses is crucial for designing new solutions aimed to enhance solar cell's performance. In this respect, physically trustworthy opto-electrical simulations are instrumental for obtaining insights in loss processes, since measured properties of a solar cell often do not give clear indications where optical and electrical losses occur in the device and of which type they are. Figure 3.15 illustrates the conservation of energy, intended as sum of reflectance, optical absorptances in all parts of the solar cell and transmittance (which is equal to zero on the whole wavelength range). In this type of plot, both optical and electrical losses can be quantified, while T is numerically negligible for the presence of the metallic back reflector.

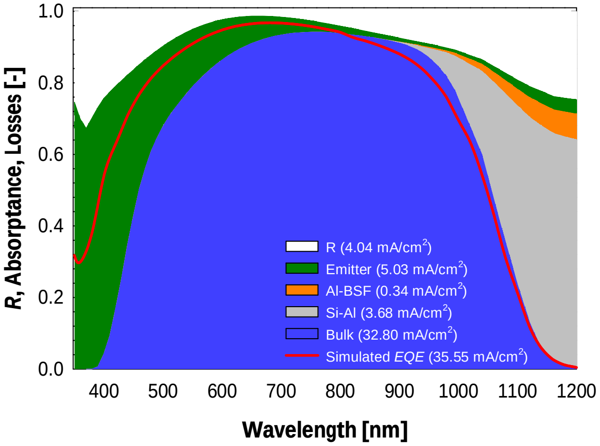

Figure 3.15. Total reflectance and absorptance in all layers of our reference cell together with simulated EQE. Implied photo-current densities are also reported.

For analysing optical losses, implied photo-current densities were calculated by integrating reflectance or absorptances with the standard photon flux ($I_{AM1.5}$) [83] as follows:

$$J_t = \int_{\lambda_1}^{\lambda_2} A_t(\lambda) \cdot I_{AM1.5} d\lambda \tag{3.16}$$

where λ_1 = 350 nm and λ_2 = 1200nm, $A_t(\lambda)$ is the wavelength-dependent reflectance or absorptance and subscript *t* indicates different parts of the solar cell. Setting $A_t(\lambda) = 1\ \forall\lambda$ in Equation 3.16, one can calculate the total photo-current density available in the considered wavelength range, the so-called Shockley-Queisser limit [84]. In the wavelength range of interest, this total photo-current density corresponds to 45.6 mA/cm^2. According to Equation 3.16, implied photo-current densities related to reflectance, emitter, bulk, Al-BSF and Si-Al back reflector are estimated to be 4.04 mA/cm^2, 5.03 mA/cm^2, 32.80 mA/cm^2, 0.34 mA/cm^2 and 3.68 mA/cm^2, respectively. The photo-generated current density (J_{ph}) in the device is the sum of the absorptions in emitter, bulk and BSF and is equal to 37.6 mA/cm^2. Such current density is higher than the J_{SC} (35.65 mA/cm^2) obtained from the simulated *EQE* reported in Figure 3.15. In particular, Figure 3.15 shows that the simulated *EQE* extends in the optical absorptance of the emitter at short wavelengths, while leaves out a part of absorptance in the bulk at long wavelengths. The origin of this behaviour can be explained in terms of electrical and optical (FCA) losses. In Table 3.6, the calculated current densities due to SRH, Auger and radiative recombination mechanisms as function of the position in our reference device are illustrated. Along device depth, the current densities associated to each mechanism were calculated as follows:

$$J_k(z_i) = q \cdot r_k{}^*(z_i) \cdot (z_{i+1} - z_i) \tag{3.17}$$

where, r is the recombination rate ($m^{-3}s^{-1}$), subscript k stays for SRH, Auger or radiative recombination and $[z_0, z_1, z_2, \ldots, z_n]$ are the grid points defined in the ASA program with z_0 individuating the interface SiN_x / emitter and z_n the interface Al-BSF / Si-Al back contact. Afterwards, these current densities were integrated in the emitter, bulk and Al-BSF within their respective thicknesses:

$$J_{y,k} = \sum_{i=d_{ys}}^{d_{yf}} J_k(z_i) \tag{3.18}$$

where, subscript y stays for emitter, bulk or Al-BSF and $[d_{y\text{-}s}, d_{y\text{-}f}]$ is the range of coordinates between the starting and finishing grid points of the equivalent y layer. Finally, current density due to recombination in each layer could be simply carried out by summing all the contributions:

$$J_y = \sum_k J_{y,k} \tag{3.19}$$

In addition, the current density associated to the SRH recombination at surface was calculated as:

$$J_{SRH\text{-}surf} = q \cdot S_n \cdot \Delta p(z_0) \tag{3.20}$$

where, $\Delta p(z_0)$ is the excess of minority carriers at SiN_x / emitter interface. The equation applies also for the rear surface with $S_{p0} = 10^6$ cm/s in place of S_n, where S_{p0} is the surface recombination velocity at Si / metal interface, and $\Delta n(z_n)$ in place of $\Delta p(z_0)$. The analysis of the electrical losses was performed at maximum power point (MPP), which is the operational point of a c-Si solar cell. As indicated in Table 3.6, the dominant recombination mechanisms at MPP are: (i) Auger recombination in the emitter, (ii) SRH recombination in the emitter bulk, front and rear sides. The comparable recombination current density for Auger and SRH into the emitter is related to large number of defects introduced by the inactive P [64]. Current densities associate to Radiative recombination were found to be negligible. This is related to the fact that impurities and defects are important losses for mc-Si and that Si has an indirect band-gap. The total current density related to the recombination mechanisms occurring in all parts of our reference cell was found to be equal to 4.2 mA/cm^2. The difference between implied photo-current densities due to optical absorption and electrical recombination (Δ_y) in the emitter, bulk, Al-BSF and surfaces constitutes the current density at MPP (J_{MPP}) of the reference mc-Si solar cell is presented in Table 3.7.

Solar cell Part	J_{SRH} [mA/cm^2]	J_{Auger} [mA/cm^2]	J_{Rad} [mA/cm^2]	$J_{SRH\text{-}Surf}$ [mA/cm^2]	**Total per part** [mA/cm^2]
Emitter	0.944	1.215	$1.33 \cdot 10^{-4}$	-	2.159
Bulk	0.816	$5.3 \cdot 10^{-3}$	$1.46 \cdot 10^{-3}$	-	0.822
Al-BSF	0.038	$1.1 \cdot 10^{-3}$	$1.33 \cdot 10^{-5}$	-	0.039
Front Surface	-	-	-	0.786	0.786
Rear Surface	-	-	-	0.402	0.402
Grand Total	1.798	1.221	0.001	1.188	**4.20**

Table 3.6. Current densities calculated for the calibrated device associated to SRH, Auger, Radiative, front and rear surface recombination mechanisms at V_{MPP} = 0.5 V.

Solar cell part	$J_{optical}$ [mA/cm^2]	$J_{optical\text{-}FCA}$ [mA/cm^2]	$J_{electrical\text{-}rec}$ [mA/cm^2]	Δ_y [mA/cm^2]
Emitter	5.03	-0.263	-2.15	2.61
Bulk	32.80	-	-0.82	31.97
Al-BSF	0.34	-0.300	-0.03	0.01
Front surface	-		-0.78	-0.78
Rear surface	-		-0.40	-0.40
	Current density at V_{MPP} -> $J_{MPP} = \Sigma_y \Delta_y$			**33.4**

Table 3.7. Analysis of implied photo-current and recombination current densities (V_{MPP} = 0.5 V) in all parts of the reference mc-Si solar cell. Subscript *y* stays for emitter, bulk, Al-BSF, front and rear surfaces.

3.7 Optimization of p-type c-Si solar cell

As discussed in Section 3.6.2 the implied photo-generated current density (J_{ph}) of the calibrated device is 37.6 mA/cm^2. The maximal J_{ph} that a silicon slab with thickness of 190 μm can deliver is equal to 43.5 mA/cm^2 according to the $4n^2$ limit [87]. This means that the light trapping scheme employed for the calibrated device presents serious optical limitations mainly due to high front reflectance (*R*), non-ideal light scattering and poor internal rear reflectance as described in Section 3.6.2. To decrease optical losses due to surface reflectance and incomplete photon absorption in the infrared region of the spectrum surface textures exhibiting better light trapping properties than the one exhibited by iso-textures are required. Random pyramids fabricated via alkaline etching of mono-c Si (<100>), are known to exhibit excellent light trapping properties [88]. The internal rear reflectance (R_b) in a solar cell can be enhanced by: (i) using a dielectric layer at the rear side locally open in correspondence of the Al-BSF contacts (ii) by replacing screen printed Al-BSF with B doped region and evaporated Al or Ag contacts (also in this case a dielectric layer locally opened is beneficial to further increase R_b). As shown in the previous section, the poor optical absorption was not the only factor limiting the performance of the calibrated device. In particular, the sum of recombination current densities at V_{MPP} was found to account for more than 10% of J_{MPP}. A selective emitter is a well-established solution to minimize emitter recombination and front surface recombination velocity. Selective emitters are formed by two doped regions with different doping concentrations: (i) high doping concentration underneath the metal contact in order to achieve low contact resistance and recombination Si / metal interface [63], (ii) lightly doped emitter (LDE) concentration underneath the passivation layer, in order to minimize recombination losses [63]. The doping profile of such region needs to be optimized in order to ensure reasonable lateral transport of the electrons and low doping surface concentration in order to minimize the electrical losses (Auger and SRH). As shown in [89] a very effective solution to minimize emitter recombination consists in fabricating a LDE with deep doping profile and low doping concentration rather than narrow but heavily doped. For this optimization study we used a LDE emitter with a sheet resistance of 100 Ω/sq, surface doping concentration of 10^{19} cm^{-3} and depth of 1μm as proposed in [89] and reported on the lefts axis of Figure 3.16. For such emitter the front surface recombination velocity (FSRV) calculated by using Equation 3.3 is equal to $4{\cdot}10^{3}$ cm/s (the extracted FSRV for the calibrated device was found to be more than 30 times larger). The P-dopants were considered fully-activated. This is a reasonable assumption for lightly doped emitter fabricated by using low rate of the N_2-$POCL_3$ carrier gas [64]. To reduce SRH recombination in the bulk, higher quality bulk material is required. For this study a p-type wafer ($N_A = 1{\cdot}10^{16}$ cm^{-3}) with τ_{bulk} of 0.6 ms was used. Such value was chosen to be almost 10 times larger than the τ_{bulk} of the mc-Si wafer used for the calibrated device in order to minimize SRH bulk recombination. To reduce rear recombination the Al-BSF can be replaced by more performing BSF. For this study the doping profile reported on the right axis of Figure 3.16 was proposed. Such doped layer was fabricated by using epitaxial growth of B-doped silicon in situ. As already analysed in Section 3.5.4, the role of the BSF is to create a high / low junction that reduces the surface recombination velocity at metal/Si interface (S_{p0}) in an effective surface at p/p+ interface ($S_{p/p+}$). Godlewski et al. [14] have derived and expression for ($S_{p/p+}$) as:

$$S_{p/p+} = \frac{D_{BSF}}{D_{bulk}} \frac{N_{BSF}}{N_{bulk}} \frac{1}{L_{BSF}} \frac{S_{p0}/D_{BSF} \cdot L_{BSF} + tanh(W_{BSF}/L_{BSF})}{1 + S_{p0}/D_{BSF} \cdot L_{BSF} \cdot tanh(W_{BSF}/L_{BSF})} \qquad 3.21$$

where, D_{BSF} (D_{bulk}) is the BSF (bulk) diffusion coefficient, N_{BSF} (N_{bulk}) is the BSF (bulk) doping concentration, W_{BSF} and the L_{BSF} are the thickness and the minority carrier diffusion length in the BSF, respectively. Such quantities are summarized in Table 3.8 together with $S_{p/p+}$ calculated with Equation 3.21 for both Al-doped and B-doped BSF. Equation 3.21, assumes that the doping concentration and charge transport properties within the doped region are constant. As shown in [90] this leads to possible deviations between the measured and calculated values of $S_{p/p+}$. In addition, under these assumptions, Equation 3.21 determines the $S_{p/p+}$ based on the built-in potential at p/p+ interface and the minority carrier recombination within the BSF, but does not account for recombination in the SCR [91]. However, Equation 3.21 was used to analytically evaluate $S_{p/p+}$ which is not a direct output of the simulator. Notice, that the simulator solves numerically the semiconductor equations and therefore does not rely on the assumptions aforementioned.

As shown in Table 3.8, in case of the epitaxial BSF, the $S_{p/p+}$ can be reduced by one order of magnitude with respect to that of Al-BSF. The *IQE* over the optimized device compared with calibrated one is presented in Figure 3.17.

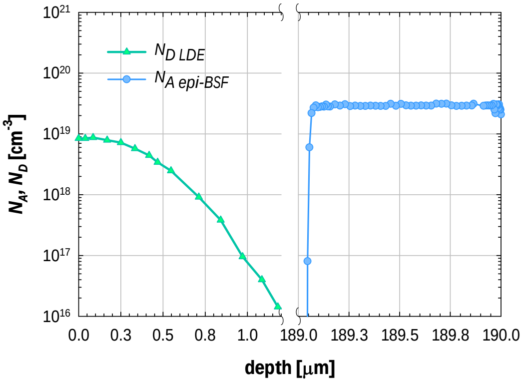

Figure 3.16. ECV doping profile of lowly doped region of the selective emitter taken from [89] and epitaxially grown B-doped BSF.

	Al-BSF	**B-epi BSF**
S_{p0} [cm/s]	10^6	10^6
W_{BSF}/L_{BSF} [-]	0.176	0.167
N_{BSF} [cm^{-3}]	$3\cdot10^{18}$	$3\cdot10^{19}$
$S_{p/p+}$ [cm/s]	550	43.5
N_{bulk} [cm^{-3}]	10^{16}	10^{16}

Table 3.8. Summary of the parameters used to calculate $S_{p/p+}$ by using equation 3.21. D_{BSF} and L_{BSF} were calculated by using the calculator in ref.[92] and constant doping profile N_{BSF} within W_{BSF}.

The figure shows a clear enhancement of the *IQE* of the optimized device on the full wavelength range with respect to the calibrated one. In particular, a strong increase of the *IQE* of the optimized device is achieved at short wavelength due to lower recombination losses at front side. The *IQE* enhancement at long wavelength is achieved because of the better light trapping (light scattering and internal rear *R*) and lower bulk and rear recombination losses of the optimized device. The simulated V_{OC} and J_{SC} for the optimized device increase of more than 50 mV and 4 mA/cm^2, respectively, compared to the Al-BSF device, leading to an absolute efficiency gain of 4.6%. A comparison of the optical and electrical losses at MPP (following the approach described in Section 3.6.2) is presented in Figure 3.18 for both devices. For the optimized device optical absorption is clearly enhanced because of the better light trapping scheme employed. This leads to an increase of J_{ph} of +2.7 mA/cm^2 with respect to the standard Al-BSF. The employment of selective emitter and B-doped BSF decrease of the front and rear recombination losses (including emitter and BSF) with respect to the calibrated cell. This increases the minority carrier concentration (*n*) in the bulk compared to the calibrated cell (see Figure 3.19) and thus V_{OC}.

	Calibrated	**Optimized**
V_{OC} [V]	0.613	0.667
J_{SC} [mA/cm^2]	35.65	40.01
FF [-]	0.775	0.807
η [%]	16.93	21.53

Table 3.9. Simulated external parameters of the calibrated (mc-Si) and optimized (mono c-Si) solar cells.

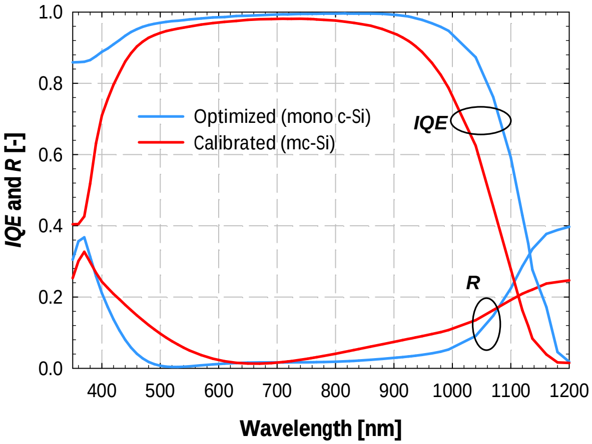

Figure 3.17. Simulated *IQE* and *R* of the calibrated (mc-Si) and optimized (mono c-Si) solar cells.

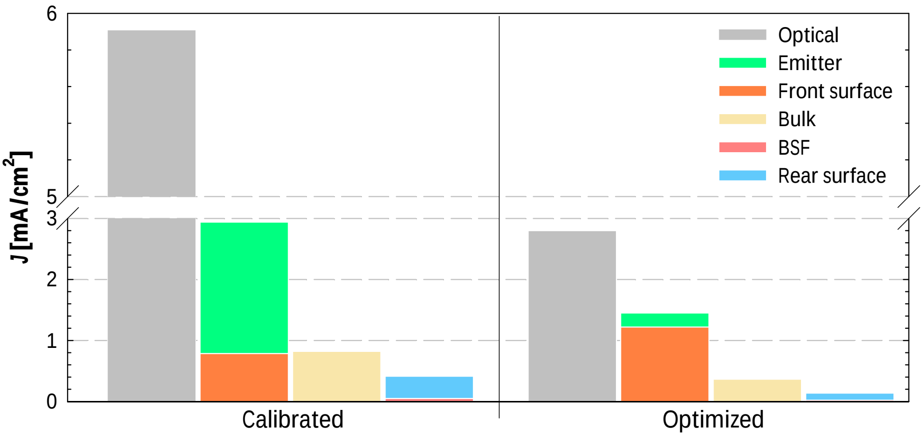

Figure 3.18. Comparison of optical (i.e. $J_{ph4n2}(180\ \mu m)$ - J_{ph}) and recombination losses analysis between calibrated (mc-Si) device at V_{MPP} = 0.5 V and optimized (mono c-Si) device and devices at V_{MPP} = 0.56 V.

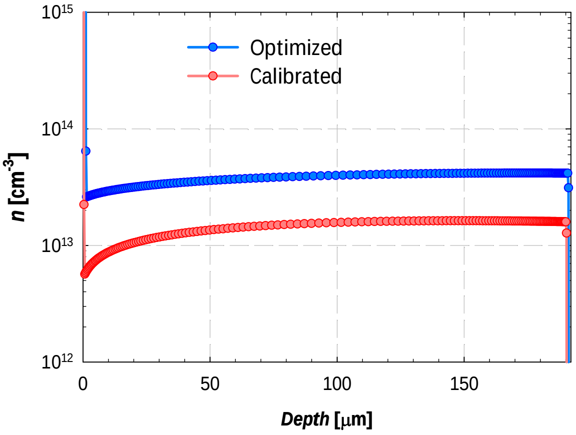

Figure 3.19. Minority carrier concentration (n) at MPP as function of the bulk depth for the calibrated (V_{MPP} = 0.5 V) and optimized (V_{MPP} = 0.56 V) solar cell, respectively.

3.8 Conclusions

An accurate opto-electrical model together with a calibration procedure based on the ASA program to simulate mc-Si solar cells was presented. Theory, measurements of optical and transport properties and realistic parameters were successfully used in the ASA program for simulating the electrical and spectral performance of a mc-Si solar cell. The front reflectance was matched along the entire wavelength range of interest (350 nm - 1200 nm) (i) by using measured scattering parameters of textured wafer to simulate the scattering effect, (ii) by considering a non-absorbing additional buffer layer stacked on SiN ARC to simulate the antireflective effect and (iii) by employing possible optical properties of Si-Al layer. At the interface SiN / emitter, front surface recombination velocity was extracted and compared with model proposed by Altermatt *et al*. The extracted value of FSRV was in agreement with one predicted by the model when an n_{active} concentration was used rather than $N_{D\ SIMS}(0)$. Min et *al*. model was used to take into account the enhanced SRH recombination rate due to inactive dopants in P-diffused emitters. Auger coefficients proposed by Richter *et al.* were used to model Auger recombination in all doped regions. Also for the Al-BSF, both Auger and SRH recombination mechanisms were taken into account. Calibrated input parameters used in the simulations carried out by the ASA program resulted in an excellent simultaneous matching between measured and simulated reflectance, spectral response, and dark and illuminated current-voltage characteristics of the reference device. Opto-electrical losses in the reference device were determined quantitatively and qualitatively. It was found that optical losses were mainly determined by the high front reflectance and high absorption in the Si-Al alloy, while electrical losses were mainly determined by high surface recombination velocities at front and back contacts, SRH recombination in the bulk, Auger and SRH recombination both pay an important role in the emitter and finally SRH dominates in the Al-BSF. A further study to enhance conversion efficiency of the calibrated cell was carried out. In particular, to enhance optical absorption iso-textures were replaced by standard random pyramids. This required switching from multi to mono c-Si wafers. To reduce front recombination, Auger and SRH recombination in the emitter and rear recombination, selective emitter and B doped BSF fabricated via epitaxial growth are proposed. By employing all the proposed solutions conversion efficiency could be increased by more than 4% abs. with respect to the calibrated device.

3.9 Appendix

3.9.1 Optical constant Al-Si alloy

Optical constants (*n,k*) of the AlSi-alloy (12.6% Si) have been measured by means of spectroscopic ellipsometer by Jaglarz et al. [93] and are reported in Figure 3.20. For comparison the figure reports also the *n,k* values of pure Al measured by Palik et al. [94]. When modelling the internal rear reflectance of the cell by using the *n,k* values of Palik et *al.*, as expected, higher values of the simulated *R* at long wavelengths (>100 nm) with respect to the measured ones are observed (see Figure 3.21). When using the optical constant provided by Jaglarz et al. even higher values of the *R* at long wavelengths were observed compared with the measured ones.

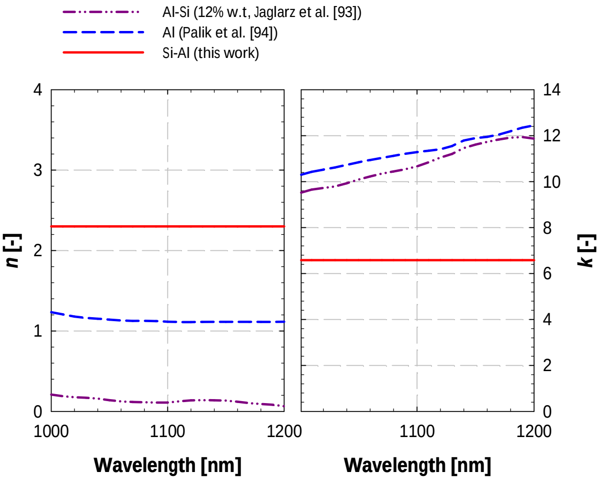

Figure 3.20. (a) n , (b) k of Al-Si (12% w.t.) measured by Jaglarz et al. [93], pure Al measured by Palik et al. [94] and the ones of the Al-Si alloy proposed in this work.

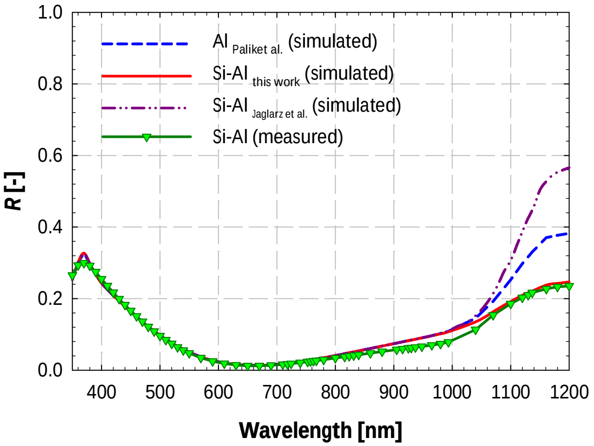

Figure 3.21. Comparison between measured and simulated *R* for the different optical constants of the BR as reported in Figure 3.20. For all simulated curves scattering properties as shown in Section 3.5.1 were used.

The reason for this effect could be related to the different structural properties of the Al-Si alloy measured by Jaglarz et al. compared with the one of the Al-Si formed after sintering process. As shown in [54] the AlSi-alloy formed after the sintering process has two different structures. The first one , in contact with Al-BSF is more compact while on top of it there are the AlSi agglomerates composing the paste. In this work, a good matching between measured and simulated *R* was obtained by modelling the internal rear reflectance of the Al-Si alloy with a wavelength independent $n_{Al\text{-}Si}$=2.3 and $k_{Al\text{-}Si}$ =6.8.

Notice, that this might not constitute the true *n,k* optical constant of the Al-Si alloy but as shown in Figure 3.21, lead to a reasonable matching between measured and simulated *R* at long wavelengths.

3.10 References

[1] M. A. Green, Solar Cells: Operating Principles, Technology, and System Applications, Prentice Hall, Englewood Cliffs, U.S.A., (1981) (ISBN: 978-0-138-22270-3).

[2] P. P. Altermatt, Models for numerical device simulations of crystalline silicon solar cells a review. Journal of Computational Electronics 10 (2011), 314-330.

[3] S. M. Sze, Semiconductor Devices: Physics and Technology, John Wiley & Sons Incorporated (2001), (ISBN: 978-0-471-33372-2).

[4] B. E. Pieters, H. Stiebig, M. Zeman, R. A. C. M. M. van Swaaij, Determination of the mobility gap of intrinsic mc-Si:H in p–i–n solar cells. Journal of Applied Physics 105 044502 (2009), DOI: 10.1063/1.3078044.

[5] M. Zeman, R. Van Swaaij, E. Schroten, L. L. A. Vosteen, J. W. Metselaar, Device modelling of a-Si:H alloy solar cells: Calibration procedure for determination of model input parameters, Materials Research Society Symposium Proceedings 507 (1998), 409-414, DOI: 10.1557/PROC-507-409.

[6] M. Zeman, J. Krč, Optical and electrical modeling of thin-film silicon solar cells, Journal of Materials Research 23 (2008), 889-898, DOI:10.1557/jmr.2008.0125.

[7] O. Isabella, H. Sai, M. Kondo, M. Zeman, Full-wave optoelectrical modeling of optimized flattened light-scattering substrate for high efficiency thin-film silicon solar cells, Progress In Photovoltaics: Research and Applications (2013), DOI: 10.1002/pip.2314.

[8] Atlas Silvaco, http://www.silvaco.com/products/device_simulation/atlas.html.

[9] Sentaurus Synopsys, http://www.synopsys.com/tools/tcad/Pages/default.aspx.

[10] M. Peters, M. Rüdiger, H. Hauser, M. Hermle, B. Bläsi, Diffractive gratings for crystalline silicon solar cells - optimum parameters and loss mechanisms, Progress In Photovoltaics: Research and Applications 20 7 (2012), 862 - 873, DOI: 10.1002/pip.1151.

[11] MicroTec Siborg Systems Inc, http://www.siborg.com/.

[12] H. K. Gummel, A self-consistent iterative scheme for one-dimensional steady state transistor calculations, Electron Devices, IEEE Transactions on 11 10 (1964), 455 - 465, DOI: 10.1109 / T-ED.1964.15364.

[13] J. G. Fossum, Computer-Aided Numerical Analysis of Silicon Solar Cells, Solid State Electronics 19 (1976), 269 - 277.

[14] M. P. Godlewski, C. R. Baraona and H. W. Brandhorst Jr, Proc. 10th Photo. Spec. Conf., (1973), 40, IEEE, New York.

[15] M.S. Lundstrom, Numerical analysis of silicon solar cells, Ph.D. thesis, School of Electrical Engineering, Purdue University (1980), http://adsabs.harvard.edu/abs/1980PhDT........93L.

[16] K. Girardini, S. Jacobsen: Tech. Rep. N87-22301, NASA, Scientific and Technical Information (STI) (1986).

[17] PC-1D, http://www.pv.unsw.edu.au/info-about/our-school/products-services/pc1d.

[18] P. A. Basore, D. T. Rover, A. W. Smith, PC-1D: Enhanced numerical solar cell modelling, Photovoltaic Specialists Conference, Conference Record of the Twentieth IEEE 1 (1988), 389 - 396, DOI: 10.1109/PVSC.1988.105730.

[19] P. A. Basore, Numerical modelling of textured silicon solar cells using PC-1D, Electron Devices, IEEE Transactions on 37 2 (1990), 337-343, DOI: 10.1109/16.46362.

[20] C.S. Baker-Finch, K. R. McIntosh, M. L. Terry, Isotextured Silicon Solar Cell Analysis and Modeling 1: Optics, IEEE Journal of Photovoltaics 2, (2012), 457 - 464, DOI: 10.1109/JPHOTOV.2012.2206569.

[21] C.S. Baker-Finch, K. R. McIntosh, M. L. Terry, Y. Wan, Isotextured Silicon Solar Cell Analysis and Modeling 2: Recombination and Device Modeling, IEEE Journal of Photovoltaics 2, (2012), 465 - 472, DOI: 10.1109/JPHOTOV.2012.2204390.

[22] A. Froitzheim, R. Stangl, M. Kriegel, L. Elstner, W. Fuhs, AFORS-HET: a computer-program for the simulation of heterojunction solar cells to be distributed for public use, Photovoltaic Energy Conversion, Proceedings of 3rd World Conference on 1 (2003), 279 - 282.

[23] A. G. Aberle, G. Heiser, M. A. Green, Two-dimensional numerical optimization study of the rear contact geometry of high-efficiency silicon solar cells, Journal of Applied Physics 75 5391 (1994), DOI:10.1063/1.355694.

[24] G. Heiser, A. G. Aberle, S. R. Wenham, M. A. Green, Two-dimensional numerical simulations of high-efficiency silicon solar cells, Microelectronics Journal 26 (1995), 273 - 286.

[25] J. Zhao, A. Wang, P. Altermatt, M. A. Green, 24% efficient silicon solar cells with double layer antireflection coatings and reduced resistance loss, Applied Physics Letters 66 26 (1995), 3636 - 3638, DOI: 10.1063/1.103610.

[26] A. G. Aberle, P. Altermatt, G. Heiser, S. Robinson, A. Wang, J. Zhao, U. Krumbein, M. A. Green, Limiting Loss Mechanisms in 23% Efficient Silicon Solar Cells, Journal of Applied Physics 77 7 (1995), 3491 - 3504, DOI: 10.1063/1.358643.

[27] PV Lighthouse portal, http://www.pvlighthouse.com.au/.

[28] J. O. Schumacher, S. Sterk, B. Wagner, W. Warta, Quantum efficiency analysis of high efficiency solar cells with textured surfaces, Proceedings of the 13th European Photovoltaic Solar Energy Conference 1 (1995), 96 - 99, ISBN: 0-9521452-7-8.

[29] A. W. Smith, A. Rohatgi, S. C. Neel, Texture: A Ray Traacing Program for the Photovoltaic Community, Photovoltaic Specialists Conference, Conference Record of the Twenty First IEEE 1 (1990), 426 - 431, DOI: 10.1109/PVSC.1990.111660.

[30] R. Brendel, SUNRAYS: a versatile tray tracing program for the photovoltaic community, Proceedings of the 12th European Photovoltaic Solar Energy Conference (1994), 1339 - 1342.

[31] J. E. Cotter, Raysim 6.0 - a free geometrical ray tracing program for silicon solar cells, Photovoltaic Specialists Conference, Conference Record of the Thirty First IEEE (2005), 1165 - 1168, DOI: 10.1109/PVSC.2005.1488345.

[32] C. Zechner, P. Fath, G. Willeke, E. Bucher, Two- and three-dimensional optical carrier generation determination in crystalline silicon solar cells, Solar Energy Materials and Solar Cells 51 (1998), 255 - 267, DOI:10.1016/S0927-0248(97)00226-2.

[33] H. Holst, P. P. Altermatt, R. Brendel, DAIDALOS - A Plugin Based Framework for Extendable Ray Tracing, Proceedings of the 25th European Photovoltaic Solar Energy Conference (2010), 2150 - 2153, DOI: 10.4229/25thEUPVSEC2010-2CV.3.24.

[34] B. Lipovšek, J. Krč, M. Topič, Design and Optimisation of Thin-Film Silicon PV Modules with Surface-Textured Front Glass by Using a Combined Geometric Optics / Wave Optics Model, Proceedings of the 27th European Photovoltaic Solar Energy Conference and Exhibition (2012), 2604 - 2607, DOI:10.4229/27thEUPVSEC2012-3DV.1.62.

[35] M. Otto, M. Kroll, T. Käsebier, R. Salzer, A. Tünnermann, R. B. Wehrspohn, Extremely low surface recombination velocities in black silicon passivated by atomic layer deposition. Applied Physics Letters 100 191603 (2012), DOI: 10.1063/1.4714546.

[36] J. Krč, M. Zeman, F. Smole, M. Topič, Optical modeling of a-Si:H solar cells deposited on textured glass/SnO_2 substrates, Journal of Applied Physics 92 749 (2002), DOI:10.1063/1.1487910.

[37] F. Leblanc, J. Perrin, J. Schmitt, Numerical modeling of the optical properties of hydrogenated amorphous-silicon-based p-i-n solar cells deposited on rough transparent conducting oxide substrates, Journal of Applied Physics 75 1074 (1994), DOI: 10.1063/1.356489.

[38] J. Krč, F. Smole, M. Topič, Potential of light trapping in microcrystalline silicon solar cells with textured substrates, Progress In Photovoltaics: Research and Applications 11 7 (2003), 429 - 436, DOI: 10.1002/pip.506.

[39] ASA simulator, User's manual v5.3, Delft University of Technology, 2012, http://www.pvmd.org/forum/.

[40] M. Zeman, O. Isabella, S. Solntsev, K Jager, Modelling of thin-film silicon soalr cells, Solar energy materilas ans dollar cells, 119, 94-111, (2013).

[41] J. Springer, A. Poruba, M. Vanecek, Improved three-dimensional optical model for thin-film silicon solar cells, Journal of Applied Physics, 96 5329 (2004), DOI:10.1063/1.1784555.

[42] K. Jäger, M. Zeman. A scattering model for surface-textured thin films, Applied Physics Letters 95 17 (2009), DOI: 10.1063/1.3254239.

[43] D. B. M. Klaassen, A unified mobility model for device simulation—I. Model equations and concentration dependence, Solid State Electron., 35, 7, 953–959, (1992) , DOI: 10.1016/0038-1101(92)90325-7.

[44] D. B. M. Klaassen, A unified mobility model for device simulation—II. Temperature Dependence of carrier mobility and lifetime, Solid State Electron., 35, 7, 961–967, (1992), DOI: 10.1016/0038-1101(92)90326-8.

[45] A. Schenk, Finite-temperature full random-phase approximation model of band gap narrowing for silicon device simulation, J. Appl. Phys., 84, 7, 3684–3695, (1998).

[46] S. Selberherr, Analysis and Simulation of Semiconductor Devices, Springer-Verlag, (1984), (ISBN: 3-211-81800-6).

[47] K. R. McIntosh, Lumps, Humps and Bumps: Three detrimental effects in the current–voltage curve of a silicon solar cell, PhD thesis, University of New South Wales (2001).

[48] A. Bentzen, G. Schubert, J. S. Christensen, B. G. Svensson, A. Holt, Influence of temperature during phosphorus emitter diffusion from a spray-on source in multicrystalline silicon solar cell processing, Prog. Photovolt: Res. Appl. 15, 4, 2007.

[49] M. Rauer, C. Schmiga, J. Krause, R. Woehl, M. Hermle, S. W. Glunz, Further analysis of aluminum alloying for the formation of p+ regions in silicon solar cells, Energy Procedia, 8, (2011), 200-206, DOI: http://dx.doi.org/10.1016/j.egypro.2011.06.124.

[50] M. Rauer, C. Schmiga, A. Tuschinsky, M. Glatthaar, S. W. Glunz, Investigation of Aluminum-boron Doping Profiles Formed by Coalloying from Screen-printed Pastes, Energy Procedia, 43, (2013), 93-99, DOI: http://dx.doi.org/10.1016/j.egypro.2013.11.093.

[51] P. Lölgen, W. C. Sinke, C. Leguijt, A. W. Weeber, P. F. A. Alkemade, L. A. Verhoef, Boron doping of silicon using coalloying with aluminium, Applied Physics Letters 65, 2792 (1994), DOI: 10.1063/1.112992.

[52] S. Narasimha, A. Rohatgi, A. W. Weeber, An optimized rapid aluminum back surface field technique for silicon solar cells, in IEEE Transactions on Electron Devices, 46, 7, 1363-1370, (1999), DOI: 10.1109/16.772477B

[53] Sopori, National Renewable Energy Laboratory (U.S.), Studies on backside Al-contact formation in Si solar cells: Fundamental mechanisms, Materials Research Society Symposium Proceedings 1123 (2009), 7-11, DOI: 10.1557/PROC-1123-1123-P07-11.

[54] F. Huster, Investigation of the alloy process of screen printed aluminium pastes for the BSF formation of silicon solar cells, , Proceedings of the 20th European Photovoltaic Solar Energy Conference and Exhibition (2005), 2DV2.49.

[55] F. Huster, G. Schubert, ECV doping profile measurements of aluminium alloyed back surface field, Proceedings of the 20th European Photovoltaic Solar Energy Conference and Exhibition (2005), 2DV2.48.

[56] S. Selberherr, Analysis and simulations of Semiconductor devices, Springer-Verlag/Wien, pp. 63-72, (1984).

[57] K. Jäger, O. Isabella, R. A. C. M. M. van Swaaij, M. Zeman, Angular resolved scattering measurements of nano-textured substrates in a broad wavelength range, Measurement Science Technology 22 105601 (2011), DOI: 10.1088/0957-0233/22/10/105601.

[58] L. Viña, M. Cardona, Effect of heavy doping on the optical properties and the band structure of silicon, Physical Review B 29 12 (1984), DOI: 10.1103/PhysRevB.29.6739.

[59] R. Hezel, K. Jaeger, Low-Temperature Surface Passivation of Silicon for Solar Cells, Journal of Electrochemical society. 136 (1989), 518 - 523, DOI: 10.1149/1.2096673.

[60] P. P. Altermatt, J.O. Schumacher, Jürgen O.,A. Cuevas, M. J. Kerr,S.W. Glunz,R.R King, G. Heiser, A. Schenk. Numerical modeling of highly doped Si:P emitters based on Fermi–Dirac statistics and self-consistent material parameters, Journal of Applied Physics 92, 3187-3197 (2002), DOI: http://dx.doi.org/10.1063/1.1501743.

[61] M. J. Kerr, A. Cuevas, Recombination at the interface between silicon and stoichiometric plasma silicon nitride, Semiconductor Science Technology 17 (2002), DOI:10.1088/0268-1242/17/2/314.

[62] A. Kimmerle, A. Wolf, U. Belledin, D. Biro. Modelling carrier recombination in highly phosphorus-doped industrial emitters, Energy Procedia 8 (2011), 275 - 281, DOI: http://dx.doi.org/10.1016/j.egypro.2011.06.136.

[63] P. P. Altermatt, K. R. McIntosh, A Roadmap for PERC Cell Efficiency towards 22%, Focused on Technology-related Constraints, Energy Procedia, Volume 55, 2014, Pages 17-21, ISSN 1876-6102, http://dx.doi.org/10.1016/j.egypro.2014.08.004.

[64] B. Min, Hannes Wagner, Amir Dastgheib-Shirazi, P. P. Altermatt, Limitation of Industrial Phosphorus-diffused Emitters by SRH Recombination, Energy Procedia, 55, (2014), 115-120, DOI: http://dx.doi.org/10.1016/j.egypro.2014.08.090.

[65] M. J. Kerr, A. Cuevas, General parameterization of Auger recombination in crystalline silicon, Journal of Applied Physics 91 2473 (2002), DOI: 10.1063/1.1432476.

[66] J. Dziewior, W. Schmid, Auger coefficients for highly doped and highly excited silicon, Applied Physics Letter 31 346 (1977), DOI: 10.1063/1.89694.

[67] P. P. Altermatt, S. Ronald, A. G. Heiser, Improvements in numerical modelling of highly injected crystalline silicon solar cells, Solar Energy Materials and Solar Cells 65 (2001), 149 - 255, DOI: 10.1016/S0927-0248(00)00089-1.

[68] P. P Altermatt, J. Schmidt, G. Heiser, A. G. Aberle, Assessment and parameterization of Coulomb-enhanced Auger recombination coefficients in lowly injected crystalline silicon, Journal of Applied Physics 82 4938 (1997), DOI: 10.1063/1.366360.

[69] A. Richter, S. W. Glunz, F. Werner, J. Schmidt, A. Cuevas, Improved quantitative description of Auger recombination in crystalline silicon, Physical review B 86, 165202 (2012), DOI: 10.1103/PhysRevB.86.165202.

[70] M. Rudiger, J. Greulich, A. Richter, M. Hermle, Parameterization of Free Carrier Absorption in Highly Doped Silicon for Solar Cells, Electron Devices, IEEE Transactions on (2013), 60, 2156 – 2163, DOI: 10.1109/TED.2013.2262526.

[71] T. Trupke, M. A. Green, P. Würfel, P. P. Altermatt, A. Wang, J. Zhao, R. Corkish, Temperature dependence of the radiative recombination coefficient of intrinsic crystalline silicon, Journal of Applied Physics 94, (2003) 4930 – 4937, DOI: 10.1063/1.1610231.

[72] R. Brendel, Thin film crystalline silicon solar cell, Wiley-VCH, Weinheim (2003), ISBN: 978-3-527-40376-9.

[73] M. A. Green, M. J. Keevers, Optical properties of intrinsic silicon at 300 K. Prog. Photovolt: Res. Appl., (1995), 3, 189–192. doi:10.1002/pip.4670030303

[74] P. A. Basore, Extended spectral analysis of internal quantum efficiency, Photovoltaic Specialists Conference, Conference Record of the Twenty Third IEEE (1993), 147 - 152, DOI: 10.1109/PVSC.1993.347063.

[75] R. Santbergen, Optical Absorption Factor of Solar Cells for PVT Systems, PhD thesis, Eindhoven University of Technology (2008), ISBN: 978–90–386–1467–0.

[76] D. Kray, M. Hermle, W. Glunz, Theory and experiments on the back side reflectance of silicon wafer solar cells, Progress In Photovoltaics: Research and Applications 16, (2008), 1 - 15, DOI: 10.1002/pip.769.

[77] http://refractiveindex.info/?group=CRYSTALS&material=AlSi.

[78] V. Meemongkolkiata, K. Nakayashikia, D. S. Kima, R. Kopecekb, A. Rohatgi, Factors Limiting the Formation of Uniform and Thick Aluminum–Back-Surface Field and Its Potential, Journal of Electrochemical society 153 (2006), 53 - 58, DOI: 10.1149/1.2129106.

[79] M. Rüdiger, M. Rauer, C. Schmiga, M. Hermle, Effect of incomplete ionization for the description of highly aluminum-doped silicon, Journal of Applied Physics 110, 024508 (2011), DOI: 10.1063/1.3603043.

[80] P. P. Altermatt, J. O. Schuhmacher, A. Cuevas, M. J. Kerr, S. W. Glunz, R. R. King, G. Heiser, A. Schenk, Numerical modeling of highly doped Si:P emitters based on Fermi–Dirac statistics and self-consistent material parameters, J. Appl. Phys. 92, 3187 (2002), DOI: 1063/1.1501743.

[81] P. P. Altermatt, S. Steingrube, Y. Yang, C. Sprodowski, T. Dezhdar, S. Koc, B. Veith, S. Herrman, R. Bock, K. Bothe, J. Schmidt, and R. Brendel, Highly Predictive Modelling of Entire Si Solar Cells for Industrial Applications, Proceedings of the 24th European Photovoltaic Solar Energy Conference (2009), 901–906, DOI: 10.4229/24thEUPVSEC2009-2AO.1.1.

[82] R. Bock, P. P. Altermatt, J. Schmidt, and R. Brendel, Formation of aluminum–oxygen complexes in highly aluminum-doped silicon, Semiconductor Science and Technology 25, 105007 (2010), DOI: 10.1088/0268-1242/25/10/105007.

[83] Air Mass 1.5 AM1.5G spectra, http://rredc.nrel.gov/solar/spectra/am1.5/.

[84] W. Shockley, H. J. Queisser, Detailed Balance Limit of Efficiency of pn Junction Solar Cells, Journal of Applied Physics 32 510 (1961), DOI: 10.1063/1.1736034.

[85] M. Z. Rahman, Status of Selective Emitters for p-Type c-Si Solar Cells, Optics and Photonics Journal 2 (2012), 129 - 134, DOI:10.4236/opj.2012.22018.

[86] T. Dullweber, S. Gatz, H. Hannebauer, T. Falcon, R. Hesse, J. Schmidt, R. Brendel, 19.4% -Efficient Large Area Rear-Passivated Screen-Printed Silicon Solar Cells, Proceedings of the 26th European Photovoltaic Solar Energy Conference and Exhibition (2011) 811 - 816 , DOI: 10.4229/26thEUPVSEC2011-2BP.1.4.

[87] T. Tiedje, E. Yablonovitch, G. D. Cody, B. G. Brooks, Limiting efficiency of silicon solar cells. Electron Devices, IEEE Transactions on 1984, 31 (5), 711-716.

[88] P. Campbell, M. A. Green, Light trapping properties of pyramidally textured surfaces. J. Appl. Phys. 1987, 62, 243.

[89] T. Janssens, N. E. Posthuma, E. Van Kerschaver, K. Baert, P. Choulat, J.-L. Everaert, J. Goosens, W. Vandervorst, J. Poortmans, Advanced phosphorous emitters for high efficiency Si solar cells, Photovoltaic Specialists Conference (PVSC), 2009 34th IEEE , 000878,000882.

[90] P. Lölgen, Surface and volume recombination in silicon solar cells, Chapter 4, PhD thesis, (1995), Utrecht University.

[91] S.N. Singh, P.K. Singh, A new expression for minority carrier surface recombination velocity at low-high junction of an n+-p-p+ silicon diode, Solid-State Electronics, 33, 7, (1990), 968-970, http://dx.doi.org/10.1016/0038-1101(90)90080-X.

[92] https://www2.pvlighthouse.com.au/calculators/Recombination%20calculator/Recombination%20calculator.aspx.

[93] J. Jaglarz, A. Grabowski, Optical investigations of AlSi–SiC composites subjected to laser CO2 annealing, Optics and Lasers in Engineering, 2010, 48, 10, 1038-1044, http://dx.doi.org/10.1016/j.optlaseng.2010.04.009.

[94] E.D. Palik, Handbook of Optical Constants of Solids, Volume 3.

4

Experimental demonstration of $4n^2$ classical absorption limit in nano-textured ultra-thin solar cells

4.1 Abstract

The experimental demonstration of the $4n^2$ classical absorption limit in solar cells has been elusive for last thirty years. Especially the assumptions on front and internal rear reflectance in a slab of absorbing material are not easily fulfilled unless an appropriate light trapping scheme is applied. An advanced metal-free light trapping scheme for crystalline silicon wafers is proposed. For different bulk thicknesses, at the front side of the wafers nano-texture known as black-silicon was fabricated. At the rear side, random pyramidal textures coated with a distributed Bragg reflector were employed. Such dielectric back reflector was designed to exhibit an omni-directional and maximized internal rear reflectance in the region of weak absorption of crystalline silicon. Integrating the measured absorptance spectra of the fabricated wafers with the reference solar photon flux between 400 nm and 1200 nm, the so-called implied photo-generated current densities were calculated. More than 98% of the implied photo-generated current density based on the theoretical $4n^2$ classical absorption limit was experimentally demonstrated. Successful implementation of the proposed mask-less and metal-free light trapping scheme in crystalline silicon solar cells requires the adequate surface passivation of the front nano-texture. Our findings, applied in a solar device structure where front side losses are minimized, open the way for the realization of next generation high-efficiency, cost-effective and ultra-thin crystalline silicon solar cells.

This Chapter is based on the following publication: A. Ingenito, O. Isabella, M. Zeman - ACS Photonics, 1, 3, 270-278, 2014, DOI: 10.1021/ph4001586.

4.2 Introduction

Light trapping using textured surfaces and metallic back reflector (BR) has contributed to a significant conversion efficiency gain in crystalline silicon (c-Si) solar cells [1]. As stated in Section 1.1, for continuing large-scale implementation of c-Si solar cells, their cost must be further lowered by optimizing manufacturing processes, by offering customized products and by using fewer materials without sacrificing the efficiency [2], [3], [4]. Focussing of the last strategy, the Si wafer contributes for more than 50% of the total cell cost, therefore a possible solution to decrease material costs would require the usage of thinner wafers. Thinner wafers are not only potentially cheaper but also lighter and more flexible [5], exhibit a lower bulk recombination and [6], in case of Czochralski wafers, also a lower light-induced degradation [7], [8]. However, as c-Si is an indirect band-gap semiconductor, the absorption in the infrared region (IR) of the solar spectrum is significantly reduced when Si wafer thickness is reduced. Thus light trapping schemes are essential to enhance light absorption in thin c-Si solar cells [9]. Light management techniques such as front light in-coupling, light scattering and internal back reflectance (R_b) have to be optimal and concurrently active in order to achieve broad-band light absorption. These techniques ultimately fulfil the ideal hypotheses of the so-called $4n^2$ classical absorption limit in a dielectric slab [10], where n is the real part of its complex refractive index: (i) a surface-textured morphology at air / dielectric interface in the role of a perfect broad-band anti-reflective coating (ARC) (reflectance $R = 0 \ \forall \ \lambda$), (ii) randomized and ideally diffused light inside the slab (the so-called Lambertian scattering), and (iii) a perfect back reflector ($R_b = 1 \ \forall \ \lambda$). In the wavelength region of weak absorption of c-Si, i.e. $\alpha d < 1$ [1] such light trapping scheme theoretically results in an absorption enhancement factor of ~50 ($4n^2$) [11].

Light trapping in commercial c-Si solar cells is achieved by using randomly textured surfaces coated with antireflection coating and metal or dielectric/metal stack as back reflector. Even though standard random pyramid texturing exhibits a nearly Lambertian scattering [11], it does not result in a perfect broad-band anti-reflective effect. In this respect, nano-textures with feature sizes in the nano-meters range are considered valid candidates for providing broad-band anti-reflective effect [12]. Among various advanced light trapping schemes that were lately presented to fulfil the hypothesis of the $4n^2$ classical absorption limit [13], [14], [15] a recent optical simulation study showed that the absorptance in c-Si can approach the $4n^2$ classical limit in just 2-µm thick structured c-Si slab. Such slab was endowed with high aspect ratio periodic nano-gratings at the front side (FS) for anti-reflective purposes and with low aspect ratio pyramidal structures at the back side (BS) for efficient long-wavelength light scattering [12]. This arrangement

---

[1] Where α and d are the absorption coefficient and thickness of the dielectric slab, respectively.

was called decoupled front and rear texturization [16]. Based on this design, a c-Si solar cell with a thickness of around 9 µm was also reported to achieve a potential photo-generated current density (J_{PH}) > 36 mA/cm^2 and a conversion efficiency > 7% [17]. In this contribution an advanced metal-free light trapping scheme for maximizing light absorption in crystalline silicon solar cells is proposed. Such light trapping scheme is based on decoupled front and rear textures and employs low-cost and industrially scalable processes for its fabrication. In particular, nano-texturing - also known as black-silicon (b-Si) - is employed at FS and random pyramids coated with a Distributed Bragg Reflector (DBR) are used at the BS [18], [19]. In the following the process and design steps for the realization of the light trapping scheme will be reported. Afterwards measured c-Si absorptance spectra will be presented and performance of dielectric and reference silver BRs will be compared with the $4n^2$ classical absorption limit. Finally, a possible scenario regarding next-generation of c-Si solar cells is discussed. As shown in Chapter 6 and in [20] [21], nano-texture can be efficiently passivated by using SiO_2 grown via dry thermal oxidation or by Al_2O_3 deposited via Atomic Layer Deposition (ALD). Moreover, it has been also demonstrated that efficiencies comparable with state-of-the-art c-Si solar cells can be achieved by using front b-Si texture (see [20] and Chapter 6 of this thesis). This opens the possibility to couple the proposed advanced light trapping scheme in ultra-thin c-Si wafers with efficient passivation techniques for realizing high-efficiency and cost-effective solar cells.

4.3 Fabrication and characterization

4.3.1 Process flow description of advanced light trapping scheme

Cz 4-inches p-type Si wafers with initial thickness 300 µm +/- 5 µm and resistivity > 1000 Ω·cm were used. The high resistivity wafers were chosen in order to minimize the free carrier absorption at high wavelengths and thus fully observe the potential of the designed light trapping scheme. The fabrication steps of the proposed advanced light trapping scheme are presented in Figure 4.1. The front b-Si texture was fabricated by mask less deep reactive ion etching (RIE) using a gaseous mixture of SF_6 and O_2 (see Figure 4.2(a)) in Drytek 384T. This plasma etcher had two opposing electrodes powered with the same frequency (13.56 MHz), with a grounded chamber wall and a grid. The RIE etching process is rather independent of wafer doping (concentration and type) and crystal orientation. During the etching the SF_6/O_2 plasma provides a continuous flow of fluorine radicals (F*) and oxygen radicals (O*) which feeds two competing chemical reactions: F* and Si react forming SF_4^+ ions, while from the reaction between O* and Si a silicon oxyfluorine (SiO_xF_y) layer is formed. The precipitation of SiO_xF_y particles which starts the formation of randomly distributed etch pits. The SiO_xF_y acts as mask against F* etching but is physically broken by sputtered ions' bombarding the surface of the sample. Such effect occurs with higher speed on the horizontal rather than the vertical plane leading to a strong anisotropy of the Si etching rate [22]. The etching parameters such as: pressure, SF_6/O_2 flow and etching time were optimized in this work. A cross sectional scanning electron microscope (SEM) of the nano-texturing fabricated on the front side of the Si wafer is shown in Figure 4.1 (step 1).

After standard cleaning, rinsing and drying of the substrates, Si_3N_4 was deposited on both sides of the wafers in a tube furnace by means of low pressure chemical vapour deposition (LP-CVD). On the non-textured side of the wafers, a photolithographic step was performed to create two openings each measuring 3 × 3 cm^2 area. In such openings the Si_3N_4 layer was dry-etched in a C_2F_6-plasma for 20 seconds. After that the photoresist

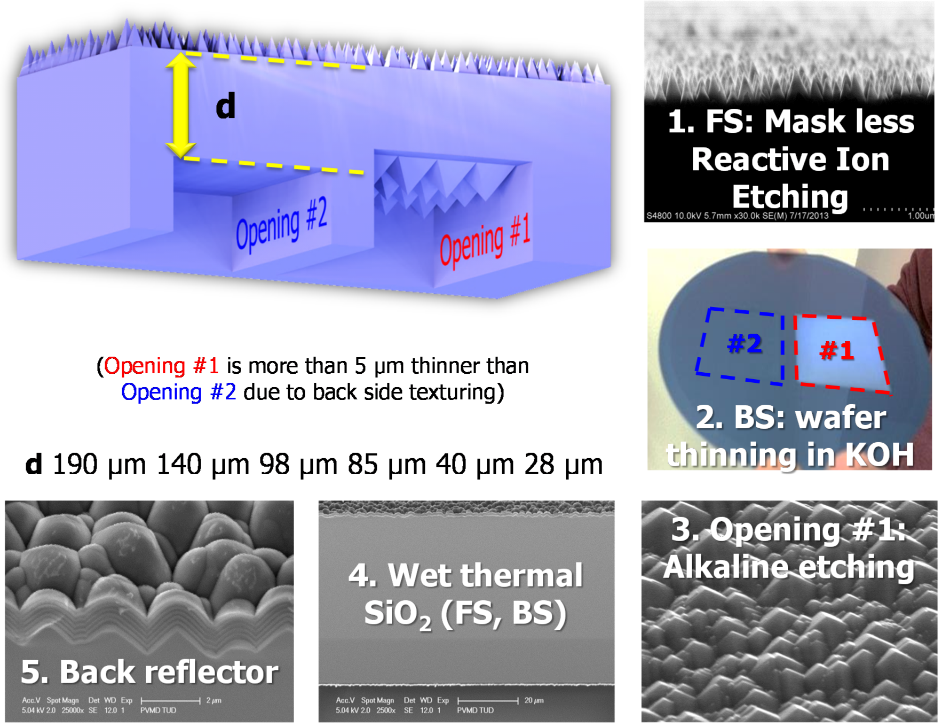

Figure 4.1. Fabrication steps of the proposed light trapping scheme. The front side of the wafer is first etched in the RIE tool (step 1). After this step the wafer is coated with a LP-CVD SiN layer followed by a photo-lithographic step to create to openings on the rear side of the wafer (step 2). After this step KOH etching is performed to thin the wafer. Different wafer thicknesses (*d*) reported in the figure were fabricated. Alkaline etching in TMAH/IPA is performed to texture one of the rear openings (step 3). This step reduce the Si thickness of opening # 1 of more than 5 μm compared with opening # 2. After etching of the SiN, wafers are oxidized in H_2O (step 4). The back reflector (Ag or DBR) is deposited on step (step 5).

outside the openings was dry-etched in a O_2 plasma for 5 minutes (Europlasma stripper), the silicon bulk in the two openings was thinned in a KOH bath at temperature of 80 °C characterized by an etching rate of 100 µm/h. Tuning the etching time, two c-Si slabs were fabricated in each of the six different c-Si wafers (see step 2 of Figure 4.1). The thickness of the slabs in the flat region was measured by means of SEM, obtaining 190, 135, 100, 85, 40 and 28-µm thick bulk c-Si, respectively. For each wafer, one of the openings was further etched in a TMAH-IPA alkaline bath to realize a textured surface characterized by random pyramids (textured BS), (see step 3 of Figure 4.1), while the other opening was kept flat by using AI Technology wax [23] as protective layer resistant to the alkaline solution (flat BS). It should be noted that TMAH-IPA etching reduces the Si thickness in the textured opening of more than 5 µm with respect to the flat one. The protective thinning wax layer was later etched in acetone at room temperature for 2 min. At this point, the LP-CVD Si_3N_4, still present on front b-Si and on the rear side outside the openings, was etched from all samples in a H_3PO_4 solution (85% wt diluted in H_2O) at 157 °C for 42 min. Wet thermal SiO_2 layer 100-nm was grown on both sides of the wafers at 1100°C in a tube furnace (see step 4 of Figure 4.1). All c-Si slabs were first coated on the rear side with 100-nm thick Ag layer (reference metallic BR) using physical vapour deposition in Provac PRO500S. For a fair comparison between the optical performance of the Ag and DBR back reflector, Ag was removed in a HNO_3 solution (69.5% HNO_3) at room temperature for 30 seconds, which left untouched the SiO_2 (after the optical characterization of the samples). Finally, the dielectric DBR was fabricated by depositing six a-Si:H / a-SiN_x:H pairs using SiH_4 and SiH_4 + NH_3 plasmas in rf-PECVD AMIGO Elettrorava cluster tool (see step 5 of Figure 4.1).

4.3.2 Characterization methods of the advanced light trapping scheme

The morphological analysis of the samples was performed with AFM using NT-MDT nTegra setup. Extracted values of σ_{rms} and L_C are reported in the inset table of Figure 4.2. For the visual investigation of the surface textures, the thickness of c-Si textured slabs and the composition of the DBR, a Philips XL-50 SEM was used. Wavelength-dependent complex refractive indexes of a-SiN_x:H, a-Si:H and SiO_2 were extracted from ellipsometry spectra using J. A. Wollam CO. M-2000DI spectroscopic ellipsometer. At the design wavelength of our dielectric DBR (λ_B = 1000 nm), the real part of the complex refractive indexes of a-SiN_x:H, a-Si:H and SiO_2 were 1.76, 3.67 and 1.5, respectively. Reflectance (R) and transmittance (T) of passivated FS/BS textured c-Si slabs with and without metallic BR or dielectric DBR were measured using an integrating sphere (IS) accessory mounted on Perkin-Elmer Lambda 950 spectro-photometer in the wavelength range between 400 nm and 1200 nm.

4.4 Results and discussions

4.4.1 Morphological analysis

A schematic cross section of the surface textures used in this work is illustrated in Figure 4.2. Two thin free-standing absorbing slabs in c-Si wafers that were originally 300-µm thick were realized. Both slabs had the same high aspect ratio b-Si FS texture, but the BS was either alkaline-textured with low aspect ratio random pyramids (textured BS) or just kept flat (flat BS). The b-Si FS texture was realized with a mask-less reactive ion etching (RIE) process, which can be implemented in all commercially available dry etching tools. The thickness of the slabs was tuned by varying the etching time as described in Section 4.3.1. A series of six pairs of slabs with different thicknesses was investigated. The thickness of the six slabs was measured in the flat opening to be 190, 140, 98, 85, 40 and 28 µm, respectively. It could be noticed that the standard alkaline etching process for fabricating the pyramids generally reduced the corresponding thicknesses of slabs in the textured opening by more than 5 µm. The AFM scans of b-Si texture, random pyramids and flat opening are illustrated in Figure 4.2 (a-c), respectively.

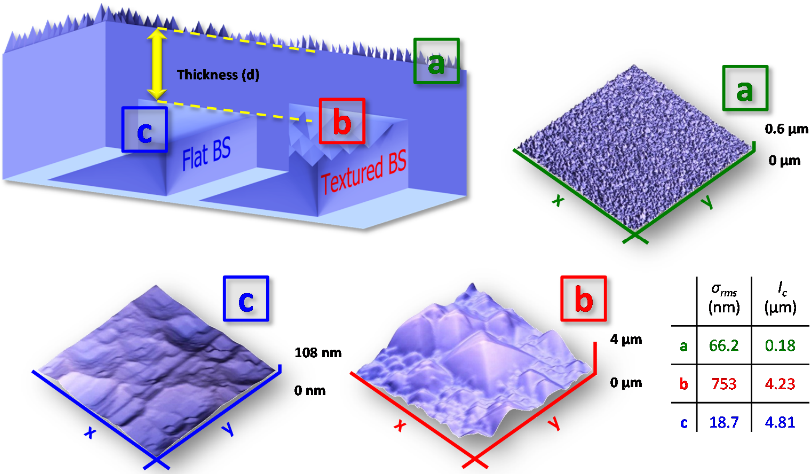

	σ_{rms} (nm)	l_c (µm)
a	66.2	0.18
b	753	4.23
c	18.7	4.81

Figure 4.2. (Top left) Schematic structure of our structured c-Si wafers: (a) nano-texture at the FS with (b) textured or (c) flat BS. Scale bars in x- and y- directions of the AFM scans are 20-µm long. In the inset table, AFM-extracted root mean square roughness (σ_{rms}) and correlation length (l_c) for the three investigated surfaces.

The extracted root mean square roughness (σ_{rms}) and correlation length (l_c) of these three surfaces are reported in the inset table in Figure 4.2. The fabricated b-Si FS texture exhibited an aspect ratio σ_{rms} / l_c close to 0.37 while the random pyramids had a shallower aspect ratio close to 0.18. Finally, the surface of the flat opening was found to be '*virtually*' flat.

4.4.2 Design of Distributed Bragg Reflector (DBR)

A 3-D Maxwell equations solver based on the finite element method [24] was used to design the dielectric DBR [25], [26]. A DBR is formed by alternating dielectric layers with refractive index mismatch. Such a multi-layer stack can be designed to deliver high reflectance in a certain wavelength range called photonic band gap (PBG) around the so-called *Bragg wavelength* (λ_B). In the context of this work, the most stringent requirement for a DBR used as BR is to achieve $R_b = 1$ in the wavelength range of weak absorption of c-Si independently from the angle of incidence and the polarization of light. This is the so-called *omni-directional* behaviour [26]. This concept is of major importance for enhancing A_{Si} at long wavelengths. In fact, for the studied light trapping scheme, long wavelength light might be fully randomized in the absorber slab (see Chapter 6). Therefore, the BR must provide the highest rear reflectance for all illumination conditions (i.e. angle of incidence and polarization). Such behaviour is typical of metal BRs but more difficult to observe for dielectric BRs. To achieve an omni-directional dielectric DBR, two conditions have to be fulfilled: (i) the maximal refraction angle at the interface between the incident medium and the DBR must not exceed the Brewster angle at the internal interface of the first DBR pair and (ii) the DBR must exhibit a high reflectance in a selected wavelength range for all angles of incidence and for both polarizations [26], [27], [28]. In particular, when the first condition is not fulfilled, the electro-magnetic field is partly transmitted throughout the dielectric reflector, which results in $R_b < 1$. The first condition can be mathematically expressed as follows [29]:

$$n_0' = \frac{n_H \cdot n_L}{\sqrt{n_H^2 + n_L^2}} > n_0 \qquad 4.1$$

where n_0, n_H and n_L are the real part of complex refractive index of the incident medium, high refractive index material and low refractive index material, respectively. Given the refractive index of the incident medium, one can choose the refractive indexes of materials that will constitute the DBR in such a way that their combination n_0' is greater than n_0. To fulfil such condition for a DBR ($n_0'=f(n_L,n_H)$) having bulk c-Si as incident medium (n_0) (see yellow area in Figure 4.3), non-absorbing materials with high n_L and n_H refractive indexes at $\lambda_B = 1000$ nm are required. Their fabrication is however not trivial. Instead, considering a SiO_2 layer ($n_0 = n_{SiO2(1000\ nm)} = 1.5$) between the bulk c-Si and DBR allows for the use of existing non-absorbing materials $\lambda_B = 1000$ nm like a-SiN_x:H ($n_L = n_{a\text{-}SiNx(1000\ nm)} = 1.76$, $d_{a\text{-}SiNx} = 146$ nm) and a-Si:H ($n_H = n_{a\text{-}Si:H(1000\ nm)} = 3.61$, $d_{a\text{-}Si:H} = 69$ nm). Real (n) and imaginary (k) part of the complex refractive indexes of a-Si:H, a-SiN_x:H and SiO_2 used in this work are shown in Figure 4.4.

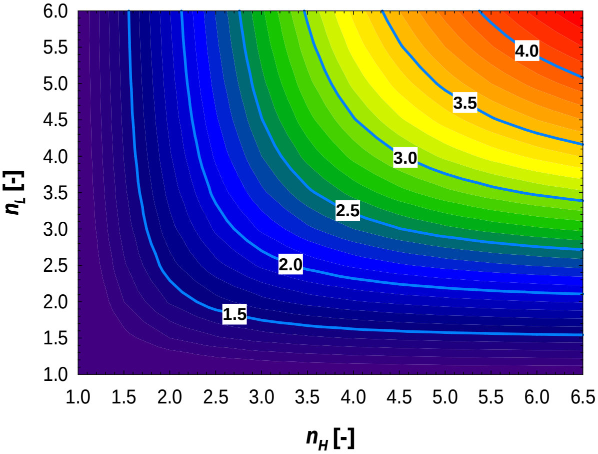

Figure 4.3. Contour plot depicting the first omni-directionality condition: $n_0' > n_0$ (Equation 4.1). Light-blue lines on the contour plot are the iso-value curves indicating the refractive index of the incident medium (n_0) on top of the DBR. The DBR was designed around the wavelength corresponding to the band-gap of c-Si with λ_B = 1000 nm. Setting SiO_2 as incident medium, a-Si:H (n_H) and a-SiN_x:H (n_L) were considered good candidates for constituting the dielectric DBR.

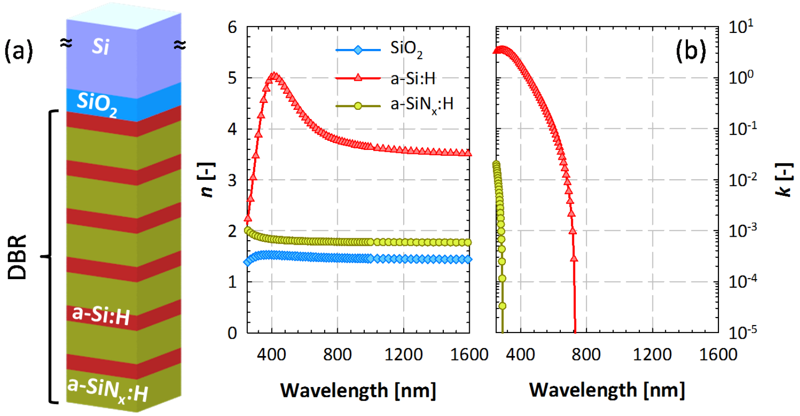

Figure 4.4. 3-D sketch of the simulated structure and (b) wavelength-dependent real (n) and imaginary part (k) of the complex refractive indexes of a-Si:H, a-SiN_x:H and SiO_2 used in this work. Measurements were carried out with a Woollam ellipsometer; SiO_2 was found to be non-absorbing in the full wavelength range. In the stack a-Si:H constitutes the n_H and a-SiN_x the n_L material, respectively.

As the figure clearly shows, all fabricated layers are non-absorbing in the weak absorption region of Si. In addition, their refractive indexes at λ_B satisfied the first omni-directionality. The first omni-directionality condition is presented in Figure 4.3.

Optical simulations of a flat stack of c-Si (half space) / SiO_2 (100 nm) / DBR, depicted in Figure 4.5, were carried out. The aim of these simulations was to find a minimum number of a-Si:H / a-SiN$_x$:H pairs resulting in R_b = 1 and fulfils the second omni-directionality condition. As Figure 4.5 shows, both requirements are met by using six pairs of a-Si:H (69 nm) / a-SiN$_x$:H (146 nm). The thicknesses of both layers of the DBR were designed in order to respect the $\lambda/4$ rule at Bragg wavelength (λ_B = 1000 nm). In this condition, the reflected waves from each layer are in phase leading to a constructive interference that maximize the internal rear reflectance. Mathematically, the thicknesses of the layers constituting the DBR can be designed according to the following equation:

$$d_{a\text{-}Si:H} = 69nm = \frac{\lambda_B}{4n_{a-Si:H}(\lambda_B)} ; \frac{\lambda_B}{4n_{a-SiNx:H}(\lambda_B)} = 146nm = d_{a\text{-}SiNx:H} \quad 4.2$$

Finally a number of six pairs represented a good compromise between processing time of the DBR and high R_b. In Figure 4.5 the theoretical angle-dependent Bragg wavelength (λ_B) and the right and left photonic band-gap edges (λ_L and λ_R, respectively) are also depicted. It is noticeable that the results of the optical modelling using materials with

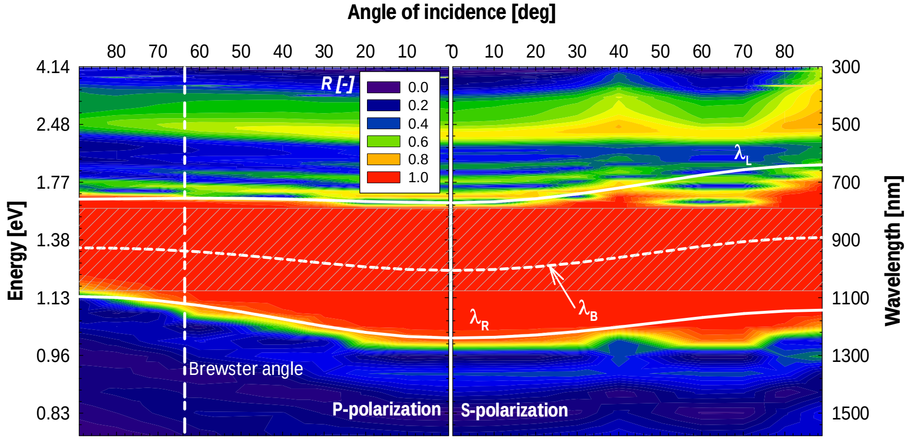

Figure 4.5. Calculated R_b for different angles of incidence and for P-polarization (left) and S-polarization (right). The grey shaded area represents the omni-directional photonic band-gap (second omni-directional condition). The white horizontal solid and dashed curves are the theoretical angle dependent photonic band edges (λ_L and λ_R) and the Bragg wavelength, respectively. For angle of incidence 0°, λ_B is equal to 1000 nm. λ_L and λ_R, theoretically calculated [26] for wavelength-independent n_L = 1.76 and n_H = 3.61, closely follow the region of high reflectance in both polarizations. In the P-polarization panel, the vertical dash-dotted line locates the Brewster angle of the optical system. The colours from violet to red represent the increasing value of R_b for both polarizations.

wavelength-dependent properties were close to the theory [26]. The typical quenching of λ_R in P-polarization was reproduced as well. This effect happens because the P-polarization coefficient is null at Brewster angle. These optical simulations rigorously describe the internal rear reflectance in the ultra-thin c-Si slabs coated with dielectric DBR at the flat BS. On the other hand, considering the textured BS, some deviation is expected in the internal rear reflectance as the simulated thicknesses can be realized in practice only on a flat surface. In Chapter 7 an experimental proof of such claim will be given. Finally, to carry out a fair comparison between the metallic (Ag) and dielectric (DBR) BRs, 100-nm thick oxide layer was used in order to reduce the metal absorption due to Ag plasmonic losses and thus enhance the internal rear reflectance [25] and [30].

4.4.3 Optical absorption of the advanced light trapping scheme

All fabricated slabs in both BS configurations and with different BRs were optically characterized by measuring the R and T in the wavelength range between 400 nm and 1200 nm by using an IS. Total absorptance (A_{tot}) was calculated as $A_{tot} = 1 - R - T$. This quantity corresponds to the absorptance in silicon (A_{Si}) only when the BR is constituted by non-absorbing materials. On the other hand, in case of metallic BR the measured A_{tot} includes also the parasitic absorption in the metal layer. To compare the difference between absorption only in the Si layer for both BR configurations, an analytical model that is capable to distinguish A_{Si} from the measured A_{tot} is shown in Section 4.6.1 and [31]. The experimentally determined A_{Si} were therefore compared with absorptances calculated from the $4n^2$ classical absorption limit (A_{4n2}) and the single pass limit (A_{SP}) [10]:

$$A_{4n^2} = 1 - \frac{1}{1 + 4n_{Si}^2 \alpha_{Si} d} \tag{4.3}$$

$$A_{SP} = 1 - e^{-\alpha_{Si} d} \tag{4.4}$$

Where n_{Si} and α_{Si} are the real part of the complex refractive index and the absorption coefficient of c-Si, respectively. The implied J_{ph} were calculated as follows:

$$J_{ph} = -q \cdot \int_{\lambda_1}^{\lambda_2} A_{Si}(\lambda) \cdot \Phi_{AM\,1.5}(\lambda) d\lambda \tag{4.5}$$

where, q is the elementary charge, A_{Si} is the Si absorptance, $\Phi_{AM\,1.5}$ is the standard $AM_{1.5}$ photon flux [32] and [λ_1, λ_2] is the wavelength range of interest. In Figure 4.6(a) the measured A_{Si} for the flat and textured BS for a 78 μm thick absorber with no additional BR (i.e. R_b is set by the refractive mismatch between SiO_2 and air) are reported as function of the wavelength between 400 and 1200 nm, together with upper (A_{4n2}) and lower (A_{SP}) absorption limits calculated with Equations 4.3 and 4.4 for the same Si absorber thickness (85 μm). Notice that for the textured BS configuration the absorber layer was found to be ~7 μm thinner than the flat one. However, for such '*thick*' absorbers the J_{ph} calculated by using Equations 4.3 and 4.4 is slightly sensitive with respect to thicknesses variations within ± 5 μm[1]. Therefore, it is reasonable to compare the measured A_{Si} for both flat and textured BS with respect to A_{4n2} calculated for 85 μm. Figure 4.6 (a) clearly shows that the front nano-texturing is capable of delivering a broad-band antireflection effect even without ARC. In addition, the A_{Si} at long wavelengths of the nano-textured sample with flat BS is much higher than the one predicted by the SP limit even though no-additional BR is applied. This indicates that the nano-texturing not only increases light in-coupling but also contributes to scatter light and enhance A_{Si} at long wavelengths. In addition, Figure 4.6 (a) shows that by combining the FS nano-texturing with BS micro-pyramids an additional degree of scattering is introduced which results in a further A_{Si} enhancement in the IR region (i.e. [950, 1200] nm). Quantitatively, the absorption enhancement in the IR region given by the decoupled FS and BS light trapping scheme compared with the respect to the case where only FS nano-texturing is employed, leads to an increase of J_{ph} of +0.8 mA/cm^2.

To achieve even higher A_{Si} at long wavelengths (λ > 950 nm) and thus approach the theoretical upper limit set by A_{4n2}, efficient BRs (i.e. high R_b) need to be employed. As shown in Figure 4.6 (b), the application of a SiO_2 / Ag BR on the rear side, resulted in a remarkable increase of the A_{Si} at $\lambda > 950$ nm for both flat and textured BS configurations compared to the case in which no-additional BR was present. The Si absorption enhancement after the application of the BR leads to an increased J_{ph} of ~1.2 mA/cm^2 (in the wavelength region [950, 1200] nm) for both BS configurations compared to the case where no additional BR is used. For a fair comparison between the performances of the two BRs here studied, the Ag BR was etched and DBR was co-deposited on both flat and textured openings. As depicted in Figure 4.6 (c), the comparison between the A_{Si} in the IR for the two BRs depicts two different behaviours: (i) for flat BS the A_{Si} in the IR region of the DBR approaches the one delivered by Ag BR; (ii) for textured BS the A_{Si} in the IR region of the DBR is lower compared to the one delivered by Ag BR. This effect can be explained by the high T losses of the DBR applied on textured surfaces. As already mentioned in Section 4.3.1 the proposed light trapping scheme was studied at different wafer thicknesses.

---

[1] For a Si absorber with a thickness of 80 ± 5 μm the J_{ph} calculated under the assumptions of the 4n^2 limit is equal to 40.5 ± 0.07 mA/cm^2.

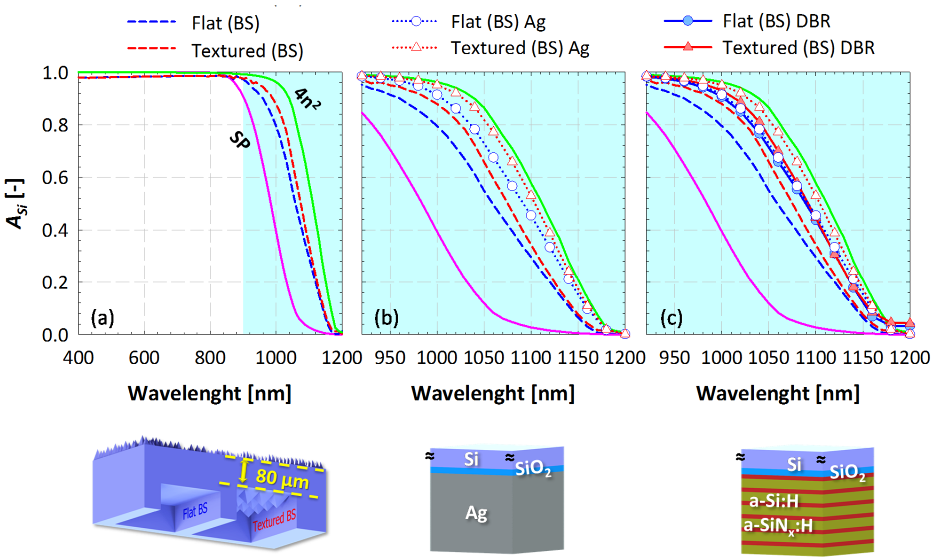

Figure 4.6. (a) Measured A_{Si} for 80 μm thick absorber in case of flat and textured BS compared with theoretical $4n^2$ (green) and *SP* (purple) absorption limits. A clear increase in the IR region can be observed when the BS of the absorber is textured compared to the flat case. (b) Measured A_{Si} at long wavelengths after application of Ag BR for both BS configurations. (c) Measured A_{Si} at long wavelengths after etching of Ag and deposition of DBR.

Focusing on the ultra-thin c-Si absorber layers, SEM images of the 20-µm thick textured and 28-µm flat c-Si slabs with dielectric omni-directional DBR are shown in Figure 4.7 (a) and Figure 4.7 (b), respectively. The b-Si FS texture (green inset) is the same for both BS configurations. Random pyramidal and flat BS coated by the designed DBR is clearly visible in the red and blue insets of Figure 4.7 (a) and (b), respectively. Analysing these images, it was found that the morphology of b-Si texture shows conical features with diameter around 250 nm and the height around 1 µm. The measured A_{Si} of 20-µm (28-µm) thick c-Si slab in case of the b-Si FS texture and alkaline-textured (flat) BS coated with either dielectric DBR or reference Ag are reported in Figure 4.8 (a) and (b), respectively. Considering the thickness of the realized slabs and using Equations 4.3 and 4.4 in the wavelength range [400, 1200] nm, A_{4n2} or A_{SP} were respectively calculated. Finally, Equation 4.5 was used to calculate the implied J_{ph} for the $4n^2$ and single pass limit. In case of 20-µm thick c-Si slab with textured BS, more than 97% of the implied J_{ph} of the theoretical $4n^2$ classical absorption limit was achieved for both BRs. This is so far the closest experimental evidence of the $4n^2$ classical absorption limit on a broad wavelength range.

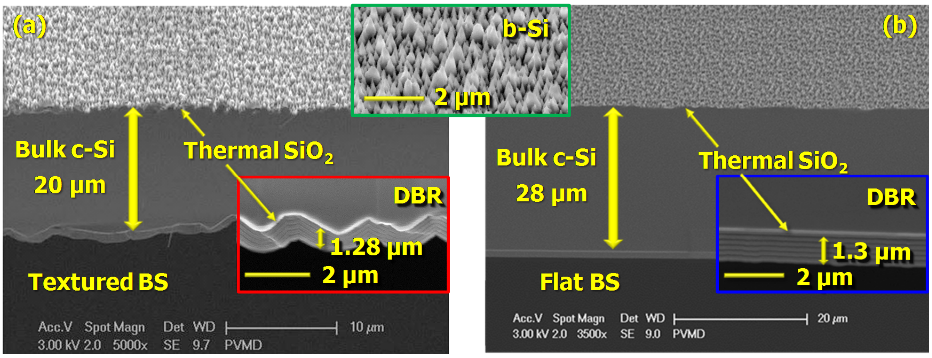

Figure 4.7. Cross-sectional SEM images of (a) 20-µm thick absorber with textured BS and (b) 28-µm thick absorber with flat BS. The three coloured insets show a close-up of the common front nano-texture coated with thermal SiO$_2$ (green) and of the textured (red) and the flat (blue) BS coated with thermal SiO$_2$ and 6 pairs of a-Si:H/ a-SiN$_x$:H conformal DBR. All SEM images were taken at a tilting angle of 45°.

In Figure 4.8 (b) the simulated R_b (for perpendicular incidence) for the flat BS coated with DBR is also reported. The designed wavelength range of high internal reflectance of the DBR (800 nm – 1200 nm) perfectly matches with the weak-absorption region of the 20-µm thick c-Si. However, in case of even thinner wafers (<10 µm), the limited bandwidth of the DBR would lead to a significant decrease of the optical absorption already in the red response. To overcome such limitation, a modulated DBR can be designed in order to deliver a broader bandwidth [26], [33]. The slab with the dielectric DBR on flat BS shows comparable absorptance with respect to the reference Ag BR. The DBR applied to textured BS leads to lower A_{Si} enhancement compared to the Ag BR. To explain this behaviour, the spectral losses of the two BRs in both BS configurations were investigated and their implied J_{ph} was calculated. The spectral losses for the two BR configurations are inferred to parasitic absorption (calculated) in the metallic layer (Ag BR) or to the measured T trough the dielectric stack (DBR BR). As Figure 4.8 (d) shows, on the contrary with the simulation results the T_{DBR} is not completely zero at long wavelengths. This indicates that the λ_B of the fabricated DBR might be slightly shifted at shorter wavelengths compared to the designed one. Such results can be related to a non-optimal thickness of the deposited layers. Overall, comparing the optical losses for flat interfaces of the DBR and Ag BRs appears that the DBR shows slightly lower optical losses than Ag BR (see Figure 4.8 (d)). Instead, in case of textured BS (see Figure 4.8 (c)), the designed DBR suffers from higher optical losses with respect to Ag BR, not being optimized for textured interfaces. The optimization of DBR on textured surfaces is shown in Chapter 7.

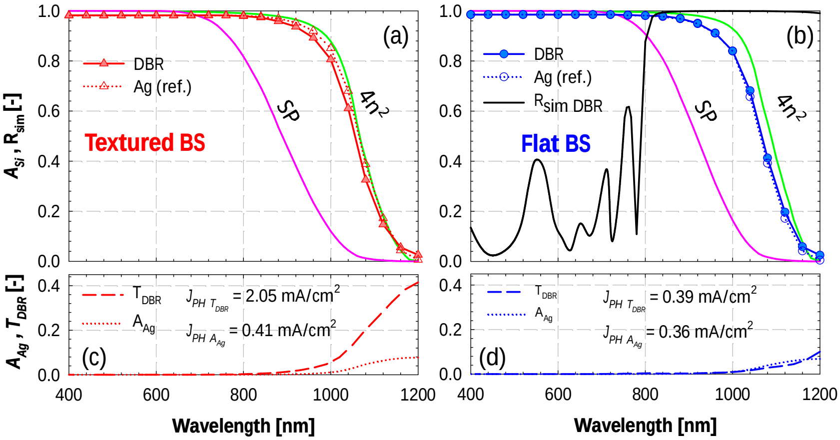

Figure 4.8. Measured absorptances in case of the b-Si FS texture and (a) 20-µm thick c-Si absorber with the alkaline textured BS or (b) 28-µm thick c-Si absorber with the flat BS. In both figures the absorptances of silicon with the optimized dielectric DBR and the reference 100-nm thick Ag layer BRs are reported. Absorptances are compared with $4n^2$ classical absorption limit and single pass absorption (green and pink curves, respectively). Black line in (b) shows the simulated internal rear reflectance in c-Si with the optimized DBR. This spectrum corresponds to perpendicular incidence (0°) and was extracted from Figure 4.5. Figures (c) and (d) show the optical losses related to the Ag absorptance (calculated) in case of metallic BR and transmittance (measured) in case of dielectric DBR for textured and flat BS, respectively. The implied photo-current densities of such optical losses were calculated by using Equation 4.5 and A_{Ag} (calculated) or T_{DBR} (measured) in place of A_{Si}.

In Figure 4.9 (a) ((b)), is reported the thickness dependence of the measured J_{ph} for the fabricated light trapping scheme employing a textured (flat) BS coated with Ag or DBR. The graph also reports the relative J_{ph} difference (ΔJ_{ph}), between the measured J_{ph} for fabricated light trapping scheme ($J_{ph\ meas}$) and the J_{ph} predicted by the $4n^2$ limit ($J_{ph\ 4n2}$) at same wafer thickness, which was calculated as:

$$\Delta J_{ph}(\%) = 100 - \frac{(J_{ph4n2} - J_{phmeas})}{J_{ph4n2}} * 100 \tag{4.6}$$

The ΔJ_{ph} for both flat (coated with Ag or DBR as BR) and textured BS (coated with Ag or DBR as BR) are reported in Figure 4.9 (a) and (b), respectively. In particular, in case of textured BS, Figure 4.9 (a), clearly shows that: (i) the J_{ph} of Ag outperforms the one of DBR independently by the thickness of the absorber; (ii) the ΔJ_{ph} is slightly dependent by the absorber's thicknesses[1]. The high ΔJ_{ph} values indicate that when both texturing scales are

---

[1] The ΔJ_{ph} averaged for all wafer thicknesses exhibited a mean value of 98.5% with a standard deviation of ± 0.4 %.

employed, A_{Si} (between [400-1200]nm) comparable to the one predicted by the $4n^2$ can be achieved. On the contrary, for the light trapping scheme employing a flat BS, Figure 4.9 (b) clearly indicates that: (i) the J_{ph} of Ag and DBR BRs are very similar independently by the absorber's thickness; (ii) the poorer light trapping properties of the structure with flat BS with respect to the textured BS one lead to a decrease of ΔJ_{ph} when thickness of the absorber[1] is reduced.

Finally, the embedding of the proposed light trapping scheme in next generation c-Si solar devices is discussed. Figure 4.10 (a) shows the 20-µm thick c-Si absorber slab extracted from the c-Si wafer support. Such slab is flexible and can be processed to fabricate an ultra-thin solar cell. Although the proposed process flow involved a photolithographic step, mostly required for mechanical support and quality control over pairs of slabs, the light trapping scheme may be straightforwardly implemented at industrial level. The solar cell architecture which would take the highest efficiency gain from the proposed light trapping scheme is the one adopted by Sunpower [34][35], as sketched in Figure 4.10 (b). The main feature of such technology consists in positioning both contacts at the BS of the device. These contacts are usually arranged in an interdigitated fashion, the so-called interdigitated back contacted design (IBC). Such type of solar cell technology does not require a metal contact on the FS (i.e. no need to contact the sharp and fragile nano-textures) and typically employs a lightly-doped front surface field [36]. For these reasons, the excellent broad-band anti-reflective effect provided by the front nano-texturing can be fully exploited on the entire solar device area. In addition, black solar cells can be achieved and used for customized BIPV applications. The effect of the encapsulation of the mechanical stability of the black-Si and its optical properties are not yet investigated. It is clear that state-of-the-art passivation of FS of the c-Si ultra-thin absorbers must be preliminarily actuated in order to fabricate the solar device sketched in Figure 4.10 (b). An advanced passivation scheme of the nano-texturing based on a wet surface treatment followed by thermally grown SiO_2 is presented in Chapter 6 of this thesis.

---

[1] For the flat BS light trapping scheme, ΔJ_{ph} is equal to ~98% for Si absorber 190 µm-thick and ~97% for Si absorber 28 µm-thick.

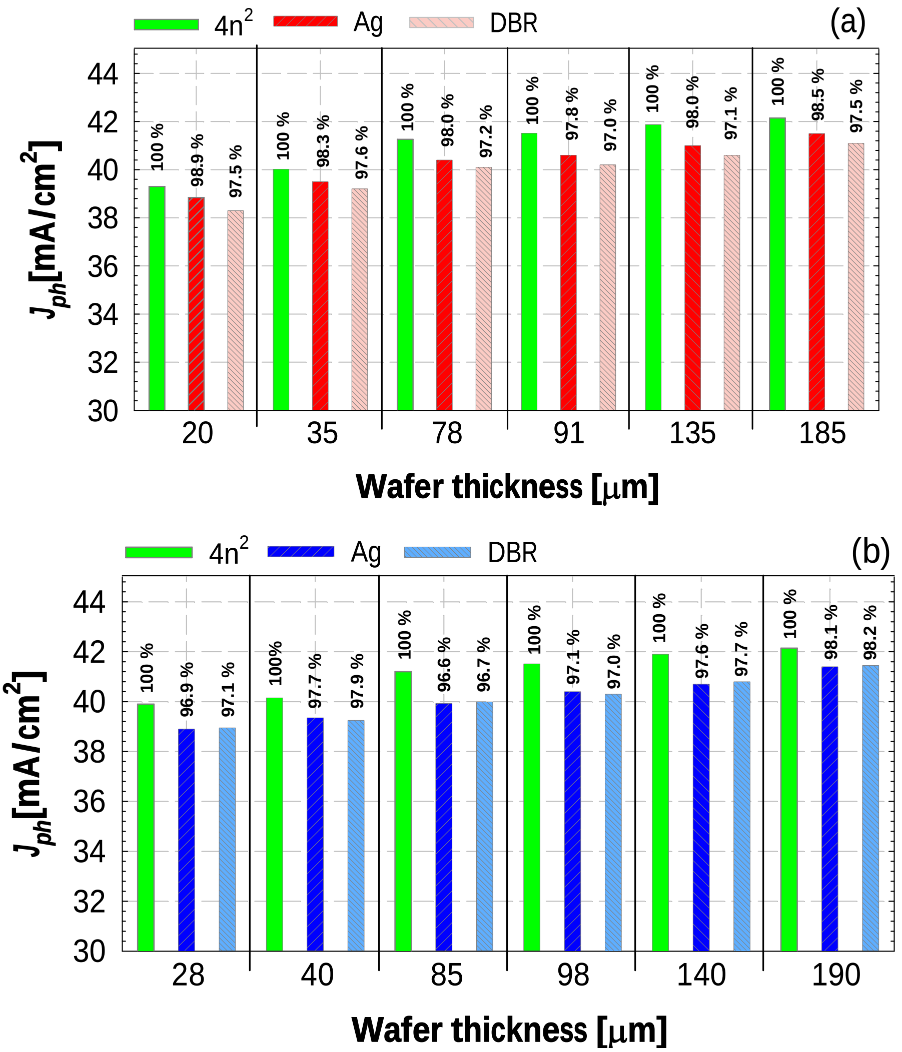

Figure 4.9. Histogram of J_{ph} calculated between 400 nm and 1200 nm for AM1.5 illumination conditions and different absorber thicknesses in case of (a) textured and (b) flat BS (see Equation 4.5). The BS is coated either with DBR or with the reference Ag BR. The graph also reports the ΔJ_{ph} calculated according to Equation 4.6.

4.5 Conclusions

An advanced light-trapping scheme based on FS nano-texture, BS random pyramids coated a metal or dielectric DBR is presented. After designing an omni-directional dilectric DBR, ultra-thin chemically etched c-Si slabs with thicknesses down to 20 µm were realized. Measured c-Si absorptance spectra, convoluted with the reference solar photon flux between 400 nm and 1200 nm, resulted in implied J_{ph} up to 98.9% of the maximal theoretical one calculated for the same wavelength range and wafer thickness. To date this is the closest experimental evidence of the $4n^2$ classical absorption limit in c-Si. Further studies, presented in Chapter 7 will aim at the fabrication of an optimized dielectric DBR that suffers less from transmittance losses in the region of weak absorption of c-Si when deposited on a textured surface. Additionally, more insights on the light scattering given by the front nano-texture should be addressed. This is to pursue an even better anti-reflective front texture which allows implied J_{ph} near the $4n^2$ absorption limit with flat BS. High efficiency ultra-thin solar cells can be fabricated if the surfaces of the presented light trapping scheme are well-passivated.

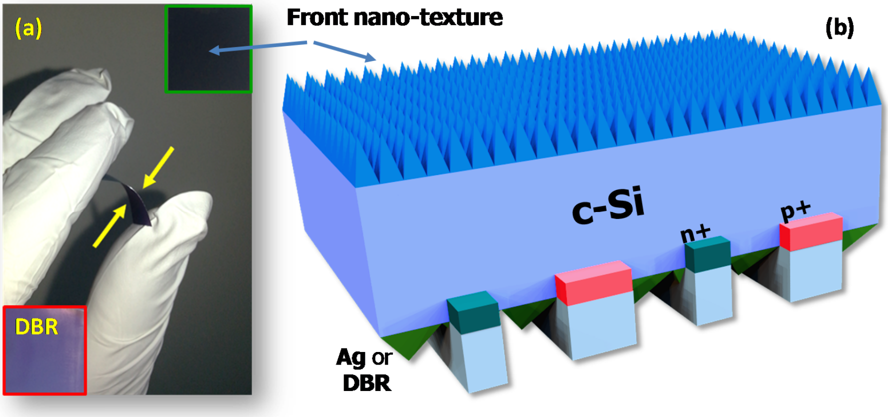

Figure 4.10. (a) Photo of 20-μm thick flexible silicon absorber extracted from the c-Si wafer support. Top-right and bottom-left inset photos indicate the b-Si front surface and the rear random pyramids coated with DBR, respectively. (b) Vision: to apply the presented light trapping scheme in IBC c-Si solar cell technology.

This can be achieved by combining a SiO_2 or Al_2O_3-based passivation with a surface treatment after RIE aiming to increase minority carrier lifetime as demonstrated in [20] and Chapter 6. Finally, IBC architecture was indicated as the most suited technology in order to fully exploit the optical advantages brought by the proposed light trapping scheme.

4.6 Appendix

4.6.1 Optical modelling

For an optical system such as c-Si / BR, an empirical model [31] was developed, for which the silicon absorptance ($A_{Si\text{-}cal}$) can be distinguished from the total measured absorption (A_{tot}) as following:

$$A_{Si-cal}(\lambda) = \frac{R_{air/Si}(\lambda)\cdot(1-R_{@1200nm})}{R_{@1200nm}} + \frac{R_{@1200nm} - R_{meas}(\lambda)}{R_{@1200nm}} \qquad 4.7$$

where R_{meas} is the measured total reflectance (at FS), $R_{@1200nm}$ is a constant and equals R_{meas} at 1200 nm and $R_{air/Si}$ is the contribution of reflected light bouncing inside the bulk c-Si at air/Si interface (also known as *first pass R*). $R_{air/Si}$ is estimated by linearly extrapolating R_{meas} between 700-900 nm and 1200 nm. Equation 4.7 was derived in order to ensure that: (i) A_{Si-cal} = A_{tot} for spectral range below the region of weak absorption in Si and (ii) $A_{Si-cal} \rightarrow 0$ for λ = 1200 nm. In more detail, for spectral range below the region of weak absorption in Si, $R_{meas} = R_{Si/air}$ and therefore, Equation 4.7 can be rewritten as $A_{Si-cal} = 1-R_{meas}$ (accounting for the only Si absorption if no / or loss-less FS coatings are employed). In addition, at λ = 1200 nm the second term in Equation 4.7 is zero while the first term becomes zero if:

$$R_{@1200} \rightarrow 1, \text{ and / or, } R_{air/Si@1200} << R_{@1200} \qquad 4.8$$

Such conditions are usually achieved for an optical system formed by c-Si endowed with BR. In fact, Si is a weak absorber at this wavelength and therefore $R_{@1200}$ becomes larger than $R_{air/Si}$ (1200). For the remaining wavelengths in the weak absorption region both terms in Equation 4.7 contribute to determine A_{Si-cal}. The validity of Equation 4.7, was proven on several optical systems and for different absorber thicknesses. Here the focus is on the opaque optical system: c-Si (280 µm) / Ag (100 nm) in both flat and pyramidally-textured configurations as sketched in the Figure 4.11 (a) and (c). Measuring the total reflectance (R_{meas}) of an opaque optical system (i.e. $T = 0$) like c-Si / Ag means identifying also the total absorptance (A_{tot}), which is given by the sum of the absorptance spectra of c-Si (A_{Si}) and Ag (A_{Ag}):

$$A_{tot} = A_{Si} + A_{Ag} = 1 - R_{meas} \Rightarrow A_{Ag} = 1 - R_{meas} - A_{Si} \qquad 4.9$$

According to Equation 4.7, knowing R_{meas} and $R_{Si/air}$ is sufficient to distinguish A_{Si} (and thus A_{Ag} according to Equation 4.9) from A_{tot}.

To validate the proposed model a three-step procedure was applied. In the first step, measured R_{meas} and A_{tot} were matched with the corresponding R_{sim} and $A_{tot-sim}$ obtained by using the opto-electrical simulator Advanced Semiconductor Analysis (ASA) software [31][37]. By achieving this goal, the simulation software provides the absorptance spectra in c-Si (A_{Si-sim}) and in Ag (A_{Ag-sim}) such that $A_{tot-sim} = A_{Si-sim} + A_{Ag-sim}$. In the second step, A_{Si-cal} was calculated according to Equation 4.7 and compared to the A_{Si-sim}. After that the absorptance spectrum in Ag (A_{Ag-cal}) was calculated as:

$$A_{Ag-cal} = 1 - R_{meas} - A_{Si-cal} \qquad 4.10$$

Finally, in the third step, R_{meas}, $A_{Si\text{-}calc}$ and $A_{Ag\text{-}calc}$ (i.e. $R_{meas} + A_{tot\text{-}cal}$) are summed up aiming to observe $1 \ \forall \ \lambda$ (energy conservation) as it would be in case of $R_{meas} + A_{tot}$. The results of the $A_{Si\text{-}cal}$ and $A_{Si\text{-}sim}$ for the opaque systems with polished and textured Si are shown in Figure 4.11 (b) and (d), respectively. For both structures, a good matching between them is achieved and energy conservation is verified. Another example proposed to validate Equation 4.7 is presented in Figure 4.12. In this case the A_{Si} absorption was measured for an optical system formed of air / textured c-Si (280 μm) / air. For this system the BR is just air (R_b is set by the refractive mismatch between Si and air) and therefore the measured total absorption (A_{tot}) corresponds to the A_{Si}. This allows having a direct comparison between the measured $A_{Si\text{-}meas}$ and $A_{Si\text{-}cal}$ calculated by using Equation 4.7 and the only R_{meas}. The latter quantity as function of the wavelength is reported in Figure 4.12 (a). A good agreement between $A_{Si\text{-}meas}$ and $A_{Si\text{-}cal}$ was achieved as reported in Figure 4.12 (b).

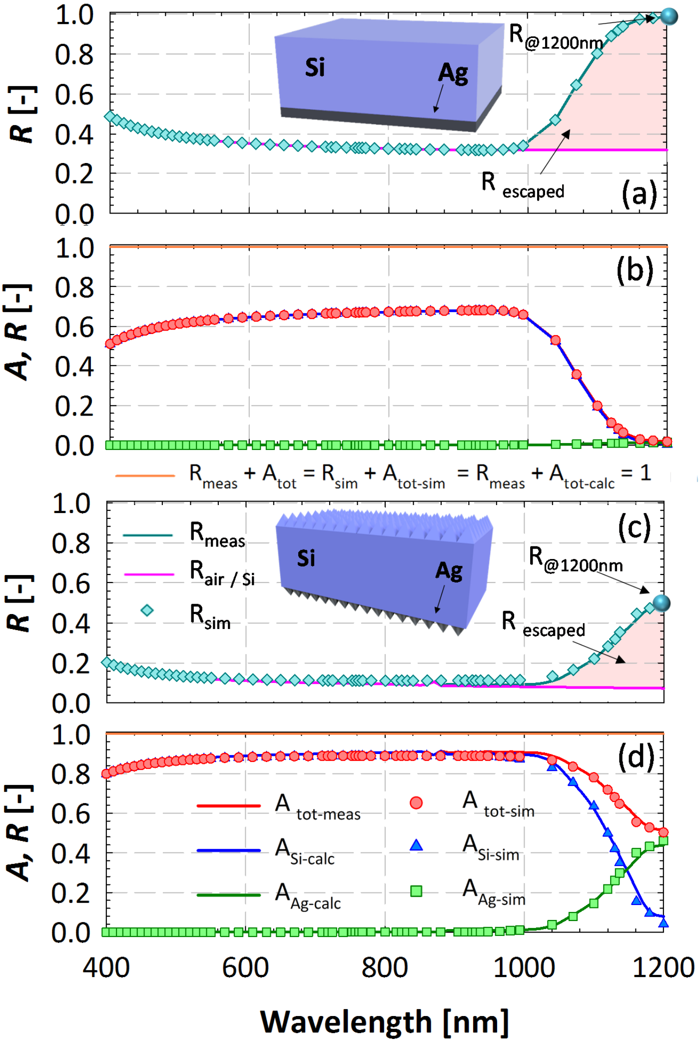

Figure 4.11. (a-c) R_{meas}, $R_{air/Si}$ and R_{sim}, of 280-µm thick wafer one-side coated with 100-nm thick Ag back reflector in (a) flat and (c) pyramidally-textured configurations. The fabricated / simulated structures are sketched in the insets. The light red region indicates the escaped reflectance ($R_{escaped}$) from the front side. (b-d) $A_{Si\text{-}cal}$ and $A_{Ag\text{-}cal}$ calculated from equations 4.7 and 4.10, respectively, and superposed to simulated $A_{Si\text{-}sim}$ and $A_{Ag\text{-}sim}$ for the respective structures illustrated in the top insets. Also A_{tot} and $A_{tot\text{-}sim}$ spectra are here reported. For both structures, the energy conservation ($R_{meas} + A_{tot} = R_{sim} + A_{tot\text{-}sim} = R_{meas} + A_{tot\text{-}cal} = 1$) is verified (orange line).

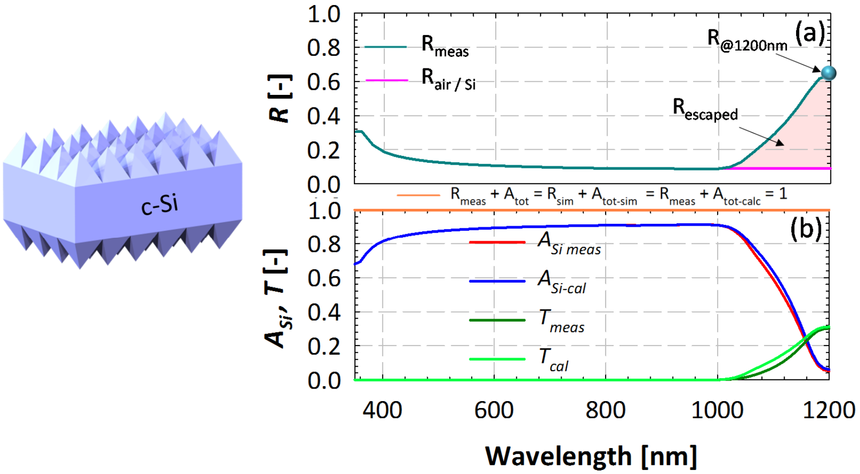

Figure 4.12. (a) R_{meas}, $R_{air/Si}$ of 280-µm thick wafer pyramidally-textured. The fabricated structure is sketched in the inset on the left side. (b) A_{Si-cal} and T_{cal} calculated from equations 4.7 and 4.10, respectively, and superposed to simulated $A_{Si-meas}$ and T_{meas} for the structure illustrated in the top insets. Also energy conservation ($R_{meas} + A_{tot} = R_{meas} + A_{tot-calc} = 1$) is verified (orange line). The light red area indicates the R escaped ($R_{escaped}$) from the front side.

4.7 References

[1] J. Zhao, A. Wang, P. P. Altermatt, M .A. Green, 24% efficient silicon solar cells with double layer antireflection coatings and reduced resistance loss. Appl. Phys. Lett. 1995, 66 (26), 3636-3638.

[2] A. Jäger-Waldau, PV Status Report 2012. Joint Research Centre, Institute for Energy and Transport 2012.

[3] C. del Cañizo, G. del Coso, W. C. Sinke, Crystalline silicon solar module technology: Towards the 1€ per watt-peak goal. Prog. Photovolt Res. Appl. 2008, 17, 199-209.

[4] A. Goodrich, P. Hacke, Q. Wang, B. Sopori, R. Margolis, T. L. James, M. A. Woodhouse, wafer-based monocrystalline silicon photovoltaics road map: Utilizing known technology improvement opportunities for further reductions in manufacturing costs. Sol. Energ. Mat. Sol. 2013, 114, 110-135.

[5] B. Micciche, B. Dingle, Understanding the causes for cell breakage during the cell interconnecting process – part I. Proceedings of the 21st European Photovoltaic Solar Energy Conference 2006.

[6] K. A. Munzer, K. T. Holdermann, R. E. Schlosser, S. Sterk, Thin monocrystalline silicon solar cells. Electron Devices, IEEE Transactions on. 1999, 46 (10), 2055-2061.

[7] S. W. Glunz, S. Rein, W. Warta, J. Knobloch, W. Wettling, On the degradation of Cz-silicon solar cells. Proceedings of the 2nd World Conference on Photovoltaic Energy Conversion 1998, 1343-1346.

[8] D. Kray, H. Kampwerth, E. Schneiderlochner, Comprehensive experimental study on the performance of very thin laser-fired high-efficiency solar cells. Proceedings of the 19th European Photovoltaic Solar Energy Conference 2004, 608-611.

[9] M. A. Green, Silicon Solar Cells: Advanced Principles & Practice. Centre for Photovoltaic Devices and Systems, University of New South Wales 1995.

[10] T. Tiedje, E. Yablonovitch, G. D. Cody, B. G. Brooks, Limiting efficiency of silicon solar cells. Electron Devices, IEEE Transactions on 1984, 31 (5), 711-716.

[11] P. Campbell, M. A. Green, Light trapping properties of pyramidally textured surfaces. J. Appl. Phys. 1987, 62, 243.

[12] K. X .Wang, Z. Yu, V. Liu, Y. Cui, S. Fan, Absorption enhancement in ultrathin crystalline silicon solar cells with antireflection and light-trapping Nanocone Gratings. Nano Lett. 2012, 12 (3) 1616-1619.

[13] E. Garnett, P. Yang, Light trapping in silicon nanowire solar cells. Nano Lett. 2010, 10, 1082-1087.

[14] L. Cao, P. Fan, A. P. Vasudev, J. S. White, Z. Yu, W. Cai, J. A. Schuller, S. Fan, M. Brongersma, Semiconductor Nanowire Optical Antenna Solar Absorbers. Nano Lett. 2010 10 (2) 439-445.

[15] C. Battaglia, M Boccard, F.-J. Haug, C. Ballif, Light trapping in solar cells: When does a Lambertian scatterer scatter Lambertianly? J. Appl. Phys. 2012, 112, 094504.

[16] O. Isabella, A. Ingenito, D. Linssen, M. Zeman, Front/Rear Decoupled Texturing in Refractive and Diffractive Regimes for Ultra-Thin Silicon-Based Solar Cells. Renewable Energy and the Environment, OSA Technical Digest. 2013, paper PM4C.2.

[17] S. Wang, B. Weil, Y. Li, K. X. Wang, E. Garnett, S. Fan, Y. Cui, Large Area Free-Standing Ultrathin Single-Crystal Silicon as Processable Materials. Nano Lett. 2013, 10.1021/nl402230v.

[18] L. Zeng, Y. Yi, C. Hong, J. Liu, N. Feng, X. Duan, L. C. Kimerling, B. A. Alamariu, Efficiency enhancement in Si solar cells by textured photonic crystal BR. Appl. Phys. Lett. 2006, 89, 111111.

[19] O. Isabella, S. Dobrovolskiy, G. A. Kroon, M. Zeman, Design and application of dielectric distributed Bragg back reflector in thin-film silicon solar cells, J. Non-Cryst. Solids. 2012, 358, 2295-2298.

[20] J. Oh, H.-C. Yuan, H. M. Branz, An 18.2%-efficient black-silicon solar cell achieved through control of carrier recombination in nanostructures. Nature Nanotechnology. 2012, 7, 743-748.

[21] H. Savin, P. Repo, G. Gastrow, P. Ortega, E. Calle, M. Garín, R. Alcubilla, Black silicon solar cells with interdigitated back-contacts achieve 22.1% efficiency, Nat Nano. 2015 10, 7,624 – 628, DOI: 10.1038/nnano.2015.89.

[22] M. Otto, M. Kroll, T. Käsebier, R. Salzer, A. Tünnermann, R. B. Wehrspohn, Extremely low surface recombination velocities in black silicon passivated by atomic layer deposition. Appl. Phys. Lett. 2012, 100, 191603.

[23] https://www.aitechnology.com/company/

[24] White papers in Ansys HFSS official website, http://www.ansoft.com/products/hf/hfss/.

[25] D. Kray, M. Hermle, S. W. Glunz, Theory and experiments on the back side reflectance of silicon wafer solar cells. Prog. Photovolt: Res. Appl. 2007, 16, 1-15.

[26] O. Isabella, Light management in thin-film silicon solar cells. PhD dissertation. 2013.

[27] Y. Fink, J. N. Winn, S. Fan, C. Chen, J. Michel, J. D. Joannopoulos, E. L. Thomas, A Dielectric Omnidirectional Reflector. Science. 1998, 282, (5394), 1679-1682. DOI: 10.1126/science.282.5394.1679.

[28] D. N. Chigrin, A. V. Lavrinenko, D. A. Yarotsky, S. V. Gaponenko, Observation of total omnidirectional reflection from a one-dimensional dielectric lattice. Appl. Phys. 1999, 68, 25-28.

[29] J. S. Orfanidis, Electromagnetic waves and antennas. Rutgers University. 2010.

[30] Z. C. Holman, M. Filipič, B. Lipovšek, S. De Wolf, F. Smole, M. Topič, C. Ballif, Parasitic absorption in the rear reflector of a silicon solar cell: Simulation and measurement of the sub-bandgap reflectance for common dielectric/metal reflectors. Sol. Energ. Mat. Sol. 2014, 120, 426-430.

[31] A. Ingenito, O. Isabella, M. Zeman, Opto-electronic evaluation of thin double-textured crystalline silicon wafers. 39th IEEE Photovoltaic Specialist conference. 2013.

[32] http://rredc.nrel.gov/solar/spectra/am1.5/

[33] J. Krč, M. Zeman, S. L. Luxembourg, M. Topič, Modulated photonic-crystal structures as broadband back reflectors in thin-film solar cells, Appl. Phys. Lett. 2009 94 153501, 10.1063/1.3109781.

[34] R. M. Swanson, Device physics for backside-contact solar cells. Proc. of the 33rd IEEE Photovoltaic Specialists Conference. 2008, San Diego, USA.

[35] http://us.sunpowercorp.com/homes/

[36] T. Ohrdes, U. Römer, Y. Larionova, R. Peibst, P. P. Altermatt, N.-P. Harder, High Fill-Factors of Back-Junction Solar Cells without Front Surface Field Diffusion. Proceedings of the 27th European Photovoltaic Solar Energy Conference 2012, 866-869.

[37] O. Isabella, H. Sai, M. Kondo, M. Zeman, Full-wave optoelectrical modeling of optimized flattened light-scattering substrate for high efficiency thin-film silicon solar cells. Prog. Photovolt: Res. Appl. 2012, 10.1002/pip.2314.

5

Simplified process for high efficiency, self-aligned IBC c-Si solar cells combining ion implantation and epitaxial growth: design and fabrication

5.1 Abstract

Front and rear contacted wafer-based c-Si solar cells characterized by P-diffused emitter and Al-screen printed back surface field currently constitute the dominant solar cell architecture in the photovoltaic market. The key success of this technology is based on the simple and cost effective fabrication process. However, its conversion efficiency is limited. High-efficiency c-Si solar cells architectures have been demonstrated at laboratory and industrial scale with the aim of decreasing the LCOE by increasing efficiency. For this reason high-efficiency solar cells are expected to increase their market share in next decade. In particular, interdigitated back contacted (IBC) c-Si solar cell architecture, which the current world record efficiency is based on, is expected to gain shortly industrial level relevance. In this work, activities of TUDelft in the fabrication of IBC c-Si solar cells are reported. In particular, a novel method for realizing high-efficiency IBC c-Si solar cells based on single-side and (relatively) low-temperature doping techniques is demonstrated. In particular, epitaxial growth of B-doped Si is used to form the emitter, while P-ion implantation is deployed to form both front and back surface fields. To pattern the rear junction, a self-aligned process based on one lithographic step has been developed. In addition, metal lift-off is used to define both the metal contacts. By using this process, efficiency higher than 20% has been demonstrated.

5.2 Introduction

Currently one technology dominates the photovoltaic (PV) market: the homo-junction (HMJ) front and rear (f/r) contacted p-type silicon (Si) solar cells fabricated via thermal diffusion of phosphorous (P) on the front side (FS) and screen printing of aluminium-based back surface field (BSF) on the rear side [1]. The success of this technology is attributed to the very simple, low-cost and high-throughput nature of the fabrication process. These advantages are however paid in terms of limited conversion efficiency. In general, conversion efficiency of such solar cell architecture has a plateau around 18-19% for mono-crystalline Si (c-Si) and 17-18% for multi-crystalline Si (mc-Si) solar cells [2]. In fact, the Al-BSF results in fairly high rear recombination losses and has a high degree of parasitic absorption of light [3]. More advanced solar cell architectures are the so-called passivated emitter and rear cell (PERC), hetero-junction (HTJ) and interdigitated back contacted (IBC) solar cells. These technologies are capable to reach efficiencies higher than 20% at industrial level but using higher quality materials and, and in case of IBC, more complicated fabrication steps. All this increases the cost of the final device, making c-Si PERC, HTJ and IBC-based PV modules to account for only 10% of the total PV market (at the end of 2014) [1]. According to the ITRPV roadmap, however, high-efficiency technologies will drastically increase their market share in the coming years. This prediction is already becoming true for PERC devices which cover almost all PV systems currently installed. HMJ-IBC c-Si solar cells are also expected to increase their market share by more than 5 times in 2024 [1]. For this reason and because of the potential high efficiency many PV research institutes and companies are focusing their research on such technology showing relevant progresses. Pioneer and main manufacturer company producing IBC c-Si solar cells on pilot line is SunPower Corporation, which has demonstrated 25.0% cell efficiency on large area (121 cm^2) [4]. Bosch and Samsung have recently reported on the development of large area IBC using ion implantation with conversion efficiency of 22.1% and 22.4%, respectively [5] and [6]. At ISC Constance large area IBC solar cells with efficiency higher than 21% have been demonstrated using only industrially-proven process equipment [7]. More recently, Trina Solar together with the Australian National University (ANU) has demonstrated small scale (2 x 2 cm^2) IBC solar cells with conversion efficiency of 24.4% [8]. At laboratory scale (2 x 2 cm^2) conversion efficiencies of 23.3%, 23% and 23.1% have been also demonstrated by imec [9], Fraunhofer Institute for Solar Energy Systems ISE [10] and Institut für Solarenergieforshung Hamelin (ISFH) [11], respectively. Such achievements clearly demonstrate that IBC c-Si solar cells can deliver high conversion efficiencies. The reason for that is related to the nature of the IBC architecture which locates both contacts on the back side (BS) of the wafer. Having both contacts on the BS introduces a series of opto-electrical advantages, and to some extent gives more freedom in the design with respect to standard f/r c-Si solar cells and definitely allows for record short-circuit current density (J_{SC}), open-circuit voltage (V_{OC}) and fill factor (FF). First, optical shading losses at FS, responsible for 4-5% decrease in J_{SC} from active area to aperture area of f/r c-Si solar cells [2], are completely eliminated in IBC solar cells. Second, as all BS area is available for contacting, metal grid design can be optimized (maximized FF) by fabricating large-coverage (locally-opened) metal contacts without caring about optical shading losses. Third, IBC architecture relaxes the design of the doped region on the FS of the cell. In standard f/r c-Si solar cells, the design of the emitter at FS is constrained between high doping to minimize contact and lateral resistance losses and low doping to decrease recombination. Differently, in IBC devices the emitter is fabricated at BS, allowing for both high lateral conductivity and high spectral response at short wavelengths. Fourth, IBC solar cells can exhibit the highest spectral response over the full wavelength range among all the c-Si solar cells. In fact, the FS of an IBC solar cell is usually either lightly doped (see below) or just undoped [8], resulting in low recombination losses at short wavelengths. All this enables the usage on the FS of (i) nano-texturing to exploit full light in-coupling (i.e. perfect anti-reflective effect) [12], (ii) micro-texturing, such as standard pyramids, to scatter light [13] or (iii) a combination of both [14] as shown in Chapter 6. In this respect, high quality surface passivation of (un-)doped (nano-) textured FS is of paramount importance [8][14][15] for achieving record collection efficiency and thus record J_{SC} and V_{OC}. On the contrary, having both contacts on the rear side introduces a 2-D current flow of the minority carriers and makes evident the so-called *electrical shading losses*. Such losses are localized in regions at BS without the emitter, and occur when the distance that a minority carrier needs to travel to be collected by the emitter region becomes comparable to the local diffusion length [16][17]. Such losses can be reduced by decreasing the BSF coverage but this introduces a fundamental trade-off between contact resistance and surface passivation [18] or by suing a front floating emitter (FFE) [7]. The performance benefits of HMJ-IBC solar cells come in exchange of (i) more complicated design and fabrication process, which makes IBC more expensive than standard fully metalized f/r c-Si solar cells, (ii) risk of p-type and n-type electrodes shunting at the BS, (iii) need of high effective minority carrier diffusion length to efficiently collect both carriers at BS. The last aspect translates in the need for high passivation quality at both FS and BS and high bulk lifetime (i.e. more expensive). This is because minority carrier collection at back contacts of an IBC device is strongly influenced by front surface recombination velocity and minority bulk carrier lifetime. Typical solutions to this aim are the implementation of front surface field (FSF) [19] or front floating emitter (FFE) [7][20] and the usage of high bulk lifetime substrates, typically n-type Czochralski (Cz) or float zone (FZ) wafers [21]. On one hand, FSF and FFE are commonly used to reduce front surface recombination by decreasing the surface concentration of one of the carriers (see Section

5.7.1 for more details). On the other hand, n-type wafers exhibit longer minority carrier lifetime since they are less sensitive to most common impurities [22] and, in case of Cz growth, are free of light induced degradation due to the absence of boron-oxygen complex with respect to p-type [23]. Once that bulk and surface recombination mechanisms are minimized, contact recombination becomes a serious impediment to reach high conversion efficiency. To minimize this type of recombination dielectrics locally opened in correspondence of the contacts, thin (doped) hydrogenated amorphous silicon layers as in HTJ [24] or passivating contacts deploying doped poly-silicon [25] [26] have to be used. The combination of IBC and HTJ technologies, the so-called silicon hetero-junction IBC (HTJ-IBC), has been recently exploited by Panasonic on a 143.7 cm^2 c-Si solar cell exhibiting world record efficiency of 25.6% [29]. Based on the same technology, Sharp has demonstrated lab scale (4 x 4 cm^2) efficiency of 25.1% [28]. Such high efficiencies devices have been demonstrated so far only at laboratory scale. They are not yet industrially scalable, since high quality materials and complicated fabrication steps are required. In general HMJ-IBC c-Si solar cells at industrial level are fabricated via thermal diffusion. Doping via ion implantation is widely used by semiconductor industry but is still facing difficulties to take-off in the PV industry. However, this doping technique allows for single side doping, which simplifies the fabrication process but requires high annealing temperature (T) for activation and drive in of the dopants. This is especially the case of boron (B), which is typically activated at T > 1000 °C [29][30]. In addition, annealing steps need to be optimized to avoid formation of the boron rich layer (BRL), which under certain diffusion conditions can lead to bulk lifetime degradation [31][32]. On the other hand, even though thermal diffusion requires lower thermal budget than implantation (around 850 °C in case of P-diffusion), other aspects need to be considered: (i) the same doping profile is obtained on both sides of the wafer, thus additional steps are required to optimize front and rear doping profiles, (ii) the doped oxides serving as dopants source during the diffusion process need to be removed afterwards, (iii) the uniformity of B diffusion across the wafer surface needs to be ensured, (iv) the BRL needs also to be removed. In this work, a novel process flow for fabricating high efficiency IBC c-Si solar cells based on single-side and (relatively) low-temperature doping techniques and still using ion implantation is demonstrated. The process allows to define the BSF and emitter regions on the rear side with a gap in between by using only one photolithograph step. The gap region between the BSF and emitter avoids possible tunnelling recombination currents occurring when a direct contact between these two doped regions is present [33]. In addition, the presented process exhibits a thermal budget up to 900 °C and uses only two lithographic steps, which can be both replaced by screen printing or laser patterning processes at industrial level. The process is based on the combination of (i) epitaxial growth of in situ B-doped Si at 900 °C to form the emitter, (ii) ion implantation of P-ions to create FSF and BSF with different doping profiles, (iii) single annealing step at 850 °C in dry molecular oxygen (O_2) to activate the implanted P and simultaneously passivate the surfaces. The usage of the B-doped epitaxial layer allows for overcoming the abovementioned limitations in case of boron implantation or diffusion. Based on such process the design of the three doped regions (emitter, BSF and FSF) constituting the IBC device is presented. Such design relies on the collection and usage of relevant data such as minority carrier lifetime, sheet resistance and doping profiles. Finally, the impact of the FSF doping profile and rear geometry on the external parameters of fabricated IBC solar cells is experimentally investigated. By using the demonstrated fabrication process, solar cell exhibiting 20.2% conversion efficiency is reported and a roadmap to reach more than 22% is briefly discussed.

5.3 Strategy for front side passivation

The design of FSF is a key aspect to reach high efficiency in all types of rear junction devices. In c-Si solar cells most of the photo-generation occurs close to the front surface. In fact, light penetration depth in Si is around 20 μm at wavelengths of 900 nm. Therefore, if front surface is not well passivated, it introduces severe front recombination losses which will prevent the minority carriers to reach the *pn* junction located at BS. Front surface recombination is a special case of Shockley-Read-Hall (SHR) recombination. One approach to reduce such recombination is to decrease the surface defect density and concentration of one of the carrier type. This is usually done by introducing a doped region (FSF or FFE) in combination with a proper passivation stack [19][20]. However, heavily-doped regions increase bulk recombination rate. Hence, the optimal design of the FSF or FFE is based on the delicate interplay between achieving high surface passivation without increasing their recombination rate. In case of relatively low surface defect density, lightly-doped FSFs can offer a good potential barrier (i.e. high-low junction) to prevent minority carrier recombination on the front surface [34]-[35] without dramatically increasing its recombination. Contrarily to FSF, when a FFE is employed minority carriers are injected from the bulk to the FFE where they become majorities. After travelling laterally in the FFE, holes can be re-injected into the bulk and vertically diffuse to the rear emitter. This effect is called pumping effect and has the main advantage of reducing the electrical shading losses of the BSF [20], which opens ways for easier module integration (relaxed patterning requirements). However, in this case to achieve efficient lateral transport into the FFE, it should be heavily doped. Nevertheless, it has been recently demonstrated that in case of extremely low J_{0s} on textured surfaces (~5 fA/cm^2) and optimal rear geometry, either FSF or FFE can be avoided [8]. In this work, it was chosen to use a P-ion implanted FSF to passivate the FS of the fabricated devices. The reason for that is mostly related to the limitations of the doping techniques here used. In particular, the quality of the epitaxy process strongly depends on the crystal orientation and cleanliness of the seed surface. This makes the application of such process on textured surfaces with respect to polished ones more challenging. For this reason FFE or FSF fabricated via epitaxial growth are not considered in this work. Also, FFE fabricated via B-ion implantation is not considered because of the higher thermal budget required for activation of B compared to P and the high recombination rate achieved so far in our laboratory.

5.4 Process flow description

The main steps of the IBC process flow are described in Figure 5.1. For this work, double side polished (DSP) FZ n-type wafers with thickness 280 ± 20 µm and resistivity 2.5 ± 1 Ω-cm were used. After dipping etch in 0.55% diluted-in-water HF, a B-doped Si layer was deposited via epitaxial growth on the whole BS of the wafer (step 1, *emitter formation*). Afterwards, a layer of PECVD SiN_x with thickness around 200 nm was deposited to mask the emitter (step 2, *SiN_x mask*). Wafers were then coated with photoresist which was subsequently exposed and developed in correspondence of the regions were the BSF will be allocated (step 3, *BS litho*). Therefore, the SiN_x was etched in buffered hydrofluoric (BHF) acid while the photoresist was removed in acetone. At this point, a wet-etching based on a mixture of HF and HNO_3 was performed for 5 minutes to etch back the emitter from the region where the BSF will be fabricated (step 4, *isotropic etching*). Such wet etching is highly isotropic in Si and selective with respect to SiN_x (i.e. etching rate of Si is much faster than etching rate of SiN_x). As consequence, a 2-µm long and free standing SiN_x cantilever was formed as shown in the SEM picture in Figure 5.2 (a). The purpose of such cantilever is to shield the Si underneath during BSF implantation defining a self-aligned silicon gap of around 2 µm between the emitter and the BSF. For the fabrication of the BSF, implantation of P-ions was employed (step 5, *self-aligned BSF*). The SiN_x used as implantation mask was etched in BHF and re-deposited on the full BS. The whole wafer was immerged in a wet solution based on TMAH and IPA diluted in H_2O with the objective to texture only the FS as shown in the SEM picture in Figure 5.2 (b) (step 6, *SiN_x mask and FS texturing*). After this step, the SiN_x mask at BS was removed and implantation of P-ions was performed at FS to create the FSF. In this case, different doping profile with respect to the one of the BSF can be employed. To activate the ion implanted dopants and to passivate surfaces at both FS and BS, an annealing / oxidation step at 850 °C in O_2 was realized (step 7, *FSF and annealing/oxidation*). The thickness of the SiO_2 was found to be between 10 and 35 nm depending on the doping concentrations used in this work. Continuing, depending on the SiO_2 thickness, a SiN_x layer with variable thickness (70 to 45 nm) for antireflection coating (ARC) and passivation purposes was deposited on the FS. On the BS of the wafer a 100-nm thick SiN_x layer was deposited to enhance the internal rear reflectance [36] and for rear passivation (step 8, *FS and BS SiN_x*). A second lithographic step at BS was performed to define the contact opening of both BSF and emitter. Afterwards the SiO_2 / SiN_x stack at BS was etched from the contact regions and 2-µm thick Al layer was evaporated on the whole BS (step 9, *BS litho and Al evaporation*). Finally, metal lift-off [37] in acetone was performed in order to separate emitter and BSF metal contacts (step 10, *Al lift-off*). SEM picture of the BS showing emitter and BSF fingers is shown in Figure 5.2 (c).

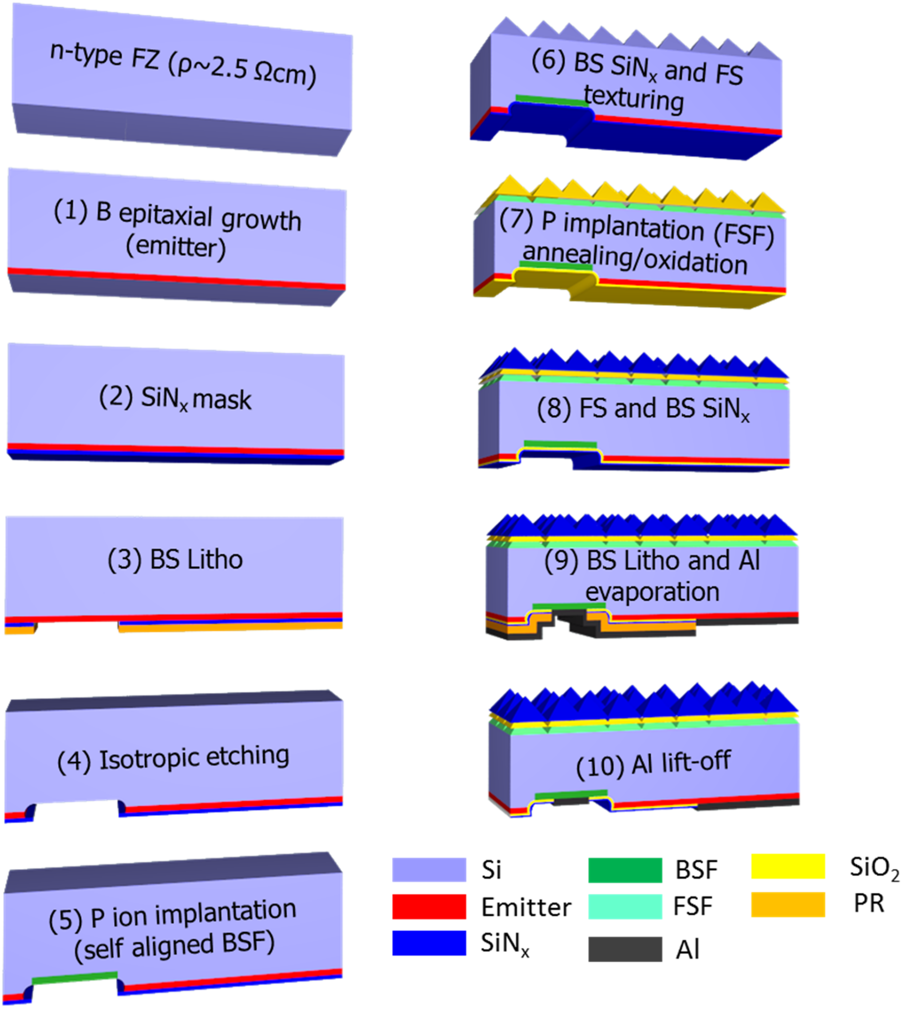

Figure 5.1. Steps of the proposed process flow for fabricating self-aligned and low temperature IBC c-Si solar cells.

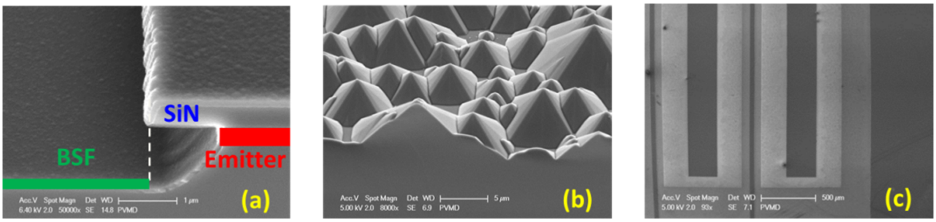

Figure 5.2. Cross-sectional SEM pictures after steps 4, 5 and 9, respectively (a), (b) and (c). All SEM pictures were taken at tilting angle of 45°. The SEM in (a) was taken after a preliminary test to check the etching rate of Si in the wet isotropic solution.

5.5 Rear geometry definition for the fabricated IBC

The IBC c-Si solar cells here presented were fabricated on 4 inches wafers and were processed during the same run. On each wafer three cells of 3 x 3 cm^2 with different rear geometries, defined in Table 5.1, were fabricated. Relevant parameters defining the rear geometry of an IBC device are: (i) pitch, defined as the distance between two doped regions of the same type (see Figure 5.3); (ii) BSF fraction (BSF_f), defined as the ratio between the width of BSF over the pitch; and (iii) contacted area, defined as the total contacted area for both emitter and BSF (bus-bar included).

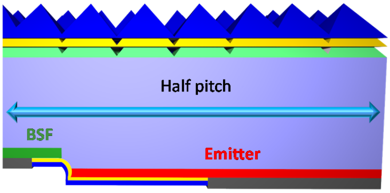

Die # [-]	*Pitch* [mm]	BSF_f [%]	Contacted area [%]
1	0.65	40	30
2	1	20	41
3	1.5	25	34

Figure 5.3. 3-D sketch of our self-aligned device where pitch and BSF fraction (BSF_f) can be individuated.

Table 5.1. For each wafer, three 3x3 cm^2 cells with different rear geometries were fabricated. They are indicated here by the die number. The definition of contacted area for both BSF and emitter includes bus-bars.

5.6 Characterization tools

Electrical properties of emitter, FSF and BSF were characterized by measuring effective minority carrier lifetime (τ_{eff}), implied V_{OC} (i-V_{OC}) and recombination current density under thermal equilibrium (J_{0s}) of symmetrical *half-fabricate* cells via quasi-steady state photo-conductance (QSSPC) measurements [38]. In addition, the sheet resistance ($R_\square$) of emitter, FSF and BSF was measured by using four-point probe measurements on DSP wafers, while their doping profiles were measured via electrochemical capacitance voltage (ECV) technique. Sinton suns-V_{OC} was used to measure ideality factor and pseudo-FF (*p-FF*) of the final devices. This measurement technique, being contactless, does not account for losses related to the series resistance. Thus *p-FF* is always larger than *FF*, indicating the upper limit of *FF* for the measured solar cell. The surface texture of fabricated IBC c-Si solar cells were visually investigated by means of scanning electron microscopy (SEM) using a Philips XL-50 setup. The thickness of both SiO_2 and SiN_x layers was extracted from ellipsometry spectra using J. A. Wollam CO. M-2000DI spectroscopic ellipsometer on DSP polished samples. Wavelength-dependent reflectance (*R*) and transmittance (*T*) were measured using a Perkin-Elmer Lambda 950 spectrophotometer in the wavelength range between 300 nm and 1200 nm. Continuous solar simulator Wacom WXS-156S AAA was used to measure the current-density voltage (*J-V*) characteristics of the final devices. The simulator consists of xenon lamp and halogen lamp that closely reproduce the spectrum and the intensity of actual sunlight. The set-up is calibrated with respect to a reference cell frequently calibrated at Fraunhofer ISE CalLab. The measured (illuminated) area included the bus-bars of the cells. The Wacom set-up is equipped with one Kelvin probe for each of the two bus-bars. The probe was always placed in the middle of the bus-bar. External quantum efficiency (*EQE*) measurements were taken with an in house built setup, comprising a Newport illuminator/monochromator, a chopper, a substrate holder with magnetic pads to hold the probes and a lock-in amplifier. A calibrated mono-crystalline silicon diode with known spectral response (SR) calibrated at Fraunhofer ISE CalLab was used as a reference. The size of the light spot of the SR setup was 2 x 2.5 mm^2. The error measurement of the EQE is within 5%. To minimize the error on the illuminated area of the cell, all J_{SC} here reported are measured by means of *EQE*. The spectral response and *J-V* of our solar cells was measured without any reflective chuck.

5.6.1 Theoretical background of QSSPC measurements

A symmetrical half-fabricate structure is typically formed by bulk Si with the same surface texture / doped regions / passivation stack on both FS and BS. The τ_{eff} as function of the injection level density (Δn) was measured via QSSPC and is defined as [39]:

$$\frac{1}{\tau_{eff}}=\frac{1}{\tau_b}+\frac{1}{\tau_s}=\left(\frac{1}{\tau_{SRH}}+\frac{1}{\tau_{Auger}}+\frac{1}{\tau_{rad}}\right)+\frac{1}{\tau_s} \tag{5.1}$$

where τ_b and τ_s are the bulk and surface minority carrier lifetime, respectively. In particular, $1/\tau_b$ is the sum of the inverse of Shockley-Read-Hall lifetime (τ_{SRH}), Auger lifetime (τ_{Auger}) and radiative lifetime (τ_{rad}) in the bulk. The latter mechanism of recombination plays a minor role in c-Si material. The term $1/\tau_s$ accounts for both FS and BS surface recombination. For symmetrical samples τ_s is related to the effective front surface recombination velocity (S_{eff}) as proposed by Sproul [40]:

$$\tau_S = \frac{W}{2S_{eff}} + \frac{1}{D_b}\left(\frac{W}{\pi}\right)^2 \qquad (5.2)$$

were D_b is the diffusion constant, W the bulk wafer thickness. The second term on the right side of Equation (5.2) is usually negligible since it sets the lower limit of τ_s in case of infinite S_{eff}. In addition, the S_{eff} can be expressed as [39]:

$$S_{eff} = \frac{J_{0s}(N_b + \Delta n)}{qn_i^2} \qquad (5.3)$$

where J_{0s} is the recombination current density under thermal equilibrium, n_i the intrinsic silicon carrier concentration and N_b the bulk doping concentration. Wafers used in this work were characterized by $N_b \approx 2 \cdot 10^{15}$ cm^{-3}. A common way to define the passivation quality of a passivating layer is by indicating its J_{0s} value. Contrarily to τ_{eff}, J_{0s} is typically Δn independent and, therefore, can be used to give a unique indication of the surface passivation quality. Typically J_{0s} can be extracted from QSSPC measurements at high or low level injection [41].

5.6.2 Determination of J_{0s} at high injection levels

At high injection levels ($n \approx \Delta n$), Auger recombination in the bulk is dominant and $2 \cdot J_{0s}$ can be extracted by using the so called *slope method* proposed by Kane and Swanson [42]. In this case replacing Equations (5.2) and (5.3) in Equation (5.1) leads to the following expression:

$$\left.\frac{1}{\tau_{eff}} - \frac{1}{\tau_{Auger}}\right|_{high\ injection} \approx \frac{2J_{0s}}{q\,n_i^2 W}\Delta n \qquad (5.4)$$

where q is the electron charge, n_i^2 the intrinsic carrier concentration and W the thickness of the wafer. In next sections, the reported J_{0s} are always extracted by using the *slope method* and divided by two. Finally, analysing Equation (5.4), it appears clear that in case of high τ_b the maximal τ_{eff} achievable is limited by τ_{Auger} in the bulk and J_{0s} of passivated surfaces.

5.6.3 Determination of J_{0s} at low injection levels.

At low injection levels ($n \approx N_{bulk} = 2 \cdot 10^{15}$ cm^{-3}) surface passivation might still contribute to the τ_{eff}, especially if the bulk has low resistivity, see Equation (5.5). In this case, both contributions (from bulk and surfaces) become indistinguishable leading to the following expression of τ_{eff}:

$$\left.\frac{1}{\tau_{eff}}\right|_{low\,injection} \approx \frac{1}{\tau_b} + \frac{2J_{0s}}{q n_i^2 W} N_b \tag{5.5}$$

Equation (5.5) clearly indicates that, even at low injection levels, high J_{0s} values due to poor surface passivation might still leads to $\tau_{eff} < \tau_b$. At low injection levels it is also possible to calculate, with Equation (5.3), a S_{eff} independent of Δn as:

$$\left.S_{eff}\right|_{low\,injection} \approx \frac{J_{0s} N_b}{q n_i^2} \tag{5.6}$$

5.7 Fabrication tools

5.7.1 Implantation of P-ions for FSF and BSF fabrication

Ion implantation is widely used in integrated circuit processing because of the high degree of dose uniformity, chemical purity of the ion beam and controlled doping profile. Such doping technique has been investigated to fabricate mono-crystalline c-Si solar cells in the 80’s [43]. However, its application was restricted to small area laboratory cells and later dropped because considered too slow and expensive for solar cell manufacturing [43]. Even though current ion implanters for c-Si solar cells can exhibit high throughput [44] their large scale application in c-Si solar cells is not yet applied. The usage of ion implantation for c-Si solar cells allows to simplify the solar cell processing when compared with standard diffusion [45][46]. In particular, such doping technique is single sided (i.e. no need to protect or etch-back one of the wafer sides) and does not require edge isolation or etching of the dopant glass while dopant activation and drive-in can simultaneously be carried out with surface passivation. In this work, implantation of P-ions was used for the fabrication of both BSF and FSF. The implantation process was performed by using Varian e220hp implanter. To activate and drive-in the implanted P ions, a thermal annealing was required. In this work the annealing is performed in O_2 ambient in order to concurrently obtain a thermal SiO_2 layer which serves for passivation purposes. The requirements for BSF design are based on the interplay between low value of $R_\square$ (to allow high lateral conductivity and low contact resistance) and low recombination rate. For the FSF a different doping design compared with BSF can be employed, since its main role is to improve FS surface passivation. The conductive / passivation properties of the implanted BSF and FSF are studied in Section 5.8.1.

5.7.2 Epitaxial growth of in situ B-doped Si for emitter fabrication

Epitaxial growth of Si is a process well-known and widely used by the semiconductor industry, but only recently has been applied in c-Si solar cells [47]-[48]-[49]. The epitaxy process used in this work was performed by using ASM Epsilon 2000 reactor. The process is based on a chemical vapour deposition (CVD) performed at T = 900 °C, where dichlorosilane (SiH_2Cl_2) is used as silicon source while B-doping is made *in-situ* using diborane (B_2H_6) carried by molecular hydrogen (H_2). The main advantages of using such doping technique compared to common B-diffusion or ion implantation are: (i) B is electrically activated during the deposition, (i.e. no extra annealing is required), (ii) the process is single sided thus, front and rear doping can be optimized separately, (iii) BRL which in some conditions can degrades the bulk carrier lifetime is not formed [31][32]. The epitaxy process was used in this work to form the emitter region. The $R_\square$ of this layer was designed in order to deliver high lateral conduction and low contact resistance. The conductive/passivation properties of the epitaxially grown emitter are studied in Section 5.8.2.

5.8 Results and discussions

5.8.1 Design of BSF and FSF

The measured $\tau_{eff}(\Delta n)$ of doped layers with different $R_\square$ and fabricated on DSP samples is reported in Figure 5.4 (a). Notice that the back side of the fabricated IBC solar cells is flat, thus the decision to perform the optimization of BSF on DSP wafers symmetrically processed. All samples, after implantation of P-ions on both sides, were first annealed / oxidized at 850 °C in O_2 for 90 min and then coated, also on both sides, with PECVD SiN_x at 400 °C. The energy (E) and dose (D) of the implantation are reported in Table 5.2 together with measured $i\text{-}V_{OC}$ and J_{0s} on DSP. The table reports also the thicknesses of the SiO_2 (d_{ox}) measured via ellipsometer for all processed samples. For all implanted samples the energy of implantation was kept constant while the dose was increased. This results in a decrease of $R_\square$ (i.e. higher doping concentration) and increase of the oxidation rate because of the larger number of crystal defects [50]. A further increase of the SiO_2 growth rate is also expected for the alkaline textured samples. In fact, wafer texturing leads to a change of the crystallographic orientation on the c-Si wafer surface from <100> to <111> and the oxidation rate on <111> plane is faster than on <100> [51]. The SiO_2 / SiN_x passivation stack, applied to a reference DSP wafer, delivered $\tau_{eff} \approx \tau_b > 2$ ms and $J_{0s\ DSP}$ of 8.5 fA/cm^2, which proves its excellent passivation properties. For P-implanted regions with $D > 5{\cdot}10^{14}$ cm^{-2}, J_{0s} increases, leading to lower τ_{eff} and $i\text{-}V_{OC}$. For the BSF, the set of implantation process conditions ($D = 2{\cdot}10^{15}$ cm^{-2} and $E = 20$ keV) leading to $R_\square = 69\ \Omega/\square$ and $i\text{-}V_{OC}$ of 658 mV were chosen. Al contact line fingers were evaporated on such layer and, by using transmission line measurement (TLM) [39], its contact resistivity (ρ_c) was measured. This resulted to be equal to 0.75 ± 0.14 m$\Omega{\cdot}$cm^2, proving the good contacting property of the layer. For the design of the FSF, the passivation properties of the SiO_2 / SiN_x stack on un-doped and P-doped textured surfaces were studied. Measured $\tau_{eff}(\Delta n)$, $i\text{-}V_{OC}$ and ratio $J_{0s\ text}$ / $J_{0s\ DSP}$ are summarized in Figure 5.4 (b) and Table 5.3, respectively. The ratio $J_{0s\ text}$ / $J_{0s\ DSP}$ was calculated in order to compare the passivation properties between textured and polished surfaces. As Figure 5.4 (b) depicts, when the same implantation process was used, a severe degradation of the τ_{eff} was observed for the textured samples with respect to the DSP samples.

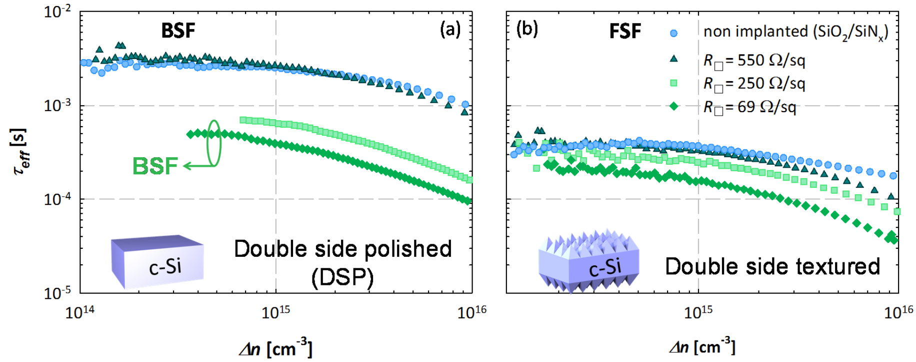

Figure 5.4. Measured $\tau_{eff}(\Delta n)$ of four symmetric samples: c-Si wafer / doped layer fabricated via implantation of P-ions followed by annealing and oxidation at 850 °C in O_2 / PECVD SiN_x at 400 °C. The four doped layers are characterized by different $R_\square$. Panel (a) reports the results on DSP wafers. The P implantation conditions leading to $R_\square = 69\ \Omega / \square$ and a reasonable i-V_{OC} of 658 mV where chosen to fabricate the BSF. The panel (b) reports the results on double side textured samples. A severe degradation of the τ_{eff} was observed with respect to the DSP samples.

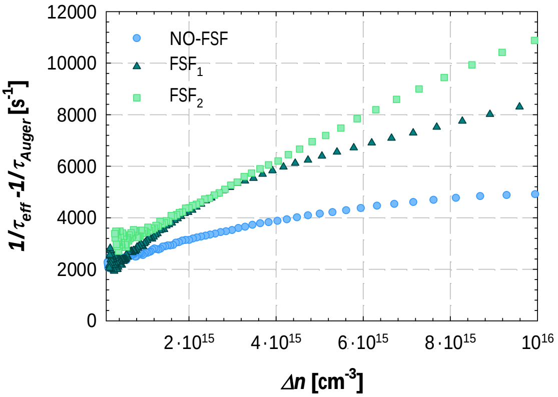

Figure 5.5. Effective lifetime corrected by the Auger lifetime calculated by using Richter model [52]. The J_{0s} are extracted at high injection levels by using the *slope method* described in section 5.6.2.

E [keV]	D [cm^{-2}]	$R_\square$ (n+ Implanted) [Ω / □]	$J_{0s\,DSP}$ [fA / cm^2]	i-V_{OC} [mV]	d_{ox} [nm]
-	-	non-implanted	10 ± 3	707	12.2
20	$1{\cdot}10^{14}$	550	18 ± 6	702	13.5
20	$5{\cdot}10^{14}$	250	74 ± 5	665	21.3
20	$2{\cdot}10^{15}$	69	140 ± 3	658	40.2

Table 5.2. Energy and dose of the implantation together with measured $R_\square$ of the three implanted layers passivated with SiO_2/SiN_x reported in Figure 5.4 (a) versus the J_{0s} and i-V_{OC} of the relative symmetric DSP wafers. J_{0s} and i-V_{OC} for non-implanted sample is also reported for reference purposes. Thicknesses of the SiO_2 of the different samples grown during oxidation at 850 °C in O_2 for 90 min is also reported.

E [keV]	D [cm^{-2}]	$R_\square$ (n+ Implanted) [Ω / □]	$J_{0s\,text}$ [fA/cm^2]	$J_{0s\,text}$ / $J_{0s\,DSP}$ [-]	i-V_{OC} [mV]
-	-	Non-implanted	48 ± 6	4.80	671
20	$1{\cdot}10^{14}$	550	62 ± 5	3.44	654
20	$5{\cdot}10^{14}$	250	120 ± 5	2.08	651
20	$2{\cdot}10^{15}$	69	386 ± 8	2.57	640

Table 5.3. Energy and dose of the implantation together with measured $R_\square$ of the three implanted layers reported in Figure 5.4 (b) versus the $J_{0s\,text}$, i-V_{OC} and $J_{0s\,text}$ / $J_{0s\,DSP}$ and calculated for the mean values of the relative symmetric double side textured wafers. J_{0s}, i-V_{OC} and $J_{0s\,text}$ / $J_{0s\,DSP}$ for non-implanted sample is also reported for reference purposes.

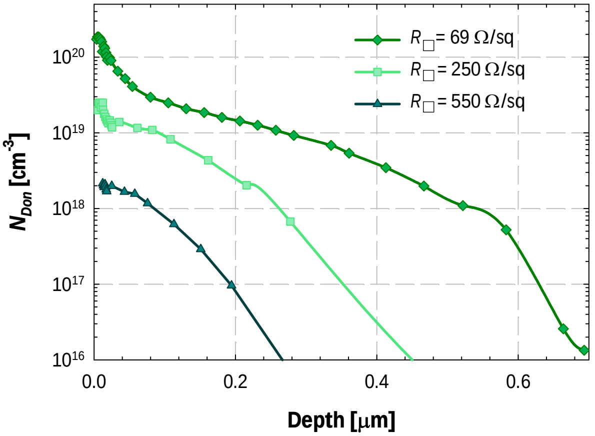

Figure 5.6. Measured ECV doping profiles of P-implanted layers after annealing / oxidation at 850 °C in O_2 ambient.

In addition, the ratio $J_{0s\,text}$ / $J_{0s\,DSP}$ is larger than 2 for all samples and reaches the highest value of 4.8 for the non-implanted one. Ideally, surface texturing with random pyramids should increase the surface area and therefore the $J_{0s\,text}$ with respect to $J_{0s\,DSP}$ by a factor equal to 1.7. The largest τ_{eff} degradation between DSP and textured samples was observed for the non-implanted case. The ratio values ($J_{0s\ text}$ / $J_{0s\ DSP}$) larger than 1.7 are indicative of the fact that surface area enlargement might not be the only cause of the increased recombination rate of the textured samples with respect to polished ones (possible explanations are given in Section 5.9.1). Also eventual surface contamination and/or additional recombination at edges and tips of the pyramids and/or poorer passivation properties of dry SiO_2 on <111> (textured) plane rather than <100> (DSP) might have drastically increased the $J_{0s\ text}$ with respect to $J_{0s\ DSP}$. In addition, notice that, in case of textured samples, $R_\square$ of the implanted region is expected to be higher due to the larger surface area. In Section 5.8.3 the SiO_2 / SiN_x stack and the FSFs with $R_\square$ of 250 and 550 Ω/□, respectively named NO-FSF, FSF_1 and FSF_2, will be studied as FS passivation schemes for the IBC devices. Measured ECV doping profiles of the P-implanted BSF, FSF_1 and FSF_2 on DSP samples after annealing / oxidation at 850 °C in O_2 ambient are shown in Figure 5.6. As the figure shows the doping profile of the BSF shows a high surface doping concentration in order to minimize contact resistance losses. FSF_1 and FSF_2 are less doped and were used as FSF.

5.8.2 Design of epitaxially grown emitter

The measured $\tau_{eff}(\Delta n)$ with respect to the $R_\square$ of three different epitaxially grown emitters is depicted in Figure 5.7. All emitters were designed to exhibit a constant acceptor doping concentration of N_{Acc} ~ $3{\cdot}10^{19}$ cm^{-3} but different thicknesses leading to different values of $R_\square$. Notice that this was also the maximal doping concentration achievable by the tool used in this work. After applying the same epitaxial growth process on both sides, the samples were first annealed / oxidized at 850 °C in O_2 ambient for 90 min and then coated, also on both sides, with PECVD SiN_x at 400 °C. As Figure 5.7 shows, by lowering $R_\square$, τ_{eff} decreases due to higher J_{0s}. In Table 5.4, the measured $i\text{-}V_{OC}$ and J_{0s} of the emitter (J_{0e}) are reported with respect to the $R_\square$ of the three fabricated doped layers. The doped layer with a $R_\square$ = 44 Ω/□ and $i\text{-}V_{OC}$ = 654 mV was chosen to be implemented in the IBC device as emitter, since it meets both requirements of relatively high $i\text{-}V_{OC}$ and low $R_\square$. For such emitter, the ρ_c with evaporated Al contact lines fingers measured via TLM resulted to be equal to 6.2 ± 1.5 $m\Omega{\cdot}cm^2$. Such value is almost one order of magnitude higher than the one measured for the BSF. Notice that the SiO_2 / SiN_x stack resulted in similar reasonable passivation properties on both emitter and BSF; thus it is an ideal candidate to passivate the whole BS of our IBC solar cell. Figure 5.8, measured ECV doping profiles of the B doped epitaxial layer as grown and after annealing / oxidation at 850 °C in O_2 ambient are reported.

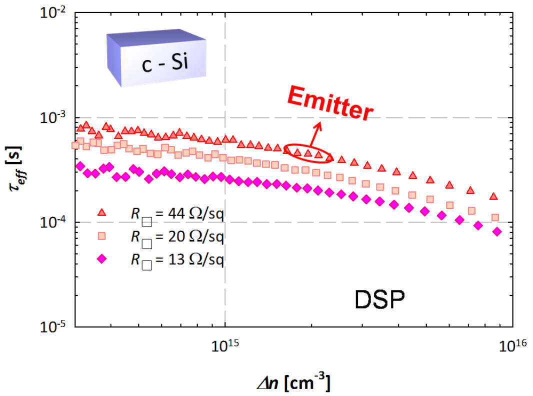

Figure 5.7. Measured $\tau_{eff}(\Delta n)$ of three symmetric samples: DSP c-Si wafer / in-situ B-doped epitaxially grown layer followed by annealing and oxidation at 850 °C in O_2 and PECVD SiN_x at 400 °C. The three doped layers are characterized by different $R_\square$. The emitter with a $R_\square$ = 44 Ω/□ and $i\text{-}V_{OC}$ = 654 mV was chosen to be implemented as emitter in the IBC devices.

$R_\square$ (p+ epi) [Ω/sq.]	$J_{0e\ DSP}$ [fA/cm²]	$i\text{-}V_{OC}$ [mV]	d_{ox} [nm]
44	110	654	13.4
20	140	647	14.5
13	170	638	13.7

Table 5.4. Measured $R_\square$ of the three doped layers reported in Figure 5.7 versus $J_{0e\ DSP}$ and $i\text{-}V_{OC}$ of the relative symmetric DSP wafers. Thickness of the SiO_2 grown after annealing oxidation at 850 °C in O_2 for 90 min is reported.

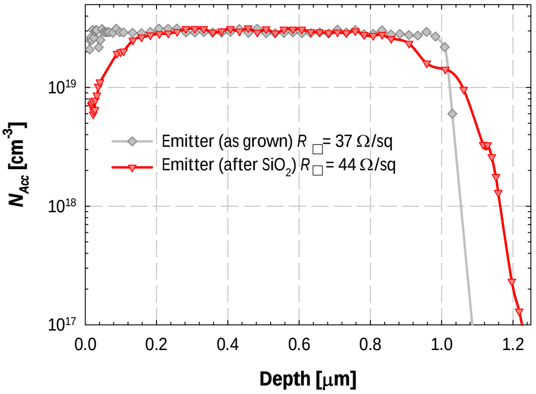

Figure 5.8. Measured ECV doping profiles B-doped epitaxial layer as grown and after annealing / oxidation at 850 °C in O_2 ambient. During the thermal oxidation, B diffuses deeper in to Si and also segregates into the SiO_2 on the surface leading to a decrease of the surface doping concentration.

The thermal oxidation step resulted in deeper diffusion of B into Si and also its diffusion into the SiO_2 due to higher solid solubility and diffusion coefficient of B in SiO_2 [53]. This leads to a decrease of the B surface doping concentration and thus high contact resistance.

5.8.3 Impact of FSF design on IBC solar cell performance

In this section, the impact of the FSF doping profiles on the IBC performance is presented. In particular, the IBC cell without FS implantation was named NO-FSF (i.e. passivated with SiO_2 / SiN_x), with FSF_1 and FSF_2 were named the IBCs with implanted FSF having $R_\square$ = 550 Ω/□ and $R_\square$ = 250 Ω/□, respectively. The FSF having same doping profile as the BSF was not studied because of the too high J_{0s} as reported in section 5.8.1. For all FSF configurations same rear geometry was used (i.e. Die #1 as defined in Table 5.1). Measured external parameters, *p-FF* and ideality factor at maximum power point under 1 sun illumination ($n_{MPP@1sun}$) [54] for the three fabricated devices are reported in Table 5.5. The table clearly shows that main parameters depending on the doping of the FSF are J_{SC} and FF. Starting with J_{SC}, the measured internal quantum efficiency (*IQE*) as function of the wavelength is reported in Figure 5.9. The figure clearly shows that: (i) the device with NO-FSF exhibits the lowest *IQE* in wavelength range between [300 -1050] nm; (ii) the devices with NO-FSF and FSF_1 exhibit an increase of the *IQE* towards longer wavelengths [800-1050 nm]; (iii) the device with FSF_2 shows a rather flat *IQE* of ~94% between [450 – 1050] nm. Regarding the FF, a drop of >1% was measured for the device with NO-FSF compared with the one with FSF_2. To understand such *FF* losses measured $n_{MPP@1sun}$ was investigated. As shown in Table 5.5, the device with NO-FSF exhibits an $n_{MPP@1sun}$ of 1.18 and a *p-FF* of 80.5%. On the contrary, the devices with FSF_1 and FSF_2 showed an $n_{MPP@1sun}$ close to one and *p-FF* higher than 81%. The highest conversion efficiency (19.4%) was reached for the FSF_2. On the right axis of Figure 5.9 the sum of *R* and *T* (*R*+*T*) is also reported. As expected, such quantity was found to be comparable for all devices between 450 and 1200 nm. For wavelengths below 450 nm, the sample with FSF_2 shows a slightly higher *R* with respect to the other FSF configurations. This effect is related to a thinner SiN_x (i.e. lower parasitic absorption) used in case of FSF_2. Oxidation rate increases with increasing the surface doping concentration (see Table 5.2). Therefore, in order to achieve a minimum of the *R* around 450 nm for all FSF configurations, the thickness of SiN_x was reduced from 75 nm in case of NO-FSF to 55 nm for the FSF_2.

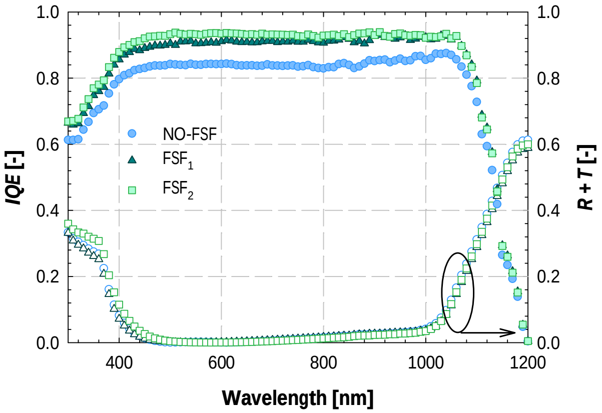

Figure 5.9. Measured *IQE* (left axis) and sum of *R* and *T* (*R*+*T*) (right axis) as function of the wavelength for IBC solar cells with Die #1 as rear geometry and different FSF. The device with FSF_2 exhibited the highest *IQE* on the whole wavelength range. The samples with FSF show a slightly higher *R* at short wavelengths with respect to the sample with NO-FSF. The reason for that is related to the higher oxidation rate of doped surfaces compared to un-doped one. In order to achieve a minimum of the *R* around 450 nm for all samples, the thickness of SiN_x for the FSF cells was reduced from 75 (NO-FSF) to 55 nm (FSF).

FSF [-]	J_{SC} [mA/cm^2]	*FF* [%]	V_{OC} [mV]	*p-FF* [%]	$n_{MPP\ @\ 1\ sun}$ [-]	η [%]
NO-FSF	34.3	76.2	634	80.5	1.18	16.6
FSF_1	38.7	77.6	632	81.7	1.12	18.9
FSF_2	39.3	78.1	633	83.2	1.08	19.4

Table 5.5. Measured external parameters, *p-FF* and $n_{MPP@1sun}$ for IBC solar cells with Die #1 as rear geometry and different FSF. The IBC device with FSF_2 exhibited the highest conversion efficiency of 19.4 %.

5.8.4 Impact of rear geometry on IBC solar cell performance

In the previous section the effect of the FSF on the performance of the IBC was studied when the rear geometry was kept constant. The conclusion of such analysis was that for the developed process the highest IBC performances were achieved with the deployment of the FSF_2. In this section, the performance of IBC solar cells with different rear geometries (i.e. Die #1, #2 and #3 as described in Table 5.1) is investigated, when the optimal FSF (i.e. FSF_2) found in the previous section is employed. Table 5.6 reports the measured external parameters, *p-FF* and the $n_{MPP@1sun}$ of the fabricated devices. The main parameters affected by the rear geometry are, once again, the J_{SC} and the *FF*. Starting with J_{SC}, Figure 5.10 (on the left axis) reports the measured *IQE* as function of the wavelength for the three rear geometries here investigated. Notice that to ensure a fair comparison among the measured performances, the three different rear designs were fabricated on the same wafer. Analysing Figure 5.10, appears clear that: (i) all dies show a quite constant *IQE* between 450 and 1050 nm; (ii) Die #3 exhibits a lower IQE with respect to Die #2 due to an increase of the BSF shading losses and larger pitch size; (iii) despite its shortest pitch, the *IQE* of Die #1 is further decreased with respect to Die #2 due to higher BSF_f. As reported in Table 5.4, *FF*, *p-FF* and $n_{MPP@1sun}$ were found to be comparable for all IBCs.

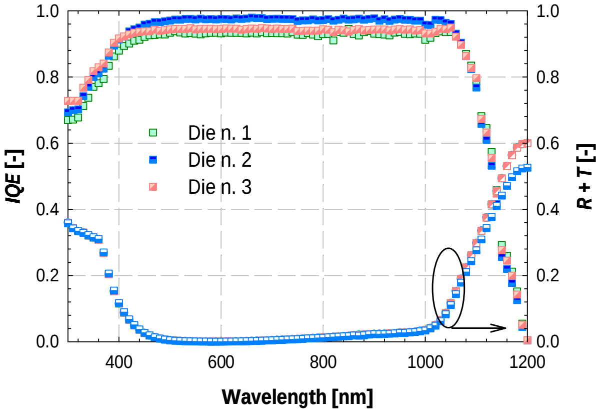

Figure 5.10. Measured *IQE* (left axis) and *R+T* (right axis) as function of the wavelength for IBC solar cells with optimal FSF (FSF_2) and different rear geometries (Die #1, #2, #3). All die show a rather constant *IQE* between 450 and 1050 nm. The *IQE* of the three devices is more sensitive to the BSF_f rather than the pitch size. In addition, *R+T* was found to be the same for all rear designs in the wavelength range between 300-1150 nm, confirming the reproducibility of texturing and SiO_2 / SiN_x. The difference at longer wavelengths is related to the different metal coverage used for the three rear designs.

Die # [-]	J_{SC} [mA / cm^2]	*FF* [%]	V_{OC} [mV]	$n_{MPP\ @\ 1sun}$ [-]	*p-FF* [%]	η [%]
1	39.3	78.1	633	1.08	83.1	19.4
2	41.0	77.0	639	1.00	83.8	20.2
3	39.9	77.3	635	1.02	83.6	19.6

Table 5.6. Measured external parameters, *p-FF* and $n_{MPP@1sun}$ for IBC solar cells with FSF_2 as FSF and different rear geometries. The IBC device with FSF_2 and rear geometry defined by Die #2 exhibited the best performance in conversion efficiency, $n_{MPP@1sun}$ and *p-FF*.

The table clearly indicates that all devices present an $n_{MPP@1sun}$ close to one and *p-FF* higher than 83% indicating that *FF* losses are mainly due to series resistance losses. For the optimal rear geometry (Die #2) with FSF_2 a J_{sc} value of 41 mA/cm^2 and overall cell efficiency of 20.2 % were measured. Notice that such efficiency was reached by using large pitch (1 mm) which is compatible with industrial application. On the right axis of Figure 5.10, *R+T* is also reported. Such quantity was found to be the same for all rear designs in the wavelength range between 300-1150 nm, confirming the reproducibility of texturing and SiO_2 / SiN_x stack. The difference at longer wavelengths is related to the different metal coverage used for the three rear designs. The high *p-FF* of these devices might be related to the fact the the developed self-aligned process avoid leakage currents due to direct contacts between the emitter and BSF regions.

5.8.5 Analysis of the FSF role in IBC c-Si solar cells

As shown in Figure 5.9, the device with FSF_2 shows the highest *IQE* compared with FSF_1 and no-FSF. However, by looking to the measured J_{0s} reported in Table 5.3 one would expect the opposite behaviour. To explain such effect and to better understand the role played by the FSF in the fabricated IBC, opto-electrical simulations were used. In particular, the *IQE* of the fabricated devices reported in Figure 5.9 were fitted by using the software Quokka [55]. As fitting procedure we have used two different approaches:

- For all three devices the input parameters of Table 5.8 were used, except for the minority bulk lifetime (τ_b) which was set as fitting parameter;
- For all three devices the input parameters were used of Table 5.7 were used, except for the front J_{0s} which was set as fitting parameter.

Figure 5.11 (a), shows that measured and simulated *IQE* are matched by using the QSSPC measured J_{0s} and τ_b of 2.5 ms for FSF_2, 1.5 ms for FSF_1 and 0.25 ms in case of NO-FSF. This effect could be related to the gettering effect of the P ion implantation which becomes more effective when the dose of the implantation increases (FSF_2) [56].

On the contrary, Figure 5.11 (b), shows a good matching between measured and simulated *IQE* by using a J_{0s} for the front surface of 96 fA/cm^2 for FSF_2, 140 fA/cm^2 for FSF_1 and 568 fA/cm^2 in case of NO-FSF and same τ_b=2.5 ms. Both simulation results indicate that either the fabrication process introduces bulk contaminations or that the J_{0s} extracted from Sinton measurements for the symmetrical samples are underestimated compared to the respective ones of the real cells. A possible explanations for the underestimation of the front J_{0s} are:

1) the measured τ_{eff} curve of the sample with NO-FSF, reported in Figure 5.4 (b), decreases at low injection levels ($\Delta n \ll N_b$). Notice that the fabricated devices might work at low injection levels at J_{SC}.
2) Possible increase of the surface recombination rate for the IBC device during the multiple fabrication steps compared with the reference symmetrical sample. The latter, in fact, experiences only doping and annealing/passivation processes.
3) The J_{0s} extracted from QSSPC measurement is considered at high injection levels and in thermal equilibrium (i.e. no carrier flow). This might lead to a correct

estimation of J_{0s} only at V_{OC}. In a real solar cell the J_{0s} under illumination might be different than the one in thermal equilibrium and in some cases could be injection level-dependent [57]. This is also shown in Figure 5.5 where only the sample with FSF_2 presents a constant slope of ($1/\tau_{eff}$ $-1/\tau_{Auger}$) with respect to Δn (i.e. J_{0s} independent by Δn).

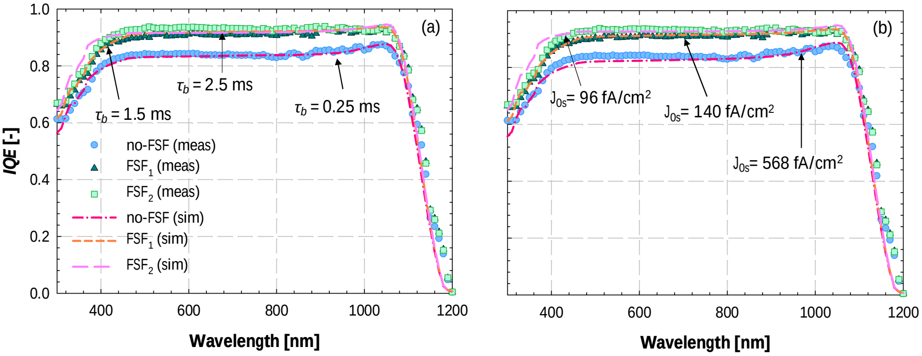

Figure 5.11. Measured and simulated *IQE* as function of the wavelengths for the three devices with different FSF and Die #3 rear geometry. Extracted (a) τ_b using the input parameters in Table 5.7 and (b) front side J_{0s} using the input parameters in Table 5.8.

Input	Value
W	280 µm
ρ_b	2.5 Ω·cm
$J_{0s\ BSF}$	200 fA/cm^2
$J_{0s\ emitter}$	150 fA/cm^2
$J_{0\ metal}$	900 fA/cm^2
τ_b	variable
$J_{0s\text{-}FSF}$	see Table 5.3

Table 5.7. Definition of the input parameters used in Quokka. The J_{0s} that resulted in the be matching of measured and simulated charatheristics used for passivated region of the BSF and emitter were comparable with the measured values as reported in Table 5.2 and Table 5.4.

Input	Value
W	280 µm
ρ_b	2.5 Ω·cm
$J_{0s\ BSF}$	200 fA/cm^2
$J_{0s\ emitter}$	150 fA/cm^2
$J_{0\ metal}$	900 fA/cm^2
τ_b	2.5 ms
$J_{0s\text{-}FSF}$	variable

Table 5.8. Definition of the input parameters used in Quokka. The J_{0s} that resulted in the be matching of measured and simulated charatheristics used for passivated region of the BSF and emitter were comparable with the measured values as reported in Table 5.2 and Table 5.4.

Once again, by using Quokka simulations, the spatially averaged Δn (Δn_{avg}) (along depth and width of the device) was carried out at J_{SC} for all three simulated devices. The extracted Δn_{avg} assumed the values of $3.08 \cdot 10^{14}$ cm^{-3}, $3.38 \cdot 10^{14}$ cm^{-3} and $3.45 \cdot 10^{14}$ cm^{-3} in case of NO-FSF, FSF_1 and FSF_2, respectively. This indicates that all simulated devices are in low injection (assuming $N_b = 2 \cdot 10^{15}$ cm^{-3}) conditions at J_{SC}. The QSSPC measurements in

Figure 5.4 (b) show that at such injection levels the samples with FSF_1 and FSF_2 exhibit similar or slightly higher τ_{eff} compared with the case when NO-FSF is employed. However, still looking at τ_{eff} measurements, this effect seems to be not enough to explain the larger increase of the J_{0s} values extracted from the simulations compared with the measured one in case of NO-FSF and FSF_1. A possible increase of the J_{0s} at device level compared to textured half fabricate samples in case of NO-FSF and FSF_1 might be related to an increase of the surface recombination due to the effects as described in (2) and (3). To explain why the FSF_2 is less sensitive to an increase of surface defects, a deeper analysis of the role played by a FSF in a rear junction device is required. The region above the emitter of an n-type IBC c-Si solar cell exhibits the same structure of an n-type f/r contacted solar cell with a rear emitter. In such device a (selective) FSF on the front side is usually employed creating a so-called *high-low* junction. In such conditions, the front surface recombination velocity (S_p) at the actual surface $x = 0$ is transformed in an effective surface recombination velocity S_{eff} defined at the edge of the depletion region (x_1) created at FSF / n-type bulk interface (see Figure 5.12).

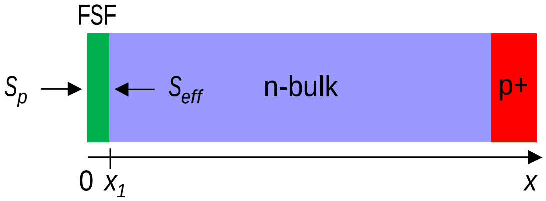

Figure 5.12. Schematic of FSF (i.e. *high-low* junction) in a rear junction device. The FSF transforms the S_p at the actual surface ($x = 0$) in S_{eff} at x_1, where x_1 is the edge of the depletion region created at FSF / n- bulk interface.

For a high-low junction the S_{eff} can be mathematically expressed as [58]:

$$S_{eff} = \frac{D_{FSF}}{D_b}\frac{p_{FSF}}{p_b}\frac{1}{L_{FSF}}\frac{S_p/D_{FSF} \quad L_{FSF} + tanh(W_{FSF}/L_{FSF})}{1+S_p/D_{FSF} \quad L_{FSF} \quad tanh(W_{FSF}/L_{FSF})} \tag{5.7}$$

where, D_{FSF} (D_b) is the diffusion coefficient of the FSF (bulk); p_{FSF} (p_b) is the minority doping concentrations in the FSF (bulk); and W_{FSF} and L_{FSF} are respectively the width and the diffusion length of the FSF region. The analytical parameterization of S_p is not trivial because it may depend on several aspects such as: (i) intrinsic properties of the passivation layer (field effect and chemical passivation), (ii) doping type and concentration of the passivated region; (iii) unpredictable surface defects (e.g. those induced by scratches, pinholes in the passivation stack, other impurities induced during the fabrication process). In this work, the following expression for S_p is proposed:

$$S_p(N_D, S_S) = S_{SD} + S_0(N_D) \tag{5.8}$$

where S_{SD} is the SRH recombination through surface defects as earlier described in (iii) while $S_0(N_D)$ is the doping-dependent SRH recombination. The latter, in case of SiO_2 / SiN_x passivation stack, can be parameterized for different surface doping (N_D) concentration as [59]:

$$S_0(N_D) = S_{ref} \frac{N_D}{N_{ref}} \tag{5.9}$$

where S_{ref} = 70 cm/s and N_{ref} = $7 \cdot 10^{17}$ cm^{-3} represent, respectively, the reference surface recombination velocity and doping concentration. The impact of S_{SD} on S_{eff} was numerically evaluated by using Equations (5.7) and (5.8) in case of NO-FSF, FSF_1 and FSF_2. The specifications of the FSF doping profiles used for the calculation of S_{eff} are summarized in Table 5.9 together with $S_0(N_D)$ and L_{FSF}, calculated by using Equation (5.9) and the calculator in [60], respectively. For simplicity, the doping profiles of the FSFs were assumed to be constant along its depth (i.e. W_{FSF}). This leads to an overestimation of the recombination rate and therefore lower L_{FSF} in the doped region compared to the case in which the real doping profile would be used. Such assumption might affect the absolute values of the calculated S_{eff} but it will not affect its dependence against S_{SD}. As Figure 5.13 shows, in case of NO-FSF there is no *high-low* junction formation and, assuming no field effect by the passivation stack, $S_{eff} = S_p$, making S_{eff} highly sensitive to any S_{SD} variation. When a FSF is employed, S_{eff} reveals two different behaviours with respect to S_{SD}: (1) $S_{SD} \ll S_0(N_D) \rightarrow S_p \approx S_0(N_D)$, thus S_{eff} is constant with S_{SD} for a given FSF doping concentration; (2) $S_{SD} \gg S_0(N_D) \rightarrow S_p \approx S_{SD}$ thus S_{eff} becomes dependent by S_{SD}. The crossing point between these two trends occurs at around $S_{SD} \approx$ 1000 cm/s. Even though the numerical model is based on simplified assumptions it is very useful to explain that FSF_2 results to be much less sensitive to possible variation of the S_{SD} rather than FSF_1 and NO-FSF, thus ensuring a better screening of high surface recombination velocities.

	N_D [cm^{-3}]	**W_{FSF} [nm]**	**$S_0(N_D)$ [cm/s]**	**L_{FSF} [nm]**
FSF_2	$2.0 \cdot 10^{19}$	$4.5 \cdot 10^{2}$	$2.0 \cdot 10^{3}$	$2.1 \cdot 10^{3}$
FSF_1	$1.5 \cdot 10^{18}$	$3.7 \cdot 10^{2}$	$1.5 \cdot 10^{3}$	$3.5 \cdot 10^{4}$

Table 5.9. Specifications of the FSF doping profile used for the calculation of S_{eff} together with $S_0(N_D)$ and L_{FSF}. The latter was carried out by taking into account latest recombination models using the calculator in [60].

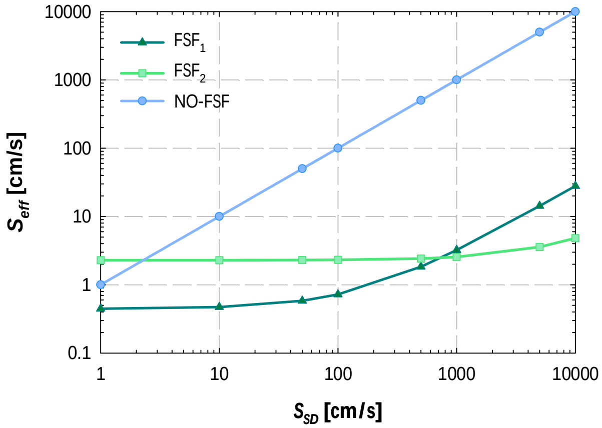

Figure 5.13. S_{eff} as function of S_{SD} for different FSF configurations. In case of NO-FSF $S_{eff} = S_p$. When a FSF is employed, two different behaviours can be identified: (1) $S_{SD} << S_0(N_D)$ -> $S_p \approx S_0(N_D)$; (2) $S_{SD} >> S_0(N_D)$ -> $S_p \approx S_{SD}$.

Finally, the identification of the main mechanism, responsible for the increase of surface defect density or bulk lifetime degradation, leading to poor carrier collection efficiency in case of no-FSF still needs to be identified. To this aim bulk lifetime measurements with *ideal* passivation layers should be carried out for the symmetrical samples with NO-FSF and for the one with FSF$_2$. For the latter, the FSF should be etched before the measurement in order to evaluate potential benefits from the gettering effect.

5.9 Roadmap for high conversion efficiency

The best fabricated IBC solar cell presented in this contribution exhibited a conversion efficiency of 20.2% mainly limited by V_{OC} and *FF*. Possible solutions to increase the *FF* without hindering the other external parameters would require numerical simulations to find optimal design rules of the rear geometry aiming to reduce the series resistance losses (i.e. pitch size metal coverage and thickness of the metal). In addition, the contact resistivity of the emitter region which was found to be one order of magnitude higher than the one on the BSF can be reduced by avoiding the decrease of the B doping concentration on the emitter surface. This can be achieved either by protecting the emitter with SiN_x or A_2lO_3 during the oxidation process or by etching back the first few tens of nanometers of the emitter after the thermal SiO_2. To enhance V_{OC}, J_{0s} for textured surfaces and at contact need to be reduced. To reduce front side J_{0s}, the development of more advanced cleaning procedure and FSF of the front side is required. To reduce contact recombination, local point contacts needs to be designed by using computer aided simulations in order to avoid substantial increase of the series resistance. Opto-electrical simulations performed in our group (not reported here), have shown that by optimizing all abovementioned aspects the proposed process can be used to fabricate industrially scalable IBC devices with conversion efficiencies well beyond 22%.

5.9.1 Optimization of implanted FSF

As shown in Section 5.8.3, the highest carrier collection at cell level was achieved using FSF_2 solution as front side passivation. As stated in Section 5.8.3, the FSF needs to be further optimized in order to enhance V_{OC} while still keeping high carrier collection efficiency. In this section, the impact of the implantation energy (E) on the τ_{eff} of symmetrically textured, doped and passivated with SiO_2 / SiN_x samples has been investigated. For this experiment the D of the P implantation was kept constant at $5\cdot10^{14}$ cm^{-2} (same dose as FSF_2) while the E was varied between: 10, 15 and 20 keV, see Table 5.10. As clearly reported in Figure 5.14, decreasing the implantation E from 20 to 15 keV a significant increase of the τ_{eff} was measured. Moreover, even higher τ_{eff} were reached when using 10 keV as E. To explain such result a deeper understanding of the physical mechanism behind the implantation process is required. In general, after ion implantation an amorphized region is created [61][62]. Typically, such region recrystallizes by solid phase epitaxial regrowth (SPER) at the onset of thermal annealing. Deeper than the amorphized region, the implantation process also creates a region with high concentration of point defects as: silicon self-interstitials (I) and vacancies (V) [61] [63] [64]. During the thermal treatment, these point defects can recombine or diffuse to the surface or form larger clusters of defects, or dislocation loops [65]. By using a proper thermal annealing (i.e. temperature and time of the annealing), these clusters dissolve again into point defects, which diffuse towards the wafer surface and recombine. The result reported in Figure 5.14 clearly indicates that the annealing process used in this work (T = 850 °C for 90 min) is more capable to recrystallize and reduce Si lattice damage after implantation only if $E \leq 15$ keV is used. In addition, as shown in Table 5.10, the $R_{\square}$ of the studied samples was found to be slightly sensitive to the E implantation while $J_{0s\ text}$ and $i\text{-}V_{OC}$ were found to significantly improve when decreasing the E. Finally, $i\text{-}V_{OC}$ of 680 mV where achieved when using $D = 5\cdot10^{14}$ cm^{-2} and E = 10 keV. The usage of such doping conditions in the IBC device would allow increasing its V_{OC} without degrading the carrier collection efficiency and therefore J_{SC}.

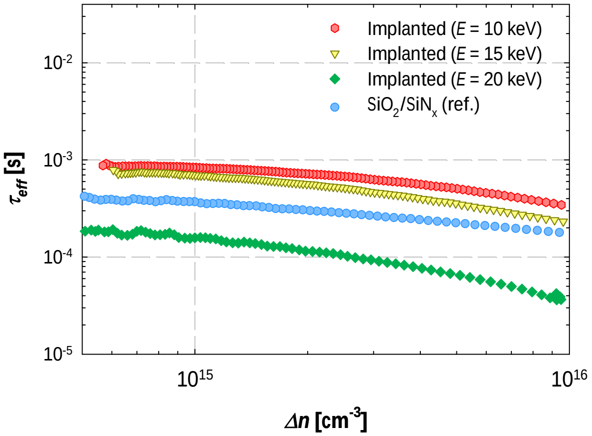

Figure 5.14. Measured $\tau_{eff}(\Delta n)$ of three symmetric samples: textured c-Si wafer / doped layer fabricated via implantation of P-ions (with same $D = 5{\cdot}10^{14}$ cm^{-2} and variable E) followed by annealing / oxidation at 850 °C in O_2 and PECVD SiN_x at 400 °C. As the figure shows, already by decreasing the implantation E from 20 to 15 keV, it is possible to achieve higher values of $\tau_{eff}(\Delta n)$ compared to the non-implanted sample. Highest $\tau_{eff}(\Delta n)$ are reached by using 10 keV as implantation energy.

E [keV]	D [cm^{-2}]	$R_\square$ (n+ Implanted) [Ω/sq.]	$J_{0s\ text}$ [fA/cm^2]	$i\text{-}V_{OC}$ [mV]
-	-	Non-implanted	48 ± 6	671
10	$5{\cdot}10^{14}$	258	30	680
15	$5{\cdot}10^{14}$	236	50	670
20	$5{\cdot}10^{15}$	250	120 ± 5	651

Table 5.10. Impact of the of the E of the P-ion implantation on the measured $R_\square$, $J_{0s\ text}$ and $i\text{-}V_{OC}$. J_{0s}, $i\text{-}V_{OC}$ and for non-implanted sample is also reported for reference purposes. The $R_\square$ appered to be sliglty affected by the implantation E. A sensitive decrease of $J_{0s\ text}$ was measured when decreasing implantation E from 20 to 10 keV. $i\text{-}V_{OC}$ of 680 mV and $J_{0s\ text}$ of 30 fA were achieved by using implantation energy of 10 keV.

5.10 Conclusions

In this Chapter a novel self-aligned process for IBC c-Si solar cells based on single-side and (relatively) low-temperature doping techniques (< 900 °C) was presented. To keep the process more industrially scalable special attention was paid to the number of lithographic steps and to the thermal budget. In particular, the proposed process is based on the combination of single-side doping techniques (epitaxial growth of in-situ B-doped Si to form the emitter and implantation of P-ions to create FSF and BSF with different doping profiles) followed by co-annealing and oxidation at 850 °C. The impact of the FSF and rear geometry on the solar cells performance has been investigated. FSF$_2$

showed the highest collection efficiency due to higher stability against possible increase of the surface recombination rate and bulk lifetime contamination induced during the fabrication process. As expected, the BSF_f and its electrical shading losses showed to have a major role on the carrier collection efficiency. Highest carrier collection and thus J_{SC} were reached using FSF_2 and a BSF_f of 20%. In such case, IBC c-Si solar cell based on the low temperature self-aligned process with a value of 41 mA/cm^2 and an overall cell efficiency of 20.2% was demonstrated.

5.11 References

[1] International technology roadmap for photovolatiac (ITRPV), edition 2014, available: http://www.itrpv.net/Reports/Downloads/2015.

[2] S. W. Glunz, Crystalline Silicon Solar Cells with High Efficiency, in Advanced concepts in photovoltaics, The Royal Society of Chemistry, 2014, pp. 1-29, DOI: 10.1039/9781849739955-00001.

[3] A. Ingenito, O. Isabella, M. Zeman, Accurate opto-electrical modeling of multi-crystalline silicon wafer-based solar cells, Sol. Energ. Mat. Sol., 123, 2014, 17-29, http://dx.doi.org/10.1016/j.solmat.2013.12.019

[4] D. Smith, P. Cousins, S. Westerberg, R. Jesus-Tabajonda, G. Aniero, Y. Shen. "Towards the Practical Limits of Silicon Solar Cells," Photovoltaics, IEEE Journal of. 2014, 4, 6,1465- 1469.

[5] Press release BOSCH Solar Energy. Available: http://www.solarserver.com/solar-magazine/solar-news/archive-2013/2013/kw33/bosch-isfh-produce-221-efficient-c-si-solar-pv-cell.html, 2013.

[6] C.B. Mo, S.J. Park, Y.J. Kim, D.Y. Lee, S.C. Park, D.S. Kim, S.B. Kim, J. Graff. Sheoran M, P.Sullivan. Presentation at: 27th. Eur. Photovoltaic Sol. Energy Conf., Munich, 2012.

[7] Halm A, Mihailetchi V, Galbiati G, Koduvelikulathu L, Roescu R, Comparotto C, Kopecek R, Peter K, Libal J. The Zebra Cell Concept – large Area n-type Interdigitated Back Contact Solar Cells and One-Cell Modules Fabricated Using Standard Industrial Processing Equipment. Proc. 27nd Eur. Photovoltaic Sol. Energy Conf., Frankfurt, 2012; 567–570.

[8] E. Franklin, K. Fong, K. McIntosh, A. Fell, A. Blakers, T. Kho, D. Walter, D. Wang, N. Zin, M. Stocks, E.-C.Wang, N. Grant, Y. Wan, Y. Yang, X. Zhang, Z. Feng, P. J. Verlinden. Design, fabrication and characterisation of a 24.4% efficient interdigitated back contact solar cell, Progr. Photovoltaics: Res. Appl., 2014, DOI: 10.1002/pip.2556

[9] M. Aleman, J. Das , T. Janssens, B. Pawlak, N. Posthuma, J. Robbelein, S. Singh, K. Baert, J. Poortmans, J. Fernandez, K. Yoshikawa, P.J. Verlinden.

Development and Integration of a High Efficiency Baseline Leading to 23% IBC Cells, Energy Procedia, 2012, 27, 638–645.

[10] C. Reichel, F. Granek, M. Hermle, S. Glunz, Back-contacted back-junction n-type silicon solar cells featuring an insulating thin film for decoupling charge carrier collection and metallization geometry, Progr. Photovoltaics: Res. Appl. 2013, 21, 1063–1076.

[11] R. Peibst, N.P. Harder, A. Merkle, T. Neubert, S. Kirstein, J. Schmidt, F. Dross, P.A. Basore, R. Brendel, High-efficiency RISE IBC solar cells: influence of rear side passivation on pn junction meander recombination Proc. 28nd Eur. Photovoltaic Sol. Energy Conf., Paris, 2013.

[12] A. Ingenito, O. Isabella, M. Zeman, Experimental Demonstration of 4n2 Classical Absorption Limit in Nanotextured Ultrathin Solar Cells with Dielectric Omnidirectional Back Reflector, ACS Photonics, 2014 1, 3.

[13] R. Brendel, Introduction, in Thin-Film Crystalline Silicon Solar Cells: Physics and Technology, Wiley-VCH Verlag GmbH & Co. KGaA, Weinheim, FRG, 2003.

[14] A. Ingenito, O. Isabella, M. Zeman, Nano-cones on micro-pyramids: modulated surface textures for maximal spectral response and high-efficiency solar cells, Progress in Photovoltaics: Research and application, 2015, 23,11 DOI: 10.1002/pip.2606.

[15] H. Savin, P. Repo, G. Gastrow, P. Ortega, E. Calle, M. Garín, R. Alcubilla, Black silicon solar cells with interdigitated back-contacts achieve 22.1% efficiency, Nat Nano, 2015, 10, 7, 624 – 628, DOI: 10.1038/nnano.2015.89.

[16] M. Hermle, F. Granek, O. Schultz-Wittmann, S.W. Glunz, Shading effects in back-junction back-contacted silicon solar cells, in Proc. of the 33rd IEEE Photovoltaic Specialists Conf.2008, San Diego, USA, 4, 1, 11-14.

[17] C. Reichel, F. Granek, M. Hermle, S. Glunz, Investigation of electrical shading effects in back-contacted back-junction silicon solar cells using the two dimensional charge collection probability and the reciprocity theorem, J. Appl. Phys.2011, 109.

[18] S. W. Glunz, F. Feldmann, A. Richter, M. Bivour, C. Reichel, J. Benick, M. Hermle, The Irresistible Charm of a Simple Current Flow Pattern – Approaching 25% with a Solar Cell Featuring a Full-Area Back Contact, 31st European Photovoltaic Solar Energy Conference and exhibition, Hamburg, Germany, (2015).

[19] F. Granek, C. Reichel, M. Hermle, D. M. Huljic, O. Schultz, S. W. Glunz, Front surface passivation of n-type high-efficiency backjunction silicon solar cells using front surface field, in Proc. 22nd Eur. Photovoltaic Sol. Energy Conf., Milan, Italy, 2007, 1262–1265.

[20] I. Cesar, N. Guillevin, A. R. Burgers, A. A. Mewe, M. Koppes, J. Anker, L.J. Geerligs, A. W. Weeber, Mercury: A Back Junction Back Contact Front Floating Emitter Cell with Novel Design for High Efficiency and Simplified Processing, Energy Procedia. 2014, 55, 633-642.

[21] K. R. McIntosh, M. J. Cudzinovic, D. D. Smith, W. P. Mulligan, and R. M. Swanson, The choice of silicon wafer for the production of low-cost rear-contact solar cells, in Proc. 3rd World Conf. Photovoltaic Energy Convers. Conf., Osaka, Japan, 2003, 971–974.

[22] S. A. McHugo, H. Hieslmair, E.R. Weber, Gettering of metallic impurities in photovoltaic silicon Appl. Phys. A Mater. Sci. 1997, 64, 127–137.

[23] S. W. Glunz, S. Rein, S. J. Y. Lee, W. Warta, Minority carrier lifetime degradation in boron-doped Czochralski silicon, Journal of Applied Physics. 2001, 90, 2397-2404, DOI: http://dx.doi.org/10.1063/1.1389076.

[24] M. Taguchi, A. Yano, S. Tohoda, K. Matsuyama, Y. Nakamura, T. Nishiwaki, K. Fujita, E. Maruyama, 24.7% Record Efficiency HIT Solar Cell on Thin Silicon Wafer, Photovoltaics, IEEE Journal of. 2014, 4, 1, 96-99.

[25] F. Feldmann, M. Simon, M. Bivour, C. Reichel, M. Hermle, S. W. Glunz, Efficient carrier-selective p- and n-contacts for Si solar cells, Sol. Energy Mater. Sol. Cells.2014, 131, 100–104.

[26] C. Reichel, F. Granek, M. Hermle, S. W. Glunz, Back-contacted back-junction n-type silicon solar cells featuring an insulating thin film for decoupling charge carrier collection and metallization geometry, Progr. Photovoltaics: Res. Appl. 2013, 21, 1063–1076.

[27] K. Masuko, M. Shigematsu, T. Hashiguchi, D. Fujishima, M. Kai, N. Yoshimura, T. Yamaguchi, Y. Ichihashi, T. Mishima, N. Matsubara, T. Yamanishi, T. Takahama, M. Taguchi, E. Maruyama, S. Okamoto, Achievement of more than 25% conversion efficiency with crystalline silicon heterojunction solar cell, Photovoltaics, IEEE Journal of. 2014, 4, 6, 1433-1435, DOI: 10.1109/JPHOTOV.2014.2352151

[28] J. Nakamura, H. Katayama, N. Koide, K. Nakamura, Development of Hetero-Junction Back Contact Si Solar Cells, in Photovoltaic Specialists Conference (PVSC), 2012 38th IEEE, 001023-001025, 3-8 June 2012, DOI: 10.1109/PVSC.2012.6317776

[29] M. G. Kang, J.-H. Lee, H. Boo, S. J. Tark, H. C. Hwang, W. J. Hwang, H. O. Kang, D. Kim, Effects of annealing on ion-implanted Si for interdigitated back contact solar cell, Current Applied Physics. 2012, 12, 6, 1615-1618.

[30] Y.-W. Ok, A. D. Upadhyaya, Y. Tao, F. Zimbardi, K. Ryu, M.-H. Kang, A. Rohatgi. Ion-implanted and screen-printed large area 20% efficient N-type front junction Si solar cells, Solar Energy Materials and Solar Cells. 2014, 123, 92-96.

[31] M. A. Kessler, T. Ohrdes, B. Wolpensinger, R. Bock, N.-P. Harder, Characterisation and implications of the boron rich layer resulting from open-tube liquid source BBR3 boron diffusion processes, in Photovoltaic Specialists Conference (PVSC), 2009 34th IEEE, 001556-001561, 7-12 June 2009, DOI: 10.1109/PVSC.2009.5411365.

[32] P. J. Cousins, Cotter, E. Jeffrey, The influence of diffusion-induced dislocations on high efficiency silicon solar cells, in Electron Devices, IEEE Transactions on. 2006 , 53, 3, 457-464, DOI: 10.1109/TED.2005.863535.

[33] R. Keding, D. Stüwe, M. Kamp, C. Reichel, A. Wolf, R. Woehl, D. Borchert, H. Reinecke, D. Biro, Co-Diffused Back-Contact Back-Junction Silicon Solar Cells without Gap Regions, in IEEE Journal of Photovoltaics, 3, 4, 1236-1242, 2013.

[34] M. Hermle, F. Granek, O. Schultz, S. W. Glunz, Analyzing the effects of front-surface fields on back-junction silicon solar cells using the charge-collection probability and the reciprocity theorem, J. Appl. Phys. 2008, 103, 5, 054507-1–054507-7.

[35] F. Granek, M. Hermle, D. M. Hulijc, O. Schultz-Wittmann, S. W. Glunz, Enhanced lateral current transport via the front n+ diffused layer of n-type high-efficiency back-junction back-contact silicon solar cells, Progr. Photovoltaics: Res. Appl. 2009, 17, 1, 47–56.

[36] Z. C. Holman, M. Filipič, B. Lipovšek, S. De Wolf, F. Smole, M. Topič, C. Ballif, Parasitic absorption in the rear reflector of a silicon solar cell: Simulation and measurement of the sub-bandgap reflectance for common dielectric/metal reflectors, Sol. Energ. Mat. Sol. 2014, 120, 426-430.

[37] J. Nijs, F. Dhoore, R. Mertens, R. van Overstraeten, Lift-off: A very fine front metallization geometry technique for high efficiency solar cells, ESA Photovoltaic Generators in Space. 1982, 37-42.

[38] R. A. Sinton, A. Cuevas, Contactless determination of current-voltage characteristics and minority-carrier lifetimes in semiconductors from quasi-steady-state photoconductance data, Appl. Phys. Lett. 1996, 69, 17, 2510–2512, 1996.

[39] D. K. Schroder, Semiconductor Material and Device Characterization, Wiley, New York, 1990.

[40] A. B. Sproul, Dimensionless solution of the equation describing the effect of surface recombination on carrier decay in semiconductors. Applied Physics Letters. 1994, 76 ,5 , 2851-2854.

[41] F. Granek, High-efficiency back-contact back-junction silicon solar cells. PhD thesis, Fraunhofer Institute für Solare Energie systeme, Freiburg im Breisgau, 2009.

[42] E. Kane, R.M. Swanson. Measurement of the Emitter Saturation Current by a Contactless Photoconductivity Decay Method, Proc of the 18th IEEE Photovoltaic Specialists Conference. 1985, 578-583.

[43] M.B. Spitzer, S.P. Tobin, C.J. Keavney, High-efficiency ion-implanted silicon solar cells. IEEE Trans. Electron Dev. 1984, 31, 546-50.

[44] A. Rohatgi, D. L. Meier, B. Mcpherson, Y.-W. Ok, A. D Upadhyaya, J.-H. Lai, and F. Zimbardi, High-Throughput Ion Implantation for Low-Cost High-Efficiency Silicon Solar Cells, Energy Procedia. 2012, 15, 10-19.

[45] P.R. Younger, S. N. Bunker, Ion implantation processing for high performance concentrator solar cells and cell assemblies, Solar Cells. 1982; 6, 79-86.

[46] A. Gupta, R.J. Low, N. Bateman, D. Ramappa, H.J.L. Gossman, Q. Zhai, P. Sullivan, W. Skinner, C. Dube, B. Tsefrekas, J. Mullin. High efficiency selective emitter cells using in-situ patterned ion implantation. Proc. 25th European Photovoltaic Solar Energy Conf., Valencia, Spain, 2010, 1158-62.

[47] T.S. Ravi, R. Hao. Silicon Wafers with p-n Junctions by Epitaxial Deposition and Devices Fabricated Therefrom, http://www.google.com/patents/US20150040979.

[48] E.K. Schmich. High-temperature CVD processes for crystalline silicon thin-film and wafer solar cells. Doctoral dissertation, 2008. Available on: http:// nbn-resolving.de/urn:nbn:de:bsz:352-opus-65498.

[49] M. R. Payo, N. Posthuma, A. U. de Castro, M. Debucquoy, J. Poortmans. Boron-doped selective silicon epitaxy: high efficiency and process simplification in interdigitated back contact cells, Progr. Photovoltaics: Res. Appl. 2014, 22, 7, 711–725.

[50] B. E. Deal, M. Sklar, Thermal Oxidation of Heavily Doped Silicon J. Electrochem. Soc. 1965, 112, 4, 430-435, DOI: 10.1149/1.2423562

[51] E. A. Lewis, E. A. Irene, The effect of surface orientation on silicon oxidation kinetics. Journal of the Electrochemical Society. 1987, 134, 9, 2332-2339.

[52] A. Richter, S. W. Glunz, F. Werner, J. Schmidt, A. Cuevas, Improved quantitative description of Auger recombination in crystalline silicon, Physical review B. 2012, 86, 165202, DOI: 10.1103/PhysRevB.86.165202.

[53] J. W. Colby, L. E. Katz, Boron Segregation at Si-SiO_2 Interface as a Function of Temperature and Orientation , J. Electrochem. Soc. 1976, 123, 3, 409-412.

[54] R.A. Sinton, A. Cuevas, A Quasi-Steady-State Open-Circuit Voltage Method for Solar Cell Characterization, in Proc. 16nd Eur. Photovoltaic Sol. Energy Conf., Glasgow, 2000.

[55] A. Fell, A free and fast three-dimensional/two-dimensional solar cell simulator featuring conductive boundary and quasi-neutrality approximations, IEEE Transactions on Electron Devices. 2013, 60, 733–738.

[56] V. Vähänissi, A. Haarahiltunen, M. Yli-Koski, H. Savin, Gettering of Iron in Silicon Solar Cells With Implanted Emitters. IEEE Journal of Photovoltaics., 2014, 4, 1. 142-147, DOI: 10.1109/jphotov.2013.2285961.

[57] A. Cuevas, The Recombination Parameter J0, Energy Procedia. 2014, 55, 53-62.

[58] M. P. Godlewski, C. R. Baraona, H. W. Brandhorst, Low-high junction theory applied to solar cells," in Proc. 10th IEEE Photovoltaic Spec. Conf., Paolo Alto, CA. 1973, 40–49.

[59] A. Cuevas, P. A. Basore, G. Giroult-Matlakowski, C. Dubois, Surface recombination velocity of highly doped n-type silicon, J. Appl. Phys. 1996, 80, 6, 3370–3375.

[60] http://www.pvlighthouse.com.au/calculators/Recombination%20calculator/Recombination%20calculator.aspx.

[61] N. E. B. Cowern, , G. Mannino, P. A. Stolk, F. Roozeboom, H. G. A. Huizing, J. G. M. van Berkum, F. Cristiano, A. Claverie, and M. Jaraız, Energetics of Self-Interstitial Clusters in Si, Phys. Rev. Lett. 1999, 82, 4460.

[62] S.U. Campisano, S. Coffa, V. Raineri, F. Priolo, E. Rimini, Mechanisms of amorphization in ion implanted crystalline silicon, Nuclear Instruments and Methods in Physics Research Section B: Beam Interactions with Materials and Atoms. 1993, 80–81, 1, 514-518, ISSN 0168-583X.

[63] J. D. Desroches, Defect Evolution and Transient Enhanced Diffusion in Sub-Amorphous Phosphorus Implanted Silicon, Master's thesis, University of Florida, 1997.

[64] T. Ohrdes, S. Steingrube, H. Wagner, C. Zechner, G. Letay, R. Chen, S.T. Dunham, P.P. Altermatt, Solar cell emitter design with PV-tailored implantation, Energy Procedia. 2011, 8, 167-173, ISSN 1876-6102, http://dx.doi.org/10.1016/j.egypro.2011.06.119.

[65] F. Cristiano, B. Colombeau, B., Mauduit, C. Bonafos, G. Benassayag, A. Claverie, Thermal Evolution of Extrinsic Defects in Ion Implanted Silicon: Current Understanding and Modelling. Mat. Res. Soc. Symp. Proc. 717. Silicon Front-End Junction Formation Technologies. 2002, C5.7.1–C5.7.12.

6

Nano-cones on micro-pyramids: Modulated surface textures for maximal spectral response and high efficiency solar cells

6.1 Abstract

The front-side reflection of state-of-the-art random textured surfaces coated with antireflection coating contributes to 5% of its total photo-generated current density (measured for 280-μm thick wafer). One way to minimize front reflection optical losses of c-Si solar cells is to nano-textured surfaces. Although nano-textured surfaces have shown a broad-band anti-reflective effect, their light scattering and surface passivation properties are found to be generally worse than those of standard micro-textured surfaces. To overcome these limitations in crystalline silicon solar cells, advanced texturing and passivation approaches are presented in this chapter. Modulated surface textures, which superimposes nano-cones on micro-pyramidal surface texture are applied at the front side of crystalline silicon wafers to reduce reflection below 1% in a broad wavelength range from 300 nm up to 1000 nm and efficiently scatters light up to 1200 nm. To reach high charge-carrier collection efficiency a method to minimize recombination at nano-textured surfaces is shown, which uses defect-removal etching followed by dry thermal oxidation. These two approaches are here applied to interdigitated back contacted crystalline silicon solar cell. The device exhibits a conversion efficiency equal to 19.8%, record external quantum efficiency (78%) at short wavelengths (300 nm), and electrical performance equal to the performance of the reference interdigitated back contacted device based on front-side micro-pyramids.

This Chapter is based on the following publication: A. Ingenito, O. Isabella, M. Zeman - Progress in Photovoltaics: Research and Applications, 23, 11, 1649-1659, 2015, DOI: 10.1002/pip.2606.

6.2 Introduction

Long before mankind began to explore systems for dewetting or light manipulation, nature had already developed for these purposes sophisticated nano-structures on the surface of leafs, feathers and cuticles [1]-[4]. In particular, the superposition of surface textures with different vertical and lateral dimensions like in case of *Euphorbia myrsinites* leafs [1] is a useful approach for designing surfaces with different functionalities [5]. Focusing on optical devices and more specifically on solar cells, this approach can be deployed to improve the light trapping in the absorber and consequently increase the solar cell conversion efficiency. In fact, the major optical losses of a solar cell are related to front-side reflection and low photon absorption in the spectral region of weak absorption. To decrease these optical losses in mono-crystalline silicon (c-Si) solar cells, surface texturing with features size between 5 and 10 µm based on alkaline etching is widely used. This is a standard production process adopted by the photovoltaic (PV) industry for decades due to its cost-effective performance gain based on light trapping [6]. Although surface micro-texturing leads to a nearly Lambertian scattering [6], it does not completely suppress reflection losses [7]. Therefore, single or multiple anti-reflection coatings (ARCs) are applied to further minimize the reflection [8]. However, a single ARC layer with a thickness optimized on a quarter wavelength approach performs well only in a limited spectral range. Multilayer ARCs can enhance light in coupling and therefore efficiency at cell level, however such gain is mostly lost after module encapsulation. In this respect, nano-texturing is a potential candidate for providing a broad-band anti-reflective effect even without ARC. Several techniques such as metal-assisted etching (MAE) [9][10], laser modification and reactive ion etching (RIE) [11]-[13] can be used to obtain nano-texturing with feature sizes smaller than the wavelength corresponding to the band gap of c-Si ($\lambda_{Si} \approx 1100$ nm) [11]. With these geometrical dimensions, light is efficiently in-coupled at the front surface. In other words, when passing from air to c-Si the incident light experiences a gradual change of the refractive index which leads to a strong light in-coupling and thus minimizes surface R [15][16]. The drawback of the nano-textured surface is that it alone does not necessarily provide Lambertian scattering, as demonstrated in Chapter 4 and [17]. Lambertian angular intensity distribution of light scattered at the randomly textured interface is one of the requirements to enhance light absorption in a thin semiconductor slab in the weak absorption region by $4n^2$, where n is the refractive index of the semiconductor [19]. Nano-texture (n-T) at the front side (FS) of a thin (< 30 µm) c-Si slab, only when combined with a micro-texture (µ-T) at the back side (BS), resulted in enhanced absorption that reached more than 98% of the one predicted by $4n^2$ enhancement factor [17]. This result pointed out that the combination of nano- and micro-texturing can provide both the ideal light in-coupling and light scattering needed to enhance light absorption in a broad wavelength range from the ultra-violet (UV) to the infrared (IR) spectral range.

Nano-texturing, despite improving the optical properties of a solar cell, increases the surface recombination which is responsible for poor collection efficiency of the photo-generated carriers [20]. A possible solution for decreasing surface recombination is a wet chemical etching of the nano-textured surface which leads to a reduction of the surface area. This approach was recently used to fabricate a c-Si solar cell with MAE nano-texturing with conversion efficiency of 18.2 % [21]. More recently cryogenic reactive ion etching has been used to fabricate interdigitated back contacted (IBC) solar cells with efficiency of 22.1% [22]. Such type of etching is defects-free compared with standard RIE but it is not suitable for large scale applications. Another possible way to reduce surface recombination by decreasing the surface area is to combine low density nano-textured with micro-textured surfaces [23]. Using this approach, c-Si solar cells with conversion efficiency of 17.1% were fabricated exhibiting low reflection and improved blue response. The superposition of textures with different vertical and horizontal geometrical dimensions is known in the PV field as modulated surface texture (MST) concept [24]. In this Chapter Advanced light trapping and passivation approaches are demonstrated and applied in a c-Si IBC solar device. A mask-less RIE process was used to fabricate nano-cones on c-Si wafers and their opto-electrical properties were analysed. To achieve a reasonable passivation of the nano-texture, a chemical defect-removal etching (DRE) followed by a dry thermal oxidation was developed. Such approach is more cost effective than the cryogenic RIE. In addition, it can be applied to all type of nano-textured devices where low recombination rate is instrumental, such as Si-based nanowire solar cells [26][27], photo-electro-chemical cells for water splitting and lithium-ion batteries [28]. Afterwards, a novel light trapping scheme was based on the superposition of nano-cones on micro-pyramids resembling the natural structure of leaves of *Euphorbia myrsinites*. The designed trapping scheme resulted in a higher light absorption than in case of standard FS micro-texturing over the whole wavelength range of interest (300 – 1200 nm). Finally, an IBC solar cell with MST at FS based on a self-aligned and low temperature process was fabricated. The c-Si IBC solar cell with MST at FS exhibited reflection below 1.5% from 300 nm to λ_{Si} and the same open-circuit voltage (V_{OC}) and Fill Factor (*FF*) compared to a reference IBC solar cell with the standard micro-texturing at FS. In addition the MST device exhibited a very high blue response close to 80% at 300 nm and a conversion efficiency of 19.8%.

6.3 Fabrication and characterization

For the processes described in this section, 4-inch FZ n-type c-Si wafers with initial thickness of 285 ± 25 µm, resistivity of 1-5 Ωcm and bulk lifetime larger than 2 ms were used. The front texturing formed by nano-cones was carried out by means of RIE using a gaseous mixture of SF_6 and O_2 (as described in Section 4.3 of Chapter 4) while the texturing formed by micro-pyramids was obtained by wet alkaline etching in mixture of TMAH and isopropyl alcohol (IPA) at 80 °C.

6.3.1 Fabrication of advanced passivation scheme

After RIE for fabricating nano-cones, standard cleaning, rinsing in deionised H_2O (DIW) and drying of the substrates, the DRE was applied. This process consists of tetramethylammonium hydroxide (TMAH) 1%-diluted in H_2O at room temperature for different etching times (0, 15, 30, 45 and 60 seconds). For each etching time four samples were processed. Such etching was followed by cleaning, DIW rinsing and drying. All samples were oxidized in dry ambient at 1050 °C for 20 minutes leading to a SiO_2 thickness of 30 ± 5 nm. The SiO_2 was also grown on five double side polished (DSP) wafers and three double side micro-textured wafers used throughout this work as reference sample.

6.3.2 Fabrication of advanced light trapping scheme

The wafers with advanced light trapping scheme were endowed with MST at FS and had flat BS. MSTs were fabricated by superposing nano-cones on micro-pyramids. As reference samples wafers with micro-pyramids at FS and polished BS were also fabricated. In both cases, a layer of 200-nm thick SiN was deposited on the BS as a protection barrier during the alkaline etching producing the micro-texturing. Such SiN_x layer, which was deposited with radio-frequency plasma-enhanced chemical vapour deposition (RF-PECVD) was subsequently etched away in buffered-HF after texturing the wafer at FS.

6.3.3 Fabrication of IBC solar cells

A boron-doped emitter with $R_\square$ equal to 44 Ω/ □ was full-area deposited on flat BS by epitaxial growth in an ASM Epsilon 2000 reactor. Instead, both back surface field (BSF) and front surface field (FSF) were formed via phosphorous implantation. To define BSF and emitter at BS, the self-aligned process described in Chapter 5 was used. The process involved one lithographic step to etch back the emitter layer from the region where the BSF would be allocated. The design and fabrication of the self-aligned process is described in Chapter 5. As shown in Chapter 5, the optimal BS emitter coverage was 80% for a pitch size of 1 mm. Oxidation and annealing were carried out in a dry ambient at 850 °C for 90 minutes leading to a $R_\square$ equal to 69 Ω/□ for the BSF and 250 Ω/□ for the FSF. The SiO_2 thickness was found to be dependent on both doping types (B or P) and concentrations. In particular, the annealing step lead to 40 ± 2-nm thick SiO_2 layer on the BSF region (heavily doped) and 20 ± 3-nm thick on the FSF (lightly doped) were measured. A 15-nm thick SiO_2 layer was instead measured on the emitter. In case of micro-textured FS, 45-nm thick SiN_x layers were deposited on both sides of the wafer by using RF-PECVD at 400 °C. The stack SiO_2/SiN_x at BS was patterned by using a second photolithographic step followed by wet etching in HF 12.5% diluted in H_2O. Physical vapour deposition of 2-µm thick Al was performed in a Provac PRO500S machine. Metal fingers were defined by lift-off of stack photoresist/Al in acetone.

6.3.4 Samples characterization

Quasi steady-state photo-conductance (QSSPC) method was used by means of Sinton WCT-120 to measure the effective minority carrier lifetime (τ_{eff}) [30]. Scanning electron microscopy (SEM) was facilitated with Philips XL-50 for the visual investigation of the surface textures and the thickness of fabricated IBC c-Si solar cells. Transmission electron microscope (TEM) analysis was performed at Technische Universiteit Eindhoven by using JOL-ARM 200F tool. Thicknesses of SiO_2 and SiN_x layers were extracted from ellipsometry spectra using J. A. Wollam CO. M-2000DI spectroscopic ellipsometer on DSP samples. Wavelength-dependent reflectance (*R*) and transmittance (*T*) were measured using the integrating sphere accessory mounted on a Perkin-Elmer Lambda 950 spectrophotometer in the wavelength range between 300 nm and 1200 nm. Wavelength dependent silicon absorptance (A_{Si}) was calculated as *1-R-T*. The characterization set-up for the J-V and EQE was described in Section 5.6 of Chapter 5.

6.4 Results and discussion

6.4.1 Advanced passivation scheme of nano-cones by using DRE and SiO_2

SEM pictures of the nano-textured samples before and after DRE are shown in Figure 6.1 (a)-(e). The as-fabricated nano-textured (no DRE) shows features with conical shape and geometrical dimensions below 1 µm (nano-cones). Application of wet etching after RIE resulted in smoother surfaces with rounded and merged nano-cones. In Figure 6.1 (a)-(e) the enlargement area is also reported. This quantity is defined as A^F/A_{Proj}, where A^F is the front effective area of the nano-texture and A_{Proj} is the flat projected area.

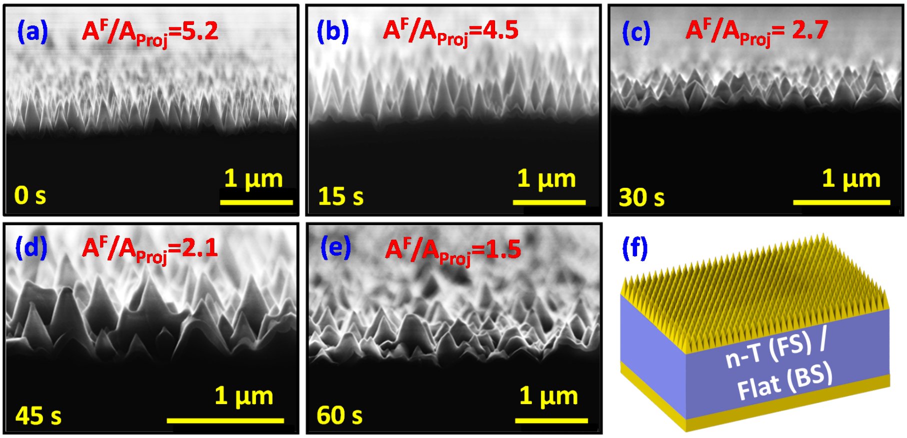

Figure 6.1 (a)-(e) Cross sectional SEM of FS n-T fabricated via RIE after 0, 15, 30, 45 and 60 seconds of DRE coated with 40-nm thick dry thermal SiO_2, respectively. In (f) a sketch of the wafer with n-T at FS and polished BS coated with ~30 nm thick dry thermal SiO_2 is reported.

In order to evaluate the impact of wet etching on the electrical passivation, the effective minority carrier lifetime τ_{eff} was measured for all samples that were processed by wet etching and coated on both sides with SiO_2. In Figure 6.1 (f) the sketch of a typical measured sample is depicted. To calculate the front surface recombination velocity (S_{eff}^F) from the measured effective lifetime (τ_{eff}), the general solution of the second order differential equation was used, which describes the carrier decay as shown by Sproul [31]. In case of high-quality (i.e. bulk lifetime > 2 ms) and symmetrical samples (see Figure 6.2(a) and (b)), $S_{eff}^F = S_{eff}^B$, where S_{eff}^B is the back surface recombination velocity, the general solution reported in [31] can be approximated as $S_{eff}^F = S_{eff}^B \approx d/2\tau_{eff}$, where *d* is the wafer thickness and τ_{eff} is the measured minority carrier lifetime at injection level Δn = 10^{15} cm^{-3}. In case of asymmetrical samples (see Figure 6.2 (c)), $S_{eff}^F \neq S_{eff}^B$. Therefore S_{eff}^F should be extracted by graphically solving the solution in [31] for the assigned τ_{eff} and assuming, $S_{eff}^B = S_{DSP}$. For the samples studied in this work, no difference was observed between the S_{eff}^F extracted by graphically solving the solution proposed in [31] and the one predicted by using the following approximated equation [32]:

$$\frac{1}{\tau_{eff}} \approx \frac{d}{S_{eff}^B + S_{eff}^F} + \frac{1}{D}\left(\frac{2d}{\pi}\right)^2 \qquad 6.1$$

where, *D* is the diffusion constant of the excess carriers. The S_{eff}^{F} as function of the ratio A^F/A_{Proj} or DRE time is reported in Figure 6.2 (d). According to the model presented by Oh et al.[21], S_{eff}^{F} and A^F/A_{Proj} are related as follows:

$$S_{eff}^{F} = \frac{A^F}{A_{Proj}} S_{loc}^{F} \qquad 6.2$$

where S_{loc}^{F} is defined as the effective local front surface recombination velocity and does not account for the surface area enhancement. Therefore, this quantity includes all recombination mechanisms that may occur on the surface. To analyse the dependence of S_{eff}^{F} as function of A^F/A_{Proj} thermal SiO_2 was used because it has low density of fixed

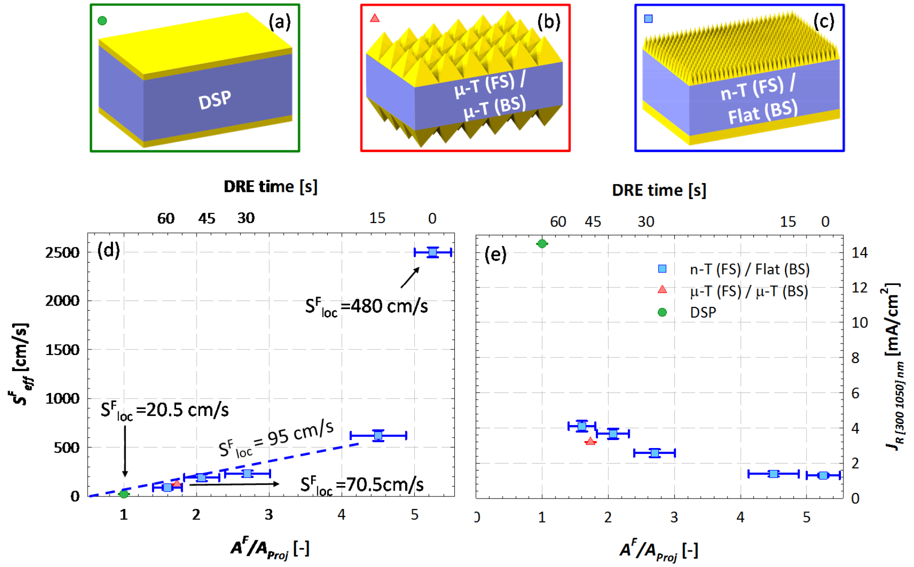

Figure 6.2. (a-c) Sketches of measured samples: symmetrical DSP (reference, green box), symmetrical µ-T (reference, red box) and n-T/flat wafers coated with 30-nm thick dry thermal SiO_2 (blue box), respectively. (d) S_{eff}^{F} as function of A^F/A_{Proj} (bottom x-axis) and DRE time (top x-axis). (d) Blue square symbols indicate the S_{eff}^{F} calculated by using the general theory as in [31] for asymmetrical samples with n-T at FS and polished BS (as sketched (c)) with different DRE time (0 - 60 s). The dashed blue line is a guide for the eyes. On the same diagram, $S_{loc}^{F}$for all fabricated samples is also reported. (e) Implied photocurrent density associated to *R* (J_R) as function of A^F/A_{Proj} (bottom x-axis) and DRE time (top x-axis). Blue square symbols indicate J_R for the samples with n-T at FS and polished BS. In both diagrams, the red triangle and the green circle symbols indicate the S_{eff}^{F} (d) and the J_R (e) of the symmetrical reference samples. The vertical and horizontal error bars represent the standard deviation calculated for four samples fabricated with same process steps (i.e. DRE time and oxidation).

charges (Q_f). In fact, having low density of fixed charges minimize the width of the depletion region induced on the Si surface by Q_f. In other words, having a weak field effect of the nano-textured surface ensures a narrow depletion region and therefore Equation 6.2 can be strictly used. The strong depletion region induced by large Q_f trapped in the dielectric coating the sharp features of nanotextured surface, makes questionable the usage of Equation 6.2 (passivation study of nanotextured samples with high Q_f is presented in Section 6.7.1). For comparison, in Figure 6.2 (d) the S_{eff}^{F} of two symmetrical DSP and micro-textured reference wafers passivated with dry SiO_2 are also reported. Moreover, for both samples, S_{loc}^{F} was calculated from equation (2) by using the correspondent S_{eff}^{F} and A^F/A_{Proj} equal to 1 and 1.7 in case of symmetrical DSP and micro-textured sample, respectively. Comparing S_{eff}^{F} of the reference micro-textured sample with nano-textured / flat samples after different DRE, one can notice that for etching time of 60 s the electrical properties of the nano-textured surface outperform those of micro-textured ones. For assessing the optical performance of our samples, the implied photocurrent density related to R (J_R) was deployed. J_R was calculated by convoluting the measured R with photon flux of the AM1.5 spectrum [33] between 300 and 1200 nm. As depicted in Figure 6.2 (e), J_R of the wet-etched nano-textured/flat samples becomes larger than the one of the micro-textured reference sample for DRE time longer than 45 s.

Therefore, 30-s long DRE of nano-cones was regarded as a good compromise to achieve

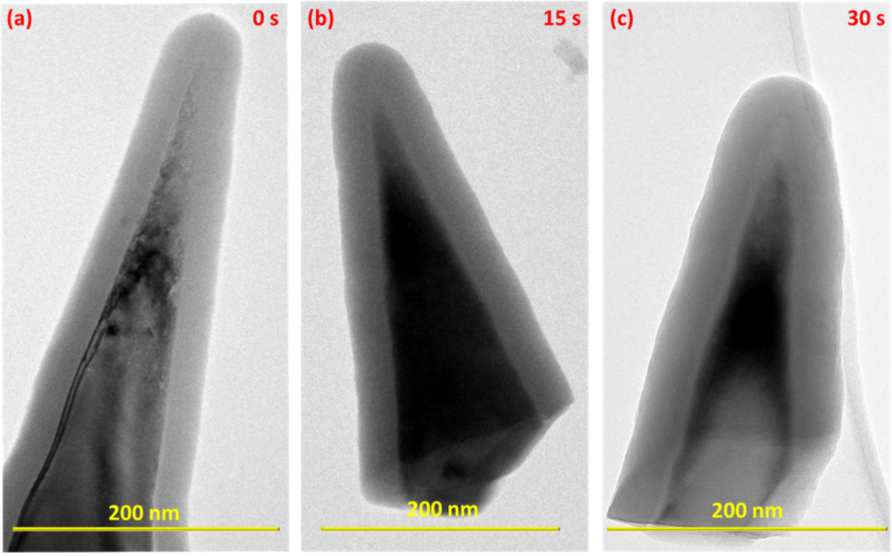

Figure 6.3. TEM of the nano-textured samples with (a) 0 s, (b) 15 s and (c) 30 s of DRE. The sample with no DRE shows evident defects especially on the tip of the Si nano-cone. Lower defect density is clearly shown for the samples with 15 and 30 s of DRE.

both low J_R and similar S_{eff}^{F} with respect to micro-pyramids. Transmission electron microscopy (TEM) of the samples with 0, 15 and 30 s of DRE is shown in Figure 6.3 (a), (b) and (c), respectively. The TEM clearly shows that the sample with 0 s of DRE presents a large density of defects especially on the surface of the Si nano-cone. On the other hand the samples with DRE clearly show that the wet treatment enables the removal of the damaged layer due to ion bombardment induced by the RIE.

6.4.2 Advanced light trapping scheme with MST surfaces

To maximize light absorption over the entire wavelength range of interest of a c-Si solar absorber, light management schemes combining the optical features of both nano-texturing and micro-texturing should be used [17]. The nano-texturing is characterized by features size smaller than the wavelength corresponding to the band gap of c-Si (see Figure 6.4 (a)). For such type of surface texturing, according to the effective medium approximation theory [34], the solar radiation is smoothly in-coupled from air to silicon leading to a nearly zero front reflectance. In case of micro-texturing (see Figure 6.4 (b)), the optical regime that occurs is refraction, since texture sizes are much larger than the wavelength corresponding to the band gap of c-Si. In this other optical regime, geometrical optics holds and solar radiation can be seen as a pool of rays whose direction changes as a consequence of the interaction with the large features onto the Si absorber. In this way the light path in c-Si absorber is prolonged resulting in an absorption enhancement especially in the NIR region.

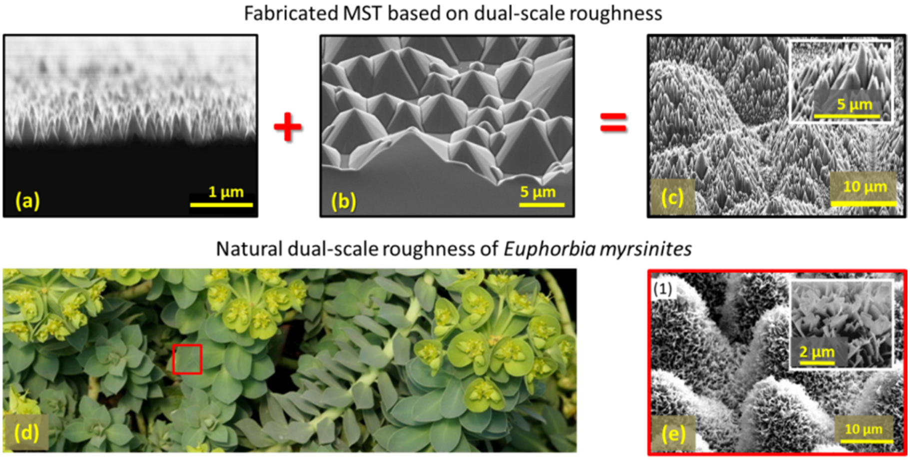

Figure 6.4**.** (a)-(e) Cross sectional SEM images of as-fabricated n-T, standard µ-T and MST followed by 30-s of DRE fabricated by superimposing n-T to µ-T, respectively. All samples are coated with 40-nm thick of dry thermal SiO_2. (d) *Euphorbia myrsinites.* (e) SEM image of *Euphorbia myrsinites* leafs showing MST formed by nanostructured wax on micropapillæ [1].

To benefit from both optical effects, a MST texture is proposed, which is obtained by micro-texturing Si wafer using wet etching followed by nano-texturing using RIE (see Figure 6.4 (c)). The fabricated MST, where nano-cones are superposed on micro-pyramids, shows clear similarities with the natural modulated surface texture of *Euphorbia myrsinites* leaves (see Figure 6.4 (d)-(e)) [1]. To experimentally prove the optical MST concept, four different combinations of texturing were fabricated and their measured A_{Si} were compared between 300 and 1200 nm as shown in Figure 6.5 (a)-(d). The samples here studied comprises of nano-cones at FS and polished BS (Figure 6.5 (a)), micro-pyramids at FS and polished BS (Figure 6.5 (b)) nano-cones FS and micro-pyramids at BS (Figure 6.5 (c)), and MST at FS with polished BS (Figure 6.5 (d)). The nano-texture used in this experiment was treated with 30-s long DRE. Figure 6.5 (e) presents the optical performance. As the figure clearly shows, nano-cones results in ideal light trapping due to strong light in-coupling only between 300 and 1000 nm. For longer wavelengths, the nearly Lambertian scattering exhibited by micro-pyramids leads to a higher NIR response with respect to the nano-cones. As already shown in Chapter 4, the sample with nano-cones at FS and micro-pyramids at BS combines both optical effects. Due to high recombination rate of epitaxially grown layers on textured surfaces, both type of textures were combined on the front side in a MST approach (see Figure 6.5 (d)). Figure 6.5 (e) demonstrates that either decoupling the two textures on FS and BS or

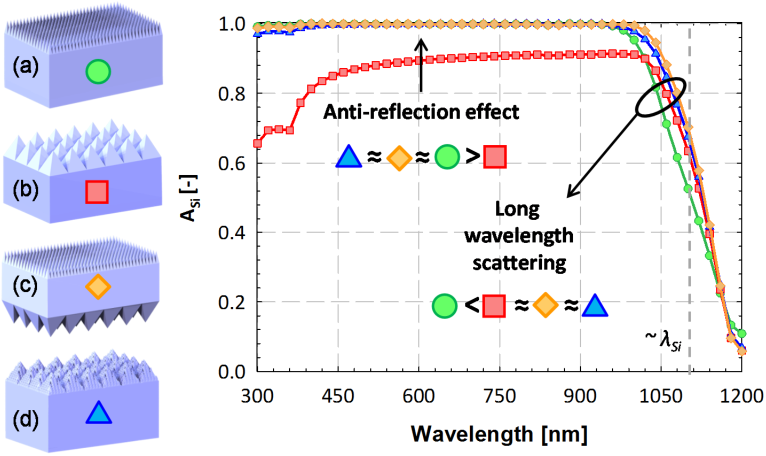

Figure 6.5. Four different combinations of texturing: (a) n-T at FS and polished BS, (b) µ-T at FS and polished BS, (d) n-T at FS and µ-T at BS and (e) MST at FS with polished BS. (e) Optical absorption in silicon (A_{Si}) measured between 300 and 1200 nm for all fabricated samples. Nano-texturing shows ideal light in-coupling leading to a nearly zero R between 300 and 1000 nm; for longer wavelength the nearly Lambertian scattering exhibited by µ-T scale leads to higher NIR response (1000 nm -1200 nm) compared to n-T scale; sample (d) based on MST at FS and flat BS combines both optical effects.

combining them on the FS similar optical enhancement can be achieved. In Figure 6.6, optical simulations performed by means of Finite Difference Time Domain (FDTD) are presented. Electro-magnetic field as result of the four light trapping structures depicted in Figure 6.5 (a)-(d) was simulated in silicon absorber at 800 nm for both transvers electric (TE) (top panel) and transvers magnetic (TM) (bottom panel) modes. In case of nano-textured surface the incident wave is smoothly in-coupled from air to silicon minimizing the intensity of the reflected wave (Figure 6.6 (a)). In case of micro-texturing, the typical diffraction pattern can be observed. For such type of texturing, the optical light path in Si absorber is prolonged resulting in an absorption enhancement especially in the NIR region (Figure 6.6 (b)). (c) n-T at FS and µ-T at BS and (d) MST at FS with polished BS shows the combination of both optical effects.

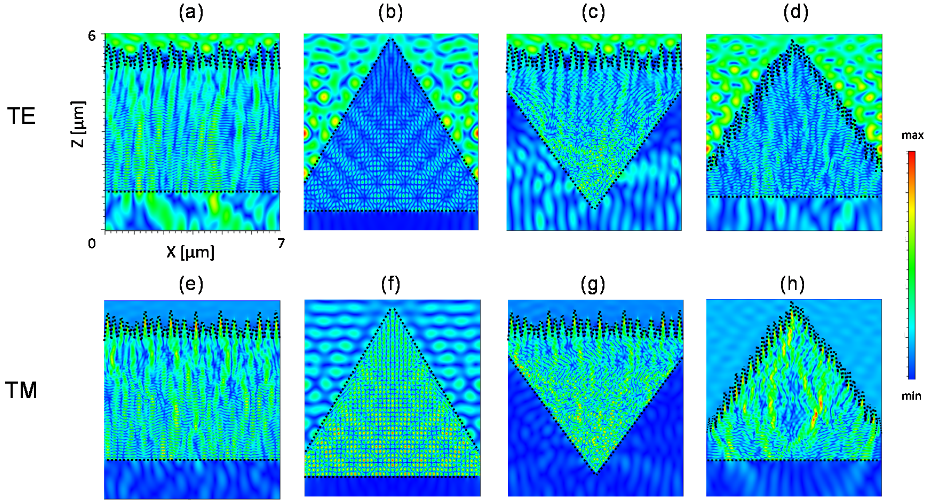

Figure 6.6. FDTD-based optical simulation of the four different combinations of texturing: (a,e) n-T at FS and polished BS, (b, f) µ-T at FS and polished BS (c, g) n-T at FS and µ-T at BS and (d, h) MST at FS with polished BS. Simulated e-field propagation in silicon absorber at 800 nm in case of TE (top panel) and TM (bottom panel) polarizations.

6.4.3 Application in high efficiency IBC solar cells

To apply the proposed advanced passivation and light trapping schemes in a solar cell, c-Si solar cells based on IBC architecture with flat BS were processed (see Figure 6.7 (a)-(d)). In the first device (reference cell), micro-texturing was made on the FS of the wafer by using alkaline etching (see inset in Figure 6.7 (a)). In the second device (MST cell), the developed mask-less RIE nano-cones on micro-pyramids were applied (see inset in Figure 6.7 (d)). For the presence of nano-cones on the MST cell, 30-s long DRE was applied to eliminate most of the surface defects induced by RIE while keeping low the total *R*. Aside the obvious difference in the FS texture, the two fabricated devices had the same design of emitter, BSF and FSF (see Figure 6.7 (b)-(c)) and the same 3x3-cm^2 wide area. In particular, at the FS of both devices, a dielectric stack formed by dry thermal SiO$_2$ and PECVD SiN$_x$ was applied. This stack had the double roles of surface passivation and ARC in the reference cell. However, in case of the MST cell, the same stack only plays a passivation role since no ARC is needed. Therefore for the MST cell, the deposited SiN was slightly thinned with respect to the reference cell which also minimize the parasitic absorption losses between 300 and 400 nm. The wafers used to fabricate the two cells, even though taken from the same supplier's box, had slightly different thicknesses. In particular, the wafer of the MST cell had a final thickness after texturing processes (d_{final} = 235 µm). The final thickness of the reference cell was instead 273 µm, meaning that its initial thickness was around the upper bound of thickness range provided by the wafer supplier.

Measured *R* spectra of both solar cells are depicted in Figure 6.8 (a) (right y-axis). The figure demonstrates that the MST cell exhibited a superior broad-band anti-reflective effect (almost zero *R*) and long wavelength light scattering comparable to the reference cell. *EQE* was also measured and is reported on the left y-axis of Figure 6.8 (a). This measurement is especially relevant as it takes both light behaviour and recombination into account. At short wavelengths, the minimization of the optical losses at FS

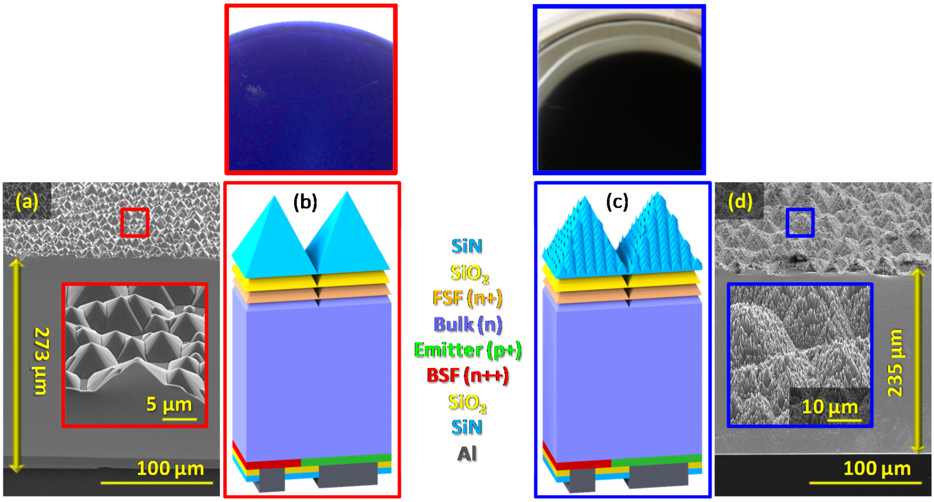

Figure 6.7. (a) and (d) SEM cross-section of the reference IBC solar cell and of the IBC solar cell with MST at FS, respectively. The insets show a magnification of both textures. The SEM images were taken with tilt angle of 45°. (b) and (c) Sketch of fabricated reference and MST IBC solar cells, respectively. Same processes for emitter, BSF and FSF were employed in both devices. The top panel on the left shows a picture of standard micro-textured surface coated with ARC. The top panel on the right shows a picture of the black nano-textured surface without ARC.

combined with the advanced surface passivation technique led to a significant increase of the MST cell EQE (78% at 300 nm) compared to that of the reference cell (42% at 300 nm) (see, left y-axis in Figure 6.8 (a)). In the wavelength range between 450 and 900 nm, the MST cell *EQE* was instead found to be lower than that of the reference solar cell. Such behaviour is explained by the fact that the MST device has a slightly higher surface recombination velocity compared with the reference one which leads to poorer carrier collection efficiency [38]. In fact the *IQE* (see Figure 6.8 (b)) of the reference device is quite constant between 450 and 900 nm. On the contrary, the *IQE* of the MST slightly increases when going to longer wavelengths. This effect might be related to the fact that, when the wavelength increases, carriers are generated deeper in the absorber layer for which carrier collection probability is higher. In addition, for wavelengths longer than 1100 nm (~$\lambda_{Si\ band\text{-}gap}$), as optically demonstrated in Section 6.4.2, the *EQE* of both cells were similar.

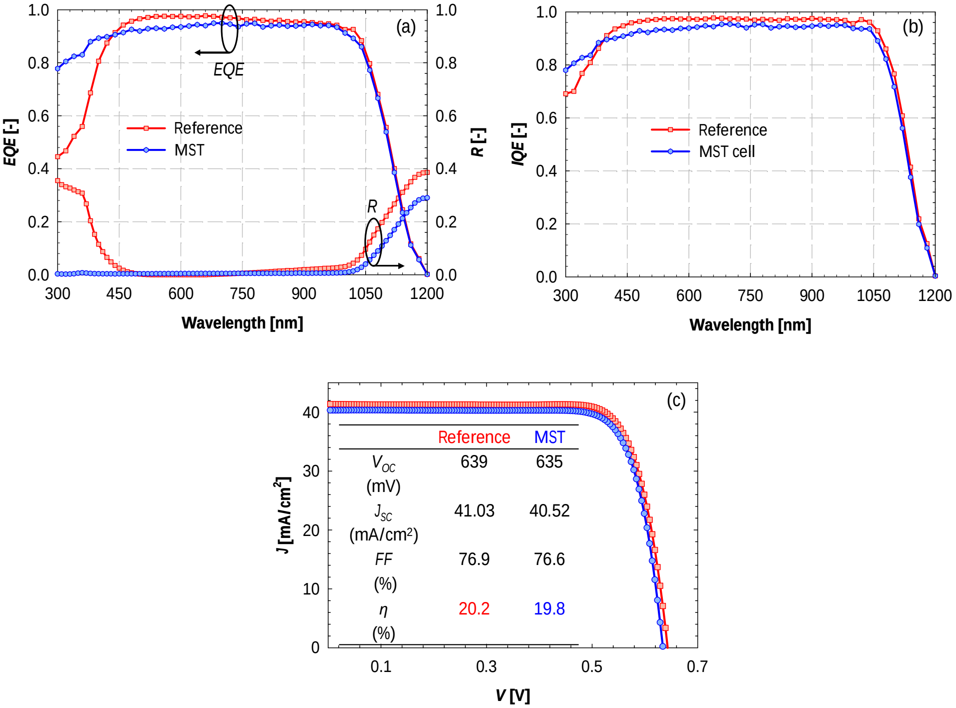

	Reference	MST
V_{OC} (mV)	639	635
J_{SC} (mA/cm^2)	41.03	40.52
FF (%)	76.9	76.6
η (%)	20.2	19.8

Figure 6.8. (a) Measured EQE (left y-axis) and R (right y-axis) as function of the wavelength of the fabricated IBC solar cells with standard µ-T (red line with squares) and MST texture (blue line with circles). (b) Measured IQE as function of the wavelength of the reference fabricated IBC solar cells with standard µ-T (red line with squares) and MST texture (blue line with circles). (c) Measured *J*-*V* characteristics of both IBC solar cells. The table summarizes the measured external parameters of both reference (red text) and MST (blue text) devices.

This is noteworthy considering that the absorber of the MST cell was roughly 40-µm thinner than that of the reference cell. The *J-V* curves of both solar cells and their external parameters are finally shown in Figure 6.8 (b). Despite the advanced texturing at FS of the MST cell, the measured V_{OC} and *FF* were found to be fundamentally the same with respect to the reference cell. This was expected having achieved the passivation of high aspect ratio nano-cones with values similar to the passivation of typical micro-pyramids. The difference in J_{SC} between the two devices, instead, could be explained by looking at the *EQE* of the two devices, in particular, their difference in the visible wavelength range. Even though with our current IBC process the reference cell recorded higher conversion efficiency than the MST cell, the latter - if opportunely optimized - holds the potential to exhibit a *maximal* EQE. This issue will be elaborated in next section.

6.5 Discussion

A DRE followed by dry oxidation (850 °C) proposed in this Chapter can be seen as a cost effective (compared with cryogenic RIE) and very efficient method to achieve superior passivation of advanced nano-textures. The photovoltaic field craves this result in order to deploy high aspect ratio texturing for increasing light absorption (high J_{SC}) and charge-carrier collection. In addition, such advanced passivation scheme helped to reveal the recombination kinetics of RIE nano-textured silicon passivated with SiO_2. According to equation (6.2) a linear trend between S_{eff}^{F} and A^{F}/A_{Proj} is expected. In this experiment, instead, two linear regions corresponding to two different values of S_{loc}^{F} were observed, as depicted in Figure 6.2 (d). In particular, a clear change of S_{loc}^{F} from 480 cm/s for samples with 0 s of DRE to 95 cm/s for the DRE samples was shown. Since the same passivation coating was used for all nano-textured samples, we can state that: (i) the dependence of S_{loc}^{F} with DRE is related to a change of defect density at wafer's surface induced by the RIE [30]; (ii) after 15 s of etching, most of the defects induced by RIE are removed and S_{loc}^{F} becomes again independent from DRE time. A MST at the FS of c-Si wafers was applied as an advanced light trapping scheme. The MST exhibits similar surface features as the hazy leaves of *Euphorbia myrsinites*. The combination of micro-texturing and nano-texturing enhances light absorption in c-Si. The texturing can be either combined at FS or decoupled between FS and BS. It was experimentally proved that the c-Si sample with MST at FS and flat BS exhibits a similar optical performance when compared to the decoupled case (nano-cones at the FS and micro-pyramids at the BS) in the entire wavelength range of interest and shows higher absorption than the standard micro-texturing. The absorption of light in c-Si samples could be influenced by placing or superposing textures in different parts of the c-Si sample (see Figure 6.5). In a device perspective, the approach of the MST at FS with polished BS could be straightforwardly implemented in IBC architecture because the flatness of the BS facilitates the fabrication process of IBC (see Figure 6.7). One can observe from the measured *R* and *T* spectra of the MST cell (see Figure 6.9) that the light in the wavelength range between 300 and 1050 nm is completely coupled into the device. Despite many promising photonic structures proposed so far and exhaustively reported by Brongersma et al. [36], the MST approach presented in this contribution constitutes the first experimental demonstration of an effective, mask-less, industrially-scalable light trapping approach in high efficiency solar cell. In fact the MST surface demonstrated the capability to achieve both ideal light in-coupling (nano-cones) and light scattering (micro-pyramids).

Light trapping is a necessary but not sufficient condition for realizing a solar cell with the *maximal* EQE. The *maximal* EQE of a solar cell matches the absorptance of a Si absorber determined the by $4n^2$ enhancement limit [19]. In Figure 6.9 the *maximal* EQE for a 235-μm thick c-Si solar cell is reported.

In the solar cell, where a part of the c-Si absorber is the MST, the presence of junctions and interfaces is a potential source of opto-electrical losses. The identification and minimization of these losses is the second necessary ingredient for achieving the *maximal* EQE. Considering the conservation of energy, the absorptance of light in the MST cell (A_{MST}) can be expressed as $A_{MST} = 1 - R - T$. By using the optical modelling proposed in Section 4.6.1 and [17][37], a first approximation of the light absorbed in the c-Si bulk (A_{Si}) was provided taking out the parasitic absorption into the emitter, BSF due to FCA and Al. The parasitic absorption in the front SiN_x at short wavelengths was subtracted as

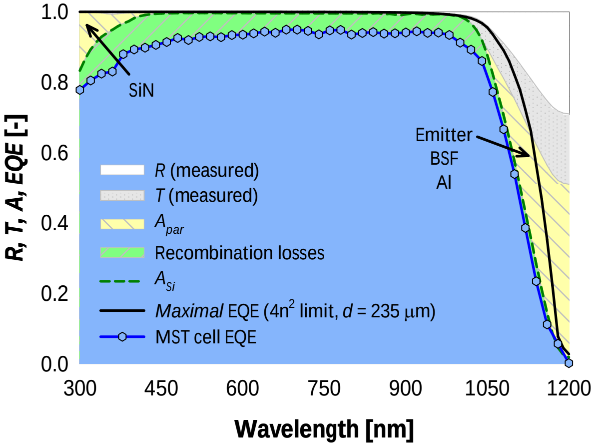

Figure 6.9. Breakdown of the energy conservation for the MST cell ($R + T + A_{par} + A_{Si} = 1$): reflectance (white area), transmittance (light grey area), absorption losses (yellow area) and absorption in c-Si (area below the dark green dashed curve). Also the *maximal* EQE ($4n^2$ limit) of c-Si calculated for d = 235 μm (black solid curve) and the MST cell EQE (light blue symbols) are reported for comparison. Recombination losses (light green area) are individuated between the absorption in c-Si and the MST cell EQE.

well. In Figure 6.9 the difference between the A_{Si} curve and the EQE of the MST cell indicates the electrical recombination losses. In order to achieve a *maximal* EQE of the MST cell, two steps can be realized: (a) quenching the recombination losses of the real EQE to match A_{Si} and (b) reducing optical losses, i.e. parasitic absorption in supporting layers and transmittance at the long wavelengths. In comparison to the spectral response of reference cell, the EQE (78%) of the MST cell at the short wavelengths (300 nm) is one of the highest reported in literature [39]. This high EQE at the short wavelengths highlights the quality of our passivation scheme and of the implanted FSF [40]. However, there is still a difference of 2.69 mA/cm^2 between the implied photo-current density calculated from the measured A_{Si} and from the EQE of the MST cell that is related to the electrical recombination of the carriers in the cell. In particular, 66% of such implied photo-current density difference is realized between 450 and 900 nm where the reference cell outperforms the MST cell. This is because the τ_{eff} of the MST cell is eventually not high enough to ensure a perfect collection of carriers in combination with the chosen periodic distance between the emitter and the BSF at the BS. Such distance, known as *pitch size*, was in fact optimized for micro-pyramids at FS. Therefore, in spite of all light being trapped in the MST cell, its design needs further electrical optimization. Three electrical strategies can be implemented to enhance the EQE of the MST cell: (a1) optimization of the FSF to improve surface passivation, (a2) improvement of the front passivation stack (from SiO_2 / SiN_x to Al_2O_3 [41]) to achieve higher τ_{eff} , and (a3) shortening of the collection path of carriers by means of optimized rear side of the IBC architecture. As regards the optical performance of the MST cell, the EQE behaviour at the long wavelengths is as good as the reference cell.

However, there is still a gap in the implied photo-current density equal to 1.09 mA/cm^2 between the A_{Si} and the *maximal* EQE. With respect to further optical optimization, three approaches can be adopted to boost the performance of the MST cell: (b1) reduction of SiN_x thickness at the FS (if still needed for passivation purposes), (b2) deployment of materials with very low absorption at long wavelengths, such as hole-selective molybdenum-oxide [42] and electron-selective nc-SiO_x:H [43] for forming the emitter and the BSF, respectively, and (b3) application of a highly reflective back sheet either coated with TiO_2 nano-particles (white paint) [44] or an optimized omni-directional distributed Bragg reflector.

6.6 Conclusions

High efficiency IBC solar cell with MST formed by nano-cones on micro-pyramids were demonstrated. In particular, an effective advanced passivation scheme for nano-cones fabricated via RIE on c-Si, was demonstrated. Such scheme was based on DRE that decreases the defect density induced by RIE nano-texturing at the FS. 30-s long DRE was found to be the best compromise to achieve state-of-the-art S_{eff}^{F} and R lower than the value obtained for typical micro-pyramids. The DRE step here studied can be applied to any type of nano-textured surfaces where having low recombination velocity is instrumental, such as Si-based nanowire solar cells, photo-electro-chemical cells for water splitting and lithium-ion batteries. In addition, it was shown that nano-cones can provide ideal light in-coupling but not ideal light scattering. In order to achieve both ideal light in-coupling and light scattering nano-cones on micro-pyramids were fabricated. Based on the self-aligned process (see Chapter 5), IBC solar cells achieving conversion efficiency of 20.2% and 19.8% with standard micro-pyramids and MST, respectively, were fabricated. On the one hand, the almost similar V_{OC} of these two solar cells and a significant increase of the high *IQE* at short wavelengths of MST cell (78% at 300 nm) highlight the quality of the designed passivation scheme for high aspect ratio nano-textures. On the other hand, the EQE of the MST cell and its measured reflectance below 1% indicates that from optical stand point exhibiting one of the best light trapping schemes ever reported. A slightly lower J_{sc} of the MST cell compared to the reference cell was due the non-optimal collection efficiency. The MST cell demonstrated in this work is a solid candidate for experimentally proving the *maximal EQE*. To this end, realistic optimization strategies at both electrical and optical level were indicated.

6.7 Appendix

6.7.1 Passivation of nano-textured surfaces with dielectric with large Q_f

In this section the passivation quality of nano-textured surfaces when passivated with a dielectric with large density of fixed charges (Q_f) is reported. In this work, Al_2O_3 (Q_f > -2·10^{12} cm^{-2}) deposited via atomic layer deposition (ALD) was used as passivation layer. Measured τ_{eff} as function of Δn for samples with nano-texturing on the FS and polished BS with different DRE time and coated on both sides with thermal SiO_2 or Al_2O_3 are reported in Figure 6.10 (a) and (b), respectively. The figures clearly show that for both cases the largest increase in τ_{eff} is obtained after 15s of DRE. For longer etching time the τ_{eff} of nano-textured samples coated with Al_2O_3 show a much weaker dependence with DRE time compared to ones coated with SiO_2. This effect might be related to the stronger field effect produced by the high Q_f of the Al_2O_3 compared to that of SiO_2. In particular, we speculate that the stronger field effect of the Al_2O_3 leads to a better scherming of the surface defects by inducing a depletion region. This depletion region might also change the electrical area enlargement factor making τ_{eff} less sensitive to the DRE and therefore A^F/A_{Proj}.

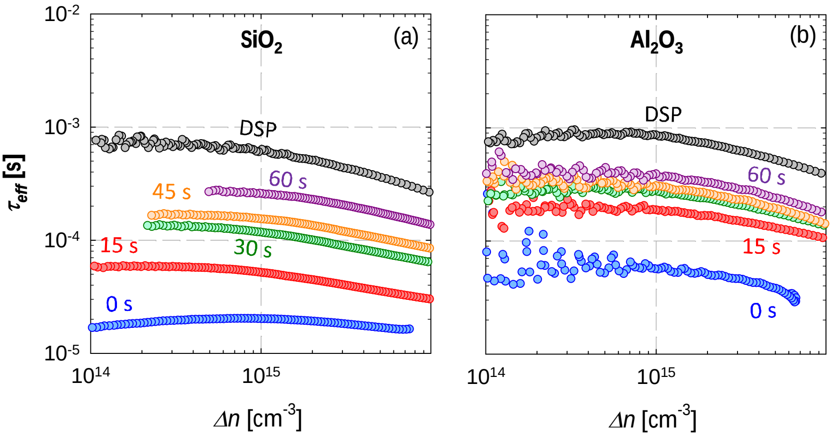

Figure 6.10 Measured τ_{eff} as function of Δn for samples with nano-texturing on the FS and polished BS with different DRE time and coated on both sides with (a) thermal SiO_2 (b) ALD Al_2O_3. For comparison measured τ_{eff} on DSP samples in reported. The high Q_f of the Al_2O_3 makes τ_{eff} less sensitive to A^F/A_{Proj} after 15s of DRE.

6.7.2 Impact of the DRE on the optical absorption

The effect of the DRE time on the light trapping properties of the nano-textured samples is here evaluated. As shown in Figure 6.11 the DRE mostly affects the antireflective effect of the nano-textured samples but does not significantly changes its light trapping properties at long wavelengths.

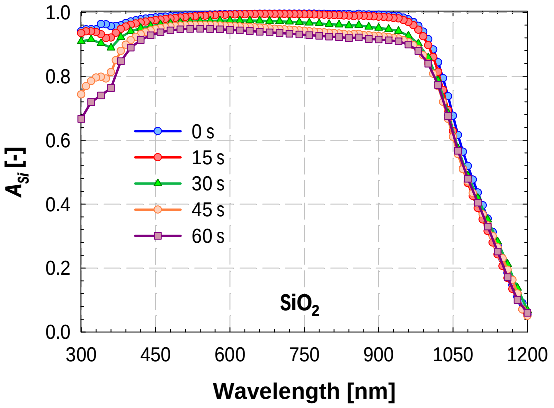

Figure 6.11. Measured A_{Si} for the nano-textured samples with different DRE time. All samples are coated on the front and rear sides with thermal SiO_2.

6.8 References

[1] K. Koch, W. Barthlott, Superhydrophobic and superhydrophilic plant surfaces: an inspiration for biomimetic materials. Philosophical transactions. Series A, Mathematical, physical, and engineering sciences. 2009, 367, 1487-1509, DOI: 10.1098/rsta.2009.0022

[2] D. G. Stavenga, S. Foletti, G. Palasantzas, K. Arikawa, Light on the moth-eye corneal nipple array of butterflies. Proceedings of the Royal Society of London. Series B, Containing papers of a Biological character. 2006, 273 , 661–667, DOI: 10.1098/rspb.2005.3369

[3] P. Vukusic, J. R. Sambles, Photonic structures in biology. Nature. 2003, 424, 852–855, DOI: 10.1038/nature01941

[4] S. Guldin, P. Kohn, M. Stefik, J. Song, G. Divitini, F. Ecarla, C. Ducati, U. Wiesner U. Steiner, Self-Cleaning Antireflective Optical Coatings. Nano Letters. 2013, 13, 5329-5335, DOI: 10.1021/nl402832u.

[5] S.-J. Choi, S.-Y. Huh, Direct Structuring of a Biomimetic Anti-Reflective, Self-Cleaning Surface for Light Harvesting in Organic Solar Cells. Macromolecular Rapid Communication. 2010, 31, 539–544, DOI: 10.1002/marc.200900658

[6] P. Campbell, M. A. Green, Light trapping properties of pyramidally textured surfaces. Journal of Applied Physics, 1987, 62: 243, DOI: 10.1002/pip.404.

[7] A. Ingenito, O. Isabella, S. Solntsev, M. Zeman, Accurate opto-electrical modeling of multi-crystalline silicon wafer-based solar cells. Solar Energy Materials & Solar cells, 2014, 123: 17-29, DOI: 10.1016/j.solmat.2013.12.019

[8] J. Zhao, A. Wang, P. P. Altermatt, M. A. Green, 24% efficient silicon solar cells with double layer antireflection coatings and reduced resistance loss. Applied Physics Letters. 1995, 66, 26, 3636-3638, DOI: 10.1016/0927-0248(95)00117-4

[9] S. Koynov, M. S. Brandt, M. Stutzmann M, Black non-reflecting silicon surfaces for solar cells. Applied Physic Letters. 2006, 88, 203107- 203107-3. DOI: 10.1063/1.2204573.

[10] H. Han, H. Huang, W. Lee, Metal-assisted chemical etching of silicon and nanotechnology applications. Nano Today. 2014, 9, 271-304, DOI: 10.1016/j.nantod.2014.04.013.

[11] H. Sai, H. Fujii, K. Arafune, Y. Ohshita, Y. Kanamori, H. Yugami, M. Yamaguchi, Wide-angle antireflection effect of sub-wavelength structures for solar cells. Japanese Journal of Applied Physics. 2007, 46, 3333–3336, DOI: 10.1143/jjap.46.3333.

[12] J. Yoo, G. Yu, J. Yi, Black surface structures for crystalline silicon solar cells. Materials Science and Engineering: B. 2009, 159, 333–337, DOI: 10.1016/j.mseb.2008.10.019.

[13] M. Kroll, M. Otto, T. Käsebier, K. Füchsel, R. Wehrspohn, E. Kley, A. Tünnermann, T. Pertsch, Black silicon for solar cell applications. Proceeding SPIE. 2012, 8438, 17-28. DOI: 10.1117/12.922380

[14] T. H. Her, R. J. Finlay, C. Wu, S. Deliwala, E. Mazur, Microstructuring of silicon with femtosecond laser pulses. Applied Physics Letters. 1998, 73, 1673–1675.

[15] R.B. Stephens, G. D. Cody, Optical reflectance and transmission of a textured surface. Thin Solid Films. 1977, 45, 19–29. DOI: 10.1016/0040-6090(77)90197-3

[16] H. M. Branz, V. E. Yost, S. Ward, K. M. Jones, B. To, P. Stradins, Nanostructured black silicon and the optical reflectance of graded-density surfaces. Applied Physics Letters. 2009, 94, 23, 231121 - 231121-3, DOI: 10.1063/1.3152244.

[17] A. Ingenito, O. Isabella, M. Zeman, Experimental Demonstration of 4n2 Classical Absorption Limit in Nanotextured Ultrathin Solar Cells with Dielectric Omnidirectional Back Reflector ACS Photonics. 2014, 1, 3, 270-278, DOI: 10.1021/ph4001586.

[18] K. X. Wang, Z. Yu, V. Liu, Y. Cui, S. Fan, Absorption enhancement in ultrathin crystalline silicon solar cells with antireflection and light-trapping nanocones gratings Nano Letters. 2012, 12, 3, 1616-1619, DOI: 10.1021/nl204550q.

[19] T. Tiedje, E. Yablonovitch, G. D. Cody, B. G. Brooks, Limiting efficiency of silicon solar cells. Electron Devices, IEEE Transactions on. 1984, 31, 5, 711-716, DOI: 10.1109/T-ED.1984.21594.

[20] H. C. Yuan, V. E. Yost, M. R. Page, P. Stradins, D. L. Meier, Efficient black silicon solar cell with a density-graded nanoporous surface: optical properties, performance limitations, and design rules. Applied Physics Letters. 2009, 95, 123501-123501-3, DOI: 10.1063/1.3231438.

[21] J. Oh, H. C. Yuan, H. M. Branz, An 18.2%-efficient black-silicon solar cell achieved through control of carrier recombination in nanostructures. Nature Nanotechnology. 2012, 7, 743-748, DOI: 10.1038/nnano.2012.166.

[22] H. Savin, P. Repo, G. von Gastrow, P. Ortega, E. Calle, M. Garín, R. Alcubilla, Black silicon solar cells with interdigitated back-contacts achieve 22.1% efficiency, Nature Nanotechnology 10, 624–628 (2015) doi:10.1038/nnano.2015.89

[23] F. Toor, M. R. Page, H. M. Branz, H.-C. Yuan, Multi-scale surface texture to improve blue response of nanoporous black silicon solar cells. Applied Physics Letters. 2011, 99, 1030501-5.

[24] O. Isabella, J. Krč, M. Zeman, Modulated surface textures for enhanced light trapping in thin-film silicon solar cells. Applied Physics Letters. 97, 10, 1011061-101106-3. DOI: 10.1063/1.3488023.

[25] R.M. Swanson, Device physics for backside-contact solar cells. Proceeding of the 33rd IEEE Photovoltaic Specialists Conference. 2008, San Diego, USA.

[26] J. Hobden, Self-assembled molecular nanowires: Electronic properties. Nano Today. 2008, 3, 8, 11, DOI: 10.1016/S1748-0132(08)70059-8.

[27] T. Song, S.-T. Lee, B. Sun, Silicon nanowires for photovoltaic applications: The progress and challenge. Nano Energy. 2012, 1, 654-673, DOI: 10.1016/j.nanoen.2012.07.023.

[28] K.-Q. Peng, X. Wang, L. Li, Y. Hu, S.-T. Lee, Silicon nanowires for advanced energy conversion and storage. Nano Today. 2013, 8, 75-97, DOI: 10.1016/j.nantod.2012.12.009.

[29] Y. H. Lee, G. S. Oehrlein, C. Ransom, RIE-induced damage and contamination in silicon, Radiation Effects and Defects in Solids: Incorporating Plasma Science and Plasma Technology. 1989, 111-112: 1-2, 221-232, DOI: 10.1080/10420158908212997

[30] A. G. Aberle, Crystalline Silicon Solar Cells: Advanced Surface Passivation and Analysis. Centre for Photovoltaic Engineering, University of New South Wales, 1999.

[31] A. B. Sproul, Dimensionless solution of the equation describing the effect of surface recombination on carrier decay in semiconductors. Applied Physics Letters. 1994, 76, 5, 2851-2854.

[32] R. K. Ahrenkiela, J. Dashdorj, Interface recombination velocity measurement by a contactless microwave technique. The European Physical Journal Applied Physics. 2004, 27, 499–501, DOI: 10.1051/epjap:2004071.

[33] http://rredc.nrel.gov/solar/spectra/am1.5/

[34] C. Tuck, Effective medium theory, Oxford University (1st ed.), 2000, ISBN 978-0-19-851892-1.

[35] S. Schaefer, R. Lüdemann, Low damage reactive ion etching for photovoltaic applications. Journal of Vacuum Science & Technology A. 1999, 17, 749-754, DOI: 10.1116/1.581644.

[36] M.L. Brongersma, Y. Cui, S. Fan, Light management for photovoltaics using high-index nanostructures. Nature Materials. 2014, 13, 451-460, DOI: 10.1038/NMAT3921

[37] M. Zeman, O. Isabella, S. Solntsev, K. Jäger, Modelling of thin-film silicon solar cells, Solar Energy Materials & Solar Cells. 2013, 119, 94-111, DOI: 10.1016/j.solmat.2013.05.037.

[38] M. Hermle, F. Granek, O. Schultz, S. W. Glunz, Analyzing the effects of front-surface fields on back-junction silicon solar cells using the charge-collection probability and the reciprocity theorem Journal of Applied Physics, 103, 054507 (2008), DOI: http://dx.doi.org/10.1063/1.2887991.

[39] M. A. Green, K. Emery, Y. Hishikawa, W. Warta, E. D. Dunlop, Solar cell efficiency tables (version 44). Progress in Photovoltaics: Research and Applications. 2014, 22, 701–710, DOI: 10.1002/pip.2525.

[40] F. Granek, M. Hermle, D. M. Huljić, O. Schultz-Wittmann, S. W. Glunz, Enhanced lateral current transport via the front N+ diffused layer of n-type high-efficiency back-junction back-contact silicon solar cells. Progress in Photovoltaics: Research and Applications. 2009, 17, 47–56, DOI: 10.1002/pip.862.

[41] M. Otto, M. Kroll, T. Käsebier, R. Salzer, A. Tünnermann, R. B. Wehrspohn, R Brendel, Extremely low surface recombination velocities in black silicon passivated by atomic layer deposition. Applied Physics Letters. 2012, 100, 191603-191603-4, DOI: 10.1063/1.4714546.

[42] C. Battaglia, S. M. de Nicolás, S. De Wolf, X. Yin, M. Zheng, C. Ballif C, A. Javey, Silicon heterojunction solar cell with passivated hole selective MoOx contact. Applied Physic Letters. 2014, 104, 113902- 113902-5, DOI: 10.1063/1.4868880.

[43] S. Kim, J.-W. Chung, H. Lee, J. Park, Y. Heo, H.-M. Lee, Remarkable progress in thin-film silicon solar cells using high-efficiency triple-junction technology. Solar Energy Materials and Solar Cells. 2013, 119, 26–35, DOI: 10.1016/j.solmat.2013.04.016.

[44] B. Lipovšek, J. Krč, O. Isabella, M. Zeman, M. Topič, Modeling and optimization of white paint back reflectors for thin-film silicon solar cells. Journal of Applied Physics. 2010, 115, 108103-108103-7, DOI: 10.1063/1.351290.

7

Optimized metal-free back reflectors for high efficiency open rear c-Si solar cells

7.1 Abstract

N-type wafers based c-Si solar cell technologies are still considered an attractive route for the photovoltaic industry. Among different n-type solar cell architectures, bifacial cells are quickly emerging. The open-rear configuration of a bifacial device results in high transmittance (T) losses at long wavelengths (>1000 nm). Such limitation is usually overcome at module level either by using a bifacial encapsulation or by placing a reflective foil on the rear side. In this work, the application of Distributed Bragg Reflector (DBR) and TiO_2-based white paint (WP) were investigated as alternative metal-free back-reflector directly applied to the textured open-rear of bifacial *n-Pasha* cells. Because of the high T losses at long wavelengths of the DBR applied on textured surface, its design and fabrication is studied in detail. The dielectric (DBR and WP) and metallic optimized Ag-based back-reflectors, used as reference, were applied to bifacial *n-Pasha* cells and their performances were evaluated. In particular, T below 20% at 1200 nm was demonstrated by optimizing the DBR thickness for textured surfaces. In addition, the optimized DBR and WP show performance comparable to state-of-the-art Ag back-reflector. The highest increase of the conversion efficiency is measured for the WP back-reflector, +0.34% absolute increase compared to *n-Pasha* measured with no-additional back-reflector.

This Chapter is based on the following publication: A. Ingenito, S.L. Luxembourg, P. Spinelli, J. Liu, J. C. Ortiz Lizcano, A. W. Weeber, O. Isabella, M. Zeman, Photovoltaics, IEEE Journal of ,6 ,1 34-40, 2016, DOI: 10.1109/JPHOTOV.2015.2487827

7.2 Introduction

The current PV market is dominated by p-type multi-crystalline silicon (mc-Si) solar cells based on a diffused emitter and screen printed aluminium back surface field (Al-BSF) [1]. The success of this technology is attributed to the low-cost and high throughput nature of the fabrication process. However, the high scalability of the process is paid in terms of limited conversion efficiency. In general, today's conversion efficiency of Al-BSF solar cells has a plateau around 18-19% for mono-crystalline Si (c-Si) and 17-18% for mc-Si solar cells [2]. In fact, the Al-BSF results in fairly high rear recombination losses and has a high degree of parasitic light absorption [3]. There has been an increased attention towards n-type c-Si solar cell technologies however, their actual market adoption remains quite limited. N-type wafers exhibit longer minority carrier diffusion lengths, are less sensitive to most common impurities [4] and even in case of Cz growth are free of light induced degradation due to the absence of boron-oxygen complex [5] with respect to p-type. To benefit from the superior performance of the n-type bulk material, recombination in the doped regions and at the metal contact need to be minimized. A possible solution to reduce these recombination losses consists in employing optimized diffusion process for both doped regions and passivating them with dielectric layers locally opened in correspondence of the metal contacts. Among the different n-type wafer based c-Si solar cell architectures, bifacial solar cells have recently gained a lot of attention at industrial level. The reasons for that are mainly related to the high scalability of the fabrication process and high conversion efficiency. In addition, the implementation of such technology does not require new equipment either at cell or at module level compared to a p-type Al-BSF device. Yingli Solar [6]-[8] and Mega Cell [9] have demonstrated conversion efficiency around 20% in pilot lines based on bifacial cells developed at ECN and ISC Konstanz, respectively. In addition, at Yingli, the Panda cell line is based on the ECN n-Pasha process and is in production line with cell efficiency exceeding 20.1% [10]. The (textured) open-rear configuration of a bifacial solar cell results in relatively high transmittance losses (T) in the weak absorption region of Si ($\lambda > 1000$ nm). For overcoming such limitation two module configurations are commonly employed. The first, so-called *bifacial module* configuration, uses front and rear transparent encapsulation, thus light can enter the device from both sides, see Figure 7.1 (a). This increases the module output power depending on the albedo light and bifaciality factor of the cells. However, in particular applications where the albedo light is insufficient, non-transparent module encapsulation is preferable. In such module configuration, a white back-sheet is utilized to reflect the transmitted IR light back into the cell, see Figure 7.1 (b). Common white foils used in bifacial solar modules are cost effective but reflect only 85% of the incoming light [11]. In this work the design and fabrication of two metal-free BRs applicable in open rear c-Si solar cells is presented. Such BRs are a possible alternative solution to the commonly used white foil with the aim of enhancing the rear internal reflectance (R_b). In particular, it is proposed the usage of (i) an omni-directional dielectric Distributed Bragg Reflector (DBR) and (ii) TiO_2 particles used as white paint (WP). These BRs are applied directly on the rear side of the cells making not possible to compare their performance with respect to the white foil at cell level. Therefore, the performance of the proposed dielectric BRs applied to *n-Pasha* cells was compared to that of optimized Ag BR (upper bound) and no-BR (lower bound, for which the R_b is set by the refractive index mismatch at the interface rear SiN_x / air). The *I-V* parameters and external quantum efficiency (*EQE*) of the fabricated solar cells are studied for all BR configurations proposed in this work.

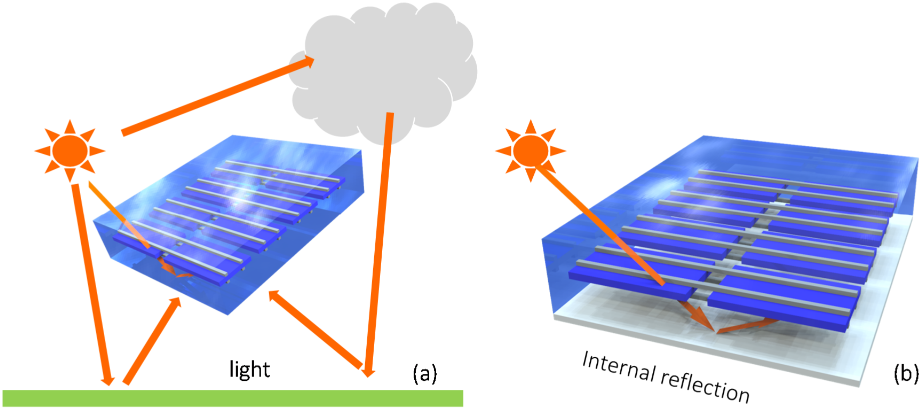

Figure 7.1 3-D sketch of (a) bifacial module configuration for which light can enter from both sides. Depending by the albedo light a bifaciality of the cells a certain gain in output module power is obtained. (b) Monofacial module configuration. A white foil is used to reflect IR light transmitted through the cells.

7.3 Experimental details

7.3.1 Distributed Bragg Reflector

A DBR is formed by pairs of alternating dielectric layers with refractive index mismatch. Such multi-layer stack can be designed to deliver high reflectance in a certain wavelength range known as photonic band gap (PBG) around the so-called Bragg wavelength (λ_B). The DBR used in this chapter was already presented in Section 4.4.2 of Chapter 4. It is formed by six pairs of a-Si:H and a-SiN_x:H pairs deposited via Plasma Enhanced Chemical Vapour Deposition (PECVD) with an Electrorava cluster tool. Prior to the DBR fabrication, a layer of SiO_2 is also deposited via PECVD in order to enhance the DBR performance (see section 7.4.1).

7.3.2 White paint back reflector

For the application of WP at back side of the sample TiO_2 particles mixed in H_2O with ratio 1:10 were drop-casted on the cell followed by drying in air for 12 hours. A thickness larger than 50 µm was found to be sufficient to ensure a $T < 5$ % at 1200 nm [12].

7.3.3 Ag back reflector

The Ag back reflector used in this work is formed by a stack of SiN_x / Ag (see Section 7.4.2). The SiN_x was deposited via PECVD technique and its thickness was optimized in order to minimize the Ag plasmonic losses [13]. The Ag was deposited via evaporation and was 100-nm thick to avoid T losses through it.

7.3.4 *n-Pasha* solar cells fabrication

The 10 x 10 cm^2 area *n-Pasha* c-Si solar cells studied in this work were fabricated at ECN [6] using n-type Cz wafers with thickness around 180 µm.

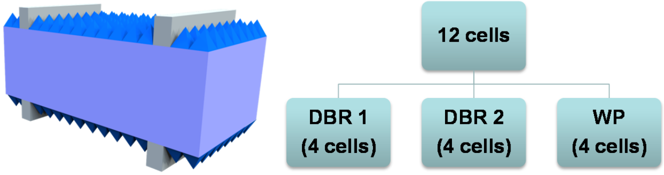

Figure 7.2. 3-D sketch of n-Pasha c-Si solar cell fabricated at ECN. The schematic on the right summarizes the type of dielectric BR and number of cells processed in this work.

	Total area	**Active area**
J_{sc} [mA/cm^2]	39.6 ± 0.1	40.6 ± 0.3
V_{oc} [mV]	650 ± 5	650 ± 5
FF [%]	76.5 ± 0.03	76.5 ± 0.03
η [%]	19.7 ± 0.21	20.2 ± 0.4

Table 7.1. Summary of total and active area *I-V* parameters for 12 bifacial c-Si solar cells (10 x 10 cm^2) fabricated at ECN. Total area measurements were performed at ECN on a Wacom solar simulator with a reflective brass chuck. The J_{sc} for the active area η was calculated from *EQE* measurements performed at TUDelft (no reflective chuck).

After wafer texturing, boron and phosphorous diffusions were employed to fabricate emitter and back surface field, respectively. SiN_x was deposited on both sides of the wafers. An Ag-based grid was screen printed on front and back with metal coverage area around 5%. After full processing, the cells were laser cut from full size semi-square (15.6 × 15.6 cm^2) to 10 × 10 cm^2 due to equipment restrictions for the DBR deposition. The n-Pasha cells used in this study differ from the ECN n-Pasha baseline [7] in the sense that the number of fingers at front and rear was equal in this cell run. In addition, front and rear metallization, were aligned to allow measurements in between the fingers (see below). Therefore, n-Pasha cell results quoted in this study cannot be compared directly to results obtained for ECN baseline cells with 20.4% efficiency [7]. Total- and active area *I-V* parameters are reported in Table 7.1. Total area *I-V* parameters, including the mismatch corrections, were measured at ECN by using Wacom solar simulator and a reflective chuck. Active area efficiency was calculated by using *FF* and V_{OC} from the total area *I-V* measurements and J_{SC} derived from EQE measurements performed between two metal fingers and without reflective chuck. The different methods used can explain the small difference in J_{SC}. For each BR configuration four bifacial cells were processed (see Figure 7.2).

7.4 Results and discussion

7.4.1 Optimized DBR for textured surfaces

The most stringent requirement for a DBR to be used as BR is to achieve the highest internal back reflectance ($R_b = 1$) in the wavelength range of weak absorption of c-Si [1] and independently from the angle of incidence and the polarization of light. This is the so-called omni-directionality. In section 4.4.2 of Chapter 4 and [14] it was demonstrated via optical simulations that a DBR formed by pairs of PECVD a-Si:H / a-SiN$_x$:H can exhibit omni-directionality as long as the incident medium (first layer before the DBR) has a refractive index around 1.5. In fact, in this case it is possible to ensure (for a wide angle range) that the maximal refraction angle at incident medium / DBR is smaller than the Brewster angle at internal interface of the first DBR pair and therefore there are no *T* losses through the DBR. For this reason a 100-nm thick PECVD SiO$_2$ layer was used as incident medium of the DBR. For this work, the DBR was designed in order to deliver an $R_b = 1$ at $\lambda_B = 1000$ nm with a photonic bandgap (PBG) of around 400 nm. In house 2-D ray tracing model developed at TUDelft was used. The simulations were performed in a spectral range between 300 and 1200 nm with steps of 10 nm and 10000 rays per each wavelength. A large parameter space was simulated with thickness of a-Si:H and a-SiN$_x$:H varying between [40, 140] nm and [70, 240] nm, respectively, with a step size of 10 nm. A number of 6 pairs of a-Si:H / a-SiN$_x$:H was found to be necessary in order to reach R_b close to 1 in the PBG. Lower number of pairs would lead to slightly wider PBG but lower R_b values [15]. As Figure 7.3 depicts, the loss in photocurrent density due to *T* (J_{phT}) was minimized for a DBR formed by 6 pairs of a-Si:H (80 nm) / a-SiN$_x$:H (180 nm). Such DBR will be called DBR 1 in the remainder of this Chapter. In order to validate the simulations results, the designed DBR was co-deposited on double-side polished and

---

[1] $\alpha d < 1$, where α and d are respectively, the Si absorption coefficient and thickness, for $d = 180$ μm the weak absorption region is defined by $\lambda \geq 1020$ nm.

double-side textured samples. As shown in Figure 7.4, for the DBR 1 deposited on a polished surface, zero *T* was achieved at long wavelengths.

When the DBR 1 was deposited (same deposition parameters and time) on a textured

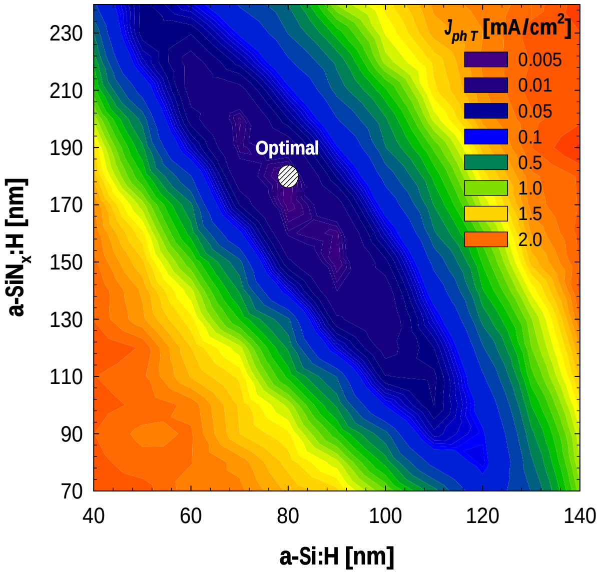

Figure 7.3. Contour plot of the loss in photocurrent density due to *T* through the DBR for the following simulated optical system air / pyramidal texture / Si (bulk) / pyramidal texture / SiO_2 / DBR / air.

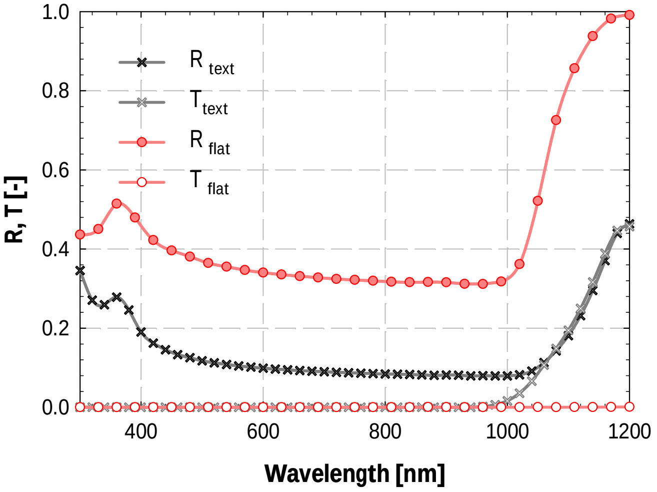

Figure 7.4. Measured *R* and for the optical system formed by air / Si (bulk) / SiO_2 / DBR 1/ air. The DBR was co-deposited on double side polished and double side textured surfaces.

surface (standard random pyramids fabricated via alkaline etching), higher *T* losses at long wavelength were observed. To explain these higher *T* losses the layer thicknesses of the deposited materials was inspected via cross-sectional scanning electron microscope (SEM). As shown in Figure 7.5 (b), the thicknesses of the individual layers in Y-direction are very close to the one co-deposited on a flat surface (Figure 7.5 (a)), while in X-direction they are scaled of a geometrical factor with respect to Y-direction. Such geometrical factor can be ideally calculated as $\sin(90°-\theta)=0.58$, where θ = 54.7° is the etching angle in case of alkaline random texturing. This effect is explained by the fact that the thickness of the layers deposited on pyramidal surface is determined by the same total growing species flow, which respect to the flat case, but on larger total area. This would mean that to reach the targeted thicknesses in the X direction the deposition time needs to be increased by a factor of 1.73 (1/0.58). In this case the DBR thickness in the X-direction of the textured surface would resemble the one obtained from the optimization process. Notice that in the deployed ray tracing model the DBR is defined as *coating* meaning that the thickness of all DBR layers in Y-direction are the same as it is for a polished surface. Because of the random nature of the alkaline etching, final angle distribution might deviate from 54.7° leading to a scaling factor different than the ideal 1.7. In addition, the non-conformal growth [16] of the deposited layers can affect geometry of the surface leading to different area enlargement factor which also changes with number (an thickness) of deposited layers. Therefore, in order to find the optimum thicknesses, a series of scaling factor *g* = [0.8, 1, 1.2, 1.5, 1.7] were applied to the layer thicknesses of the DBR optimized for flat substrates. To evaluate the performance of the DBR stacks with different *g* factors, *R* and *T* spectra were measured for the optical system sketched Figure 7.6 (a): light > air / pyramidal texture / Si (bulk) / pyramidal texture / SiO_2 / DBR / air using a PerkinElmer Lambda 950 spectro-photometer with integrating sphere.

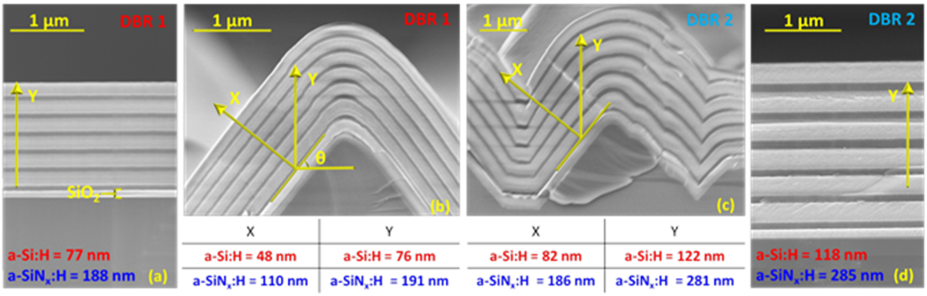

Figure 7.5.Cross-sectional SEM of DBR 1 deposited on flat (a) and textured surfaces (b). X and Y axis indicate the directions orthogonal to the pyramid facet and parallel to the PECVD deposition growth, respectively. Cross sectional SEM of DBR 2 deposited on textured (c) and flat surfaces (d). In order to achieve the desired layer thicknesses of 80 nm (a-Si:H) and 180 nm (a-SiN_x:H) on textured surfaces, deposition time for DBR 2 on textured and flat surfaces was increased by a factor equal to 1.5. SiO_2 is the first layer on top of the DBR.

As depicted in top and bottom panels of Figure 7.6, for g = 1.5, T losses were minimized and escaped R at 1200 nm was increased indicating higher internal R [13]. The resulting DBR will be called DBR 2 in the remainder of this chapter. From the cross-sectional SEM in Figure 7.5 (c) it is evident that the layer thicknesses of XDBR in the X-direction are close to the desired ones optimized for polished surface (see Figure 7.5 (a)). Even for the optimized layer thicknesses in case of textured substrates T losses still occur above 1100 nm. To make sure that such T losses are not related to an insufficient number of pairs, the number of DBR pairs were also increased from 6 to 10 for the sample with a the scaling factor of 1.5. As shown in Figure 7.6, R and T measured for DBRs formed by 6 and 10 pairs with same g (1.5) are comparable. Therefore, it can be concluded that on textured surfaces T losses at long wavelengths could be reduced by more than 60% when using a g = 1.5 compared with g = 1. However, even for the optimized DBR, T losses could not be completely eliminated. A possible explanation for this effect might be related to the fact that for tips and valleys of the pyramids thicknesses of DBR layers should be considered in Y-direction and change of the area enlargement for each DBR pair. Tips and valleys optically behave as the DBR 2 deposited on polished surface (Figure 7.5 (d)) for which the λ_B is shifted at longer wavelengths (> 1200 nm).

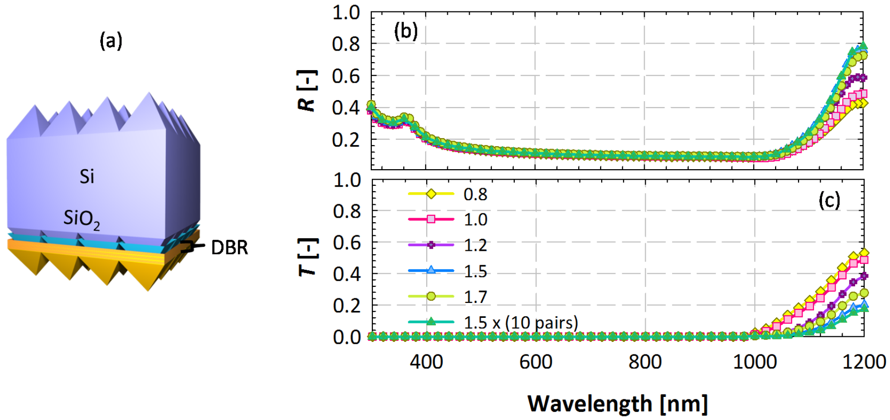

Figure 7.6. (a) Sketch of the optical system formed by air / pyramidal texture / Si (bulk) / pyramidal texture / SiO_2 / DBR / air. Measured R (b) and T (c) for the structure sketched in (a). Thicknesses of the individual layers of the DBR were multiplied for five scaling factors. T losses were minimized by more than 60% for a scaling factor of 1.5 when compared to g = 1. Only slightly lower T was achieved by using 10 pairs and scaling factor g of 1.5

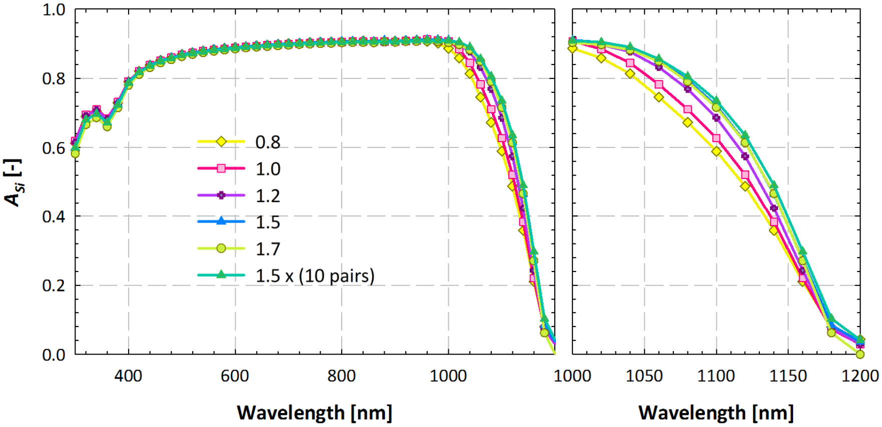

Figure 7.7. Measured A_{Si} for the optical structure sketched Figure 7.6 (a) employing DBR formed by different number of pairs and scaling factor *g*. The enhancement of the IR response for the samples with 6 pairs and *g* equal to 1.5 or 1.7 and the sample with 10 pairs and *g* equal to 1.5 are comparable.

This makes DBR 2 to suffer from higher T losses when deposited on polished surface. To explain the non-zero *T* of the DBR even after its thickness compensation, 3-D optical simulations were performed. A 3-D Maxwell solver [17] was used to evaluate the electromagnetic filed propagation of the electromagnetic filed in the optical system formed by air / Si / SiO_2 / DBR / air for both flat and randomly textured surfaces (3-D sketches in Figure 7.8 (a) and (b), respectively) at 950, 1050 and 1150 nm. For the flat structure, thicknesses of a-Si:H (80 nm) and a-SiN_x (180 nm), which minimize *T* losses as shown in section 7.4.1, were used. As simulation results in Figure 7.8 (a) show, even at very long wavelength, the electric field only propagates through the first two DBR pairs leading to zero *T* losses. For textured structure, the thicknesses of a-Si:H and a-SiN_x:H were multiplied by *g* = 1.5 along X-direction as shown in Figure 7.5 (c). As Figure 7.8 (b) shows, the electric field can propagate through the full DBR especially in correspondence of the tips and valleys of the DBR as previously mentioned. One could speculate that the electric field is coupled in wave-guided modes with some of the layer forming the DBR. Additional modelling which also takes into account the geometrical surface changes due to non-conformal growth is required.

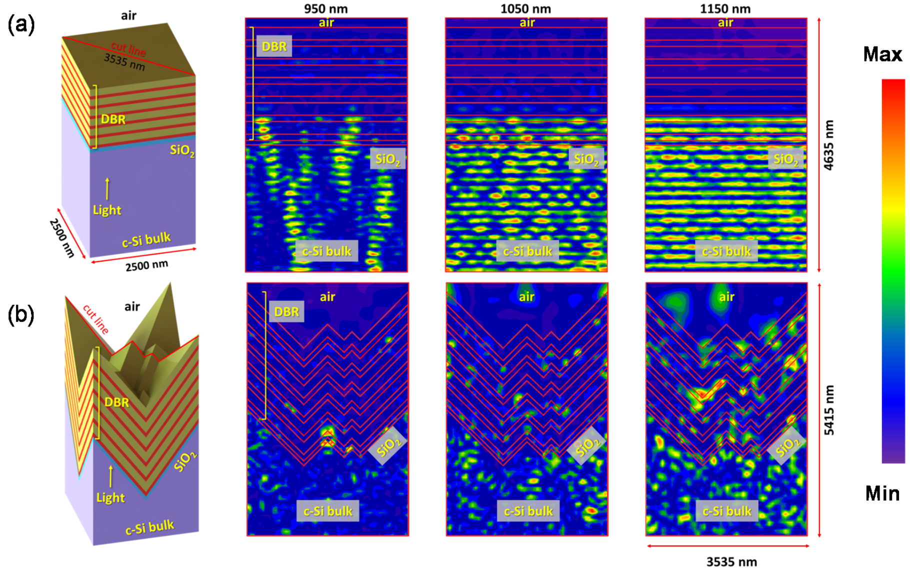

Figure 7.8. 3-D sketch and electric field propagation at wavelengths 950, 1050 and 1150 nm of the simulated optical system formed by: air / Si / SiO$_2$ / DBR / air for both (a) flat and (b) randomly textured surfaces.

Experimentally determined silicon absorption ($A_{Si}= 1-R-T$) for all samples is shown in Figure 7.7. The figure clearly demonstrates that the infrared response (IR) is enhanced when increasing g from 0.8 to 1.5. In addition, the A_{Si} for the samples with 6 pairs and g = 1.5 or 1.7 and the sample with 10 pairs and g = 1.5 are comparable. This indicates that the increase of the deposition time when using more than 6 pairs and g higher than 1.5 does not lead to a significant enhancement of the infrared absorption in silicon. Implied photocurrent density (J_{ph}) was calculated by convoluting the measured A_{Si} with AM1.5 spectrum [18] in the wavelength range between 300 and 1200 nm. An absolute increase in J_{ph} equal to 0.8 (0.9) mA/cm^2 was achieved when going from the DBR with g = 0.8 and 6 pairs to g = 1.5 and 6 (10) pairs. This absorption enhancement is related to the shift of λ_B as function of the layer thicknesses of the DBR. Even though such quantity is not directly measurable, a correlation between the measured Bragg wavelength at DBR / air (λ_B air) interface and the A_{Si} behaviour was found. In particular, Figure 7.9 (a) shows that λ_B-*air* is shifted to longer wavelengths when the scaling factor is increased and the samples are flipped, being illuminated from the DBR side. In addition, with increasing scaling factor (i.e. thickening DBR constituting layers) the PBG becomes wider [15]. This means that most likely λ_B for the sample with scaling factor equal to 1.5 is located at long wavelengths and thus enhancing A_{Si} in the IR. On the contrary, the PGB of the sample with g = 0.8 would be located a short wavelength leading to poorer A_{Si} in the IR. Moreover, the sample with g = 1.5 formed by 10 pairs shows almost the same PBG as the one with 6 pairs but delivers higher *R*. Because of their narrow PBG and high reflectance in the visible range, the samples with scaling factor between 0.8 and 1 show very bright colours (see Figure 7.9 (d) and (e)). On the other hand, samples with *g* from 1.2 to 1.7 have the maximum *R* outside the visible range and their colour perception is related to the lower *R* peaks present at short wavelengths (see Figure 7.9 (f) and (h)-(j)). For comparison purposes, Figure 7.9 (b) also reports the *R* measured in air ($R_{in\ air}$) for the Ag and WP BRs. For both BRs high *R* values in a broad wavelength range are observed. The photograph of WP and Ag BRs deposited on textured surfaces are shown in Figure 7.9 (c) and (g), respectively.

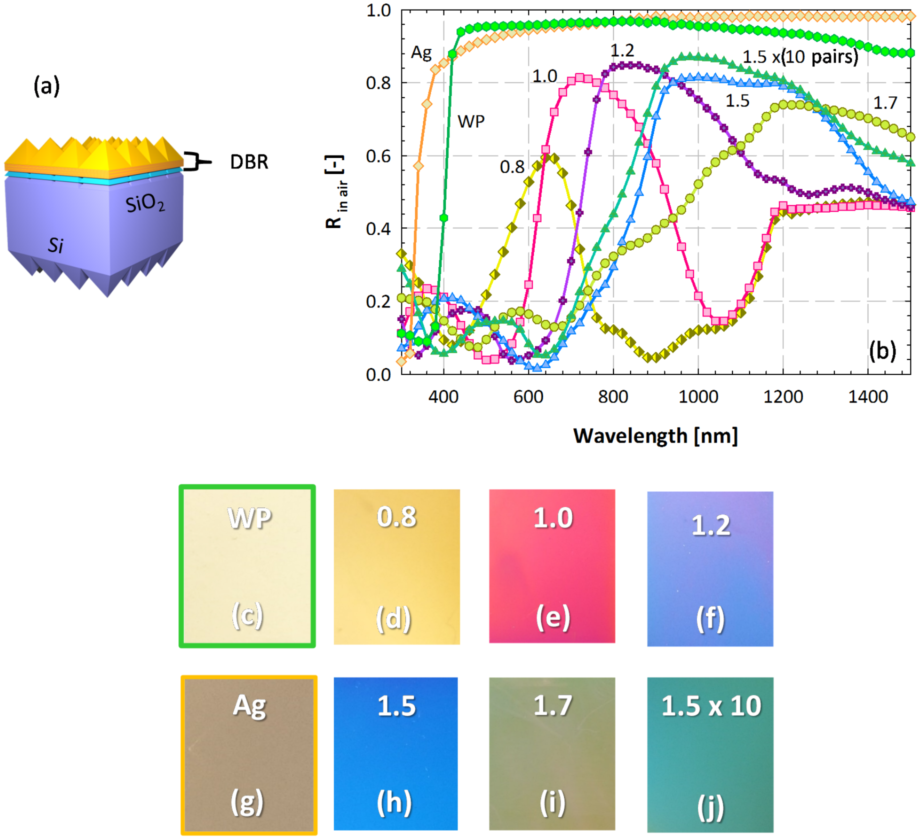

Figure 7.9. (a) Sketch of the optical system formed by air / BR / pyramidal texture / Si (bulk) / pyramidal texture / air and its measured $R_{in\ air}$. The thicknesses of the individual layers of the DBR were multiplied for five scaling factors. For the sample with *g* equal to 1.5 the number of pairs was also increased to 10. WP and Ag back BR deliver the highest *R* in air. In (c)-(j) the actual pictures of the fabricated BRs are shown.

7.4.2 Optimized Ag Back reflectors

The ECN 3D ray-tracing model [17] was used to optimize the rear SiN_x thickness in combination with the Ag BR. This home-built model combines geometrical and thin-film optics and includes a regular pyramid front and rear texture. Simulations were performed in the spectral range between 340 and 1190 nm; steps of 10 nm were used and 10000 rays per wavelength were simulated.

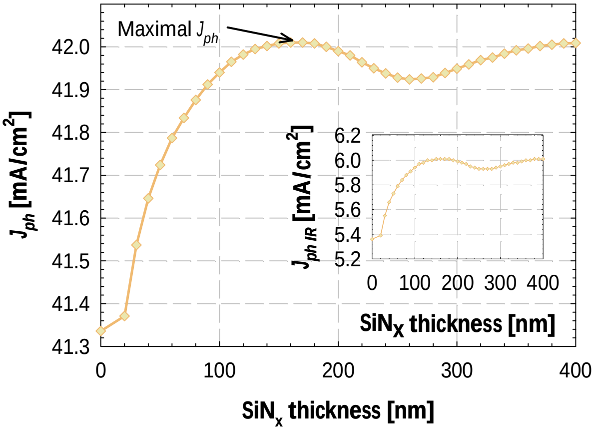

Figure 7.10 J_{ph} as function of the rear SiN_x thickness for the full spectral range (340 - 1190 nm) and for the IR ($J_{ph\ IR}$) part (990 - 1190 nm) only (see inset). J_{ph} is maximized for 160-nm thick SiN_x.

The thickness of SiN_x was varied between 10 and 400 nm in steps of 10 nm. From the simulations the A_{Si} was determined and subsequently the J_{ph} was derived. Ray-tracing simulations were used to optimize the thickness of rear SiN_x combined with the Ag BR. As reported in [13], both absorption in the metal due to evanescent waves and thin-film interference due to SiN_x presence affect the thickness of SiN_x itself for which parasitic absorption in metal is quenched and the reflection is maximized. In Figure 7.10, the J_{ph} is plotted versus the rear SiN_x thickness for the full spectral range (340 - 1190 nm) and, in the inset, for the IR ($J_{ph\ IR}$) part (990 - 1190 nm) only. J_{ph} is maximized for 160-nm thick SiN_x. Subsequently, for the fabricated cells the rear SiN_x thickness was varied around the maximum. The cells with the best performing SiN_x thickness were included in the comparison with the other BR configurations. The differences in performance were minimal. Through this procedure cells with 140-nm thick SiN_x were selected.

7.4.3 Performance of the optimized BRs in n-Pasha c-Si solar cells

WP and DBR BRs were deposited at the backside (BS) of the bifacial solar cells on top of their metallization. The outer edges of the BS bus-bars were masked to be able to contact the cells. For the Ag BR configuration, 140-nm thick SiN_x was used at rear side (see section 7.4.2) followed by 100-nm thick evaporated Ag. Measured *R* and *T* including front side shading losses for the fabricated devices are shown in Figure 7.11. As the figure depicts, the fabricated cells with no BR and DBR 1 delivered the lowest *R* and the highest *T* losses at long wavelengths. On the contrary, WP and the optimized DBR 2 delivered the highest *R* and lowest *T* losses at long wavelengths. These performances were very close to those obtained for the Ag blanket evaporated on rear SiN_x of n-Pasha control cells. Notice that the *R* and *T* values measured for the cells in Figure 7.11 are lower than the ones obtained for the test structures reported in Figure 7.3. A possible reason for such behaviour is related to the free carrier absorption of emitter and BSF.

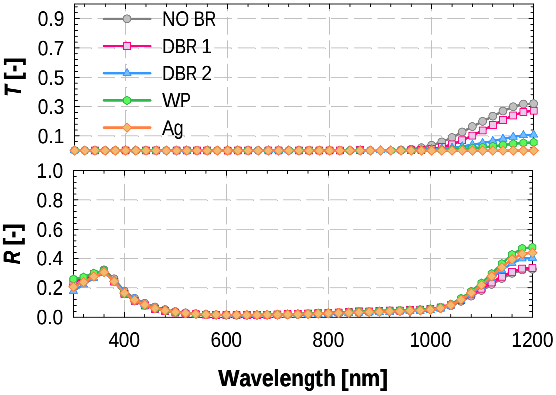

Figure 7.11. Measured *R* and *T* spectra of *n-Pasha* c-Si solar cells endowed with different BRs (optical shading losses from the metal grids are included).

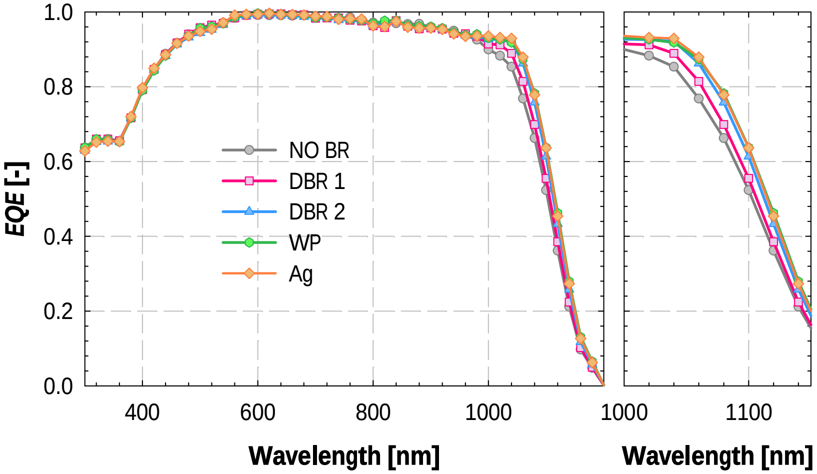

Figure 7.12. Measured averaged *EQE* (4 cells for each BR) for different BR configurations. *EQE* of the WP delivered the highest enhancement in the IR response among the dielectric BRs.

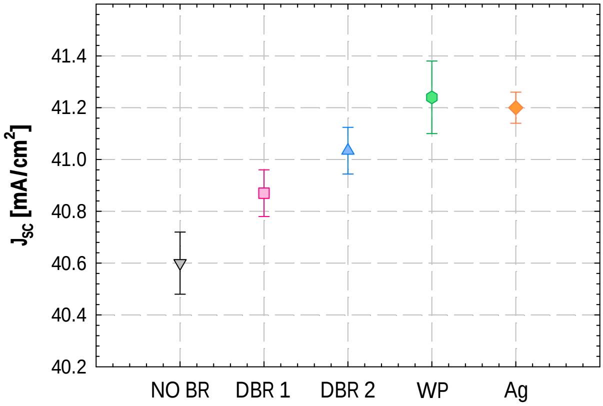

Figure 7.13. J_{SC} from measured EQE of cells endowed with BRs studied in this work. The error bars represent the standard deviation calculated for four cells in each BR configuration.

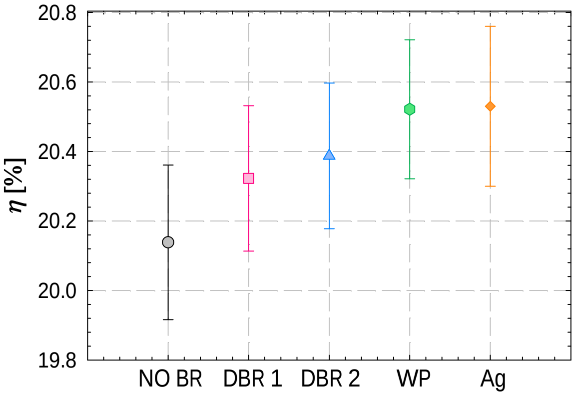

Figure 7.14 Measured (active area) conversion efficiency of the fabricated solar cells with different BRs. In case of WP used as BR, an average cell efficiency gain of 0.34% was achieved with respect to the device with no BR.

To accurately evaluate the impact of the studied BR configurations on cells performances, *EQE* measurements were performed at TUDelft in between fingers and without (reflective) chuck at BS of the cells. Front and back metallization were aligned to ensure that only the (dielectric) BR was probed in the measurement. *EQE* spectra were measured using a silicon solar cell calibrated at Fraunhofer ISE calLab. Figure 7.12 clearly shows that the cell with DBR 1 exhibits the lowest EQE enhancement in the IR region with respect to the configuration with no BR. The application of DBR 2, optimized for textured substrates, results in a clear improvement of the EQE of in the IR. Finally, the largest IR improvement was obtained for the WP, which shows an IR response -

within the error margins - equal to that of the more expensive Ag BR. As reported in Figure 7.13, the WP BR gives in average the highest absolute gain of 0.57 mA/cm^2 on the J_{SC} with respect to the configuration with no BR. The conversion efficiency gain for the different BRs was calculated by using the J_{SC} values with the external parameters (V_{OC} and FF) summarized in Table 7.1. In Figure 7.14, the conversion efficiencies for all BR configurations studied in the work is reported. An absolute efficiency gain of 0.34% compared to the cell with no BR was found in case of WP BR. Notice that such efficiency gain comes only from the increase of J_{SC}. Actual colour perception of the rear side of the bifacial c-Si coated with DBR 1 is shown in Figure 7.15 (a). The colour tuning of the DBR enables the possibility of fabricating rear side coloured bifacial glass/glass modules for building integrated applications (Figure 7.15 (b)).

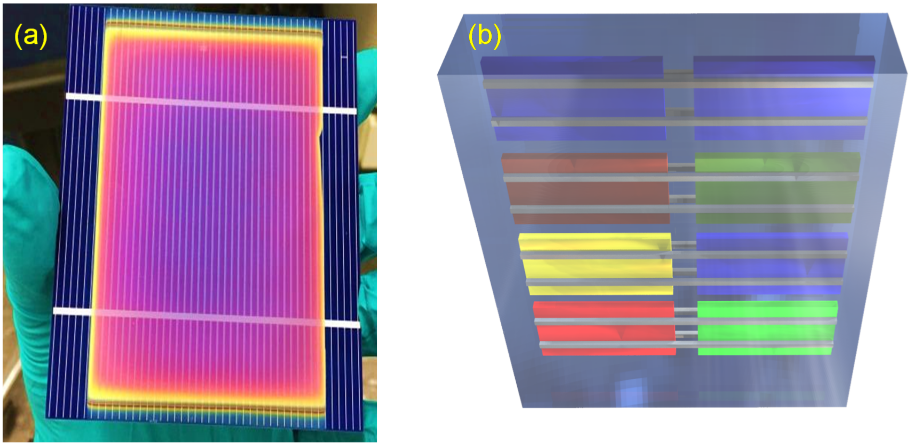

Figure 7.15. (a) Actual photograph of the rear side of the bifacial c-Si solar cell coated with DBR 1. (b) Example of rear side coloured bifacial cells in a glass/glass module.

7.5 Conclusions

In this Chapter different back reflectors applied to open rear *n-Pasha* diffused c-Si solar cells were studied. A DBR was optimized for application on the BS of textured cells. With respect to the DBR optimized for flat surface the PECVD deposition time was increased by a factor g equal to 1.5 to achieve the optimized thicknesses in the direction orthogonal to the pyramids' facets. T losses at long wavelengths of the DBR deposited on textured surface could be reduced by more than 60% when using a $g = 1.5$ compared to $g = 1$ but yet not completely eliminated. It can be speculated that this effect might be related to: (i) the fact that the tips and valleys of the pyramids are sources of T losses as DBR layers are thicker in such regions (ii) non-conformal growth leads to a change of the geometrical surface for each DBR pair. Measured R from the DBR / air interface showed a correlation with A_{Si} behaviour as function of the thicknesses of the individual layers of the DBR pair. In particular, the DBR showing a PBG in the IR region, when illuminated and measured from the rear side (air / DBR / Si (bulk) / air), is also the one that delivers the highest IR A_{Si} enhancement when illuminated from the front side (air / Si (bulk) / DBR / air). DBR with scaling factor g equal to 1 and 1.5, WP and Ag BRs were applied to open rear n-Pasha c-Si solar cells. Measured *EQE* and external parameters of the fabricated solar cells in case of no BR were compared to DBR, WP and Ag BRs. The highest *EQE* in the NIR was observed in case of the WP and Ag BRs due to the minimization of the optical losses at long wavelengths. The highest average gain in J_{SC} (0.57 mA/cm^2) was achieved in case of WP used as BR. This led to an average efficiency gain of 0.34% absolute compared with the cells with no BR. Finally, the performances of the optimized DBR (DBR 2) were found to be slightly lower than the one exhibited by evaporated Ag. In exchange, coloured BS is enabled, opening new possibilities in building-integration of such open rear c-Si solar cells[1].

7.6 References

[1] International Technology Roadmap for Photovoltaic (ITRPV.net) Results 2014. http://www.itrpv.net/Reports/Downloads/.

[2] S. W. Glunz, Crystalline Silicon Solar Cells with High Efficiency, in Advanced concepts in photovoltaics, The Royal Society of Chemistry. 2014, 1-29, DOI:10.1039/9781849739955-00001.

[3] A. Ingenito, O. Isabella, M. Zeman, Accurate opto-electrical modeling of multi-crystalline silicon wafer-based solar cells, Sol. Energ. Mat. Sol. 2014, 123, 17-29, http://dx.doi.org/10.1016/j.solmat.2013.12.019.

[4] S.A. McHugo, H. Hieslmair, E.R. Weber, Gettering of metallic impurities in photovoltaic silicon Appl. Phys. A Mater. Sci. 1997, 64, 127–137.

[5] S. W. Glunz, S. Rein, J.-Y. Lee, W. Warta, Minority carrier lifetime degradation in boron-doped Czochralski silicon, Journal of Applied Physics. 2001, 90, 2397-2404, DOI:http://dx.doi.org/10.1063/1.1389076.

[6] I. G. Romijn, A. Gutjahr, D. Saynova, J. Anker, E. J Kossen, K. Tool, Cost effective n-Pasha solar cells with efficiency above 20%, Photovoltaics International. 2013, 20, 33-40.

[7] I. G. Romijn, G. Janssen, M. Koppes, J. Liu, Y. Komatsu, J. Anker, A. Gutjahr, E. Kossen, A. Mewe, K.. Tool, O. Siarheyeva, M. Ernst, Towards 21%: front side improvements for n-Pasha solar cells, Proceedings of SNEC 8th International Photovoltaic Power Generation Conference & Exhibition, Shanghai, China, 2014.

[8] T. S. Boscke, D. Kania, A. Helbig, C. Schollhorn, M. Dupke, P. Sadler, M. Braun, T. Roth, D. Stichtenoth, T. Wutherich, R. Jesswein, D. Fiedler, R. Carl, J. Lossen, A. Grohe, H.-J. Krokoszinski, Bifacial n-Type Cells With >20% Front-Side Efficiency for

---

[1] Notice that because of the large light parasitic absorption of the DBR bifaciality is no longer possible.

Industrial Production, Photovoltaics, IEEE Journal of. 2013, 3, 2, 674-677, doi: 10.1109/JPHOTOV.2012.2236145.

[9] A. Edler et al., BiSoN : Bifacial Industrial Solar Cell on N-type, 3rd nPV workshop, Chambéry, France, 2013.

[10] Available on: http://www.yinglisolar.com/en/products/monocrystalline/panda-60-cell-series/.

[11] S. Ponce-Alcántara, A. A. Vivas Arangú, G. S.Plaza, The importance of optical characterization of PV backsheets in improving solar module power, 8th International Photovoltaic Power Generation Conference & Exhibition, Shanghai, 2014.

[12] J. Blanker, TiO_2 Nanoparticles as Back Reflector in Thin-Film Solar Cells, MSc thesis, Delft University of Technology, The Netherlands, 2013.

[13] Z. C. Holman, M. Filipič, B. Lipovšek, S. De Wolf, F. Smole, M. Topič, C. Ballif, Parasitic absorption in the rear reflector of a silicon solar cell: Simulation and measurement of the sub-bandgap reflectance for common dielectric/metal reflectors, Sol. Energ. Mat. Sol. 2014, 120, 426-430.

[14] A. Ingenito, O. Isabella, M. Zeman, Experimental Demonstration of 4n2 Classical Absorption Limit in Nanotextured Ultrathin Solar Cells with Dielectric Omnidirectional Back Reflector, ACS Photonics, 2014, 1, 270-278.

[15] O. Isabella, Light management in thin-film silicon solar cells, Ph.D. dissertation, Photovoltaic Materials and Devices group, Delft Univ. of Technology, Delft, the Netherlands, 2013, 6, 6.3.1, 128-132.

[16] M. Sever, B. Lipovšek, J. Krč, A. Čampa, G. S. Plaza, F.-J. Haug, M. Duchamp, W. Soppe, M. Topič, Combined model of non-conformal layer growth for accurate optical simulation of thin-film silicon solar cells, Sol. Energ. Mat. Sol., 119, 2013, 59-66, DOI : http://dx.doi.org/10.1016/j.solmat.2013.05.016.

[17] White papers in Ansys HFSS official website, http://www.ansoft.com/products/hf/hfss/.

[18] http://rredc.nrel.gov/solar/spectra/am1.5/.

[19] A. R. Burgers, L .H. Slooff, R. Kindeman, J. A. M. Van Roosmalen, Modelling of luminescent concentrators by ray-tracing, Proceedings of 20th EC Photovolt. Solar Ener. Conf. 2005, 394-397

8

Conclusions and outlook of the thesis

8.1 Conclusions

Wafer based c-Si solar cells dominates the PV market. To keep this technology as PV leader also in the coming years, continuous improvement in conversion efficiency without increasing processing costs are required. In this thesis novel concepts to increase conversion efficiency and decrease the cost of solar cells via opto-electrical surfaces engineering were presented. In particular, advanced light management techniques were developed to enhance light absorption in thin c-Si absorber and to fabricate customized PV products for building integrated photovoltaic (BIPV).

In Chapter 1 the theoretical efficiency limit and light management techniques for wafer based c-Si solar cells were reviewed. In addition the main objectives of this thesis were outlined.

In Chapter 2 the general working principle and main recombination mechanisms in c-Si solar cells were described. The status of fabricated high efficiency wafer based c-Si solar cells based on different architectures was also presented.

In Chapter 3 the analysis of main opto-electrical losses in the fabricated mc-Si solar cell was performed by using the ASA simulation tool. Such analysis showed that the main optical losses for a mc-Si solar cell are due to high R, incomplete absorption at long wavelength and poor internal rear reflectance of the Al-BSF. These observations led to the work presented in the remainder chapters.

In Chapter 4 an advanced light trapping scheme capable of minimizing the major optical losses of state-of-the-art c-Si solar cells was demonstrated. For such light trapping scheme a combination of surface textures with different geometric scales were used. In this way different optical effects can be triggered enhancing silicon absorption over a broad wavelength range. In particular, the light trapping here studied employed nano-texturing fabricated via reactive ion etching (RIE) on the front side and micro texturing based on alkaline etching on the rear side. Almost ideal back reflectors such as Ag or Distributed Bragg reflectors (DBR) were applied on the rear side. The light trapping scheme was applied to a ultra-thin (20 μm) absorber layer resulting in the closest experimental demonstration ever reported of the upper limit of light absorption in Si (known as $4n^2$). Interdigitated back contacted c-Si solar cell was indicated as the most promising solar cell architecture to apply such light trapping scheme.

In Chapter 5 a simplified self-aligned process for fabrication high efficiency IBC c-Si solar cells was demonstrated. The process involved the combination of ion implantation and epitaxial growth of in-situ doped Si. The process flow was optimized to minimize the thermal budget and the number of lithographic steps. By using only two lithographic steps, a conversion efficiency equal to 20.2% on 9 cm^2 device was demonstrated. For such solar cell architecture it was shown that a lightly doped front surface field improves carrier collection.

In Chapter 6 the application in IBC device of the advanced light management technique studied in Chapter 4 was presented. For the application of such light trapping scheme two major issues were tackled. The first was to remove surface defects induced by the RIE process and decrease surface recombination, for which a cost effective process was developed. This step was based on highly diluted alkaline etching and resulted in a remarkable decrease of the surface recombination rate while still maintaining outstanding optical properties. The second was to adapt the IBC process developed in this thesis to the light trapping scheme since the IBC process requires a polished rear side. Therefore, the decoupled front (nano-textured) and rear side (mico-texturing) light trapping scheme of Chapter 4 was modified to be applied in such device. As a solution two textures were superposed on the front side of the wafer; forming a modulated surface texture (MST) and leading to similar absorption enhancement as shown for the decoupled scheme demonstrated in Chapter 4. The combination of the advanced light trapping and surface passivation schemes was employed in IBC c-Si solar cells. Top efficiency of 19.8% for MST-IBC solar cell was demonstrated.

Chapter 7 was focused on the application of advanced light management techniques in bifacial c-Si solar cells. The objective of this study was twofold: (i) enhancing cell efficiency by increasing the internal rear reflectance and (ii) providing novel solutions for BIPV applications. In particular, DBR and TiO_2 particles in the role of white paint (WP) were used as back reflectors of bifacial c-Si solar cells. The WP BR showed higher solar cells performance enhancement compared with DBR. However, the DBR thanks to colour tuning enables the fabrication of rear side coloured bifacial modules, which can be used for BIPV applications. Bifacial c-Si solar cells with efficiency of 0.3% absolute with respect to the case where no back reflector is applied were demonstrated.

8.2 Outlook of the thesis

During my PhD program I have conceived many ideas on how to improve the conversion efficiency of the solar cell architectures reported in this thesis. However, due to time limitation, such ideas could not be applied. Nevertheless a future prospective about their implementation is given in this section.

Starting from the self-aligned IBC device developed in this thesis (Chapter 5), a roadmap for achieving high conversion efficiency is proposed in Figure 8.1. The approaches to improve conversion efficiency were studied by deploying SENTAURUS t-cad modelling [1]. In more detail, by optimizing the rear design and improving the front side passivation quality, efficiency higher than 21% can be reached without changes in the process flow. To further increase conversion efficiency, solutions aiming to minimize contact recombination and increase *FF* are required. The solution studied to improve *FF* are the usage multiple and thicker metal fingers and/or etch back of the B region with low doping concentration (see Figure 5.8). To improve V_{OC}, lower J_{0s} of the passivated and metallized region are required. In case of optimized point contacts efficiency higher than 22.5% were simulated.

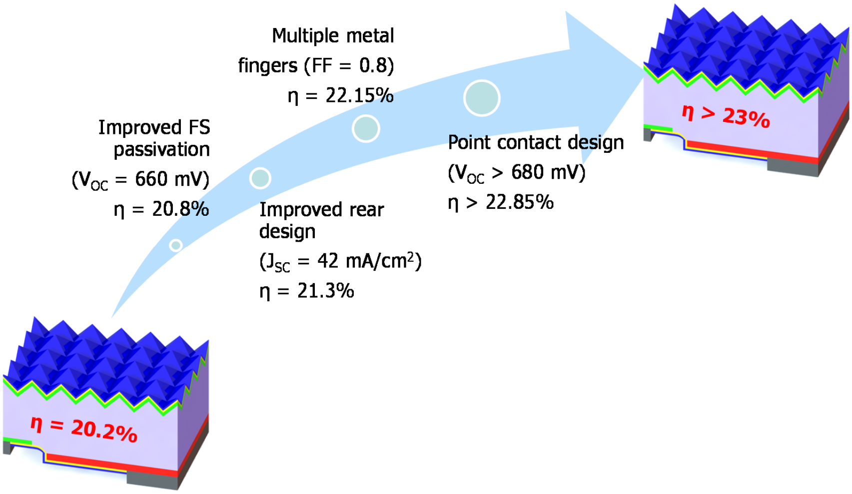

Figure 8.1. Roadmap for high efficiency IBC c-Si solar cell with self-aligned process designed in this thesis.

The advanced light trapping and passivation scheme developed in Chapter 6 could be used to demonstrate high efficiency ultra-thin c-Si solar cells where both optical and electrical losses are minimized. In my vision, the next generation c-Si solar cell will be based on ultra-thin (< 50 µm) c-Si absorber and will involve advanced passivation schemes and light management techniques (see Figure 8.2 (a)). By using Quokka [2] software I have simulated the conversion efficiency dependence as function of the bulk lifetime (τ_{bulk}) and wafer thickness (for the n-type c-Si absorber). For the opto-electrical simulations I have used the following assumptions:

1. Absorption calculated by using $4n^2$ enhancement (practical solutions to approach such limit are shown in Chapter 4 and 6);
2. Passivating contacts for which contact recombination is minimized [3]-[4];
3. Advanced surface passivation of the nano-texturing as shown in Chapter 6.

As Figure 8.2 (b) shows, for τ_{bulk} range studied in this work one can notice that:

i. The conversion efficiency of thinner wafer are less sensitive to the τ_{bulk} rather that thick ones. This enables the usage of thinner and cheaper substrates to reduce cell material costs;
ii. Efficiency has a maximum of 25.7% for a τ_{bulk} below 1 ms and thickness of 40 µm. Notice that similar conversion efficiency constitutes the actual world record and has been demonstrated by Panasonic by using hetero-junction IBC architecture on 100-µm thick high-quality substrate [4].

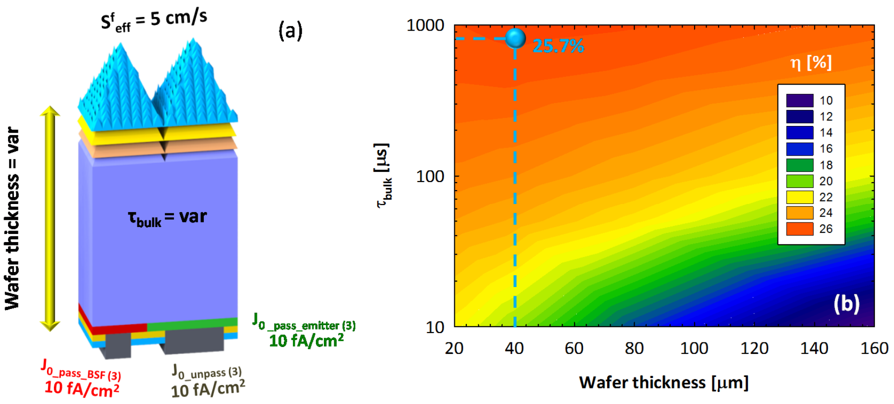

Figure 8.2. (a) 3-D sketch of IBC c-Si solar cell employing advanced light management and passivation schemes. (b) Conversion efficiency (η) as function of the wafer thickness and τ_{bulk}.

8.3 References

[1] http://www.synopsys.com/tools/tcad/Pages/default.aspx.

[2] A. Fell, A free and fast three-dimensional/two-dimensional solar cell simulator featuring conductive boundary and quasi-neutrality approximations, IEEE Transactions on Electron Devices. 2013, 60, 733–738.

[3] F. Feldmann, M. Simon, M. Bivour, C. Reichel, M. Hermle, S.W. Glunz, Efficient carrier-selective p- and n-contacts for Si solar cells, Sol. Energy Mater. Sol. Cells. 2014, 131, 100–104.

[4] http://news.panasonic.com/press/news/official.data/data.dir/2014/04/en140410-4/en140410-4.html

Summary

Climate changes due to increase of CO_2 emission are becoming a serious issue for this planet. The so called *climate crisis* has been the main topic of the last United Nations Climate Change Conference (COP 21) . Direct conversion of sunlight into electricity is one of the most promising technology for achieving the COP 21 agreement. Wafer-based crystalline silicon (c-Si) solar cells account for more than 90% of the total PV market because silicon is a non-toxic and abundant material and Si-based PV modules have demonstrated long term stability and high durability. To maintain this technology dominant also in the coming years, continuous improvement in conversion efficiency without increasing processing costs are required. In this thesis novel solutions based on opto-electrical surface engineering are presented as potential solutions to increase conversion efficiency and/or decrease the costs of wafer-based c-Si solar cells. In particular, advanced light management techniques were developed to enhance light absorption in thin c-Si absorber and to fabricate customized PV products for building integrated photovoltaic (BIPV) applications. This thesis begins with introducing, theoretical limits (Chapter 1), working principles and current status (Chapter 2) of wafer-based c-Si solar cells. In Chapter 3 the losses analysis of industrial multi-crystalline silicon (mc-Si) solar cell was performed by using the ASA simulation tool. Such analysis pointed out the main opto-electrical losses for a mc-Si solar cell which were tackled in the next Chapters. In particular, Chapter 4 deals with design and fabrication of advanced light trapping scheme for minimizing optical losses of state-of-the-art c-Si solar cells. To this aim a combination of surface textures with different geometrical scales were used in order to trigger several optical effects. In particular, nano-texturing fabricated via reactive ion etching (RIE) on the front side and micro texturing based on alkaline etching on the rear side were used providing broadband light-in coupling and light scattering. Almost ideal back reflectors such as Ag or Distributed Bragg reflectors (DBR) were applied on the rear side. By using such light trapping scheme, the so-called $4n^2$ absorption enhancement limit, which has been elusive for more than 30 years was experimentally demonstrated on a broad wavelength range. The interdigitated back contact (IBC) c-Si solar cell was indicated as the most promising solar cell architecture to apply such light trapping scheme. This technology was not available within the PVMD group. Therefore, in Chapter 5 a simplified self-aligned process for fabrication high efficiency IBC c-Si solar cells was demonstrated. The process involved the combination of ion implantation and epitaxial growth of in-situ doped Si. The process flow was optimized to minimize the thermal budget and the number of lithographic steps. By using only two lithographic steps, a conversion efficiency equal to 20.2% on 9 cm^2 device was demonstrated. For such solar cell architecture it was shown that a lightly doped

front surface field improves carrier collection. After developing a process flow for fabricating IBC c-Si solar cells, the application of the advanced light management technique to IBC was presented in Chapter 6. To this aim two major issues were tackled. The first was related to the removal of surface defects induced by the RIE process to decrease surface recombination. To achieve this goal a cost effective process was developed. The second dealt with adapting the light trapping scheme to the IBC process integration. To this aim, the decoupled front (nano-textured) and rear side (mico-texturing) light trapping scheme of Chapter 4 was modified by superposing both texture scales on the front side of the wafer. This approach is called modulated surface texture (MST). The combination of the advanced light trapping and surface passivation schemes was employed in IBC c-Si solar cells. Top efficiency of 19.8% for MST-IBC solar cell was demonstrated. Advanced light management techniques were also applied to bifacial c-Si solar cells. The objective of this study was twofold: (i) enhancing cell efficiency by increasing the internal rear internal reflectance and (ii) providing novel solutions for BIPV applications. In particular, DBR and TiO_2 particles in the form of white paint were used as back reflectors of bifacial c-Si solar cells. The DBR enabled the possibility of fabricating rear side coloured bifacial modules, which can be attractive for BIPV applications.

Samenvatting

Klimaatveranderingen, veroorzaakt door een toename in CO_2-uitstoot, worden een steeds groter probleem voor onze planeet. Deze zogenaamde klimaatcrisis was het hoofdonderwerp bij de laatste VN Klimaatconferentie (COP 21). De directe omzetting van zonlicht in elektriciteit is een van de meest veelbelovende technologieën om de gemaakte COP21-afspraken na te kunnen komen. Omdat silicium een niet giftig en een voorradig materiaal is, en op silicium gebaseerde PV modules bewezen stabiel en duurzaam zijn, vertegenwoordigen zonnecellen op basis van wafers van kristallijn silicium (c-Si) meer dan 90% van de PV markt. Om ook in de toekomst dominant te zijn, moet het omzettingsrendement van deze technologie continu worden verbeterd zonder dat de productiekosten hierdoor toenemen. In dit proefschrift worden nieuwe oppervlakte-engineering oplossingen gepresenteerd voor het verhogen van het omzettingsrendement en/of het verlagen van de productiekosten van wafer-gebaseerde c-Si zonnecellen. Geavanceerde lichtmanagement-technieken zijn ontwikkeld om de absorptie van licht in dunne c-Si wafers te verhogen en om toegesneden PV producten te ontwikkelen voor gebouw-geïntegreerde PV (BIPV) toepassingen. Dit proefschrift begint met de introductie van de theoretische limieten (hoofdstuk 1), de onderliggende principes en de huidige status van wafer-gebaseerde c-Si zonnecellen (hoofstuk 2). In hoofdstuk 3 worden de verliezen in multikristallijn silicium (mc-Si) zonnecellen geanalyseerd met behulp van het ASA simulatieprogramma. Aan de hand van deze analyse worden de belangrijkste opto-elektrische verliezen in mc-Si geïdentificeerd, welke in de volgende hoofdstukken worden aangepakt. Hoofdstuk 4 gaat over het ontwerp en de fabricage van geavanceerde lichtvangmethodes om de optische verliezen in c-Si zonnecellen te minimaliseren. Oppervlaktetexturen met verschillende geometrische schalen zijn gebruikt om verschillende optische effecten te benutten. Nanotexturen aan de voorzijde, gemaakt met behulp van reactief ion-etsen (RIE), en microtexturen aan de achterzijde, gemaakt met behulp van etsen in basische oplossing, zijn gebruikt voor breedbandige lichtinkoppeling en -verstrooiing. Bijna ideale achterzijdereflectoren zoals zilver of Bragg reflectoren (DBR) zijn toegepast op de achterzijde. Met behulp van deze lichtvangmethodes is na meer dan 30 jaar de zogenaamde $4n^2$ absorptielimiet experimenteel aangetoond in een breed golflengtebereik. De *interdigitated back contact* (IBC) c-Si zonnecel is geselecteerd als de meest veelbelovende zonnecelarchitectuur om dergelijke lichtvangmethodes op toe te passen. Deze technologie was niet aanwezig binnen de PVMD groep. Daarom is een vereenvoudigd, zelf-uitlijnend proces voor de fabricage van hoog-rendement IBC c-Si zonnecellen ontwikkeld in hoofdstuk 5. Het proces bevat een combinatie van ion implantatie en epitaxiale groei van in-situ gedoteerd silicium. Het proces is geoptimaliseerd om het thermische budget en het aantal lithografische stappen te minimaliseren. Met het gebruik van slechts twee lithografische stappen is een omzettingsrendement van maar liefst 20.2% gerealiseerd op een cel van 9 cm^2. Voor dergelijke zonnecelarchitecturen is aangetoond dat een licht gedoteerd *front surface field* de collectie van ladingsdragers verbetert. Na de ontwikkeling van het proces voor de fabricage van IBC c-Si zonnecellen, zijn in hoofdstuk 6 geavanceerde lichtmanagementtechnieken op IBC zonnecellen toegepast. Hier zijn twee grote kwesties aangepakt. Het eerste is het verwijderen van oppervlaktedefecten veroorzaakt door het RIE proces om de oppervlakterecombinatie te verminderen. Een kosteneffectieve werkwijze is hiervoor ontwikkeld. Het tweede probleem heeft betrekking op het aanpassen van de lichtvangmethodes voor het IBC proces. Hiervoor zijn de ontkoppelde voorzijde (nanotextuur) en achterzijde (microtextuur) uit hoofdstuk 4 door middel van superpositie gecombineerd op de voorzijde van de wafer. Dit word een *modulated surface texture* (MST) genoemd. De combinatie van geavanceerde lichtvang- en oppervlaktepassiveringsmethodes is toegepast op IBC c-Si zonnecellen. Een toprendement van 19.8% voor MST-IBC zonnecellen is aangetoond. Geavanceerde lichtmanagementtechnieken zijn ook toegepast op *dubbelzijdige* c-Si zonnecellen. Het doel van deze studie was tweeledig: (i) het verbeteren van het zonnecelrendement door het verbeteren van de interne achterzijdereflectiviteit en (ii) het verstrekken van nieuwe oplossingen voor BIPV toepassingen. Een DBR en TiO_2 deeltjes, in de vorm van witte verf, zijn gebruikt als achterzijdereflectoren in dubbelzijdige c-Si zonnecellen. De DBR bied de mogelijkheid om de achterzijde van dubbelzijdige modules te kleuren, wat aantrekkelijk is voor BIPV toepassingen.

List of publications

Peer-reviewed papers

1. Accurate opto-electrical modelling of multi-crystalline silicon wafer-based solar cells, Solar Energy Materials & Solar Cells- Journal, 123,17-29, (2014).
A. Ingenito, O. Isabella, S. Solntsev, M. Zeman

2. Experimental Demonstration of 4n2 Classical Absorption Limit in Nanotextured Ultrathin Solar Cells with Dielectric Omnidirectional Back Reflector, ACS Photonics 1 (3), (2014).
A. Ingenito, O. Isabella, M. Zeman

3. Nano-cones on micro-pyramids: modulated surface textures for maximal spectral response and high-efficiency solar cells, Progress in Photovoltaics: Research and application, DOI: 10.1002/pip.2606, (2015).
A. Ingenito, O. Isabella, M. Zeman.

4. Optimized back reflectors for rear diffused c-Si solar cells, Energy procedia 4th International Conference on Silicon Photovoltaics, SiliconPV, (2014).
A. Ingenito, J. C. O. Lizcano, S. L. Luxembourg, R. Santbergen, A. Weeber, O. Isabella, M. Zeman

5. Wet-chemical treatment for improved surface passivation of textured silicon heterojunction solar cells, Energy procedia 4th International Conference on Silicon Photovoltaics, SiliconPV, (2014).
D. Deligiannis, S. Alivizatos, **A. Ingenito**, D. Zhang, M. van Sebille, R. A. C. M. M. van Swaaij, M. Zeman

6. Optimized metal-free back reflectors for high efficiency open rear c-Si solar cells, in Photovoltaics, IEEE Journal of , 6, 1, 34-40, (2016).
A.Ingenito, S. L. Luxembourg, P. Spinelli, J. Liu, J. C. O. Lizcano, A. W. Weeber, O. Isabella, M. Zeman

7. Design and application of ion-implanted polySi passivating contacts for IBC c-Si solar cells, Applied physics letter, 108, (2016).
G. Yang, **A. Ingenito**, N. van Herman, O. Isabella, M. Zeman

8. Simplified process for high efficiency, self-aligned IBC c-Si solar cells combining ion implantation and epitaxial growth: design and fabrication. Solar energy materials & solar cells (paper under rerview).
A. Ingenito, O. Isabella, M. Zeman

Proceedings papers, extended abstracts, technical digests

1. Opto-electronic evaluation of thin double-textured crystalline silicon wafers, Photovoltaic Specialists Conference (PVSC), IEEE 39th, (2014)
A. Ingenito, O. Isabella, M. Zeman

2. Front/rear decoupled texturing in refractive and diffractive regimes for ultra-thin silicon-based solar cells, Optical Nanostructures and Advanced Materials for Photovoltaics, (2013).
O. Isabella, **A. Ingenito**, D. Linssen, M. Zeman

3. Accurate opto-electrical modelling of multi-crystalline silicon wafer-based solar cells, Proceeding on 27th EUPVSEC, (2012).
A. Ingenito, O. Isabella, M. Zeman

4. Opto-electrical approaches for high efficiency and ultra-thin c-Si solar cells, (Oral presentation). Advanced Semiconductor Devices & Microsystems (ASDAM), 10th International Conference on, (2014).
A. Ingenito, O. Isabella, M. Zeman

5. Photonic and plasmonic structures for applications in solar cells, Advanced Semiconductor Devices & Microsystems (ASDAM), 2014 10th International Conference on (Invited talk)
M. Zeman, **A. Ingenito**, H. Tan, D.N. Linssen, R. Santbergen, A. Smets, O. Isabella

6. Light Trapping Concepts for Enhanced Absorption in Thin Silicon Solar Cells. Optical Nanostructures and Advanced Materials for Photovoltaics, PW4C. 4, (2014).
M. Zeman, **A. Ingenito**, H. Tan, D.N. Linssen, R. Santbergen, A. Smets, O. Isabella

7. Radial heterojunction c-Si nanowire solar cells with 11.8% conversion efficiency. Optical Nanostructures and Advanced Materials for Photovoltaics, PW3C. 3, (2014).
O. Isabella, R. Vismara, **A. Ingenito**, F.T. Si, M. Zeman

8. Optimized metal free back reflectors for high efficiency open rear c-Si solar cells, proceeding on 39th PVSC IEEE, (2015).

A. Ingenito, S. L. Luxembourg, P. Spinelli, A. Weeber, O. Isabella, M. Zeman

9. A Benchmarking Study of the Application of a Distributed Bragg Reflector as Back-Reflector on n-Pasha Solar Cells, Proceeding on 31th EUPVSEC, (2015).
S. L. Luxembourg, P. Spinelli, **A. Ingenito**, J. Liu, A. Weeber, O. Isabella, M. Zeman

Invited lectures

1. Design and implementation of advanced light management techniques for absorption enhancement in thin c-Si solar cells. Institute of Silicon Photovoltaics at Helmholtz Zentrum fur Materialen und Energie (30 April, 2015).

2. Advanced light management techniques for building integrated PV (BIPV), Sundays, Arnhem, The Netherlands, (2015).

3. Advanced light management for decreasing cost of c-Si PV: electrically-aware texturing and opto-thermal filters, OSAPV, Suzhou, China, (2015).

Acknowledgments

Finally here I am, writing the last pages of my thesis. The past years flew by like nothing and the first day I arrived in Delft feels like yesterday. In reality in between there is an unforgettable period of my life. For this reason I want to thank all people that contributed to this amazing experience.

My adventure started in September of 2010, when I came to Delft to have an interview for a PhD position in the PVMD group where I met my promoter prof. dr. Miro Zeman. The PhD position was suggested me by my MSc promoter prof. dr. Niccolo' Rinaldi (thanks for that) who also put me in contact with dr. Olindo Isabella. I loved the topic of the Ad-Ligth project, which dealt with light management for c-Si solar cells, from the first day.

I would like to start by expressing my gratitude to my promoter prof. dr. Miro Zeman for believing in me since the beginning and for supporting me to tackle the scientific (and not) challenges faced during the project. Miro, I also want to thank for being such an inspiring group leader and for creating the PVMD family. You are also a good person I really enjoyed our conversations especially about soccer and also thanks for being Slovakian as the captain of SSC Napoli. Another crucial person of my PhD has been dr. Olindo Isabella. Olindo I want to thank you for encouraging me always and for getting the best out of me. We achieved great results and we won many battles together. I hope to continue working with you also in the future. I also want to thank you for being such a good friend. I still remember you and your wife Joelle at Delft station welcoming me the first day I arrived in Delft. Our friendship has become stronger with the time and I hope that will remain the same even though soon I will not be in Delft anymore. My greetings also to your parents and the little Ilaria. I want to thank prof. dr. Rene van Swaaij (thanks for proofreading my propositions), prof. dr. Arthur Weeber and prof. dr. Arno Smets for the scientific discussions and insight on solar cells. Thank you, Arno, for spicing up boring working days with your jokes. I will hear your voice at 12:00 o' clock: 'lunch is the most important meal of the day' for ever. I also want to thank prof. dr. Lina Sarro. I have enjoyed out conversations and I appreciated a lot your advices, support and pragmatic attitude in solving problems.

I am also really grateful with the committee members of my PhD defence for the time and effort they spent in reviewing and commenting my PhD thesis: prof. dr. Arthur Weeber, dr. Pietro Altermatt, prof. dr. Jef Poortmans, dr. Aleš Poruba and prof. dr. Stefan Glunz. Your comments have been a valuable contribution for improving the quality of this manuscript. Your scientific results are an example and a source of inspiration for young researchers. Special thanks goes to Aleš for having me at Fill Factory in Czech Republic for three months. This experience constituted of the most formative period of my PhD, so Aleš thanks for teaching me a lot about c-Si solar cells. I also had a great time in Rožnov pod Radhoštěm bring my regards to Šárka and everyone at Fill Factory. Also special thanks to Arthur for his precious discussions on c-Si solar cells and not only. We could only work together for a short time but I hope there will be more occasions. Many thanks also to Pietro for being such a great scientist and at same time easy-going person. I still remember the first time we meet at EUPVSEC in Frankfurt in 2011. Thanks for inviting me at Leibniz University in Hannover and for the lunch at your place. Good luck and congratulations with your new job at Trina Solar.

Ad-Light project was very successful project thanks also to the industrial partners. I want to thank Solland B.V. and in particular, Luc Augustin for providing the insight on the fabrication process and characterization of the mc-Si solar cell presented in Chapter 3. Unfortunately, our collaboration was really short since Solland got bankrupt after few month Ad-Light project begun. Thanks to ECN for taking over Solland tasks and for processing the solar cells presented in Chapter 7. In particular, thanks to dr. Stefan Luxembourg, dr. Piero Spinelli and prof. dr. Arthur Weeber for the discussions and for actively contributing to the project.

To achieve amazing results you also need an amazing laboratory and people that take care of it. In this respect I am grateful to MartijnTijssen, Stefaan Heirman and Remko Koornneef from the PVMD group for taking care of the measurement setups and the equipment of class 10000. Most of my experiments were carried out at Else Kooi Laboratory (EKL). I would like to thank all technicians for running such complex system. Especially I acknowledge Silvana Milosavljevic for welcoming me and my group in c 100. Special thanks also to: Gregory Pandraud (The boss), Cassan Visser, Johan van der Cingel, Jan Cornelis Wolff, Mario Laros, Wim van der Vlist, Hugo Schellevis, Wim Wien, Alex van den Bogaard, Charles de Boer and Koos van Hartingsveldt and Tom Scholtes (thanks for processing of all epi and implanted samples) for the experiments or measurements they helped me to carry out.

I also want to thanks the secretaries of the PVMD and EKL for the perfect job in solving bureaucratic problems. Especially, I want to thank Laura Bruns, Ilona van der Wenden (get well soon), Diane Vedder, Sharmila Rattansingh, Ellen Schwencke-Karlas and Bianca Knot.

During the PhD I had the pleasure and honour of working and becoming friend with many bright scientists. In particular, I want to thank my office mates: Martijn van Sebille (thanks for translating my summary in Dutch), Paula Perez Rodriguez, dr. Mirjam Theelen, Fai Tong Si, dr. Karol Jarolimek and Mark Workum. Special thanks also to: dr. Jimmy Melskens, Joke Westra, Pavel Babal, Dimitris Deligiannis, Marinus Fischer, Lihao Han, Nasim Rezaei, dr. Hairen Tan, Ravi Vasudevan (The american), dr. Dong Zhang, Johan Blanker, dr. Klaus Jager, dr. Rudi Santbergen (thanks for proofreading of the samenvatting and by the way I am still shocked seeing you drinking a beer ☺), Robin Vismara, Cinzia Silvestri, Bruno Morana, Giuseppe Fiorentino, Daniele Romano, Pangfei Sun (my best chinese friend), dr. Sten Vollebregt, Nikolas Gaio, Yelena Grachova, Aleksandar Jovic, Marta Kluba, dr. Paolo Sberna, dr. Gianpaolo Lorito, dr. Theodoros Zoumpoulidis, dr. Silvio Perro, Paul Procel, Vincenzo Maccaronio, dr. Jia Wei, dr. Rene Poelma, dr. Amir Sammak and Violeta Prodanovic for scientific discussions and not only. Special thanks to Gianluca Limodio (o zi') and dr. Guangtao Yang, we have been a good team during the last year, good luck with your research.

During my PhD, I also supervised some M.Sc. students. I really want to thank Lamprini Gkountakou, Juan Camilo Ortiz Lizcano and Herman Dijkslag for the amazing results carried out. I hope you have all a nice memories of your M.Sc. project and I wish you all the best.

Special thanks to dr. Fabio Santagata and dr. Elina Iervolino, dr. Luigi Mele, dr. Agata Sakic, dr. Alessandro Baiano and Maria De Biase, Francesco Vitale for the time spent together. I really miss you in Delft.

During my PhD I also enjoyed going out, drinking a cup of coffee, playing and watching soccer. Therefore, I want to thank especially: Francesco Vitale (how was it? 20 minutes always straight!) and Benjamin Mimoun (congratulations to you Saskia and Elya for the new born) but also Riccardo Donatatonio (the party organizer), Antonio Farace and Roberto Amabile for the many nights out. It was always a pleasure to drink a coffee with dr. Mauro Marchetti, prof. dr. Marco Spirito, Michele Squillante, Alferio La Pastina, Luca Galatro, Gennaro Gentile, Gianluca Limodio, Carmine De Martino e Raffaele Romano and many others. I want to thank: Fabio Santagata, Roberto Amabile, Alferio La Pastina, Alessandro Baiano, Francesco Vitale, Michele Squillante for making me to feel home every time that Napoli was playing. I really enjoyed playing soccer in Delft and I want to thank: Marco Spirito, Michele Squillante, Alessandro Baiano, Mauro Marchetti, Fabio Santagata, Luigi Mele, Francesco Vitale, Benjamin Mimoun, Marco Di Rosa (We will not forget you) and many others.

I want to thank my friends in Italy Ubaldo Proto, Alfonso Capone Sergio Di Martino, Marco Cioffi e Antonio Crescenzo. Guys every time I come back home it feels like I

never left. I really thank Chantal’s family, Gilbert (thanks also for translating the propositions), Yolande and Xander, for welcoming me as part of it. I really enjoyed the time with you all. Voglio poi ringraziare la mia famiglia, per il continuo sostegno e supporto soprattutto da parte dei mie genitori, Maria e Aniello, mio fratello Antonio e la sua famiglia, mia sorella Ilaria e i miei nonni. Le continue chiamate su Skype non mi hanno fatto sentire mai solo. Mamma e papa’ e’ grazie alla vostra educazione e all’aver lavorato giorno e notte se sono diventato quello che sono. Finally I want to thank the love of my life Chantal. Thanks for su(o)pporting me always, I know sometimes it is not easy but I could not have made it without you. It is thanks to you that I have realized how amazing is being a father. You gave me the best gift ever, our little beauty Ilaria. Piccola thanks for not being a crying baby in this busy period.
Vi amo da morire my girls.

Curriculum Vitae

Andrea Ingenito was born in Salerno (Italy) the 4th of June of 1984. In May 2010 he received the M.Sc. degree (cum laude) in electronics engineering from the University of Naples Federico II. In November 2010 he joined the Photovoltaic Materials and Devices group (PVMD) at Faculty of Electrical Engineering, Mathematics and Computer Science at Delft University of Technology, Delft (The Netherlands) under the supervision of prof. dr. Miro Zeman. At PVMD group he perused the PhD degree with thesis titled opto-electrical surface engineering of wafer-based c-Si solar cells. During his PhD, Andrea has started the activities on homo-junction wafer-based c-Si at PVMD. He was also visiting research at Fill Factory s.r.o in Czech Republic where he acquired fundamental knowledges on the fabrication of wafer-based c-Si solar cells. Andrea has designed and fabricated wafer based c-Si solar cells employing innovative concepts and fabrication processes. He has patented a simplified process flow for the fabrication of interdigitated back contacted (IBC) c-Si solar cells. The cell results based on this process were presented at Silicon PV (Konstanz, 2015). His areas of expertise encompass also the design and application of advanced light management concepts for wafer-based c-Si solar cells. An advanced light trapping scheme capable to demonstrate the $4n^2$ theoretical limit was presented at 28th EUPVSEC (Paris 2013) and 40TH IEEE PVSEC conference (Tampa, 2013). Its further integration in IBC c-Si solar cells with conversion efficiency of 19.8%, received the poster award at 6th WCPEC, (Kyoto, 2014). He also presented this concept and its development at 29th EUPVSEC (Amsterdam, 2013), OSAPV (Canberra 2014), and 10th ASDAM (Smolenice, 2014) conferences. In addition, Andrea has studied and manufactured metal free-photonic crystal as potential solution to enhance light absorption and provide customized PV solutions. For this work he was nominated as finalist for the student award at 42th IEEE conference (New Orleans, 2015) and he won the best student award at the 31th EU-PVSEC (Hamburg, 2015).